ACS SYMPOSIUM SERIES 1092

Nanocatalysis for Fuels and Chemicals

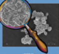

EDITED BY

Ajay K. Dalai

Downloaded by 89.163.35.42 on May 30, 2012 | http://pubs.acs.org
Publication Date (Web): January 20, 2012 | doi: 10.1021/bk-2012-1092.fw001

Nanocatalysis for Fuels and Chemicals

Downloaded by 89.163.35.42 on May 30, 2012 | http://pubs.acs.org
Publication Date (Web): January 20, 2012 | doi: 10.1021/bk-2012-1092.fw001

Downloaded by 89.163.35.42 on May 30, 2012 | http://pubs.acs.org
Publication Date (Web): January 20, 2012 | doi: 10.1021/bk-2012-1092.fw001

ACS SYMPOSIUM SERIES **1092**

Nanocatalysis for Fuels and Chemicals

Ajay K. Dalai, Editor
Professor of Chemical and Biological Engineering
and Canada Research Chair
University of Saskatchewan
Saskatoon, Saskatchewan, Canada

American Chemical Society, Washington, DC

Distributed in print by Oxford University Press, Inc.

Downloaded by 89.163.35.42 on May 30, 2012 | http://pubs.acs.org
Publication Date (Web): January 20, 2012 | doi: 10.1021/bk-2012-1092.fw001

Library of Congress Cataloging-in-Publication Data

Nanocatalysis for fuels and chemicals / Ajay K. Dalai, editor.
p. cm. -- (ACS symposium series ; 1092)
Includes bibliographical references and index.
ISBN 978-0-8412-2685-2 (alk. paper)
1. Catalytic reforming. 2. Nanochemistry. 3. Catalytic cracking. 4. Energy development.
I. Dalai, Ajay Kumar, 1959-
TP690.45.N36 2012
541′.2--dc23
2011048749

The paper used in this publication meets the minimum requirements of American National Standard for Information Sciences—Permanence of Paper for Printed Library Materials, ANSI Z39.48n1984.

Copyright © 2012 American Chemical Society

Distributed in print by Oxford University Press, Inc.

All Rights Reserved. Reprographic copying beyond that permitted by Sections 107 or 108 of the U.S. Copyright Act is allowed for internal use only, provided that a per-chapter fee of $40.25 plus $0.75 per page is paid to the Copyright Clearance Center, Inc., 222 Rosewood Drive, Danvers, MA 01923, USA. Republication or reproduction for sale of pages in this book is permitted only under license from ACS. Direct these and other permission requests to ACS Copyright Office, Publications Division, 1155 16th Street, N.W., Washington, DC 20036.

The citation of trade names and/or names of manufacturers in this publication is not to be construed as an endorsement or as approval by ACS of the commercial products or services referenced herein; nor should the mere reference herein to any drawing, specification, chemical process, or other data be regarded as a license or as a conveyance of any right or permission to the holder, reader, or any other person or corporation, to manufacture, reproduce, use, or sell any patented invention or copyrighted work that may in any way be related thereto. Registered names, trademarks, etc., used in this publication, even without specific indication thereof, are not to be considered unprotected by law.

PRINTED IN THE UNITED STATES OF AMERICA

Downloaded by 89.163.35.42 on May 30, 2012 | http://pubs.acs.org
Publication Date (Web): January 20, 2012 | doi: 10.1021/bk-2012-1092.fw001

Foreword

The ACS Symposium Series was first published in 1974 to provide a mechanism for publishing symposia quickly in book form. The purpose of the series is to publish timely, comprehensive books developed from the ACS sponsored symposia based on current scientific research. Occasionally, books are developed from symposia sponsored by other organizations when the topic is of keen interest to the chemistry audience.

Before agreeing to publish a book, the proposed table of contents is reviewed for appropriate and comprehensive coverage and for interest to the audience. Some papers may be excluded to better focus the book; others may be added to provide comprehensiveness. When appropriate, overview or introductory chapters are added. Drafts of chapters are peer-reviewed prior to final acceptance or rejection, and manuscripts are prepared in camera-ready format.

As a rule, only original research papers and original review papers are included in the volumes. Verbatim reproductions of previous published papers are not accepted.

ACS Books Department

Downloaded by 89.163.35.42 on May 30, 2012 | http://pubs.acs.org
Publication Date (Web): January 20, 2012 | doi: 10.1021/bk-2012-1092.pr001

Preface

Nanocatalysis includes the basics of working with particles 1 billionth of a meter (atomic particle level) in size. Approximately one third of the gross chemical product material involves a catalytic process somewhere in the production chain. Nanocatalysis is one of the most exciting fields emerging from nanoscience. The central focus of nanocatalysis is its contribution to chemical reactions by influencing size, dimension, chemical composition, and morphology, as well as changing the kinetics through nanopatterning. This approach opens new avenues for atom-by-atom design of nanocatalysts with distinct and tunable chemical activity, specificity, and selectivity. This book gives a pedagogical and methodological overview of this exciting and growing field and highlights specific examples in the fields of fuels and chemicals, serving as an instructive introduction for research. It can provide ideas for research and graduate work and as a reference for scientists already active in the field and related areas.

The principle of nanocatalysis is based on the premise that the catalytic materials applied at the nanoscale have better properties, compared to what they exhibit on a macroscale. They enable unique applications in both basic and applied research. The synthesis of nanomaterials for catalytic applications has been the focus for academia and industry, leading to numerous research publications and patents. The topics in this book include the challenges and developments of new nanocatalysts for fuels and chemicals, focusing on the production of synthesis gas, hydrogen, mid-distillates, and alcohols. Hydrodesulphurization (HDS), hydrodenitrogenation (HDN), hydrodearomatization (HAD), hydrodemetalization (HDM), Fischer-Tropsch (FT) process, and other catalytic reactions are presented. The book also includes novel preparation methods and characterization techniques for synthesis of nanocatalysts for fuels and chemicals.

We hope that the collection of papers on “Nanocatalysis for Fuels and Chemicals” will serve as "fuel" for further research and lead to new applications and discoveries.

Dr. Ajay K. Dalai, P.Eng.

Associate Dean, Research and Partnerships
Professor and Canada Research Chair in Bio-Energy and
Environmentally Friendly Chemical Processing
College of Engineering, University of Saskatchewan
57 Campus Drive, Saskatoon, SK Canada S7N 5A9
ajay.dalai@usask.ca (e-mail) ; (306) 966-4768/4771 (telephone) ; (306) 966-4777 (fax)
http://www.engr.usask.ca/~dalai (web)

Downloaded by UNIV OF GUELPH LIBRARY on May 31, 2012 | http://pubs.acs.org
Publication Date (Web): January 20, 2012 | doi: 10.1021/bk-2012-1092.ot001

Editor's Biography

Ajay K. Dalai

Ajay K. Dalai, Ph.D., P.Eng., FEIC, an expert in biochemical technologies, is an associate dean and professor at the College of Engineering, The University of Saskatchewan. He currently holds a Tier 1 *Canada Research Chair in Bioenergy and Environmentally Friendly Chemical Processing*. His research focus is novel catalyst development for gas to liquid (GTL) technologies, biodiesel production and applications, hydrogen/syngas production from waste materials, hydroprocessing of heavy gas oil, value-added products from biomass, and developing environmentally friendly processing methods for improved, reformulated gasoline. The worldwide impact of this research is tremendous in terms of combating pollution and finding alternate energy resources. Dr. Dalai's groundbreaking research in environmentally friendly processing and the conversion of biomass to bio-energy have made him highly sought after as a guest lecturer/speaker at many National and International conferences, Universities, and discussion forums. His leading use of synchrotron radiation research and the *Catalysis and Chemical Reaction Engineering Laboratory* (CCREL) he established at the University of Saskatchewan have generated much interest and collaborative projects with research institutes and universities around the world. His expertise and strategic initiatives in bio-economy have earned him several national and international awards, including the 2011-2012 *Canadian Catalysis Lectureship Award*.

In Nanocatalysis for Fuels and Chemicals; Dalai, A.;
ACS Symposium Series; American Chemical Society: Washington, DC, 2012.

Chapter 1

Investigation of the Role of Surface Nanometric Sulfur and Carbon Moieties in Ni-Catalyzed Steam Reforming of Hydrocarbons

Nicolas Abatzoglou,* Kandaiyan Shanmugapriya, Nadi Braidy, and Jasmin Blanchard

Department of Chemical and Biotechnological Engineering,
Université de Sherbrooke, 2500 Boul. Université,
Sherbrooke, Quebec, Canada J1K 2R1
***E-mail: Nicolas.Abatzoglou@USherbrooke.ca**

Downloaded by 89.163.35.42 on May 30, 2012 | http://pubs.acs.org
Publication Date (Web): January 20, 2012 | doi: 10.1021/bk-2012-1092.ch001

The present study involves the surface modification of unsupported micrometric metallic nickel powder (Ni-255) with varying carbon chain lengths of dialkyl disulfide (DADS) and its use as catalysts in steam reforming of methane (SRM). The mass spectrometry results of methane conversion was investigated under time on stream (TOS) conditions during SRM reaction as a function of temperature (T)=700°C for 12 h at a working condition of CH_4:H_2O molar ratio=1:2 and gas hourly space velocity=19,600 ml/g/h. Graphitic carbon formation on the spent catalysts is quantified by X-ray photoelectron spectroscopy analysis. Catalytic activity and inhibition of carbon formation due to the modification of catalyst surface are reported, and preliminary mechanistic explanations are proposed as well as discussed. A significant effect of sulfur and carbon moieties of the modified catalyst surface on catalytic activity occurs during SRM towards reforming and water-gas shift reaction. Surface modification of the catalysts with DADS molecules inhibits carbon formation to a large extent (by a factor of about 3) during the SRM process.

In Nanocatalysis for Fuels and Chemicals; Dalai, A.;
ACS Symposium Series; American Chemical Society: Washington, DC, 2012.

Downloaded by 89.163.35.42 on May 30, 2012 | http://pubs.acs.org
Publication Date (Web): January 20, 2012 | doi: 10.1021/bk-2012-1092.ch001

Introduction

Heterogeneous catalysis of steam reforming of methane (SRM) is the main industrial process employed for large-scale hydrogen production (*1–3*). Nickel (Ni) nanoparticles supported on high surface area ceramic materials are commercially available robust catalysts for steam reforming of hydrocarbons (*4*). Although precious metal based catalytic formulations have proven highly efficient and show lower carbon formation tendency than Ni, both reasonable catalytic activity and affordable price render Ni-based catalysts more attractive. The formation of carbon species and sintering (*5–8*) are considered to be the main causes of Ni-based catalyst deactivation. Recently, Shen et al. (*9*) carried out SRM over ordered mesoporous Ni-Mg-Al oxide catalysts and demonstrated the important role of mesopores in preserving Ni metal from sintering as well as in preventing inactive coke accumulation during the process. Coke deposits, originating mainly from decomposition of methane and Boudouard reaction, can be minimized by employing higher than stoichiometric steam-to-methane molar ratio (typically between 2 and more than 3). The carbon-forming tendency of Ni-supported catalysts has been well documented in the literature (*10*, *11*). Studies have been devoted to developing Ni catalysts more resistant against coke deposition, the major problem inhibiting the wide scale application of these materials (*12–15*).

Many approaches have been attempted to avoid carbon formation by modifying the surface properties of Ni catalysts. The first approach was based on the control of Ni atom ensemble size via catalyst surface passivation by sulfur moieties. Further studies proved that the ensemble size required for CH_4 dissociation is smaller than that of graphite nucleation. Thus, chemisorbed sulfur decreases the surface density of carbon nucleation sites, substantially reducing the carbon formation rate more than the reforming rate (*16*, *17*). Alloying of Ni-based catalysts is considered as another approach in improving carbon resistance by decreasing the carbon deposition rate or increasing the carbon gasification rate (*18*, *19*). Bengaard et al. (*18*) performed density functional theory (DFT) calculations in combination with kinetic measurements and microkinetic simulations. They concluded that the step edges of Ni, where promoters, such as S, K and Au, bind preferentially, are reactive sites for both CH_4 activation and graphite nucleation. Recently, using DFT, Nikolla et al. reported that, on Ni-Sn alloy, barrier to carbon gasification is lower than that of carbon deposition, while on monometallic Ni, these 2 barriers are considered to be similar (*20*).

Some of our published results raised the possibility of utilizing micrometric Ni-255 catalyst in SRM, circumventing the complexities of supporting catalysts (*21–24*). It was demonstrated that the morphology of ‘fractal’ Ni powder played a dominant role in determining the high coke resistance, stability and catalytic activity of the reforming process and the required temperature level (*21*). It was experimentally verified that as low as stoichiometric water-to-fuel molar ratio (2:1) are possible while retaining excellent levels of steam reforming activity. Rostrup-Nielsen and co-workers performed studies based on the influence of sulfur on catalysts employed for SRM (*1*, *16*, *17*). The basic idea behind these experiments is to modify the catalyst surface with sulfur molecules which do not prohibitively

Downloaded by 89.163.35.42 on May 30, 2012 | http://pubs.acs.org
Publication Date (Web): January 20, 2012 | doi: 10.1021/bk-2012-1092.ch001

poison the reforming process, whereas the graphite formation rate is decreased to such an extent that the net effect is an improved steam reforming catalyst. Abild-Pedersen et al. (*25*) investigated the deactivation of steps in the presence of carbon and sulfur and revealed that the amount of deposited carbon decreases rapidly with increasing sulfur coverage, up to 0.06 monolayer, after which the effect of additional sulfur is less pronounced. They emphasized that the small amount of sulfur present on the surface does not lead to deactivation, but the desired quantity is sufficient to block the steps alone. This has a pronounced effect in eliminating coke formation with moderate deactivation of the methane dissociation rate.

Sulfur adsorbed on metals at both submonolayer and monolayer levels has also attracted considerable attention, especially in the field of surface science (*26*). Alkanethiol and DADS adsorption on metal surfaces forms self-assembled monolayers (SAMs) which are highly ordered and densely packed (*27*, *28*). Studies have investigated the adsorption sites and orientation of thiols on Ni(111), Ni(100) and Ni(110) (*29–31*). Based on various spectroscopic techniques, 3 distinct forms of surface S-phases have been clearly identified, namely, intact molecules, thiolates and atomic sulfur species (*31*, *32*). An interesting study (*33*) into alkane thiol adsorption on Ni(111) was conducted according to the *ab initio* embedding theory to ascertain bonding geometry and adsorption energies on Ni(111). The results revealed that sulfur adsorption at the 3-fold site blocked hydrogen adsorption at the nearby surface. On most metal surfaces, the S-H bond in thiol molecules dissociates on adsorption, leaving surface hydrogen and thiolate gets bound to the surface. According to theoretical calculations, surface hydrogen is expected to induce a recombinative reaction of thiolate to desorb thiol from the surface (*34*). When treated thermally the thiolate typically leads to hydrogenolysis to form the corresponding hydrocarbon. Sulfur compounds are generally present in natural gas in the form of dimethyl disulfide and tert-butyl mercaptan mixture (via deliberately added odorants (*35*)) and/or naturally-occurring hydrogen sulphide. Most previous work focused on nickel metal catalyst poisoning by hydrogen sulphide but, for the first time in the literature, our previous studies addressed the effect of poisoning by organothiols on carbon formation-related catalyst inhibition during SRM (*22*). Initial chemisorption of n-alkanethiol on Ni catalysts was confirmed by infrared spectroscopy and X-ray photoelectron spectroscopy (XPS) analysis. It was determined that the quantities of carbon deposits for n-butanethiol-pretreated catalysts are 2 orders of magnitude lower than those obtained over pristine Ni, under the same temperature and pressure conditions. A subsequent study (*36*) was undertaken to demonstrate the high thermal stability of the Ni-alkanethiol surface by diffuse reflectance infra-red Fourier transform spectroscopy up to 1030°C under Ar carrier gas. It was evident that the so-obtained alkanethiolate SAMs adsorbed on Ni decompose much slower than expected, even at such a high temperature. The interaction of methyl thiol and dimethyl disulfide with Ni(111) was investigated by spectroscopic analysis to identify the local phases and structures associated with it (*37*). This investigation indicated the formation of surface methyl thiolate species, with further dissociation at higher temperature, result in the formation of atomic S along with some co-adsorbed carbon. It is well-known that the dissociative adsorption of dialkyl disulfide (DADS) takes place through the cleavage of unstable S-S bonds without the formation of surface hydrogen and results in the formation of SAMs similar to those of alkanethiols (*26*, *27*, *38*).

In the present study, we examined the effect of Ni catalyst impregnation with DADS on catalyst activity during SRM for a 1:2 molar ratio of CH_4:H_2O. The DADS-impregnated Ni catalysts are denoted herein as Ni-C_nS_2 where n=4, 6, 10 and 12. DADS-impregnated Ni powders were prepared by extended immersion in a DADS/methanol solution under continuous stirring. Coke formation on the spent catalysts was analyzed by XPS.

Materials and Methods

The unsupported Ni catalyst employed in this study is a pure nickel powder (Inco Ni-255). DADS (Aldrich, 99%) of varying carbon chain lengths, such as $C_4H_{10}S_2$, $C_6H_{14}S_2$, $C_{10}H_{22}S_2$ and $C_{12}H_{26}S_2$, served to modify the Ni-255 catalyst surface. They were all liquids at room temperature and were used as received. Methanol solvent (Aldrich, 99%) was also used as received.

The Ni catalyst was impregnated with DADS by immersion of the pristine Ni powder in 10^{-1} M DADS/methanol solutions (5 g of Ni in 100 ml of solution) at room temperature. Immersion time for the preparation of modified catalysts was 20 h. After immersion, all such treated samples were rinsed with fresh methanol until DADS could no longer be detected in the rinsing solution. Finally, the samples were dried for 12 h at ambient temperature and then underwent characterization and reforming tests.

Experimental Set-Up and Protocol

Catalytic activity was measured at atmospheric pressure in a differential reactor set-up that was constructed for real-time monitoring of the reforming reaction (see Figure 1). The experimental set-up is equipped with a gas humidification system, a programmable furnace and a quadrupole mass spectrometer (QMS 300 Gas analyzer). The reactant gas is composed of CH_4 (Praxair, Ultra high purity), Ar (Praxair, Ultra high purity) and steam. Partial pressure of water in the gas, to regulate the CH_4:H_2O molar ratio, is fixed by controlling water temperature through which the reaction gas is bubbled and ensures sufficient gas-liquid contact time. The flow rate is 25 ml min^{-1}. The weighed amount of catalyst (0.25 g) is lightly packed into the inner quartz tube and retained by quartz wool. The inner tube includes a porous, fused quartz disk (coarse porosity 40-90 μm, diameter 1.5 cm) that supports the Ni catalyst bed (see photo in Figure 1). No entrainment of catalyst particles occurs downstream because the catalyst pellet is already lightly compressed and there is sufficient sintering during the early stages of the catalytic reaction to preserve structural integrity of the pellet. Product gases from the reactor cell are sampled with a computer-controlled valve assembly (Valco) and directed to the mass spectrometer for identification. Mass-selected intensities are calibrated with pure standard gases diluted in Ar carrier gas. Overall measurement accuracy is

Downloaded by 89.163.35.42 on May 30, 2012 | http://pubs.acs.org
Publication Date (Web): January 20, 2012 | doi: 10.1021/bk-2012-1092.ch001

Downloaded by 89.163.35.42 on May 30, 2012 | http://pubs.acs.org
Publication Date (Web): January 20, 2012 | doi: 10.1021/bk-2012-1092.ch001

±3%, and reproducibility is ±2%. The protocol for time on stream (TOS) and thermal treatment followed by TOS (TT-TOS) is given in Figure 2. For the sake of convenience, the Ni-255 catalyst after TOS and TT-TOS will be indicated as TOS-Ni-255 and TT-TOS-Ni-255, respectively, and will be referred similarly for other impregnated catalysts, such as TOS-Ni-C_4S_2, TT-TOS-Ni-C_4S_2, etc. In each experiment, furnace temperature is increased at a constant rate of 3°C/min^{-1}. The temperatures reported herein are measured in free-volume of the furnace system with a type K thermocouple that is independent of the temperature control system. Temperature at the surface of the catalyst is tested to determine if the endothermic nature of the reforming reaction causes significant cooling of the active surface. A thermocouple is placed on the surface of the Ni catalyst and another on the surface of the porous, fused quartz disk. The temperature at these 2 places, measured during these tests, is equal to or higher by 12±2°C than in the free-space of the oven when it is kept at 700°C in the latter. These differences are due to uneven radiation emissivity and non-homogeneous convection current profiles, but they are not considered as significant.

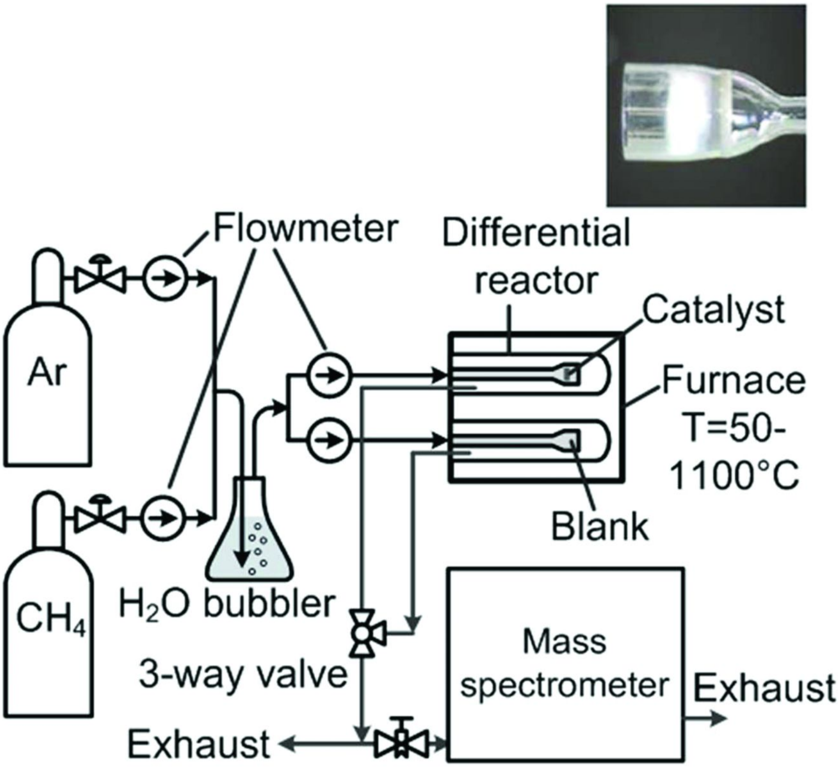

Figure 1. Schematic view of the reformer evaluation bench.

Downloaded by 89.163.35.42 on May 30, 2012 | http://pubs.acs.org
Publication Date (Web): January 20, 2012 | doi: 10.1021/bk-2012-1092.ch001

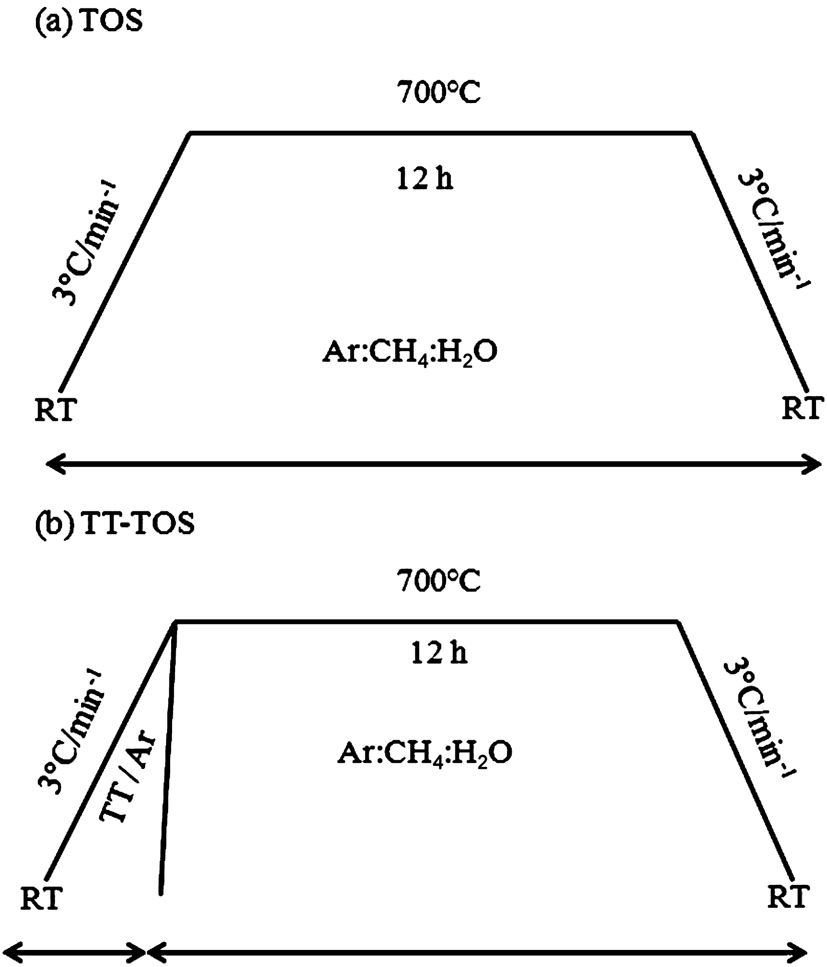
(a) TOS
700°C
12 h
3°C/min-1
3°C/min-1
Ar:CH4:H2O
RT
RT
(b) TT-TOS
700°C
12 h
3°C/min-1
TT/Ar
3°C/min-1
Ar:CH4:H2O
RT
RT

Figure 2. Description of the experimental protocol.

Methane conversion is calculated as follows:

$$CH_4 \text{ conversion } (\%) = ((P_{in,CH_4} - P_{out,CH_4}) / P_{in,CH_4}) \times 100\%$$

Catalyst Characterization

The unsupported Ni catalyst in this study (Inco Ni-255) was a pure nickel powder, with an open filamentary structure and irregular spiky surface; it was produced by the thermal decomposition of nickel tetracarbonyl (*39*). The BET surface area (S_{BET}=0.44 m^2 g^{-1}, particle size range of 1-20 μm) was measured at

77 K with a Quantachrome Autoasorb 1, assuming a 0.162 nm^2 cross-sectional area of N_2. The catalyst's morphology was examined with a JEOL JSM 840 scanning electron microscope (SEM). X-ray photoelectron spectra for catalyst samples were acquired at room temperature with a Kratos HS system and a monochromatized Al Kα (hν = 1486.6 eV) X-ray source operated at 120 W; a 12,000 μm^2 region of the sample was probed. The samples were introduced and maintained at room temperature throughout the measurements. Photoelectron kinetic energies were quantified in a hemispherical electrostatic analyzer working in constant pass energy mode. Background pressure in the analyzing chamber was below 2×10^{-8} Torr. Survey scans (0-1200 eV) and high-resolution Ni 3p, S 2p, C 1s and O 1s spectra were obtained at pass energy of 160 and 40 eV, respectively. Charging effects were corrected by referencing all binding energies with respect to C(1s) binding energy to 284.5 eV (*40*). The uncertainty in peak position was estimated to be ±0.2 eV for all spectra. Ni 3p, S 2p, C 1s and O 1s high-resolution spectra envelopes were analyzed by curve-fitting synthetic peak components with CASAXPS software. The raw experimental data were considered with no preliminary smoothing. Gaussian-Lorentzian product functions and Shirley background subtraction procedures approximated line shapes of the fitting components. Sulfur and carbon atomic percentages were quantified from the integration of S 2p and C 1s core-level spectra with appropriate corrections for photo-ionization cross-sections. Curve fitting was undertaken by starting at the low binding energy side of the S 2p envelope and systematically adding component core levels toward higher binding energies as required.

Downloaded by 89.163.35.42 on May 30, 2012 | http://pubs.acs.org
Publication Date (Web): January 20, 2012 | doi: 10.1021/bk-2012-1092.ch001

Results and Discussion

Catalytic activity of the Ni-255 catalyst impregnated with varying carbon chain lengths of DADS, Ni-C_4S_2, Ni-C_6S_2, Ni-$C_{10}S_2$ and Ni-$C_{12}S_2$ was tested for SRM reaction ($CH_4+2H_2O \rightarrow CO_2+ 4H_2$; $CH_4+H_2O \rightarrow CO+3H_2$) and compared to that of a pristine Ni-255 catalyst. Figure 3 reports the mass spectrometry results of CH_4 conversion under TOS conditions (see Figure 2, Protocol a) during SRM reaction as a function of time at temperature (T)=700°C for 12 h at a working condition of CH_4:H_2O molar ratio=1:2 and gas hourly space velocity=19,600 ml/g/h. The corresponding theoretical value at this T and CH_4:H_2O molar ratio was calculated by Factsage software (*21*) and compared with the experimental results obtained in the present study. Another set of experiments was performed with the thermal treatment of Ni-255, Ni-C_4S_2 and Ni-C_6S_2 catalysts prior to TOS study (see Figure 2, Protocol b). Experimental carbon balance at 700°C was evaluated from feed gas methane and the carbon source from by-products of the reformate, such as CO, CO_2 and CH_4. Carbon balance for all active catalysts involved in the present study was calculated and found to be closer (±0.1) to the theoretical value of 1. The percentage of error in calculation was ±0.04.

Downloaded by 89.163.35.42 on May 30, 2012 | http://pubs.acs.org
Publication Date (Web): January 20, 2012 | doi: 10.1021/bk-2012-1092.ch001

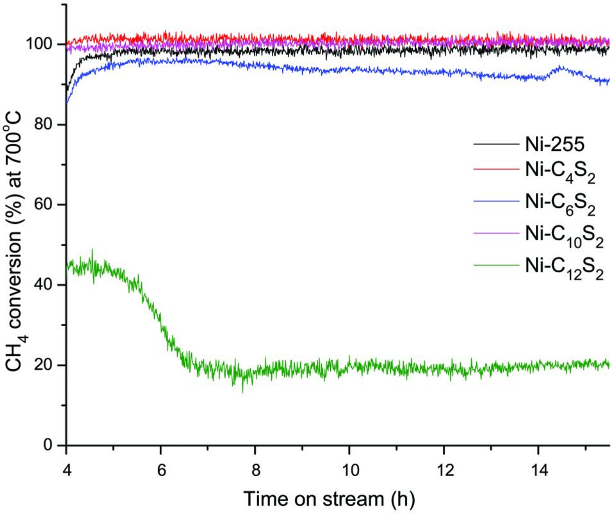

Figure 3. Methane conversion at 700°C under TOS conditions as a function of time. (see color insert)

Figures 4a and b show X-ray photoelectron spectra of the C 1s and S 2p binding energy regions, respectively, for the as-synthesized catalysts Ni-255, Ni-C$_4$S$_2$, Ni-C$_6$S$_2$, Ni-C$_{10}$S$_2$ and Ni-C$_{12}$S$_2$. The C 1s and S 2p spectra obtained after SRM (see Figure 2) under TOS (Protocol a) and TT-TOS (Protocol b) are shown in Figures 5 (a and b) and 6 (a and b), respectively. Curve fitting analysis of the near-surface atom compositions of all samples identified 3 types of carbon moieties in these spectra: graphitic-like carbon (BE≈284.4 eV), aromatic-aliphatic carbon (BE≈285.1 eV) and moieties of carbon attached to oxygen through single, double and triple bonds (BE≈286-289 eV) (*41*, *42*). The peak located at ≈288.2 eV should have mainly originated from the Ni catalyst powder, which was produced commercially by the thermal decomposition of Ni(CO)$_4$ (*39*) and some atmospheric carbon adsorption. The peak observed at BE≈285.1 eV (aromatic-aliphatic) in C 1s spectra of as-synthesized catalysts (see Figure 4) will be referred to as aromatic for TOS and TT-TOS catalysts (see Figure 5 and 6) due to the high probability of aromatic type of carbon build-up during SRM (*22*). The area ratio of S, C and O with respect to Ni and the ratio of graphitic and aliphatic-aromatic type of carbon with respect to the total carbon content of the catalysts were calculated and presented in Table I. In the case of the sulfur S 2p spectral region of as-synthesized catalysts (see Figure 4b), 2 peaks were distinguished at 162.7 and 168 eV (*27*, *31*, *41*). The first peak, corresponding to thiolates, was observed only for the Ni-C$_{12}$S$_2$ as-synthesized catalyst. The second peak, which was typical for sulfonates, was perceived for all DADS-impregnated catalysts. However, the presence of sulfur moieties on the TOS-Ni-C$_4$S$_2$ catalyst was identified qualitatively by time of flight-secondary ion mass spectroscopy (TOF-SIMS). The sulfur signal was not seen in XPS, in case of Ni-C_4S_2, possibly because of less sulfur coverage on the catalyst surface, highly influenced by the short alkyl chain length of the DADS molecule. It is clear from Table I that carbon moieties of the DADS catalysts determine sulfur coverage on the catalyst surface; the higher is the carbon chain of DADS, the higher is the sulfur coverage in case of as-synthesized catalysts.

Downloaded by 89.163.35.42 on May 30, 2012 | http://pubs.acs.org
Publication Date (Web): January 20, 2012 | doi: 10.1021/bk-2012-1092.ch001

Table I. Area ratio of total sulfur, carbon and oxygen on Ni calculated for Ni-255, Ni-C_4S_2, Ni-C_6S_2, Ni-$C_{10}S_2$, and Ni-$C_{12}S_2$ as-synthesized catalysts, after their use in steam reforming tests (TOS) and in steam reforming tests preceded by thermal treatment under Ar carrier gas at 700°C (TT-TOS)

Catalysts	*S/Ni*	*C/Ni*	*O/Ni*	*Graphitic carbon/Total carbon content of the catalyst*	*Aliphatic-aromatic carbon/Total carbon content of the catalyst*
As-synthesized					
Ni-255	0	0.68	1.62	0.08	0.40
Ni-C_4S_2	N.D.	2.90	2.42	0.1	0.69
Ni-C_6S_2	0.01	1.36	2.30	0.1	0.44
Ni-$C_{10}S_2$	0.01	1.66	2.41	0.18	0.42
Ni-$C_{12}S_2$	0.03	1.63	2.17	0.11	0.52
TOS					
TOS-Ni-255	0	2.16	1.12	0.5	0.32[a]
TOS-Ni-C_4S_2	N.D.	0.75	1.16	0.02	0.72[a]
TOS-Ni-C_6S_2	0.03	1.50	1.14	0.1	0.69[a]
TOS-Ni-$C_{10}S_2$	0.02	1.77	1.54	0	0.79[a]
TOS-Ni-$C_{12}S_2$	0.05	1.18	1.56	0	0.80[a]
TT-TOS					
TT-TOS-Ni-255	0	0.87	1.08	0	0.81[a]
TT-TOS-Ni-C_4S_2	0.02	0.76	1.27	0	0.67[a]
TT-TOS-Ni-C_6S_2	0.02	0.58	1.03	0	0.76[a]

*N.D.: Not detectable by XPS analysis. [a] Aromatic carbon/total carbon content of the catalyst.

Downloaded by 89.163.35.42 on May 30, 2012 | http://pubs.acs.org
Publication Date (Web): January 20, 2012 | doi: 10.1021/bk-2012-1092.ch001

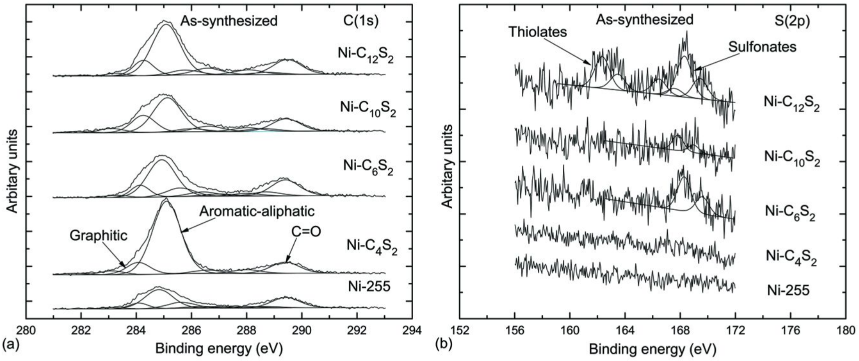

Figure 4. X-ray photoelectron spectra of Ni-255, Ni-C_4S_2, Ni-C_6S_2, Ni-$C_{10}S_2$ and Ni-$C_{12}S_2$ as-synthesized catalysts for (a) carbon C1s and (b) sulfur S 2p.

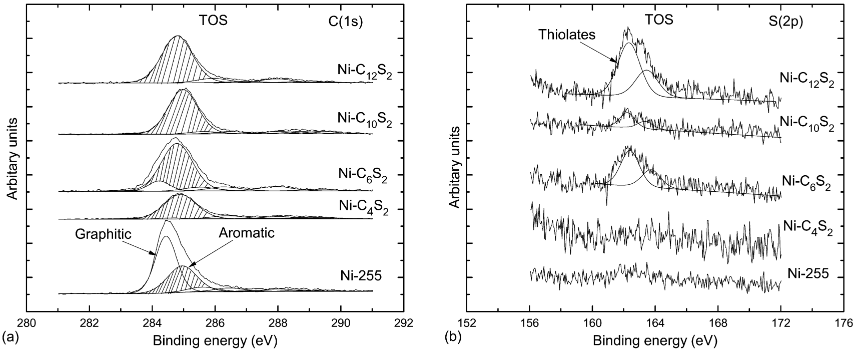

Figure 5. X-ray photoelectron spectra of Ni-255, Ni-C_4S_2, Ni-C_6S_2, Ni-$C_{10}S_2$ and Ni-$C_{12}S_2$ catalysts measured after TOS for (a) carbon C1s and (b) sulfur S 2p.

The morphology (SEM) of the as-synthesized Ni-255 catalyst is presented in Figure 7, and the inset clearly shows the spiky Ni surface. The morphology of the catalysts after TOS and TT-TOS is depicted in Figure 8 and 9, respectively. It can be seen from the SEM pictures that, particularly in the case of the TOS-Ni-C_4S_2 catalyst (see Figure 8b), there are 2 different types of structures (indicated as A and B) which are clearly distinct in the TT-TOS-Ni-C_4S_2 catalyst (see Figure 9b). It is evident that the spiky Ni surface morphology of the as-synthesized catalyst changed to a faceted polyhedral-like structure A during SRM that followed either Protocol a or b (see Figure 2). In all other catalysts under study, the morphology mainly resembled structure A. This type of structure is formed during the initial heating process, the catalysts do not undergo further morphological changes during the reforming operations, and no macroscopic accumulation of carbon particles can be detected. Structure B (see Figures 8b and 9b) resembles the morphology of the as-synthesized catalyst (see Figure 7), and the influence of structure B on catalytic activity and carbon inhibition property during SRM is not yet known because (a) it is difficult to isolate these structures and (b) the observed differences are not conclusive. Furthermore, structure B is not apparent in all other DADS-impregnated catalysts with carbon chain length greater than C_4 (see Figure 8 and 9). Both selectivity and catalytic activity of the Ni-C_4S_2 catalyst (see Figure 10-13) ensure that suitable modification of the Ni-255 catalyst with C_4S_2 molecules plays an important role in maintaining pristine Ni-255 catalytic activity while considerably inhibiting the carbon formation tendency (see Figure 5) during SRM in comparison to all other DADS-impregnated catalysts. The above fact is also well supported by the C/Ni ratio obtained from XPS analysis (Table I), which predicts that carbon content with respect to Ni in TOS-Ni-C_4S_2 is decreased by a factor of about 3 compared to that of the TOS-Ni-255 catalyst.

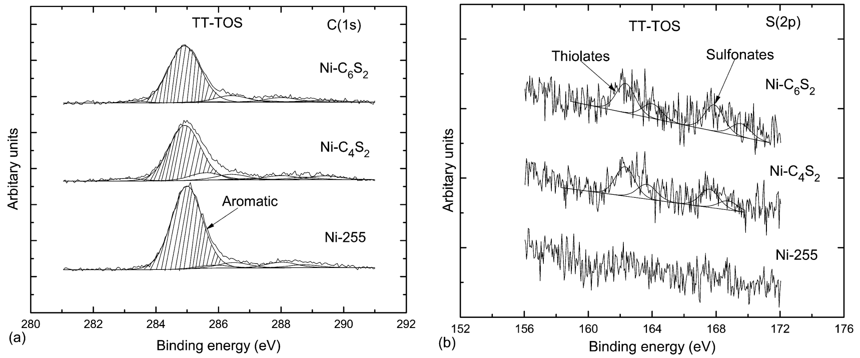

Figure 6. X-ray photoelectron spectra of Ni-255, Ni-C_4S_2 and Ni-C_6S_2 catalysts measured after TOS preceded by thermal treatment (TT) under Ar carrier gas at 700°C for (a) carbon C1s and (b) sulfur S 2p.

The activation of hydrocarbon molecules was not hindered, and catalytic activity of all the catalysts was prolonged for the entire TOS, except for the Ni-$C_{12}S_2$ catalyst (see Figure 3). For the TOS-Ni-$C_{12}S_2$ catalyst, CH_4 conversion was ≈20%. C_{12} carbon in Ni-$C_{12}S_2$ could lead to higher than shorter alkyl moiety-inductive effects and thus alter the geometric and electronic structure of the catalyst surface (*43*). Moreover, XPS analysis of TOS-Ni-$C_{12}S_2$ shows that the presence of an aromatic peak at BE=285.1 eV) in Figure 5 is of greater importance than in shorter carbon chain DADS-impregnated Ni-255 catalysts. The S/Ni ratio of the TOS-Ni-$C_{12}S_2$ catalyst is higher (0.05) in comparison to all other DADS catalysts under TOS conditions (Table I). When the O/Ni ratio of the as-synthesized catalysts is compared with that of counterpart catalysts subjected to TOS and TT-TOS conditions, the O/Ni ratio appears to be decreased for all catalysts. The results indicate that the identity of the carbon moiety attached to the alkyl tail group of the modified catalyst along with partial sulfur coverage (S/Ni) on the surface of the catalysts plays a critical role in determining catalytic activity (Table I). A previous study pointed out that the high stability of the Ni catalysts promoted with sulfur was due to changes in the superficial structure of Ni sites as a consequence of the ensemble size effect (*16*, *17*, *44*), but when the S/Ni ratio reached 0.05 (Table I), as in case of TOS-Ni-$C_{12}S_2$, it then led to deactivation of the catalyst.

Downloaded by 89.163.35.42 on May 30, 2012 | http://pubs.acs.org
Publication Date (Web): January 20, 2012 | doi: 10.1021/bk-2012-1092.ch001

Downloaded by 89.163.35.42 on May 30, 2012 | http://pubs.acs.org
Publication Date (Web): January 20, 2012 | doi: 10.1021/bk-2012-1092.ch001

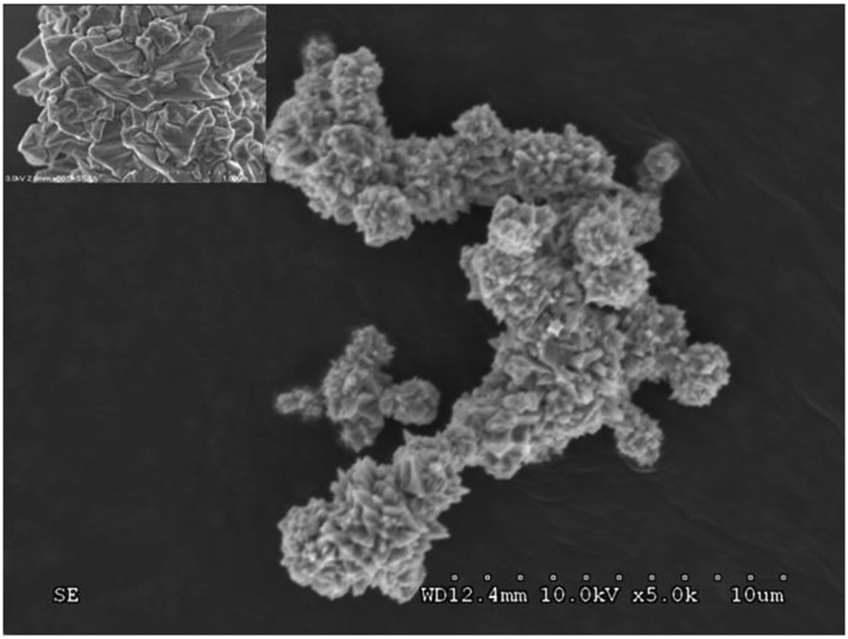

Figure 7. SEM of Ni-255 as-synthesized catalyst (inset shows the spiky Ni surface).

From XPS analysis of the C 1s region of both TOS and TT-TOS catalysts (see Figures 5a and 6a) 2 interesting points should be noted: (i) During TOS (see Figure 2, Protocol a), a well-defined, narrow peak at BE≈284.4 eV assigned to graphitic-like carbon is evident in the TOS-Ni-255 sample, whereas in all other impregnated catalysts, signal intensity due to graphitic-like carbon is lower. This particular graphitic peak is not seen in TT-TOS catalysts with Protocol b in Figure 2. The C 1s and S 2p spectra of the catalysts subjected to TOS conditions (see Figure 5a and b) during SRM illustrate the following factors. It is evident that graphitic type of carbon is inhibited, to a large extent, by the thiolate form of sulfur moieties on the surface of DADS-impregnated catalysts. The S 2p spectra of the catalysts subjected to TT-TOS conditions during SRM are shown in Figure 6b. It is evident that both thiolate and sulfonate forms of sulfur moieties exist on the surface of the DADS-impregnated catalysts. Comparison of Figure 4, 5 and 6 indicates that during TT-TOS, the sulfonate form of sulfur moieties, initially present on the surface of the as-synthesized catalysts (see Figure 4), is not completely transformed to the thiolate form as it occurs during TOS conditions. This suggests that TT modifies the surface so that both thiolate and sulfonate forms of sulfur moieties exist on the catalyst surface. Steam content in the inlet gaseous stream plays an active role in determining the formation of thiolate species under TOS conditions.

Downloaded by 89.163.35.42 on May 30, 2012 | http://pubs.acs.org
Publication Date (Web): January 20, 2012 | doi: 10.1021/bk-2012-1092.ch001

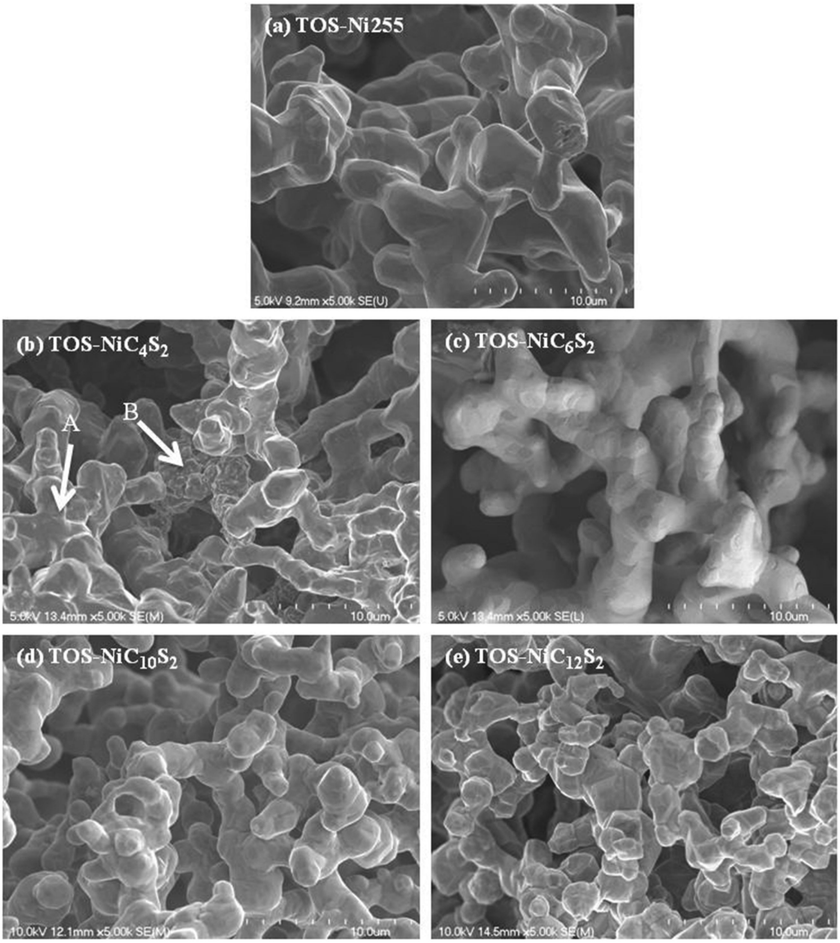
(a) TOS-Ni255
5.0kV 9.2mm x5.00k SE(U)
10.0um
(b) TOS-NiC$_4$S$_2$
A
B
5.0kV 13.4mm x5.00k SE(M)
10.0um
(c) TOS-NiC$_6$S$_2$
5.0kV 13.4mm x5.00k SE(L)
10.0um
(d) TOS-NiC$_{10}$S$_2$
10.0kV 12.1mm x5.00k SE(M)
10.0um
(e) TOS-NiC$_{12}$S$_2$
10.0kV 14.5mm x5.00k SE(M)
10.0um

Figure 8. SEM of (a) TOS-Ni-255, (b) TOS-Ni-C_4S_2, (c) TOS-Ni-C_6S_2, (d) TOS-Ni-$C_{10}S_2$ and (e) TOS-Ni-$C_{12}S_2$ catalysts.

XPS spectral deconvolution studies led to the following conclusions:

(i) Graphitic-like carbon build-up takes place during temperature increase from the ambient condition to 700°C with the gaseous stream inlet during TOS, and it is plausible that TT alters the surface in a way that graphitic-type of carbon formation is controlled effectively. Since the thermal stability of alkanethiols has been shown in a previous publication (*36*) to be highly enhanced when adsorbed at Ni-255, it is possible that, under TOS and TT-TOS conditions, the alkyl groups are altered and form some carbon moieties at the surface of the catalysts. Relative measurement of aromatic carbon and graphitic carbon ratio with respect

to the total carbon content of all catalysts is reported in Table I. The decreased carbon formation/deposition tendency (Table I) can be well correlated to the sulfur moieties observed as thiolates distributed at the surface of the catalysts (see Figures 5b and 6b) .

(ii) A peak associated with aromatic-like carbon located at 285.1 eV (see Figure 5 and 6) is evident in all catalysts that follow either Protocol a or b (see Figure 2) during SRM. During TOS, the intensity of the aromatic-like carbon peak increases gradually in all impregnated catalysts and can be assigned to the increasing chain length of the DADS molecule, but during TT-TOS, the relative ratio of aromatic carbon to total carbon content (Table I) proves that it is particularly higher in TT-TOS-Ni-255 compared to the DADS-impregnated catalysts under study. This essentially confirms the above hypothesis (point *(i))* that relatively small amounts of sulfur moieties (S/Ni = 0.01-0.02) present on the modified catalyst surface highly determine carbon content and are responsible for the formation of different carbon species on the surface of the catalysts.

Downloaded by 89.163.35.42 on May 30, 2012 | http://pubs.acs.org
Publication Date (Web): January 20, 2012 | doi: 10.1021/bk-2012-1092.ch001

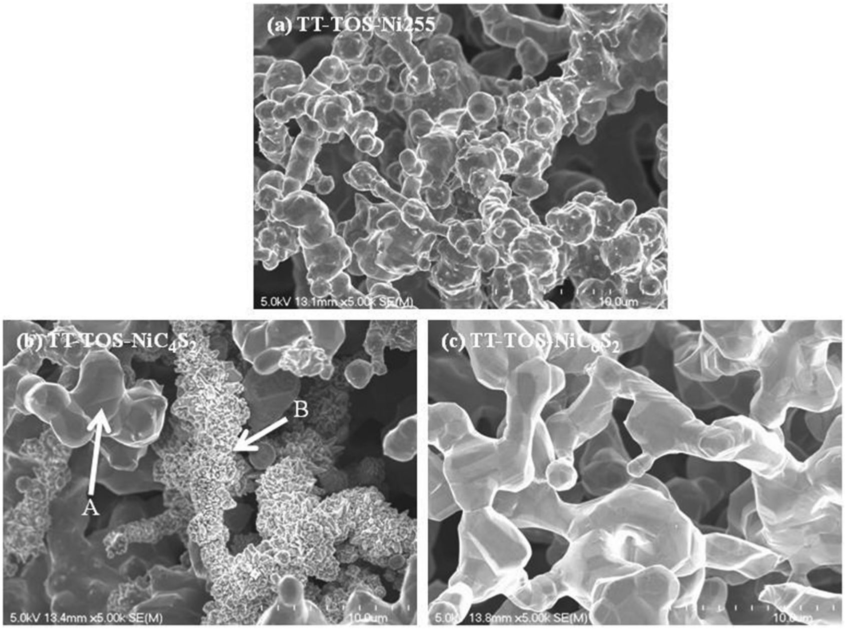

Figure 9. SEM of (a) TT-TOS-Ni-255, (b) TT-TOS-Ni-C_4S_2 and (c) TT-TOS-Ni-C_6S_2 catalysts.

Downloaded by 89.163.35.42 on May 30, 2012 | http://pubs.acs.org
Publication Date (Web): January 20, 2012 | doi: 10.1021/bk-2012-1092.ch001

Figure 10 reports the selectivity of H_2, CO and CO_2 in the gaseous by-product stream over TOS-Ni-255, TOS-Ni-C_4S_2, TOS-Ni-C_6S_2 and TOS-Ni-$C_{10}S_2$ along with theoretical equilibrium values of steam reforming reactor at 1 atm total pressure. The SRM results at 700°C show that although H_2 selectivity is relatively constant and linearly follows CH_4 conversion, CO and CO_2 selectivity varies with carbon chain length of the DADS organic molecule. Under TOS conditions, the increased CO/CO_2 ratio (see Figure 11) over all catalysts along with theoretical equilibrium values of steam reforming reactor at 1 atm total pressure follows the order TOS-Ni-C_6S_2>TOS-Ni-C_4S_2>TOS-Ni-255>TOS-Ni-$C_{10}S_2$≈theoretical. The S 2p spectra of TOS catalysts (see Figure 5) are highly reflected in the CO/CO_2 ratio (see Figure 11). It is clear from Figure 11 that in the TOS-Ni-C_6S_2 catalyst, as long as the thiolate form of sulfur moieties is high (S/Ni=0.03), the CO/CO_2 ratio is superior to all other DADS-impregnated catalysts. When S/Ni=0.02 (Table I), as observed in the case of TOS-Ni-$C_{10}S_2$ catalyst, the CO/CO_2 ratio is also found to be lower. Thus, it can be concluded that the variation in the amount of sulfur moieties present on the TOS catalysts determines the CO/CO_2 ratio and further serves as a key factor to control water-gas shift (WGS) extent during SRM. The stable catalytic activity of the catalysts towards reforming and WGS reaction during TOS over all catalysts along with theoretical equilibrium values of steam reforming reactor at 1 atm total pressure is depicted in Figure 12 along with CH_4 conversion. In Figure 12, it is clear that CH_4 conversion (98±2%) is complete in TOS-Ni-255 and TOS-Ni-C_4S_2 catalysts, and the reforming activity of TOS-Ni-C_4S_2 is slightly higher than in the TOS-Ni-255 catalyst. Furthermore, the influence of thermal treatment (TT-TOS) (see Figure 2, Protocol b) of the catalysts on reforming vs. WGS activity was determined and shown in Figure 13. The results are compared with those obtained from catalysts subjected to TOS conditions (see Figure 2, Protocol a), and it can be concluded that thermal treatment had no influence on CH_4 conversion in case of TT-TOS-Ni-255 and TT-TOS-Ni-C_4S_2, but slightly increased CH_4 conversion (≈10±2%) in the TT-TOS-Ni-C_6S_2 catalyst relative to the TOS results (compare Figure 12 and 13, respectively). Similarly, the reforming activity of TT-TOS-Ni-255 and TT-TOS-Ni-C_6S_2 was not altered, but a decrease in reforming activity (≈10%) was encountered in the case of the TT-TOS-Ni-C_4S_2 catalyst due to thermal treatment compared to the TOS counterpart. WGS activity of the catalysts is much more pronounced after TT-TOS than during TOS and can be correlated with the presence of both thiolates and sulfonates on the surface of the catalysts (see Figure 6). The underlying mechanism influencing the activity of the catalysts in reforming vs. WGS is not well understood at this stage. Table II presents the findings of the reproducibility study under TOS conditions: the data illustrate that the reported results have a low statistical error. Thus, it can be concluded that the modified surface properties of the Ni-255 catalyst through impregnation of the lower chain DADS molecule are influential in determining both catalytic activity and carbon tolerance of the catalyst.

Downloaded by 89.163.35.42 on May 30, 2012 | http://pubs.acs.org
Publication Date (Web): January 20, 2012 | doi: 10.1021/bk-2012-1092.ch001

Table II. Reproducibility of the catalysts

Catalysts	*TOS*			*TOS reproducibility*			*Error*		
	(%)			*(%)*			*(%)*		
	Conversion	*Reforming*	*WGS*	*Conversion*	*Reforming*	*WGS*	*Conversion*	*Reforming*	*WGS*
TOS-Ni-255	98.4	83.1	15.3	98.4	83.8	14.6	0	0.84	4.79
TOS-Ni-C_6S_2	93.2	84.8	8.4	94	85.5	8.5	0.85	0.82	1.18
TOS-Ni-C_4S_2	100	89.3	10.7	100	89.5	10.6	0	0.22	0.94

Downloaded by 89.163.35.42 on May 30, 2012 | http://pubs.acs.org
Publication Date (Web): January 20, 2012 | doi: 10.1021/bk-2012-1092.ch001

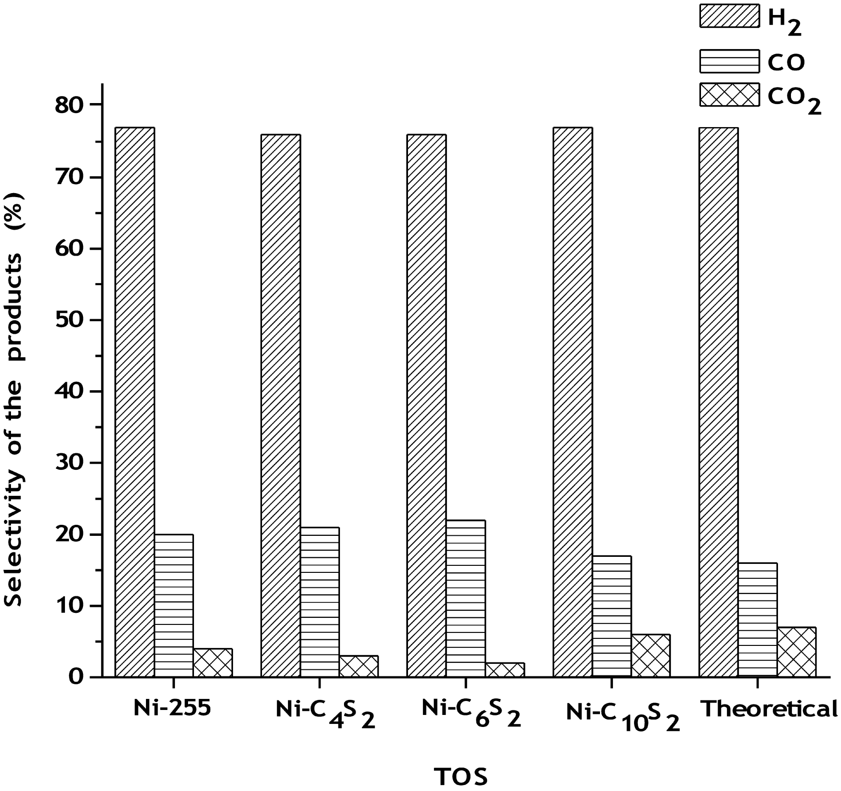

Figure 10. Selectivity of the products obtained for Ni-255, Ni-C_4S_2, Ni-C_6S_2 and Ni-$C_{10}S_2$ catalysts during time on stream (TOS) along with theoretical equilibrium values of steam reforming reactor at 1 atm total pressure.

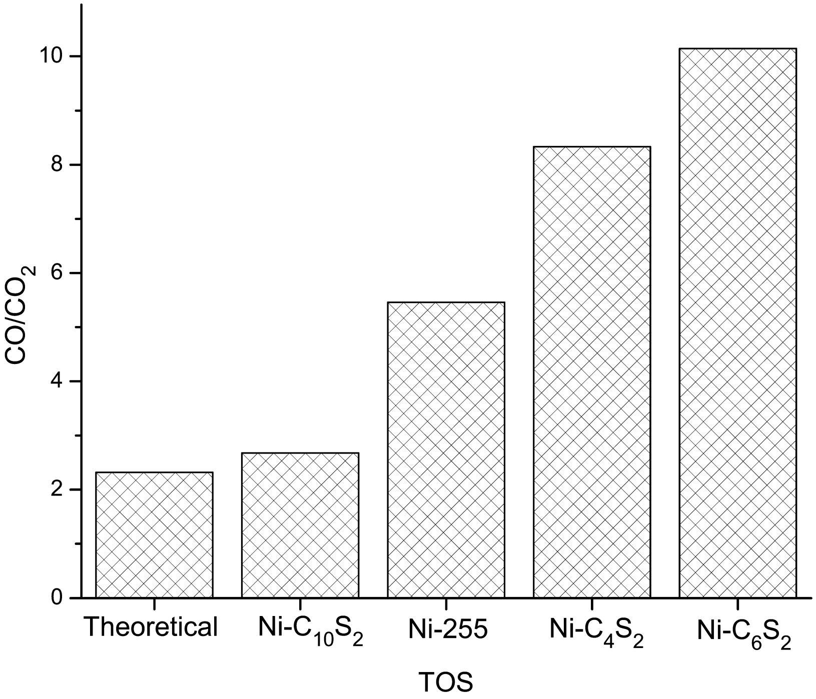

Figure 11. CO/CO$_2$ ratio obtained for Ni-255, Ni-C$_4$S$_2$ and Ni-C6S2 catalysts during time on stream (TOS) along with theoretical equilibrium values of steam reforming reactor at 1 atm total pressure.

Downloaded by 89.163.35.42 on May 30, 2012 | http://pubs.acs.org
Publication Date (Web): January 20, 2012 | doi: 10.1021/bk-2012-1092.ch001

Downloaded by 89.163.35.42 on May 30, 2012 | http://pubs.acs.org
Publication Date (Web): January 20, 2012 | doi: 10.1021/bk-2012-1092.ch001

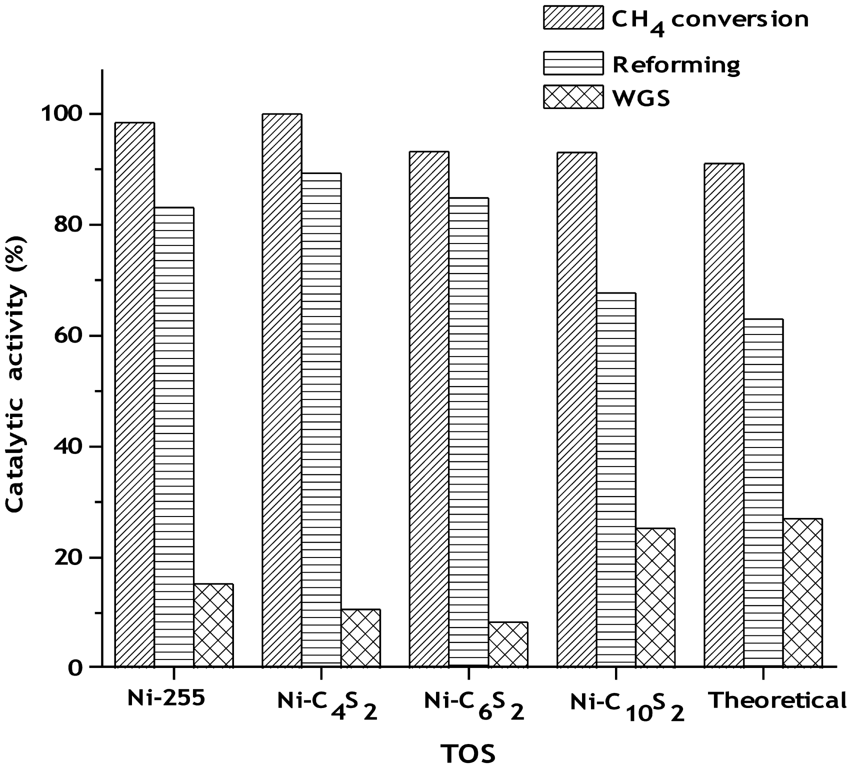

Figure 12. Catalytic activity of Ni-255, Ni-C_4S_2, Ni-C_6S_2 and Ni-$C_{10}S_2$ catalysts towards reforming and WGS during time on stream (TOS) along with theoretical equilibrium values of steam reforming reactor at 1 atm total pressure.

Downloaded by 89.163.35.42 on May 30, 2012 | http://pubs.acs.org
Publication Date (Web): January 20, 2012 | doi: 10.1021/bk-2012-1092.ch001

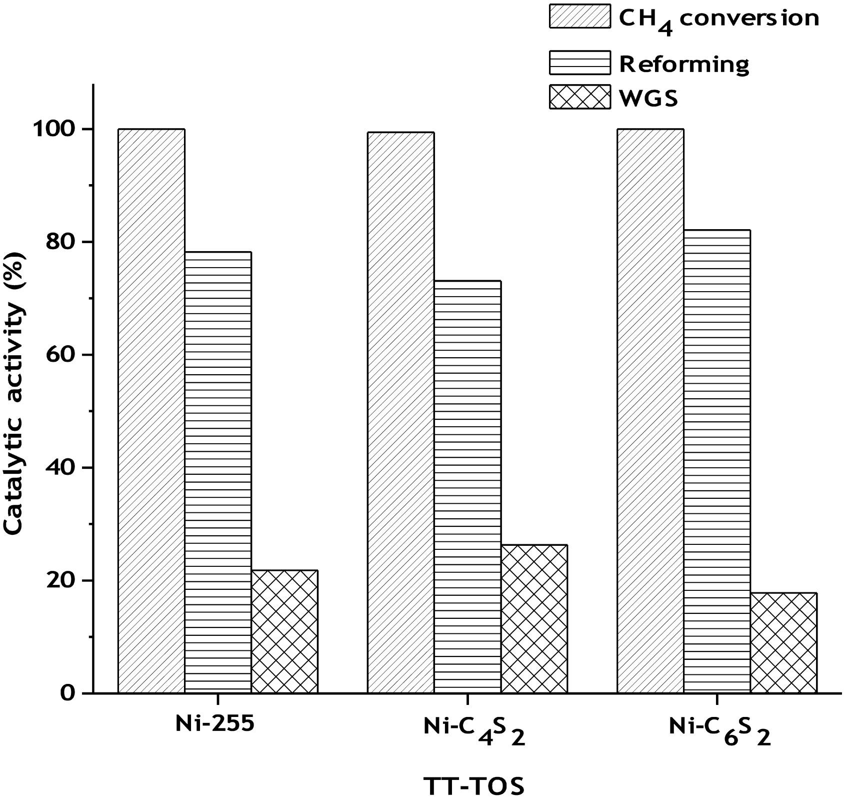

Figure 13. Catalytic activity of Ni-255, Ni-C_4S_2 and Ni-C_6S_2 catalysts towards reforming and WGS during time on stream (TOS) preceded by thermal treatment (TT) under Ar carrier gas at 700 °C.

Conclusion

The conclusions from the present study are as follows:

A. Short-chain DADS-impregnated Ni-255catalysts, namely, Ni-C_4S_2, Ni-C_6S_2 and Ni-$C_{10}S_2$, were the most stable impregnated catalysts with respect to deactivation during SRM. An intriguing result is that the quantities of carbon deposits for the Ni-C_4S_2 catalyst were 3 orders of magnitude lower than with pristine Ni, under the same temperature and pressure conditions. This illustrates the increased carbon tolerance of the modified catalyst with respect to the pristine Ni-255 catalyst under the same reaction conditions during SRM.

B. The main proven advantage of modifying the catalysts by impregnation with DADS molecules is the decrease of graphitic-like carbon formation/ deposition at the catalyst surface during SRM.

C. The aromatic-like carbon peak increases gradually with augmented chain length of the DADS molecule during TOS.
D. Relatively small amounts of sulfur moieties ($S/Ni \leq 0.03$) on the surface of the modified catalysts highly determine the carbon content and are found to be responsible for the formation of different carbon species on the catalyst surface, but when the S/Ni ratio exceeds the relative amount ($S/Ni=0.05$), it serves as the inducing factor for deactivation of the TOS-Ni-$C_{12}S_2$ catalyst.
E. Variation in the amount of sulfur moieties on the TOS catalysts is highly reflected in the CO/CO_2 ratio and serves as a key factor to control WGS extent during SRM.
F. By suitable modification of the catalyst with a lower carbon chain length DADS molecule, it is possible to maintain the high catalytic activity of pristine metallic Ni-255 while considerably inhibiting carbon formation during SRM.

It can thus be concluded that the surface chemistry of the catalysts tested is highly complex. Ni, S and C species/moieties, differentially affecting chemisorption and adsorbed C, H and O bearing chemical groups, must be studied thoroughly with advanced surface analysis techniques (i.e., TOF-SIMS and nano-SIMS).

Downloaded by 89.163.35.42 on May 30, 2012 | http://pubs.acs.org
Publication Date (Web): January 20, 2012 | doi: 10.1021/bk-2012-1092.ch001

Acknowledgments

We thank Sonia Blais for her assistance in XPS measurements and Stéphane Gutierrez for the SEM pictures.

References

1. Rostrup-Nielsen, J. R.; Sehested, J.; Norskov, J. K. *Adv. Catal.* **2002**, *47*, 65–139.
2. Rostrup-Nielsen, T. *Catal. Today* **2005**, *106*, 293–296.
3. Pena, M. A.; Gomez, J. P.; Fierro, L. G. *Appl. Catal., A* **1996**, *144*, 7–57.
4. Matsumara, Y.; Nakamori, T. *Appl. Catal., A* **2004**, *258*, 107–114.
5. Sehested, J. *Catal. Today* **2006**, *111*, 103–110.
6. Rostrup-Nielsen, J. R.; Trimm, D. L. *J. Catal.* **1997**, *48*, 155–65.
7. Bartholomew, C. H. *Appl. Catal., A* **2001**, *212*, 17–60.
8. Van Hook, J. P. *Catal. Rev.: Sci. Eng.* **1980**, *21*, 1–51.
9. Shen, W.; Komatsubara, K.; Hagiyama, T.; Yoshida, A.; Naito, S. *Chem. Commun.* **2009**, 6490–6492.
10. Yamazaki, O.; Tomishige, K.; Fujimoto, K. *Appl. Catal., A* **1996**, *136*, 49–56.
11. Kim, J. H.; Suh, D. J.; Park, T. J.; Kim, K. L. *Appl. Catal., A* **2000**, *197*, 191–200.
12. Silva Neto, A. V.; Sartoratto, P. P. C.; Rangel, M. C. *Stud. Surf. Sci. Catal.* **2007**, *167*, 475–480.

13. Mondal, K. C.; Choudhary, V. R.; Joshi, U. A. *Appl. Catal., A: Gen* **2007**, *316*, 47–52.
14. Jeong, H.; Kimb, K.; Kimb, D.; Songa, I. K. *J. Mol. Catal. A: Chem.* **2006**, *246*, 43–48.
15. Triantafyllopoulos, N. C.; Neophytides, S. G. *J. Catal.* **2006**, *239*, 187–199.
16. Rostrup-Nielsen, J. R. *J. Catal.* **1984**, *85*, 31–43.
17. Andersen, N. T.; Topsoe, F.; Alstrup, I.; Rostrup-Nielsen, J. R. *J. Catal.* **1987**, *104*, 454–465.
18. Bengaard, H. S.; Norskov, J. K.; Sehested, J.; Clausen, B. S.; Nielsen, L. P.; Molenbroek, A. M.; Rostrup-Nielsen, J. R. *J. Catal.* **2002**, *209*, 365–384.
19. Besenbacher, F.; Chorkendroff, I.; Clausen, B. S.; Hammer, B.; Molenbroek, A. M.; Norskov, J. K.; Stensgaard, I. *Science* **1998**, *279*, 1913–1915.
20. Nikolla, E.; Holewinski, A.; Schwank, J.; Linic, S. *J. Am. Chem. Soc.* **2006**, *128*, 11354–11355.
21. Rakass, S.; Oudghiri-Hassani, H.; Rowntree, P.; Abatzoglou, N. *J. Power Sources* **2006**, *158*, 485–496.
22. Rakass, S.; Oudghiri-Hassani, H.; Abatzoglou, N.; Rowntree, P. *J. Power Sources* **2006**, *162*, 579–588.
23. Oudghiri-Hassani, H.; Abatzoglou, N.; Rakass, S.; Rowntree, P. *J. Power Sources* **2007**, *171*, 811–817.
24. Oudghiri-Hassani, H.; Rakass, S.; Abatzoglou, N.; Rowntree, P. *J. Power Sources* **2007**, *171*, 850–855.
25. Abild-Pedersen, F.; Lytken, O.; Engbaek, J.; Nielsen, G.; Chorkendroff, Ib.; Norskov, J. K. *Surf. Sci.* **2005**, *590*, 127–137.
26. Love, J. C.; Estroff, L. A.; Kriebel, J. K.; Nuzzo, R. G.; Whitesides, G. M. *Chem. Rev.* **2005**, *105*, 1103–1169.
27. Nuzzo, R. G.; Zegarski, B. R.; Dubois, L. H. *J. Am. Chem. Soc.* **1987**, *109*, 733–740.
28. Tamada, K.; Akiyama, H.; Wei, T. X.; Kim, S. A. *Langmuir* **2003**, *19*, 2306–2312.
29. Kahn, B. E.; Chaffins, S. A.; Gui, J. Y.; Lu, F.; Stern, D. A.; Hubbard, A. T. *Chem. Phys.* **1990**, *141*, 21–39.
30. Parker, B.; Gellman, A. J. *Surf. Sci.* **1993**, *292*, 223–234.
31. Rufael, T. S.; Huntley, D. R.; Mullins, D. R.; Gland, J. L. *J. Phys. Chem.* **1995**, *99*, 11472–11480.
32. Fischer, C. J.; Woodruff, D. P.; Jones, R. G.; Cowie, B. C. C.; Formoso, V. *Surf. Sci.* **2002**, *496*, 73–86.
33. Mullins, D. R.; Huntley, D. R.; Tang, T.; Saldin, D. K.; Tysoe, W. T. *Surf. Sci.* **1997**, *380*, 468–480.
34. Voznyy, O.; Dubowski, J. J. *J. Phys. Chem. C* **2008**, *112*, 3726–3733.
35. Scentinel F-20 Product Literature, Chevron Phillips Chemical Company.
36. Oudghiri-Hassani, H.; Abatzoglou, N.; Rakass, S.; Rowntree, P. *WIT Trans. Ecol. Environ.* **2007**, *105*, 177−186.
37. Fernandez, A.; Espinos, J. P.; Gonzalez-Elipe, A. R.; Kerkar, M.; Thompson, P. B. J.; Ludecke, J.; Scragg, G.; de Carvalho, A. V.; Woodruff, D.

Downloaded by 89.163.35.42 on May 30, 2012 | http://pubs.acs.org
Publication Date (Web): January 20, 2012 | doi: 10.1021/bk-2012-1092.ch001

P.; Fernandez-Garcia, M.; Conesa, J. C. *J. Phys.: Condens. Matter* **1995**, *7*, 7781–7796.

38. Biebuyck, H. A.; Bain, C. D.; Whitesides, G. M. *Langmuir* **1994**, *10*, 1825–1831.
39. Lenel, F. V. *Powder Metallurgy: Principles and Applications*; MPIF, Princeton, NJ, 1980; p 40.
40. Volmer, M.; Stratmann, M.; Viefhaus, H. *Surf. Interface Anal.* **1990**, *16*, 278–282.
41. Huntley, D. R. *J. Phys. Chem.* **1992**, *96*, 4550–4558.
42. Rufael, T. S.; Huntley, D. R.; Mullins, D. R.; Gland, J. L. *J. Phys. Chem. B* **1998**, *102*, 3431–3440.
43. John, N. S.; Kulkarni, G. U.; Datta, A.; Pati, S. K.; Komori, F.; Kavitha, G.; Narayana, C.; Sanyal, M. K. *J. Phys. Chem. C* **2007**, *111*, 1868–1870.
44. Alstrup, I.; Andersen, N. T. *J Catal.* **1987**, *104*, 466–479.

Downloaded by 89.163.35.42 on May 30, 2012 | http://pubs.acs.org
Publication Date (Web): January 20, 2012 | doi: 10.1021/bk-2012-1092.ch001

Chapter 2

Photocatalytic Hydrogen Production from Aqueous Alcohol Solution with Titanium Dioxide Nanocomposites

**Satoshi Kaneco,*,[1] Takuya Miwa,[1] Katsumasa Hachisuka,[1]
Hideyuki Katsumata,[1] Tohru Suzuki,[2] Suresh Chand Verma,[3]
and Kunihiro Sugihara[3]**

**[1]Department of Chemistry for Materials, Graduate School of Engineering,
Mie University, Tsu, Mie 514-8507, Japan
[2]Environmental Preservation Center, Mie University,
Tsu, Mie 514-8507, Japan
[3]Chubu Electric Power Co., Inc., Midori-ku, Nagoya 459-8522, Japan
*E-mail: kaneco@chem.mie-u.ac.jp**

Downloaded by OHIO STATE UNIV LIBRARIES on May 31, 2012 | http://pubs.acs.org
Publication Date (Web): January 20, 2012 | doi: 10.1021/bk-2012-1092.ch002

The photocatalytic hydrogen production from aqueous alcohol solution was evaluated with ZnO/TiO_2, SnO/TiO_2, CuO/TiO_2, Al_2O_3/TiO_2 and $CuO/Al_2O_3/TiO_2$ nanocomposites. A mechanical mixing method, followed by the solid-state reaction at elevated temperature, was used for preparing of nanocomposite photocatalyst. Among these nanocomposite photocatalysts, the maximal photocatalytic hydrogen production was obtained by using $CuO/Al_2O_3/TiO_2$ nanocomposites. Nano-sized TiO_2 photocatalytic hydrogen technology has great potential for low-cost, environmentally friendly solar-hydrogen production to support the future hydrogen economy.

As natural oil reserves become depleted, attention will increasingly focus on alternative energy sources. Hydrogen is one of the most promising energy carriers for future energy systems, consisting of the fuel-cell vehicles and the fuel-cell power-generation technologies. Hydrogen can be extracted from water, alcohol, natural gas, biomass, and other carbonaceous sources. Methanol has

In Nanocatalysis for Fuels and Chemicals; Dalai, A.;
ACS Symposium Series; American Chemical Society: Washington, DC, 2012.

Downloaded by OHIO STATE UNIV LIBRARIES on May 31, 2012 | http://pubs.acs.org
Publication Date (Web): January 20, 2012 | doi: 10.1021/bk-2012-1092.ch002

been recommended as the most preferred source for hydrogen fuel among the high energy density liquid fuels. It can be converted to hydrogen by several reactions, containing oxidative methanol reforming, partial oxidation of methanol, methanol steam reforming, methanol decomposition and photocatalytic oxidation. The photocatalytic hydrogen formation with the methanol decomposition appears to be very powerful method for the practical and low-cost technologies in the hydrogen-based energy system. For hydrogen production from aqueous methanol solution, depending on reaction conditions and on whether metal (or metal oxide) catalyst used, Sakata et al. (*1–4*) have described that the reaction can proceed either stepwise, involving stable intermediates such aldehydes and acids (Eqs. (1)–(3)).

$$\mathrm{MeOH(l)} \xrightarrow[\text{Catal.}]{h\upsilon} \mathrm{HCHO(g)} + \mathrm{H_2(g)} \quad \Delta G^\circ{}_1 = 64.1\ \mathrm{kJ/mol}\ [25] \qquad (1)$$

$$\mathrm{HCHO(g)} + \mathrm{H_2O(l)} \xrightarrow[\text{Catal.}]{h\upsilon} \mathrm{HCOOH(l)} + \mathrm{H_2(g)} \quad \Delta G^\circ{}_2 = 47.8\ \mathrm{kJ/mol} \qquad (2)$$

$$\mathrm{HCOOH(l)} \xrightarrow[\text{Catal.}]{h\upsilon} \mathrm{CO_2(g)} + \mathrm{H_2(g)} \quad \Delta G^\circ{}_3 = -95.8\ \mathrm{kJ/mol} \qquad (3)$$

One-step on the catalyst surface to give the overall reaction (Eq. (4)) has been reported by Chen et al. (*5*).

$$\mathrm{MeOH(l)} + \mathrm{H_2O(l)} \xrightarrow[\text{Catal.}]{h\upsilon} \mathrm{CO_2(g)} + 3\mathrm{H_2(g)} \quad \Delta G^\circ{}_4 = 16.1\ \mathrm{kJ/mol} \qquad (4)$$

Hydrogen is produced in all of these steps. The water-splitting reaction is endothermic and requires an input energy of 237 kJ/mol (*6*). Methanol has a lower splitting energy relative to water.

In this article, we describe the photocatalytic hydrogen production from aqueous methanol solution with photocatalyst nanocomposite.

Experimental

Photocatalyst TiO_2 P-25 was supplied from Degussa Co. Ltd., Germany (anatase 75%, rutile 25%, BET specific surface area 48 m^2/g, mean particle size 25 nm). Nanopowders (ZnO, SnO, CuO and Al_2O_3) were purchased from Sigma-Aldrich. The mean diameter and specific surface area were 50−70 nm and and 15−25 m^2/g for ZnO, 18 nm and 47 m^2/g for SnO, 33 nm and 29 m^2/g for CuO and 40−47 nm and 35−40 m^2/g for Al_2O_3. Methanol (99.8%, Nacalai Tesque, Inc., Japan) was used as received without further purification. Laboratory

Downloaded by OHIO STATE UNIV LIBRARIES on May 31, 2012 | http://pubs.acs.org
Publication Date (Web): January 20, 2012 | doi: 10.1021/bk-2012-1092.ch002

pure water was obtained from an ultrapure water system resulting in a resistivity > 18 MΩ cm.

A mechanical mixing method was used for the preparation of nanocomposite photocatalyst. The oxide powders were mixed with the mortar. An electric furnace was used for sintering at 500 °C under an air atmosphere. The furnace was heated from ambient to the final calcinating temperature of 773 K at a rate of 4.7 K/min and then the temperature was kept constant for 3 h.

The pyrex column vessel reactor (inner volume: 55.6 mL) was used for the photocatalytic production of hydrogen from aqueous methanol solution. The pyrex glass cuts off all wavelength below 300 nm. Typically, 20 mg of the nanocomposite photocatalysts were added to 30 mL of 10 vol% methanol solution in the photoreactor. A 15 W black light with a maximum emission of ~352 nm was applied as light source, which was positioned on the side of photoreactor. The light intensity was 1.0 mW/cm^2 for 320 to 410 nm wavelengths. The nanocomposite photocatalysts were continuously dispersed in the aqueous methanol solution by a magnetic stirrer during the irradiation. The temperature of the suspension in the photoreactor was kept constant by the water bath. The irradiation time was 3 h. The hydrogen product from the aqueous methanol solution was analyzed by gas chromatography with thermal conductivity detector (TCD).

Results and Discussion

TiO_2 is considered as an excellent photocatalyst for hydrogen production because of its resistance to chemical and photochemical corrosion in aggressive aqueous environments and due to its activity towards both light and aqueous solutions such as water and methanol. Noble metal loading onto titanium oxide has been widely studied for hydrogen formation, and has been reported to be very effective to improve its photocatalytic activity since it can contribute to efficient electron hole-separation. However, considering the high costs incurred by the consumption of noble metals, it is very important to fabricate a highly efficient and cost-effective photocatalyst, meanwhile, converting them into environment-friendly products. Because Cu-containing titanium dioxide is cheaper compared with noble metal loaded one, its utilization has been energetically investigated for the photocatalytic hydrogen production. Sreethawong and Yoshikawa (*7*) have reported that Cu-loaded TiO_2 gave about 2-fold higher hydrogen generation activity compared with the optimum value of the Ni loaded case. Wu and Lee (*8*) have investigated hydrogen generation with TiO_2 with deposited Cu, and proven that oxidation of metal copper occurred during reaction induced high hydrogen generation activity. Bandara et al. (*9*) and Choi el al. (*10*) have produced TiO_2 photocatalysts loaded with CuO, and found that hydrogen production was dramatically improved by CuO relative to pure TiO_2. From these studies (*7–10*), it can be known that Cu component is very useful for the photocatalytic production of hydrogen gas.

The quick recombination of photogenerated electrons (e^-) and holes (h^+) lowers the photocatalytic efficiency of TiO_2. The use of a charge transfer catalyst

(CTC) to prepare a binary photocatalyst is an alternative way to achieve better photocatalytic activities because the charge transfer catalyst is able to trap the photogenerated electrons (e^-) and holes (h^+) in its domain. Hence, the effect of metal oxide cocatalysts on the photocatalytic hydrogen production over TiO_2 was investigated for the simple mixing fabrication methods.

Effect of ZnO Cocatalyst

The effect of ZnO cocatalyst on the photocatalytic hydrogen production from aqueous methanol solution with titanium dioxide was investigated. The results are shown in Table 1. The photocatalytic hydrogen formation with 1.5 wt% ZnO/TiO_2 was larger 1.3 times relative to that obtained in pure TiO_2. Therefore, ZnO cocatalyst was slightly effective for enhancing the photocatalytic hydrogen production from aqueous methanol solution using titanium dioxide.

Downloaded by OHIO STATE UNIV LIBRARIES on May 31, 2012 | http://pubs.acs.org
Publication Date (Web): January 20, 2012 | doi: 10.1021/bk-2012-1092.ch002

Table 1. Photocatalytic hydrogen production from 10 vol% methanol solution with ZnO/TiO_2. Reproduced from ref (*11*). Copyright 2010, with permission from Elsevier

ZnO doping concentration (wt%)	*H_2 production (μmol/g)*
0	135
0.5	35
1.0	75
1.5	180
2.0	20

Photocatalyst, 20 mg; Reaction time, 3 hours; Methanol concentration, 10 vol%.

Effect of SnO Cocatalyst

The influence of SnO cocatalyst on the photocatalytic hydrogen formation from aqueous 10 vol% methanol solution with TiO_2 was studied. The results are shown in Table 2. The maximum hydrogen formation was obtained with 1.0 wt% SnO/TiO_2, and the amout was larger 2.0 times compared with that observed with only TiO_2. Hence, the addition of SnO oxide as the cocatalyst was moderately effective for the enhanced photocatalytic hydrogen formation from methanol solution with TiO_2.

Table 2. Photocatalytic hydrogen production from 10 vol% methanol solution with SnO/TiO_2. Reproduced from ref (*11*). Copyright 2010, with permission from Elsevier

ZnO doping concentration (wt%)	*H_2 production (μmol/g)*
0	135
0.5	85
1.0	270
1.5	215
2.0	40

Photocatalyst, 20 mg; Reaction time, 3 hours; Methanol concentration, 10 vol%.

Table 3. Photocatalytic hydrogen production from 10 vol% methanol solution with CuO/TiO_2. Reproduced from ref (*11*). Copyright 2010, with permission from Elsevier

ZnO doping concentration (wt%)	*H_2 production (μmol/g)*
0	135
0.5	350
1.0	540
1.5	370
2.0	425
3.0	0

Photocatalyst, 20 mg; Reaction time, 3 hours; Methanol concentration, 10 vol%.

Downloaded by OHIO STATE UNIV LIBRARIES on May 31, 2012 | http://pubs.acs.org
Publication Date (Web): January 20, 2012 | doi: 10.1021/bk-2012-1092.ch002

Effect of CuO Cocatalyst

The effect of CuO cocatalyst addition on the photocatalytic hydrogen production in aqueous 10 vol% methanol solution using titanium oxide was investigated. The results are shown in Table 3. The trend for the photocatalytic hydrogen formation was roughly convex pattern, and the mximum efficiency was 540 μmol/g•cat with 1.0 wt% CuO. Wu and Lee (*8*) have investigated the photocatalytic hydrogen evolution with copper-deposited TiO_2 from the aqueous methanol solution (42%), and reported that the optimum Cu loading was approximately 1.2 wt%. The incident radiation forms electrons from the valence band to the conduction band, the band gap energy being lowered by copper incorporation. A photo-induced electron reduces water to hydrogen while methanol, the sacrificial reagent for hole, gets oxidized. Because the CuO conduction band is located below that of TiO_2, electron transfer to the conduction band of CuO is possible. The phenomenon becomes significant when a part of incident radiation has wavelength in the UV range. The hole transfer from the valance band of TiO_2 to that of CuO is also allowable for the same reason. The

Downloaded by OHIO STATE UNIV LIBRARIES on May 31, 2012 | http://pubs.acs.org
Publication Date (Web): January 20, 2012 | doi: 10.1021/bk-2012-1092.ch002

combined effects of CuO with TiO_2 are responsible for the enhanced hydrogen production.

Effect of Al_2O_3 Cocatalyst

The influence of the addition of Al_2O_3 cocatalyst on the photocatalytic hydrogen formation in aqueous 10 vol% methanol solution with TiO_2 was evaluated. The results are shown in Table 4. The optimal of Al_2O_3 doping concentration was 0.5 wt%, and the hydrogen production amount was 815 μmol/g•cat. With only 0.5 wt% Al_2O_3/TiO_2, the production of hydrogen was extraordinary. Even after the remeasurement, the results were same and the reason could not be made clear. The phoocatalytic activity for hydrogen formation increased in the order ZnO, SnO, CuO and Al_2O_3. The 0.5 wt% Al_2O_3/TiO_2 photocatalytic activity was approximately 6 times better than that obtained with TiO_2. When the electron–hole (e–h) pair is produced by the UV light, the activated energy is large enough to excite the photogenerated electron (e^-) from the TiO_2 band (3.2 eV) into the Al_2O_3 band (>5.0 eV) (*12*, *13*). Nevertheless, the photogenerated hole (h^+) in the TiO_2 cannot transfer to the Al_2O_3 region energetically. Therefore, the recombination of the photogenerated electron (e^-) and hole (h^+) pair is suppressed by the separation. Hence, the estimated phenomenon may be attributed to the enhanced hydrogen formation.

Table 4. Photocatalytic hydrogen production from 10 vol% methanol solution with CuO/TiO_2. Reproduced from ref (*11*). Copyright 2010, with permission from Elsevier

Al_2O_3 doping concentration (wt%)	*H_2 production (μmol/g)*
0	135
0.3	125
0.5	815
1	35
1.5	135

Photocatalyst, 20 mg; Reaction time, 3 hours; Methanol concentration, 10 vol%.

Hydrogen Formation over $CuO/Al_2O_3/TiO_2$ Composite

The photocatalytic hydrogen production with the nanocomposite composed of ternary components, TiO_2, CuO and Al_2O_3, were investigated in the aqueous methanol solution. Table 5 shows the effect of CuO doping concentration on the photocatalytic H_2 production with CuO/0.2 wt% Al_2O_3/TiO_2. As the doping concentration for CuO increased until 0.4 wt%, the hydrogen formation amount incrased. Over 0.4 wt% CuO, the hydrogen amount decrased. The maximum hydrogen production was observed with 0.4 wt% CuO/0.2 wt% Al_2O_3/TiO_2, and the amount was 1185μmol/g•cat.

Downloaded by OHIO STATE UNIV LIBRARIES on May 31, 2012 | http://pubs.acs.org
Publication Date (Web): January 20, 2012 | doi: 10.1021/bk-2012-1092.ch002

Table 5. Effect of CuO doping concentration on the photocatalytic hydrogen production with CuO/0.2 wt% Al_2O_3/TiO_2 from 10 vol% methanol solution. Reproduced from ref (*11*). Copyright 2010, with permission from Elsevier

CuO doping concentration (wt%)	*H_2 production (μmol/g)*
0.1	340
0.2	685
0.3	1070
0.4	1185
0.5	935

Photocatalyst, 20 mg; Reaction time, 3 hours; Methanol concentration, 10 vol%.

Table 6 presents the influence of doping CuO concentration on the photocatalytic hydrogen formation with CuO/0.3 wt% Al_2O_3/TiO_2. With increasing the CuO content until 0.2 wt%, the photocatalytic H_2 formation increased up to 1200 μmol/g•cat. Above 0.2 wt% CuO doping concentration, the amount for hydrogen production decreased.

Table 6. Effect of CuO doping concentration on the photocatalytic hydrogen production with CuO/0.3 wt% Al_2O_3/TiO_2 from 10 vol% methanol solution. Reproduced from ref (*11*). Copyright 2010, with permission from Elsevier

CuO doping concentration (wt%)	*H_2 production (μmol/g)*
0	125
0.1	715
0.2	1200
0.3	1015
0.4	855
0.5	755

Photocatalyst, 20 mg; Reaction time, 3 hours; Methanol concentration, 10 vol%.

Table 7 shows the effect of doping concentration for CuO on the photocatalytic hydrogen production with CuO/0.4 wt% Al_2O_3/TiO_2. The optimum CuO doping concentration was obtained with 0.2 wt%, and the hydrogen amount was 1075μmol/g•cat. When the Al_2O_3 doping concentration was 0.2 wt%, the maximum hydrogen formation was obtained in the doping concentration of CuO 0.4 wt%. As the doping concentration of Al_2O_3 increased to 0.3 and 0.4 wt%, the optimal doping concentrations for CuO shifted to 0.2 wt%.

Downloaded by OHIO STATE UNIV LIBRARIES on May 31, 2012 | http://pubs.acs.org
Publication Date (Web): January 20, 2012 | doi: 10.1021/bk-2012-1092.ch002

Table 7. Effect of CuO doping concentration on the photocatalytic hydrogen production with CuO/0.4 wt% Al_2O_3/TiO_2 from 10 vol% methanol solution. Reproduced from ref (*11*). Copyright 2010, with permission from Elsevier

CuO doping concentration (wt%)	*H_2 production (μmol/g)*
0.1	665
0.2	1075
0.3	585
0.4	755

Photocatalyst, 20 mg; Reaction time, 3 hours; Methanol concentration, 10 vol%.

The influence of Al_2O_3 doping concentration on the photocatalytic hydrogen production with 0.2 wt% $CuO/Al_2O_3/TiO_2$ was investigated in the methanol solution. The data is shown in Table 8. The photocatalytic hydrogen production roughly had a convex pattern, and the maximum amout was observed with 0.3 wt% Al_2O_3 doping concentration (1200 μmol/g•cat).

Table 8. Effect of Al_2O_3 doping concentration on the photocatalytic hydrogen production with 0.2 wt% $CuO/Al_2O_3/TiO_2$ from 10 vol% methanol solution. Reproduced from ref (*11*). Copyright 2010, with permission from Elsevier

Al_2O_3 doping concentration (wt%)	*H_2 production (μmol/g)*
0.2	685
0.25	935
0.3	1200
0.35	880
0.4	1075

Photocatalyst, 20 mg; Reaction time, 3 hours; Methanol concentration, 10 vol%.

Table 9 reports the effect of Al_2O_3 doping concentration on the photocatalytic H_2 formation with 0.3 wt% $CuO/Al_2O_3/TiO_2$. The best hydrogen formation was obtained with 0.2 wt% Al_2O_3 doping concentration, and the formation amount was 1070μmol/g•cat.

Table 9. Effect of Al_2O_3 doping concentration on the photocatalytic hydrogen production with 0.3 wt% $CuO/Al_2O_3/TiO_2$ from 10 vol% methanol solution. Reproduced from ref (*11*). Copyright 2010, with permission from Elsevier

Al_2O_3 doping concentration (wt%)	*H_2 production (μmol/g)*
0.1	715
0.2	1070
0.3	1015
0.4	585

Photocatalyst, 20 mg; Reaction time, 3 hours; Methanol concentration, 10 vol%.

Downloaded by OHIO STATE UNIV LIBRARIES on May 31, 2012 | http://pubs.acs.org
Publication Date (Web): January 20, 2012 | doi: 10.1021/bk-2012-1092.ch002

Table 10 presents the influence of Al_2O_3 doping concentration on the photocatalytic hydrogen formation with 0.4 wt% $CuO/Al_2O_3/TiO_2$. The optimum composite photocatalyst was 0.4 wt% CuO/0.2 wt% Al_2O_3/TiO_2 for the H_2 prodcution. With increasing the CuO doping concentration, the peak of convex curves moved to the lower Al_2O_3 content.

Table 10. Effect of Al_2O_3 doping concentration on the photocatalytic hydrogen production with 0.4 wt% $CuO/Al_2O_3/TiO_2$ from 10 vol% methanol solution. Reproduced from ref (*11*). Copyright 2010, with permission from Elsevier

Al_2O_3 doping concentration (wt%)	*H_2 production (μmol/g)*
0.1	620
0.2	1185
0.3	855
0.4	755

Photocatalyst, 20 mg; Reaction time, 3 hours; Methanol concentration, 10 vol%.

Consequently, it was found that the photocatalytic hydrogen production proved a close relationship between the CuO and Al_2O_3 doping concentrations. The maximum hydrogen formation (1200 μmol/g•cat) was obtained using 0.2 wt% CuO/0.3 wt% Al_2O_3/TiO_2 nanocomposite photocatalysts.

Reaction Mechanism

In order to better understand the photocatalytic hydrogen formation process from the aqueous methanol solution, a possible mechanism based on the literature (*7–10*) is estimated as follow.

Step A

$$CuO/Al_2O_3/TiO_2 \xrightarrow{h\upsilon} e^{-}(CuO/Al_2O_3) + h^{+}(TiO_2) \qquad (5)$$

$$h^{+} + H_2O \longrightarrow H^{+} + \bullet OH \qquad (6)$$

$$2H^{+} + 2e^{-} \xrightarrow[CuO,\ Al_2O_3]{} H_2 \qquad (7)$$

Step B

$$CH_3OH + h^{+} \longrightarrow H^{+} + \bullet CH_2OH \qquad (8)$$

$$\bullet CH_2OH + h^{+} \longrightarrow H^{+} + HCHO \qquad (9)$$

$$2H^{+} + 2e^{-} \xrightarrow[CuO,\ Al_2O_3]{} H_2 \qquad (10)$$

$$HCHO + \bullet OH + h^{+} \longrightarrow H^{+} + HCOOH \qquad (11)$$

Step C

$$HCOOH \longrightarrow HCOO^{-} + H^{+} \qquad (12)$$

$$HCOO^{-} + 2h^{+} \longrightarrow H^{+} + CO_2 \qquad (13)$$

$$2H^{+} + 2e^{-} \xrightarrow[CuO,\ Al_2O_3]{} H_2 \qquad (14)$$

Downloaded by OHIO STATE UNIV LIBRARIES on May 31, 2012 | http://pubs.acs.org
Publication Date (Web): January 20, 2012 | doi: 10.1021/bk-2012-1092.ch002

Downloaded by OHIO STATE UNIV LIBRARIES on May 31, 2012 | http://pubs.acs.org
Publication Date (Web): January 20, 2012 | doi: 10.1021/bk-2012-1092.ch002

The overall process can be divided into three steps. In the initial step (Eqs. (5)−(7)), there exists a water-splitting process on the surface of TiO_2 photocatalyst which can be found anywhere. The rate of water-splitting is limited by accumulation of active photogenerated holes and hydroxyl radicals. In second step (Eqs. (8)−(11)), the photogenerated holes attack the produced methanol to form formaldehyde, which further oxidized by both hydroxyl radicals and photogenerated holes to produce formic acid (*14*). At third step (Eqs. (12)−(14)), the formic acid is decarboxylated by the photo-Kolbe reaction to release CO_2 [28]. The H^+ deprotonated during whole process transfers to the loaded CuO and Al_2O_3 particles and then reduce to hydrogen by the photogenerated electrons.

Wang et al. (*15*) have produced $ZnO/TiO_2/SnO_2$ mixtures with the molar ratio of $ZnO:TiO_2:SnO_2 = 4:1:1$ from the component oxide powders ZnO, TiO_2 and SnO_2 by solid-state reaction at elevated temperature. In the photocatalytic degradation of methyl orange, the mass photocatalytic activity of $ZnO/TiO_2/SnO_2$ mixture was 2.0 times that of TiO_2, 16.4 times that of SnO_2 and 0.92 times that of ZnO, i.e. $ZnO/TiO_2/SnO_2$ composite was photocatalytically more active than the pure TiO_2 and SnO_2 but less active than ZnO. The photocatalytic activity for hydrogen production with $CuO/Al_2O_3/TiO_2$ nanocomposites was approximately ten times that of pure TiO_2.

The photocatalytic hydrogen production with $CuO/Al_2O_3/TiO_2$ nanocomposites was better compared with those obtained with CuO/TiO_2 and Al_2O_3/TiO_2. Hence, $CuO/Al_2O_3/TiO_2$ nanocomposites represented the synergy effect for the hydrogen production. Loading of metal and metal oxide particles on the surface of TiO_2 can inhibit charge recombination. The most frequently used metal is Pt, which is very efficient but expensive. Lower cost alternative metals, such as Cu and Al should become possible substitution. Metal ion doping on TiO_2 can expand its photo-response to visible region through formation of impurity energy levels (*16*).

Conclusion

The deposition of CuO and Al_2O_3 into TiO_2 greatly enhance the photocatalytic activity of TiO_2 toward hydrogen production from aqueous methanol solution. The photocatalytic activity with 0.2 wt% CuO/0.3 wt% Al_2O_3/TiO_2 for hydrogen production was about 10 times that of pure TiO_2. Methanol dehydrogenation has application in indirect methanol fuel cells, where methanol is first reformed to hydrogen in an energy-consuming step (*17*). Photocatalytic dehydrogenation of methanol has the advantage of supplying the reforming energy from sunlight.

Acknowledgments

The authors gratefully acknowledge the support that received from the Chubu Electric Power Co. Inc. The present research was partly supported by Grant-in-Aid for Young Scientists (B) 21710079 from the Ministry of Education, Culture, Sports, Science, and Technology of Japan. All experiments were conducted at Mie University. Any opinions, findings, conclusions, or recommendations expressed

in this paper are those of the authors and do not necessarily reflect the view of the supporting organizations.

References

1. Kawai, T.; Sakata, T. *J. Chem. Soc., Chem. Commun.* **1980**, 694.
2. Kawai, T.; Sakata, T. *Chem. Lett.* **1981**, *10*, 81.
3. Sakata, T.; Kawai, Y. *Chem. Phys. Lett.* **1981**, *80*, 341.
4. Sakata, T.; Kawai, T.; Hashimoto, K. *Chem. Phys. Lett.* **1982**, *88*, 50.
5. Chen, J.; Ollis, D. F.; Rulkens, W. H.; Bruning, H. *Water Res.* **1999**, *33*, 669.
6. Choi, H. J.; Kang, M. *Int. J. Hydrogen Energy* **2007**, *32*, 3841.
7. Murcia-Mascarós, S.; Navarro, R. M.; Gómez-Sainero, L.; Costantino, U.; Nocchetti, M.; Fierro, J. L. G. *J. Catal.* **2001**, *198*, 338.
8. Wu, G-S.; Wang, L-C.; Liu, Y-M.; Cao, Y.; Dai, W-L.; He-Yong, H.; Fan, K-N. *Appl. Surf. Sci.* **2006**, *253*, 974.
9. Yoong, L. S.; Chong, F. K.; Dutta, B. K. *Energy* **2009**, *34*, 1652.
10. Xu, S.; Sun, D. D. *Int. J. Hydrogen Energy* **2009**, *34*, 6096.
11. Miwa, T.; Kaneco, S.; Katsumata, H.; Suzuki, T.; Ohta, K.; Verma, S. C.; Sugihara, K. *Int. J. Hydrogen Energy* **2010**, *35*, 6554.
12. Yang, C-S.; Wang, Y-J.; Shih, M-S.; Chang, Y-T.; Hon, C-C. *Appl. Catal., A* **2009**, *364*, 182.
13. Shibata, K.; Kiyoura, T.; Kitagawa, J.; Sumiyoshi, T.; Tanabe, K. *Bull. Chem. Soc. Japan* **1973**, *46*, 2985.
14. Chen, T.; Feng, Z. C.; Wu, G. P.; Shi, J. Y.; Ma, G. J.; Ying, P.; Can, L. *J. Phys. Chem. C* **2007**, *111*, 8005.
15. Wang, C.; Xu, B-Q.; Wang, X.; Zhao, J. *J. Solid State Chem.* **2005**, *178*, 3500.
16. Ni, M.; Leung, M. K. H.; Leung, D. Y. C.; Sumathy, K. *Renewable Sustainable Energy Rev.* **2007**, *11*, 401.
17. Ishihara, A.; Mitsushima, S.; Kamiya, N.; Ota, K. *J. Power Sources* **2004**, *126*, 34.

Downloaded by OHIO STATE UNIV LIBRARIES on May 31, 2012 | http://pubs.acs.org
Publication Date (Web): January 20, 2012 | doi: 10.1021/bk-2012-1092.ch002

Downloaded by STANFORD UNIV GREEN LIBR on May 31, 2012 | http://pubs.acs.org
Publication Date (Web): January 20, 2012 | doi: 10.1021/bk-2012-1092.ch003

Chapter 3

Effect of Metal Ions on Light Gas Oil Upgrading over Nano Dispersed MoS_x Catalysts Using *in Situ* H_2

Lei Jia, Abdulaziz Alghamdi, and Flora T. T. Ng[*]

Department of Chemical Engineering, University of Waterloo,
200 University Avenue West, Waterloo, Ontario, Canada N2L3G1
[*]E-mail: fttng@uwaterloo.ca

Hot water extraction and steam injection techniques are used to recover the bitumen from the oil sands or from deep underground deposits generating bitumen emulsions. A novel one-step bitumen upgrading process was developed in our laboratory where the water in the bitumen emulsion was activated through the water gas shift reaction (WGSR) to provide *in situ* H_2 for hydrodesulfurization (HDS) and upgrading of the bitumen. The catalyst precursor, phosphomolybdic acid, was transformed into a nano dispersed Mo sulfide catalyst *in situ* during the upgrading reaction. This nano dispersed Mo catalyst was found to be effective for upgrading light gas oil (LGO) derived from Alberta oil sands with *in situ* H_2. The effect of Ni, Co, Fe, V and K on the nano dispersed Mo sulfide catalyst for the upgrading of LGO was investigated. Ni, Co promoted both WGSR and HDS. V and K inhibited HDS although they promoted WGSR. Fe showed no significant effect on either WGSR or HDS. Ni was found to be the best promoter for HDS. Atthough K was the best promoter for WGSR, however, K apparently inhibited HDS completely but did not affect the boiling point distribution of the oil product. The effects of water content, syn-gas composition and reaction temperature were also discussed. Extra water inhibited HDS when usingeither *in situ* H_2 or molecular H_2. Syn-gas could be used for providing *in situ* H_2 for LGO upgrading. Higher reaction temperature favoured both HDS and hydrocracking.

Downloaded by STANFORD UNIV GREEN LIBR on May 31, 2012 | http://pubs.acs.org
Publication Date (Web): January 20, 2012 | doi: 10.1021/bk-2012-1092.ch003

Introduction

Recently the depletion of conventional petroleum sources has attracted worldwide attention. Heavy oil especially oil sands bitumen is considered as a valuable form of energy. The production of clean fuel from heavy oil and bitumen is limited by the high production cost and in complying with stricter environmental regulations. Canada has a large reserve of oil sands bitumen and heavy oil. Currently, hot water extraction or steam injection techniques are used to recover the bitumen from the oil sands or heavy oil from deep underground deposits. Recovery of bitumen via steam injection or hot water extraction of oil sands produces bitumen emulsion, which is a mixture of water and oil. As water is known to be an inhibitor for upgrading and other hydrotreating processes, normally surfactants are added to break the bitumen emulsion and remove water before the bitumen is upgraded. Molecular hydrogen (H_2) is applied for hydrotreating processes, such as vis-breaking and upgrading which includes hydrodesulfurization (HDS) and hydrodenitrogenation (HDN). This conventional technique requires expensive surfactants and molecular H_2. A novel one step process wherein emulsion breaking and upgrading occurred in the same reactor using *in situ* H_2 generated from the water present in the emulsion via the water gas shift reaction (WGSR) was developed in our research laboratory (*1*). This process does not involve any surfactant and molecular H_2. The key for this process is a nano-dispersed catalyst (unsupported) derived from a Mo precursor. A nano-dispersed Mo sulfide catalyst can interact more efficiently with the large molecules present in the bitumen, and achieve better quality and yield of the oil product.

Previous research by Moll et. al. (*2*) has demonstrated that *in situ* H_2 was even more effective than molecular H_2 for upgrading a sample of Cold Lake bitumen emulsion (22wt% H_2O, 4.4 wt% S dry, 8780 CP@40°C), which meant *in situ* H_2 is a promising and economical alternative source of molecular H_2 for industrial upgrading processes. Fundamental studies were carried out on the hydrotreating of different model compounds such as HDS of dibenzothiophene (DBT) (*3*), 4,6-dimethyldibenzothiophene (4,6-DMDBT) (*4*), HDN of quinoline (*3*, *5*) and carbazole (*4*), hydrodearomatization (HDA) of naphthalene (*5*, *6*) to understand the different processes that occurred inside this complex bitumen upgrading reaction system. In these fundamental studies, the catalyst isolated at the end of reaction indicated that nano sized MoS_x were generated in the reaction. In this research, the application of this novel emulsion upgrading technology to the upgrading of light gas oil (LGO) derived from oil sand bitumen emulsion was investigated. Upgrading of LGO was conducted using *in situ* H_2 produced via the water gas shift reaction (WGSR) using an *in situ* generated nano dispersed molybdenum sulfide catalyst. LGO was used as a more complex model feedstock for upgrading bitumen emulsions, extending the previous fundamental studies closer to the upgrading of bitumen emulsions. Since bitumen contains metals such as Fe, V and Ni, the effects of these metal ions on upgrading LGO in the presence of nano dispersed Mo were investigated. In addition, the effect of Co and K on the upgrading of LGO was also investigated since Co and K have been reported to be promoters for HDS and WGSR respectively. Furthermore, the influences of reaction conditions such as water content, temperature and syngas on upgrading LGO was also investigated.

Experimental Details

Materials

The light gas oil sample containing 24362 ppmw of sulfur was derived from the Athabasca oil sands bitumen. The sample was black in color and became light yellow after processing as shown in Figure 1. Phosphomolybdic acid (PMA) ($12MoO_3 \cdot H_3PO_4 \cdot xH_2O$) purchased from Aldrich Chemical Co. was used as a catalyst precursor. For evaluating effects of different metal ions, $NiSO_4$, $CoSO_4$, $FeSO_4$, $C_{10}H_{14}O_5V$, and K_2CO_3 were chosen as the precursors for Ni, Co, V, Fe and K respectively. Metal precursors were dissolved in different amount of de-ionized water before loading into the reactor.

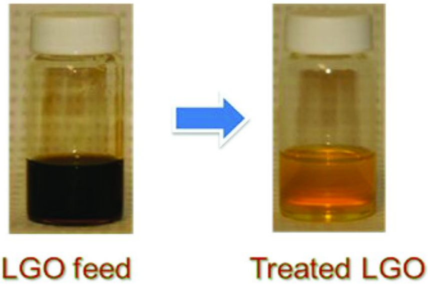

Figure 1. LGO feedstock and treated LGO product. (see color insert)

Catalyst *in Situ* Synthesis and Upgrading Reaction

For each experiment, 100 ml of LGO, a certain amount of de-ionized water and 1500 ppm Mo and other metal catalyst precursors in the 0.6:1 (metal to Mo) molar ratio were loaded into the 300cc batch-autoclave stainless steel reactor. After sealing the reactor with a metal gasket, 1800 psi N_2 was purged into the autoclave for leak test. Then the reactor was purged with CO or H_2 to 300 psi three times in order to get rid of any remaining N_2. The system was pressurized with reagent gases (CO, H_2, CO/H_2 or N_2) up to 600 psi before heating from initial room temperature to the required temperatures (391°C and 410°C) with stirring at 800rpm. The reaction was carried out for 2 hours at the required temperature. The reactor temperature and pressure were recorded to calculate the amount of final gaseous mixture in the reactor. When the reactor was cooled to room temperature, gases were collected in a gas bag for subsequent analysis. After collecting the gases, the reactor was opened for collecting the liquid products and catalyst residues. With the help of a cone shape graduated cylinder, the final water and oil volume was measured. The residue solids which included the catalyst were obtained by filtration.

Downloaded by STANFORD UNIV GREEN LIBR on May 31, 2012 | http://pubs.acs.org
Publication Date (Web): January 20, 2012 | doi: 10.1021/bk-2012-1092.ch003

Downloaded by STANFORD UNIV GREEN LIBR on May 31, 2012 | http://pubs.acs.org
Publication Date (Web): January 20, 2012 | doi: 10.1021/bk-2012-1092.ch003

Characterization

A Varian CP-3800 gas chromatograph equipped with a 30 m X 0.32 mm VF-05MS capillary column, flame ionization detector (FID), therminoic specific detector (TSD) and pulsed flame photometric detector (PFPD) was utilized for simultaneously analyzing oil products. The TSD and PFPD are specific for nitrogen and sulfur species present in the oil samples respectively. An Agilent 6890N Simulated distillation (GC-SimDis) equipment was used to analyze the boiling point distribution of the products. The ASTM D2887 method was used, which included boiling points from 55°C to 538°C. Before each injection, the oil samples were diluted 50 times by CS_2. An Agilent 3000A micro GC refinery gas analyzer (RGA) was used to analysis the gaseous products including CO, H_2, etc and to follow the progress of the water gas shift reaction. The micro GC was equipped with four thermal conductivity detectors (TCD) and with four columns: 5A molecular sieve, Plot U, Alumina and OV-1 columns. The total sulfur content in liquid sample was analyzed via an Oxford Lab-X 3000s X-Ray Fluorescence spectrometer. The detection limit was 10 ppmw of sulfur.

Results and Discussion

Effect of Metal Ions on the WGSR and HDS of LGO

The effect of five different metal ions, namely; Ni, Co, Fe, V and K on the WGSR and HDS of LGO were investigated. Ni and Co are common promoters of the HDS reaction, while Fe, Ni and V are present in heavy oil and bitumen. Zhang (*5*) investigated the effect of adding Ni to Mo for the WGSR and naphthalene hydrogenation. The experiments, carried out with different mole ratios of Ni to Mo, revealed that the optimum mole ratio of Ni:Mo was 0.6:1. This molar ratio was used to calculate the amount of metal ions required in the experiments in this study. All experiments were performed using 100 ml LGO with 10 ml water under CO at 391°C in the experiments described in this section unless otherwise specified. The mole percentages of CO and CO_2 were obtained through RGA analysis and the conversion for the WGSR was evaluated accordingly through calculating CO conversion based on these mole percentages, as shown in eq 1.

$$\text{CO Conversion\%} = \frac{n(CO_2)\%}{n(CO)\%+n(CO_2)\%} \times 100\% \qquad (1)$$

where n is the number of moles.

Based on the XRF measurement of the total sulfur amounts in both LGO feedstock and products, the total sulfur removal was calculated according to eq 2.

$$\text{Sulfur removal\%} = \frac{m(\text{sulfur in LGO}) - m(\text{sulfur in product})}{m(\text{sulfur in LGO})} \times 100\% \qquad (2)$$

where m refers to the mass.

It was found in our previous studies that MoS_x could catalyze both WGSR and HDS. The CO conversion and S removal were increased when Ni or Co was introduced. As shown in Figure 2, when Ni or Co was added, 77% and 75% of CO conversion were obtained, more than that obtained with MoS_x catalyst alone. When WGSR was increased, more H_2 was produced and hence could improve the HDS reaction. With the addition of Ni or Co, the total sulfur removal was increased to 56% and 36% respectively, which were higher than the sulfur removal of 32% obtained using unpromoted the MoS_x catalyst. This result was interesting since bitumen contains Ni which could potentially promote the WGSR and HDS in the upgrading of bitumen emulsion with the nano-dispersed MoS_x catalyst. In the gas product, higher percentages of H_2S were detected in experiments carried out using Ni-Mo (5.46%) and Co-Mo (4.20%) than the Mo catalyst alone (1.85%), indicating more sulfur was removed. Ni was found to be the best additive which removed 20% more sulfur than Co. It should be noted the amount of H_2S can be used only as a qualitative indicator of the amount of sulfur removed due to the solubility of H_2S in the liquid and the influence of pressure on the solubility.

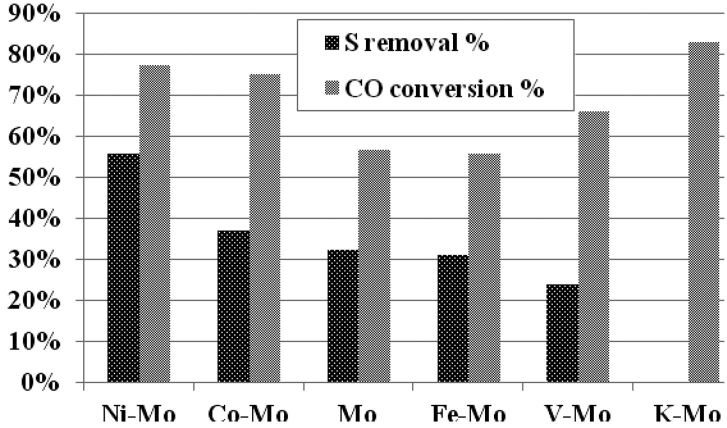

Figure 2. Effects of different metal ions on sulfur removal and CO conversion at 391°C, 1500 ppm Mo, 0.6:1 molar ratio of metal ions to Mo, 100 mL of LGO and 10 mL of water.

It was interesting that K was found to be the best WGSR promoter (83% CO conversion) but the strongest HDS inhibitor (almost no sulfur removed). This result was similar to that reported by Kantschewa (*7*) where the activity of HDS was reduced significantly in the presence of K, while the activity of WGSR was enhanced. It was suggested that the original octahedral coordination of Mo^{6+} in the $NiMo/Al_2O_3$ catalyst was changed into a tetrahedral coordination (*7*). The presence of K strongly decreased the reducibility of Mo^{6+} and that the degree of sulfidation was reduced in $KNiMo/Al_2O_3$. V was found to be an inhibitor of the HDS reaction although it promoted WGSR. Hence in the bitumen emulsion upgrading with CO, although the removal of V from the bitumen will likely help the generation of H_2 via the WGSR, V will likely reduce HDS. It was also observed

Downloaded by STANFORD UNIV GREEN LIBR on May 31, 2012 | http://pubs.acs.org
Publication Date (Web): January 20, 2012 | doi: 10.1021/bk-2012-1092.ch003

Downloaded by STANFORD UNIV GREEN LIBR on May 31, 2012 | http://pubs.acs.org
Publication Date (Web): January 20, 2012 | doi: 10.1021/bk-2012-1092.ch003

that Fe improved neither HDS nor WGSR, as there was no significant change in the activity compared to the unpromoted Mo catalyst. These results suggest that the native metal ions such as Ni, V and Fe present in the bitumen will not have a strong inhibition effect on the HDS of bitumen. In the processing of bitumen with nano-dispersed Mo catalyst, the issue of recycling of Mo is of economic importance. Therefore it would be desirable to remove the V from the residue before recycling the Mo back into the reactor.

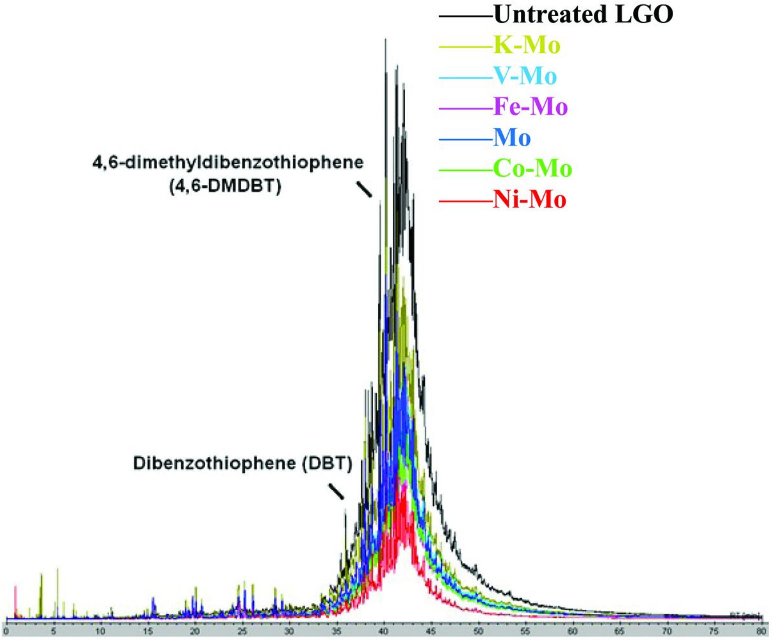

Figure 3. GC analysis of sulfur compounds in the liquid product obtained by GC-PFPD over MoS_x catalysts with different added metal ions at 391°C, 1500 ppm Mo, 0.6:1 molar ratio of metal ions to Mo, 100 mL of LGO and 10 mL of water. (see color insert)

LGO has a large number of sulfur and nitrogen containing species. GC-PFPD/TSD was applied in an attempt to analyze these different sulfur- and nitrogen- containing species. By comparing the chromatographs obtained by GC-PFPD which is specific for sulfur species as shown in Figure 3, the lowest sulfur concentration was obtained for the sample obtained after processing with Ni promoted MoS_x catalyst, while the product derived from the reaction with added K to MoS_x contained the highest sulfur concentration. Some typical sulfur-containing species such as dibenzothiophene (DBT) and 4,6-dimethdibenzothiophene (4,6-DMDBT), two of the most refractory sulfur containing compounds were identified. The concentration of the nitrogen-containing species, carbazole was identified using GC-TSD. The removal of DBT, 4,6-DMDBT and carbazole were listed in Table I. Figure 4 shows the concentrations of DBT, 4,6-DMDBT and carbazole in the products obtained for the different reaction systems. The trends for the concentration of DBT and 4,6 DMDBT were shown as expected based on the HDS data obtained from total S analysis using XRF. For example, around 50% of DBT were removed with Mo, Fe-Mo, Co-Mo or Ni-Mo while K-Mo and V-Mo has very limited DBT removal abilities. 28.0% and 29.1% of 4,6-DMDBT were removed respectively with Co-Mo and Ni-Mo, while K-Mo and V-Mo could remove only 15.2% and 20.5% 4,6-DMDBT. It should be noted that the GC/PFPD is more sensitive to the concentration of S-containing species than XRF and hence it appears that some S was removed in the K-Mo system. By analyzing the carbazole removal obtained by GC-TSD, it was interesting to note that Ni-Mo eliminated 81.2% carbazole, while Co removed only 24.3% carbazole. The removal of carbazole with the unpromoted MoS_x was 58.5%, hence Co actually inhibited the carbazole removal by Mo in this LGO upgrading reaction system. The inhibitive effect of the nitrogen-containing compounds such as carbazole on HDS is very strong even at a concentration as low as 5 ppm (*8*). Even with more H_2 produced through WGSR over Co-Mo in this process, the limited carbazole removal ability of Co-Mo very likely inhibited the HDS performance. Therefore, the excellent performance of Ni-Mo sulfide catalyst on carbazole removal possibly contributed to the higher HDS ability of Ni-Mo compared with Co-Mo. It was observed that K-Mo and V-Mo only removed 1.0% and 0.1% carbazole respectively, which probably contributed to the inhibition effects of these two metals. Fe-Mo resulted in carbazole removal of 38.7% which is also less than Ni-Mo or Mo itself. Since addition of Fe to Mo did not inhibit the carbazole removal completely, this may explain the relatively small change in HDS activity of Fe-Mo compared with Mo.

Downloaded by STANFORD UNIV GREEN LIBR on May 31, 2012 | http://pubs.acs.org
Publication Date (Web): January 20, 2012 | doi: 10.1021/bk-2012-1092.ch003

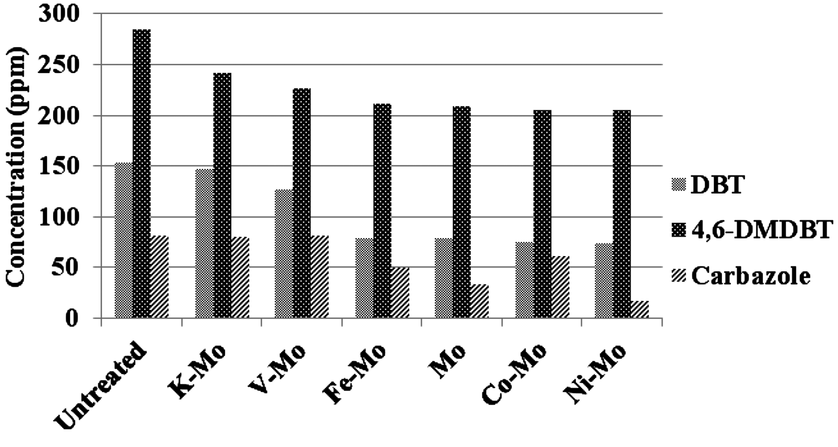

Figure 4. DBT, 4,6-DMDBT and carbazole concentrations before and after the treatments over MoS_x catalysts with different added metal ions at 391°C, 1500 ppm Mo, 0.6:1 molar ratio of metal ions to Mo, 100 mL of LGO and 10 mL of water.

Downloaded by STANFORD UNIV GREEN LIBR on May 31, 2012 | http://pubs.acs.org
Publication Date (Web): January 20, 2012 | doi: 10.1021/bk-2012-1092.ch003

Table I. Typical Removal of Sulfur and Nitrogen containing Compounds over MoS_x Catalysts with different added metal ions, 1500 ppm Mo, 0.6:1 molar ratio of metal to Mo, 391°C, 100 mL of LGO and 10 mL of water

	K-Mo	*V-Mo*	*Fe-Mo*	*Mo*	*Co-Mo*	*Ni-Mo*
DBT	4.6%	17.3%	48.9%	48.3%	50.9%	51.4%
4,6-DMDBT	15.2%	20.5%	25.7%	26.5%	28.0%	29.1%
Carbazole	1.0%	0.1%	38.7%	58.5%	24.2%	81.3%

GC-SimDis was also carried out to determine the effect of different added metal ions on the boiling point distribution of the oil product. In Figure 5, the results revealed an improvement in the boiling point range of the treated oil compared to the untreated one, where 75% of the pitch fraction was converted to lighter cuts. However, as the boiling point ranges suggested, there was no significant difference between the liquid products among all of these experiments as shown in Figure 5. This was attributed to the narrow boiling range of the feed (200-450°C) and the limited cracking occurred at 391°C. It is important to note that although different metal ions provided different degrees of HDS, the pitch conversions and the boiling fractions are very similar for all the metal ions. Therefore sulfur removal did not necessarily correspond to pitch conversion or the distribution of naphtha, kerosene, distillate and heavy gas oil fractions.

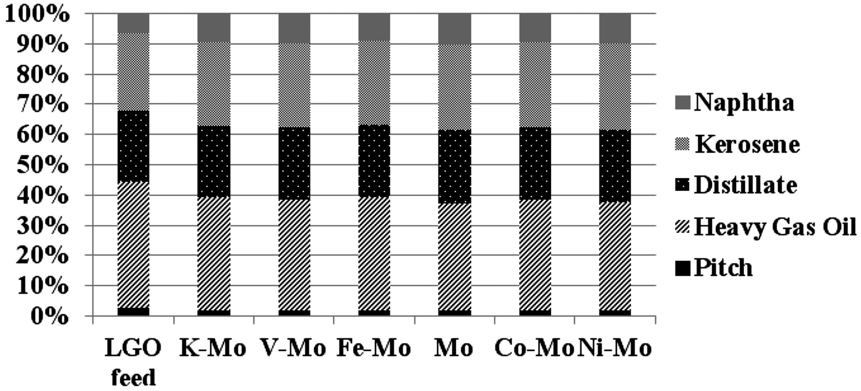

Figure 5. LGO fraction distributions before and after treatment over MoS_x catalysts with different added metal ions at 391°C, 1500 ppm Mo, 0.6:1 molar ratio of metal ions to Mo, 100 mL of LGO and 10 mL of water (Boiling point ranges: naphtha: <204°C, kerosene: 204-288°C, distillate: 288-343°C, heavy gas oil: 343-524°C, pitch: >524°C).

Effect of Water Content on LGO Upgrading under Different H_2 Sources

The water associated with emulsion could be used to produce *in situ* H_2 instead of the current two separate steps: (a) emulsion breaking to remove water; (b) hydrotreating processes using expensive molecular H_2. When WGSR is combined with bitumen emulsion upgrading process by reacting water with CO or syn-gas, water becomes essential as it reacts with CO to produce *in situ* H_2. However, water inhibits every individual steps in the HDS reaction network, especially blocking the hydrogenation pathway (*3*, *9*). Therefore, the water amount plays a critical role in this novel HDS process, and the optimization of water contents should be carried out in the HDS of LGO reaction system. In Lee and Ng's study, the optimal H_2O: CO mole ratio was 1.35 at both 340°C and 380°C (*3*). Three different amounts of water (5, 10, and 15 ml to 100 ml of LGO) were added to LGO in reactions carried out under CO (*in situ* H_2) and molecular H_2 in this study. As shown in Figure 6, water was consumed in WGSR after 2 hours at reaction conditions at 391°C, so the excess water percentages were all lower using *in situ* H_2 than the percentages under molecular H_2. It was noticed that the sulfur removals were lower when excess amount of water was higher in the reaction system for both *in situ* H_2 and molecular H_2. This result was consistent with the water inhibition effect on HDS as described in previous literature reports. It was also observed that the inhibition of HDS was more significant when using *in situ* H_2 than molecular H_2, although the reason for this observation is not clear. When 15 ml water was used, molecular H_2 was slightly more active than *in situ* H_2 for HDS. This result was similar to the finding of Siewe and Ng (*9*), where H_2 performed better than *in situ* H_2 when 30 vol% of water was used to treat a diesel cut.

Downloaded by STANFORD UNIV GREEN LIBR on May 31, 2012 | http://pubs.acs.org
Publication Date (Web): January 20, 2012 | doi: 10.1021/bk-2012-1092.ch003

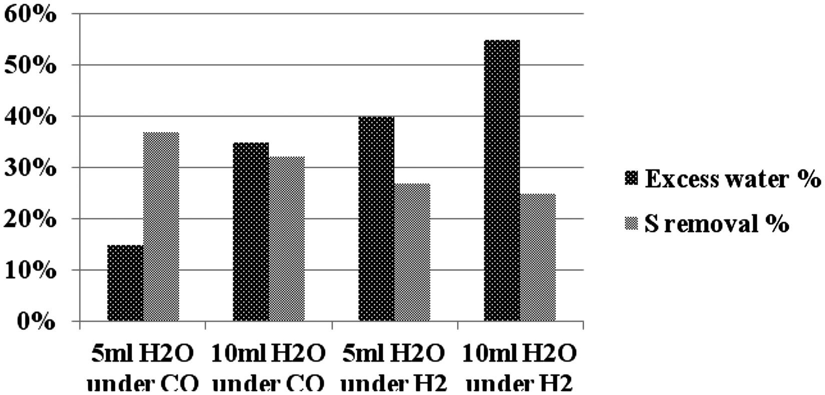

Figure 6. Excess water and sulfur removal percentages with different water loadings under in situ H_2 or molecular H_2 at 391°C, 1500 ppm Mo, 100 mL of LGO.

GC-SimDis provided the changes in boiling point distribution of the oil product with different water loading under CO and H_2 (Figure 7). No significant difference in the boiling point distribution was detected when molecular H_2 was used. When *in situ* H_2 was used, apparently 5 ml of water produced liquid product with the lowest boiling point distribution where the GC-SimDis data indicated that there was about 3% more lighter fraction from 220°C to 450°C. It was possible that this improvement in oil quality was due to more effective upgrading at 5 ml water under CO. More studies are in progress to understand the beneficial effect of in situ H_2 .

Downloaded by STANFORD UNIV GREEN LIBR on May 31, 2012 | http://pubs.acs.org
Publication Date (Web): January 20, 2012 | doi: 10.1021/bk-2012-1092.ch003

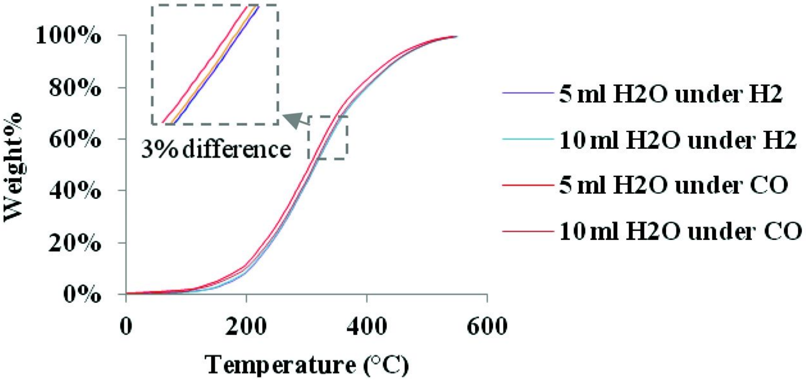

Figure 7. LGO product boiling point distributions with different water loading under in situ H_2 and molecular H_2 at 391°C, 1500 ppm Mo, 100 mL of LGO. (see color insert)

Effect of Syn-Gas Composition on HDS of LGO

The effect of the composition of syn-gas (different ratio of H_2:CO) on the WGSR and HDS were carried out. Initial loading of CO compared to the total initial pressure of both CO and H_2 was varied at 100, 60, 30, and 0 percent. All of these experiments were performed in a 1 L batch reactor with sampling during the run at 391°C using MoS_x. Gas content analysis for typical syn-gas (60%CO+40%H_2) reaction is shown in Figure 8. WGSR occurred even when syn-gas was used as a feedstock since CO_2 was generated while CO decreased.

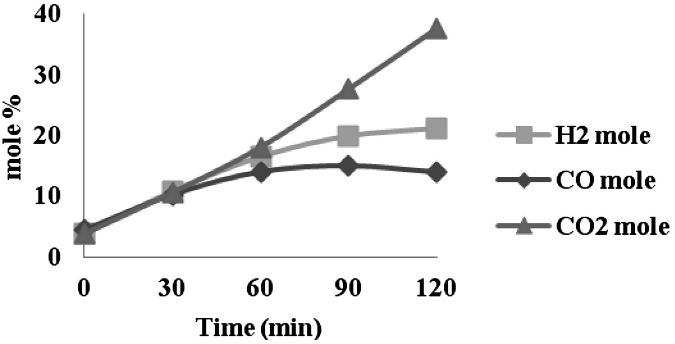

Figure 8. Gas content changes with WGSR under syn-gas (60%CO+40%H_2) at 391°C, 1500 ppm Mo, with 100 mL of LGO and 10 mL of water.

Sulfur contents for the samples obtained during the reaction were plotted against time (Figure 9). It was clear that the rate of sulfur removal in the case of pure CO was the fastest. Figure 9 shows that more sulfur was removed in the early stages when the molecular H_2 used, because molecular H_2 provided enough H_2 partial pressure for HDS while CO did not provide enough *in situ* H_2 at the beginning of the reaction. It is not clear why the reaction with 30% CO had relatively low reaction rate and low sulfur removal. Due to the relative complex reaction system and sampling at high temperature and pressure which could lead to quite high experimental error, more experiments are required before a conclusion can be drawn. However, one could say with certainty that syn-gas could be used as a source to provide *in situ* H_2 for HDS of LGO with added water.

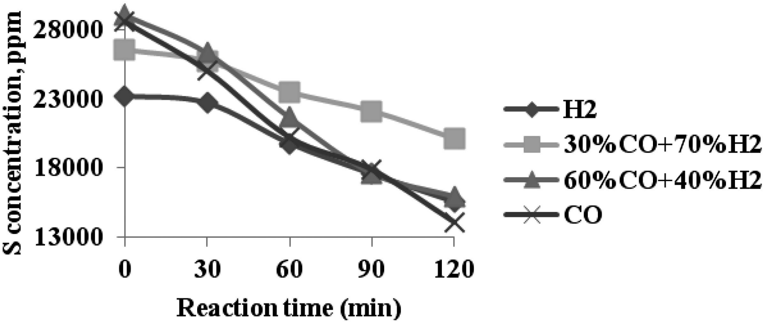

Figure 9. Changes of sulfur concentration with time under different syn-gas compositions at 391°C, 1500 ppm Mo, with 100 mL of LGO and 10 mL of water.

Effect of Reaction Temperature on LGO Upgrading

Reaction temperature was increased from 391°C to 410°C to study the effect of the temperature on the reaction when it enters the hydrocracking regime. As shown in Table II, more sulfur was removed when the temperature was increased to 410°C. Further investigation was accomplished using the GC-SimDis to analyze the boiling range of the products obtained at both temperatures. The GC-SimDis results in Figure 10 showed that liquid products became lighter when the temperature was increased from 391°C to 410°C. The naphtha and kerosene volume percents were improved by 57.2% and 12.2% respectively; while distillate, heavy gas oil and pitch volume percents were decreased by 8.1%, 18.9% and 42.4% respectively.

Table II. Sulfur removals and pitch conversions at different reaction temperatures with 1500 ppm Mo, 100 mL of LGO and 10 mL of water

Reaction Temperature (°C)	*391*	*410*
Sulfur Removal	32.3%	41.7%
Pitch Conversion	36.5%	63.5%

In Nanocatalysis for Fuels and Chemicals; Dalai, A.;
ACS Symposium Series; American Chemical Society: Washington, DC, 2012.

Downloaded by STANFORD UNIV GREEN LIBR on May 31, 2012 | http://pubs.acs.org
Publication Date (Web): January 20, 2012 | doi: 10.1021/bk-2012-1092.ch003

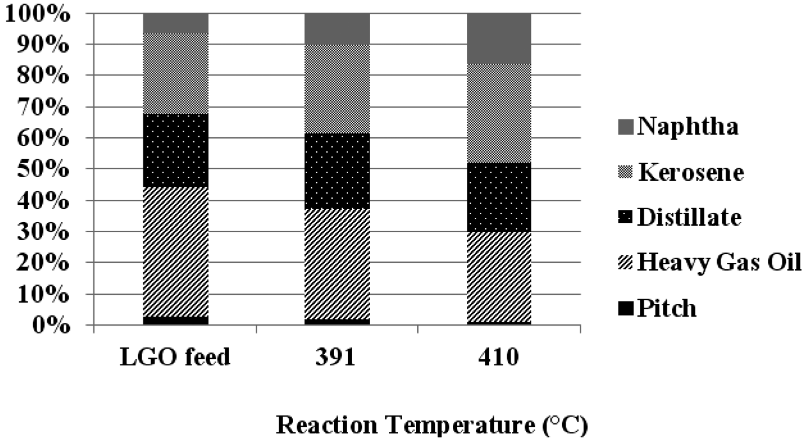

Figure 10. LGO fraction distributions at different reaction temperatures (391°C and 410°C) with 1500 ppm Mo, 100 mL of LGO and 10 mL of water (Boiling point ranges: naphtha: <204°C, kerosene: 204-288°C, distillate: 288-343°C, heavy gas oil: 343-524°C, pitch: >524°C).

Downloaded by STANFORD UNIV GREEN LIBR on May 31, 2012 | http://pubs.acs.org
Publication Date (Web): January 20, 2012 | doi: 10.1021/bk-2012-1092.ch003

Conclusion

LGO was studied as a model compound for a novel bitumen emulsion upgrading process combining water gas shift reaction (WGSR) with upgrading over nano dispersed MoS_x catalysts. The effects of metal ions, H_2O amount, syn-gas composition and reaction temperature on the upgrading of LGO derived from Athabasca bitumen were investigated. At 391°C, it was found that the WGSR provided *in situ* H_2 for the HDS of LGO in the presence of the nano dispersed MoS_x catalyst. Total sulfur analysis obtained from XRF showed that sulfur removal is about 32% in the presence of dispersed Mo catalyst. In the presence of added Ni, the sulfur removal increased to 56%. GC-TSD/PFPD identified DBT, 4,6-DMDBT and carbazole in the complex mixture of sulfur and nitrogen containing compounds in LGO. It was interesting that the concentration of carbazole decreased most significantly in the presence of added Ni to the nano dispersed MoS_x catalyst. Analysis of the gaseous products indicated that Ni also promoted the WGSR. Fe showed no significant promoting effect for both the WGSR and HDS. V and K promoted the WGSR but apparently inhibited the HDS reaction. K was found to be the strongest inhibitor for the HDS reaction since essentially no sulfur was removed during the reaction. Nevertheless, this inhibition of K on HDS did not affect hydrocracking of LGO. Water was found to have a significant inhibiting effect on the HDS reaction. Syn-gas was capable to provide *in situ* H_2 for LGO upgrading. *In situ* H_2 generated via WGSR from CO provided higher HDS activity and reaction rate compared with molecular H_2. At a higher temperature, more HDS and lighter products were produced as seen in the GC-SimDis results.

Downloaded by STANFORD UNIV GREEN LIBR on May 31, 2012 | http://pubs.acs.org
Publication Date (Web): January 20, 2012 | doi: 10.1021/bk-2012-1092.ch003

Acknowledgments

Financial support from Natural Sciences and Engineering Research Council of Canada (NSERC) Strategic Projects program is gratefully acknowledged. Lei Jia would like to thank Waterloo Institute for Nanotechnology (WIN) for a fellowship. Abdulaziz Alghamdi would like to thank Saudi Aramco for a scholarship.

References

1. (a) Ng, F. T. T.; Tsakiri, S. K. U.S. Patent 5055175 (A), Canadian Patent 1317250 (C), 1991. (b) Ng, F. T. T.; Tsakiri, S. K. *Fuel* **1992**, *71*, 1309−1314.
2. Moll, J. K.; Li, Z.; Ng, F. T. T. *American Chemical Society National Meeting*; American Chemical Society: Washington, DC, ETATS-UNIS, 2000; Vol. 45, pp 599−602.
3. Lee, R. Z.; Ng, F. T. T. *Catal. Today* **2006**, *116*, 505–511.
4. Liu, K.; Ng, F. T. T. *Catal. Today* **2010**, *149*, 28–34.
5. Zhang, A. Master of Applied Science Thesis, University of Waterloo, Waterloo, ON, Canada, 2005.
6. Choy, C. Master of Applied Science Thesis, University of Waterloo, Waterloo, ON, Canada, 2009.
7. Kantschewa, M.; Delannay, F.; Jeziorowski, H.; Delgado, E.; Eder, S.; Ertl, G.; Knözinger, H. *J. Catal.* **1984**, *87*, 482–496.
8. Laredo, G. C.; Altamirano, E.; De los Reyes, J. A. *Appl. Catal., A* **2003**, *243*, 207–214.
9. Siewe, C. N.; Ng, F. T. T. *Energy Fuels* **1998**, *12*, 598–606.

Downloaded by CORNELL UNIV on May 31, 2012 | http://pubs.acs.org
Publication Date (Web): January 20, 2012 | doi: 10.1021/bk-2012-1092.ch004

Chapter 4

Pore Size Control of a Novel Amorphous Silica-Alumina with Large Mesopore by the Gel Skeletal Reinforcement and Its Catalytic Cracking Properties

Atsushi Ishihara,[*] Kohei Nakajima, Motoki Hirado,
Tadanori Hashimoto, and Hiroyuki Nasu

Division of Chemistry for Materials, Mie University,
1577 Kurima Machiya-Cho, Tsu-City,
Mie Pref. 514-8507, Japan
[*]E-mail: ishihara@chem.mie-u.ac.jp

Recently much attention has been focused on the preparation of silica and silica-alumina with large pore volume and pore diameter. In this study, silica and silica-alumina with large pore size and pore volume were synthesized from aerogels prepared using the gel skeletal reinforcement. Tetraethyl orthosilicate (TEOS) was used as a precursor of silica. To prevent the shrinkage of the pores, the strength of silica-gel skeleton was enhanced by aging with TEOS / 2-propanol mixed solution (the gel skeletal reinforcement). After drying the silica aerogel obtained was calcined at 500°C for 3hours. Aluminum species (alumina sol) was added during preparation of silica aerogel to prepare silica-alumina. When silica aerogel reinforced by TEOS solution was calcined, pore volume and pore size of prepared silica increased. These values decreased with increasing the amount of alumina sol. When alumina sol was not added, the pore volume and average pore diameter reached 2.9cm^3/g and 23nm, respectively. Synthesized silica and silica-alumina were amorphous identified by XRD patterns. Subsquently the effects of their pore sizes on the catalytic activity and the product selectivity of catalytic cracking of n-dodecane were investigated. Catalytic clacking reaction was carried out by using n-dodecane as feed at 500 °C. The conversion of dodecane

In Nanocatalysis for Fuels and Chemicals; Dalai, A.;
ACS Symposium Series; American Chemical Society: Washington, DC, 2012.

for the mixed catalyst, which included 25wt% of beta-zeolite and 58wt% of the silica-alumina with large mesopore, was 89 % higher than that with single use of zeolite (conv. 84%). The silica-alumina with large mesopore had unique selectivity where large amounts of branched products were formed.

Downloaded by CORNELL UNIV on May 31, 2012 | http://pubs.acs.org
Publication Date (Web): January 20, 2012 | doi: 10.1021/bk-2012-1092.ch004

Introduction

Recently, much attention has been focused on the preparation of silica and silica-alumina aerogels because they have a large surface area, high porosity, low bulk density, extremely low thermal conductivities etc (*1–4*). In preparation of these materials, supercritical or subcritical conditions (*1–4*) and alkoxysilylation (*3*, *5*) or methylsilylation (*6*, *7*) are used to inhibit the extensive shrinkage of large pores during removal process of entrapped solvent from the wet gel. Among them, alkoxysilylation and methylsilylation are the promising methods because they can produce aerogels at ambient pressure by inhibiting the rapid hydrolysis and the successive condensation which leads to the shrinkage of pore. These methods include the concept of the gel skeletal reinforcement. However, the importance of this concept was not necessarily stressed and has not been described in detail. Since the silylating agent and the subcritical condition were used simultaneously in some reports (*3*, *5*), it has not been clarified which effect is more important to prepare aerogels. Further, most of these reports are related to the preparation of bulk materials and there are very few reports where the prepared extremely large mesopore has been utilized for various catalysts or supports for catalysts.

On the other hand, FCC (Fluid Catalytic Cracking) is now one of most important processes because crude oils have become heavier year after year and further low value heavier fractions such as vacuum gas oil (VGO) and atmospheric residue (AR) have increased. FCC catalysts generally include not only zeolite as a major component but also silica-alumina as a matrix (*8*). Although zeolite is a very active catalyst (*9*), the pores of zeolite, which mainly consist of micropore, are disadvantageous to carry and diffuse hydrocarbons with large molecular structure such as VGO or AR (*10*). Silica-alumina is used to control activity of zeolite or selectivity of catalytic cracking reaction. However, academic studies of silica-alumina are fewer than those of zeolite in this field (*11*, *12*).

Recently we have reported that silica-aluminas with about 5nm of mesopore prepared using malic acid influence the production of branched hydrocarbons in catalytic cracking of n-dodecane (*11*, *12*). Further, it was demonstrated that the pore size of silica and silica-alumina could be controlled by the gel skeletal reinforcement and that such large mesopore materials promoted the rapid diffusion of molecules and the preferential formation of branched hydrocarbons when used in catalytic cracking as matrices (*5*). The purpose of this paper is to clarify whether both the gel skeletal reinforcement and the subcritical condition are simultaneously needed or not to prepare materials with large pore volume and meopore. Therefore aerogels were prepared using the gel skeletal reinforcement with and without subcritical conditions. Further, catalytic cracking properties of prepared catalysts with large mesopores were also investigated.

Downloaded by CORNELL UNIV on May 31, 2012 | http://pubs.acs.org
Publication Date (Web): January 20, 2012 | doi: 10.1021/bk-2012-1092.ch004

Experimental

Silica-alumina was synthesized by the acid-base-catalyzed sol-gel process including the gel skeletal reinforcement according to the flow chart in Figure 1 and the amount of reagents in Table 1. A typical method was as follows: Tetraethyl orthosilicate (TEOS) was used as a precursor of silica. To TEOS/2-propanol solution was added 0.1wt% HCl at 25°C, and the mixture was stirred for 30min in a sealed bottle (or a normal open bottle). Then alumina sol (Cataloid AP-1, Shokubai Kasei) was added and the mixture was stirred for 30 min. After pH of the solution was arranged to 5 by adding aqueous NH_3 solution, the gelation was performed at 50°C. After gelation, temperature was maintained for 5h. Then the gel was immersed in deionized water at 50°C for 24h. After that, the gel was taken out from water. The gel was cut to several fragments and was washed with 2-propanol for 5min five times at 50°C to remove the remaining water in pores thoroughly. After that, the gel was maintained in 80%TEOS/20%2-propanol solution at 50°C for 48h. The weight ratio of TEOS for the gel skeletal reinforcement in this solution was 362 for 100 of TEOS silica precursor. That is, 362 means that the amount of TEOS in the reinforcement solution was 3.62 times of the amount of TEOS silica precursor. 80%TEOS/20%2-propanol reinforcement solution was removed and the reinforced gel was washed with 2-propanol for 5min five times at 50°C to remove the remaining 80% TEOS/20% 2-propanol solution. After maintaining the gel product at 70°C for 72h, the prepared aerogel was calcined at 500°C for 3 h. Synthesized silica-alumina was mixed with alumina sol (Cataloid AP-1, as an alumina binder), beta-zeolite (HSZ-940 HOA, Tosoh) and deionized water. It was shaped into a cylindrical pellet type (diameter 0.5mm, length <2mm) after kneading. The prepared pellets were calcined at 600 °C for 3 h. The amounts of silica-alumina, alumina from the binder, and zeolite in the mixed catalyst were 58, 16 and 26wt%, respectively.

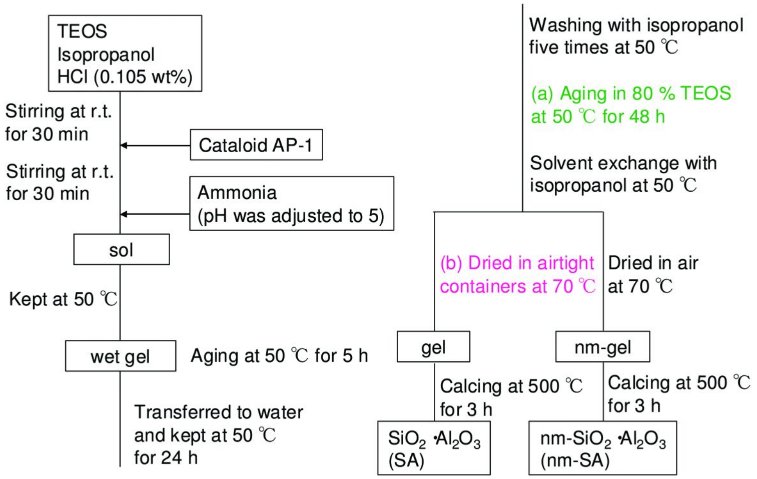
TEOS
Isopropanol
HCl (0.105 wt%)
Stirring at r.t. for 30 min
Cataloid AP-1
Stirring at r.t. for 30 min
Ammonia (pH was adjusted to 5)
sol
Kept at 50 ℃
wet gel
Aging at 50 ℃ for 5 h
Transferred to water and kept at 50 ℃ for 24 h
Washing with isopropanol five times at 50 ℃
(a) Aging in 80 % TEOS at 50 ℃ for 48 h
Solvent exchange with isopropanol at 50 ℃
(b) Dried in airtight containers at 70 ℃
Dried in air at 70 ℃
gel
nm-gel
Calcing at 500 ℃ for 3 h
Calcing at 500 ℃ for 3 h
$SiO_2 \cdot Al_2O_3$ (SA)
nm-$SiO_2 \cdot Al_2O_3$ (nm-SA)

Figure 1. Flowchart for preparation of SiO_2 and SiO_2-Al_2O_3.

Table 1. Compositions of solution for preparation of SiO_2-Al_2O_3

*Sample name**	*Molar ratio*			*wt% as alumina*
	TEOS	*HCl (pH=1.54)*	*Isopropanol*	*Alumina sol*
SiO_2 nm-SiO_2	1	4	16	0
SA5% nm-SA5%	1	4	16	5
SA25% nm-SA25	1	4	16	25

* SA=silica-alumina; nm=a normal open bottle was in preparation of aerogel.

Downloaded by CORNELL UNIV on May 31, 2012 | http://pubs.acs.org
Publication Date (Web): January 20, 2012 | doi: 10.1021/bk-2012-1092.ch004

The structural characteristics of the catalysts were measured by N_2 adsorption (Bel Sorp mini), X-ray diffraction (XRD, Rigaku RAD-C) and NH_3 adsorption and desorption (GC-TCD, Shimadzu GC-8A).

In naming of samples, nm was added when silica-alumina was prepared in the normal open bottle. SA represents silica-alumina. The number at the back of SA represents the alumina content by wt%. For the mixed catalyst with zeolite and the binder, MAT- was represented in front of sample name of SA.

Catalytic clacking of n-dodecane was carried out using a fixed bed reactor (length 300mm, ID 8mm, stainless) under the conditions of 500 °C, catalyst 1g, n-dodecane 1.3ml/min, 80s, WHSV 58.5h^{-1}. After the reaction, N_2 was introduced at 30ml/min for 30min and gas products were recovered in a tedlar bag, and liquid products were collected in a cold trap. The gas and liquid products were determined by GC-FID (Shimadzu GC-2014) referring to the Japanese Industrial Standards (JIS) K 2536-2. The condition for GC measurement was as follows: Injection temp. 250°C, detector temp. 320°C, ATTN 1, injection press. 158kPa, column flow 1.56 ml/min, line spead 27.64 cm/sec, total flow 320 ml/min, split ratio 200, column BP-1, column length 60m, column diameter 0.25mm, film thickness 0.5micrometer, column initial temp 0°C 16min, heating rate 2°C/min, final temp 228°C, liquid sample 0.2 microliter, gas sample 0.5 ml.

Results and Discussion

There is no peak in XRD patterns of synthesized silica and silica-alumina (Figure 2a), and it was confirmed that they were amorphous. Results from N_2 adsorption are summarized in Table 2. When silica-gel was reinforced by TEOS solution, silica with large mesopores was prepared. For example, BJH surface area, pore volume and pore diameter (PD) for SiO_2 were 417m^2/g, 2.82cm^3/g and 18.5nm, respectively. When silica and silica-aluminas were prepared in the normal open bottle, values for surface area, pore volume and pore diameter were somewhat smaller while those values for nm-SA5% were 395m^2/g, 2.57cm^3/g and 16.0nm, respectively. Large pore diameter and pore volume were obtained, while surface area decreased, indicating that, although moisture in the atmosphere may affect the pore structure, materials with high porosity can be prepared using the gel skeletal reinforcement even without subcritical conditions. As reported previously these three values for silica without the gel skeletal reinforcement were 703m^2/g, 1.30cm^3/g and 7.1nm (PD), respectively (*5*). Further, three values of ref.SA (JRC-SAH-1 supplied from Catalysis Society of Japan), which is prepared by a conventional method using water glass and aluminum sulfate, were 537m^2/g, 0.86cm^3/g and 6.2nm (PD), respectively. Although the Ostwald ripening effect to strengthen a gel surface is often described (*1–7*), our results suggest that both the thorough removal of water in the inside of the gel and the gel skeletal reinforcement are essential for making large mesopore. The thorough removal of water in the inside of the gel in solvent exchange inhibits the hydrolysis of reinforcing TEOS/2-propanol solution. The surface silanol is modified by TEOS to form the new surface covered by triethoxysilyl groups which inhibit the further condensation of the gel skeletal structure in the absence of water. When alumina content was 0 or 5wt%, surface areas and pore volumes by the BET method were very close to those by the BJH method, indicating that most pores of silicas and silica-aluminas prepared by the gel skeletal reinforcement consist of mesopores. In the BJH pore size distribution, silica and silica-alumina had larger and broader pore size distribution. The pore volume and average pore diameter measured by the BET method reached about 2.9cm^3/g and 23nm, respectively. Although some papers have reported higher porosity (*4*, *6*), thermal stabilities for the materials were about 200°C even at maximum which is much lower than our condition, 500°C for 3h.

Downloaded by CORNELL UNIV on May 31, 2012 | http://pubs.acs.org
Publication Date (Web): January 20, 2012 | doi: 10.1021/bk-2012-1092.ch004

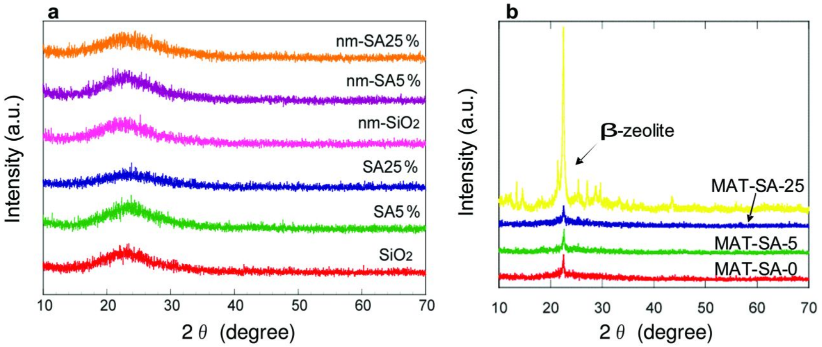

Figure 2. XRD patterns of various catalysts a: amorphous SiO_2 and SiO_2-Al_2O_3; b: zeolite and zeolite-SiO_2-Al_2O_3 mixed catalysts.

Downloaded by CORNELL UNIV on May 31, 2012 | http://pubs.acs.org
Publication Date (Web): January 20, 2012 | doi: 10.1021/bk-2012-1092.ch004

Table 2. Surface area and pore volume of SiO_2 and SiO_2-Al_2O_3

Catalyst	*BET*			*BJH*		
	Surface area (m^2/g)	*Pore volume (cm^3/g)*	*Pore diameter (nm)*	*Surface area (m^2/g)*	*Pore volume (cm^3/g)*	*Pore diameter (nm)*
SiO_2	**493**	**2.85**	**23.1**	**417**	**2.82**	**18.5**
SA5 %	**780**	**2.70**	**13.8**	**601**	**2.60**	**18.5**
SA25 %	**273**	**0.84**	**12.3**	**153**	**0.79**	**3.7**
nm-SiO_2	**480**	**1.42**	**11.8**	**495**	**1.39**	**21.3**
nm-SA5 %	**521**	**2.59**	**19.9**	**395**	**2.57**	**16.0**
nm-SA25 %	**455**	**0.57**	**5.1**	**50**	**0.05**	**3.3**

Silica and silica-aluminas (SiO_2, SA5% and SA25%) were mixed with zeolite and alumina sol (binder). As shown in Figure 2b, MAT-SA-0, MAT-SA-5 and MAT-SA-25 exhibited some zeolite peaks, indicating that zeolite was maintained in structure and was dispersed into amorphous silica and silica-alumina. Surface areas and pore volumes of mesopores measured by the BJH method decreased as shown in Table 3; however larger pore distributions for MAT-SA-5 and MAT-SA-0 were still maintained when compared with that of MAT-(refSA) as shown in Figure 3.

Table 3. Surface area and pore volume of zeolite and zeolite-SiO_2-Al_2O_3 mixed catalysts

Catalyst	*BET*			*BJH*		
	Surface area (m^2/g)	*Pore volume (cm^3/g)*	*Pore diameter (nm)*	*Surface area (m^2/g)*	*Pore volume (cm^3/g)*	*Pore diameter (nm)*
MAT-SA-0	**380**	**1.11**	**11.7**	**308**	**1.03**	**16.0**
MAT-SA-5	**481**	**0.93**	**7.8**	**347**	**0.81**	**12.1**
MAT-SA-25	**279**	**0.63**	**9.0**	**171**	**0.55**	**3.7**
zeolite	**613**	**0.32**	**2.1**	**24**	**0.07**	**3.3**
MAT-(ref.SA)	**765**	**0.64**	**5.7**	**340**	**0.57**	**6.2**

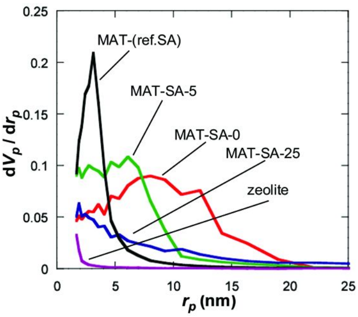

Figure 3. BJH pore-size distributions of zeolite and zeolite-SiO_2-Al_2O_3 mixed catalysts.

Downloaded by CORNELL UNIV on May 31, 2012 | http://pubs.acs.org
Publication Date (Web): January 20, 2012 | doi: 10.1021/bk-2012-1092.ch004

As shown in Figure 4, the conversion of n-dodecane with single use of zeolite was 84% and the yield of paraffins was much larger than those of olefins and aromatics, indicating that significant hydrogen transfer to olefins in the formation of aromatics proceeded. When silica-alumina was used in cracking of n-dodecane, the conversion was only a few percent as shown in the previous papers (*5*, *11*, *12*). The results show that the ability of cracking in the catalytically active sites is limited to extremely low level for single use of silica-alumina. When mixed catalysts were prepared with zeolite and silica-alumina with large mesopore, the comparable activities were obtained in cracking of n-dodecane although the mixed catalyst included only 26wt% of zeolite. The conversions of dodecane for the mixed catalysts, MAT-SA-5 and MAT-SA-25, were 82% and 89%, respectively, which were almost the same as that for single use of zeolite, indicating that the presence of acid sites in matrix silica-alumina and the dispersed zeolite in the mixed catalyst promoted the conversion and diffusion of reactant molecules effectively. When the distribution of carbon numbers on catalytic cracking was compared in Figure 5, the difference between MAT-SA-0, MAT-SA-5 and MAT-SA-25 was very small while single zeolite produced larger amounts of gaseous products, C3 and C4. To clarify the difference between the mixed catalysts and the single zeolite or the mixed catalyst using a conventional silica-alumina (refSA), the product distribution of gas (C1-C4) and gasoline (C5-C11) fractions and some parameters in the gasoline fraction were compared and the results are summarized in Table 4. In the mixed catalysts with silica-alumina using the gel skeletal reinforcement and conventional MAT-(ref.SA), the distribution of gasoline and the olefin selectivity increased compared with those of single zeolite. Although the ratio of iso/n was very similar each other, the major differences were observed in the ratios of multi-branched products and single-branched products (multi/single branch, m/s) (Table 4) for the mixed catalysts. In particular, the m/s ratio of the mixed catalyst MAT-SA-5 using the gel skeletal reinforcement were clearly larger than that for single zeolite. The result suggests that the presence of larger mesopore in the matrix of the cracking catalysts would promote not only the diffusion of reactant molecules to approach acid sites of zeolite and to produce bulky branched products but also the effective elimination of the branched products to prevent the excess cracking of those products.

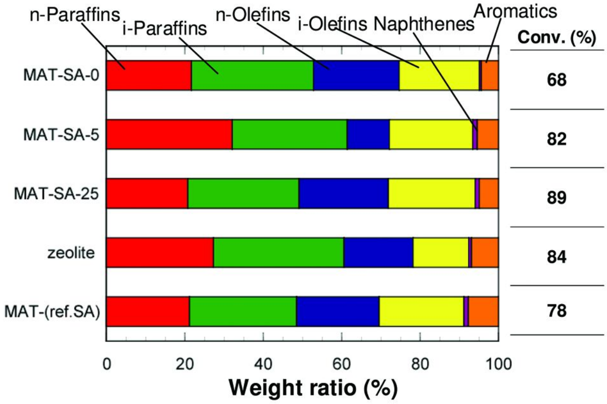

Figure 4. Selectivity for paraffins, olefins, naphthenes and aromatics on catalytic cracking of n-dodecane at 500°C.

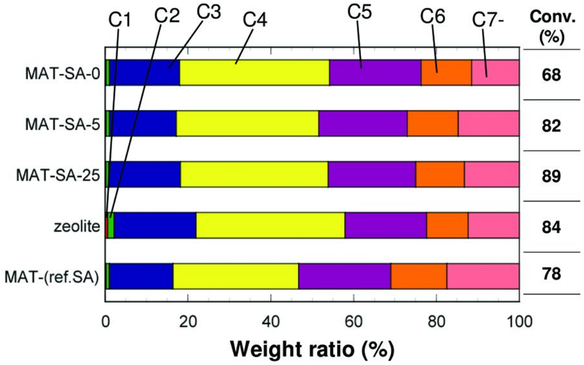

Figure 5. Distributions of carbon numbers on catalytic cracking of n-dodecane at 500°C.

Downloaded by CORNELL UNIV on May 31, 2012 | http://pubs.acs.org
Publication Date (Web): January 20, 2012 | doi: 10.1021/bk-2012-1092.ch004

Downloaded by CORNELL UNIV on May 31, 2012 | http://pubs.acs.org
Publication Date (Web): January 20, 2012 | doi: 10.1021/bk-2012-1092.ch004

Table 4. Product distribution and parameters in gasoline fraction on catalytic cracking of n-dodecane at 500°C

Catalyst	*Product distribution (wt.%)*			*Conv. (%)*	*Parameters in gasoline fraction*			
	C1-C4	*Gasoline (C5-C11)*	*C12-*		*Olefin/ Paraffin*	*iso-/n-*	*multi/ single branch*	*RON*
MAT-SA-0	**54**	**46**	**0.07**	**68**	**0.61**	**2.76**	**0.07**	**85**
MAT-SA-5	**52**	**48**	**0.4**	**82**	**0.65**	**2.83**	**0.10**	**85**
MAT-SA-25	**54**	**46**	**0.3**	**89**	**0.71**	**2.91**	**0.09**	**86**
zeolite	**58**	**42**	**0.5**	**84**	**0.46**	**2.89**	**0.07**	**86**
MAT-(ref.SA)	**47**	**53**	**0.6**	**78**	**0.76**	**2.68**	**0.09**	**85**

Conclusions

The gel skeletal reinforcement was developed to prepare amorphous silica and silica-alumina with large mesopore size and pore volume. To prevent the shrinkage of the pores, the strength of silica-gel skeleton was enhanced by aging with TEOS / 2-propanol mixed solution in the gel skeletal reinforcement. Aerogels were able to be prepared using the gel skeletal reinforcement under both atmospheric and subcritical conditions. When the prepared aerogel was calcined at 500°C for 3h, the mesopore volume and average pore diameter of the obtained silica reached 2.9cm^3/g and 23nm, respectively. Catalytic clacking of n-dodecane was performed using mixed catalysts, which included beta-zeolite and silica-aluminas with large mesopore, at 500 °C. The mixed catalysts showed the comparable activity to that with single use of zeolite. The silica-alumina with large mesopore produced larger amounts of branched products than zeolite single.

Acknowledgments

This work was entrusted by the Japan Petroleum Energy Center under a subsidy of the Ministry of Economy, Trade and Industry.

References

1. Rigacci, A.; Einarsrud, M.-A.; Nilsen, E.; Pirard, R.; Ehrburger-Dolle, F.; Chevalier, B. *J. Non-Cryst. Solids* **2004**, *350*, 196.
2. Reichenauer, G. *J. Non-Cryst. Solids* **2004**, *350*, 189.
3. Smitha, S.; Shajesh, P.; Aravind, P. R.; Rajesh Kumar, S.; Pillai, P. K.; Warrier, K. G. K. *Microporous Mesoporous Mater.* **2006**, *91*, 286.
4. He, F.; Zhao, H.; Qu, X.; Zhang, C.; Qiu, W. *J. Mater. Process. Technol.* **2009**, *209*, 1621.
5. Ishihara, A.; Nakajima, K.; Hirado, M.; Hashimoto, T.; Nasu, H. *Chem. Lett.* **2011**, *40*, 558.

6. Hilonga, A.; Kim, J.-K.; Sarawade, P. B.; Kim, H. T. *J. Alloy. Compd.* **2009**, *487*, 744.
7. Wei, T.-Y.; Chang, T.-F.; Lu, S.-Y.; Chang, Y.-C. *J. Am. Ceram. Soc.* **2007**, *90*, 2003.
8. Gates, B. C.; Katzer, J. R.; Schuit, G. C. A. *Chemistry of Catalytic Processes*; McGraw-Hill: Hightstown, NJ, 1979; Chapter 1, pp 1−111.
9. Inagaki, S.; Takechi, K.; Kubota, Y. *Chem. Commun.* **2010**, *46*, 2662.
10. Sato, S.; Morimoto, Y.; Takatsuka, T.; Hashimoto, H. *Sekiyu Gakkaishi* **1986**, *29*, 60.
11. Ishihara, A.; Negura, H.; Hashimoto, T.; Nasu, H. *Appl. Catal., A*, **2010**, *388*, 68 and references cited therein.
12. Ishihara, A.; Negura, H.; Inui, K.; Hashimoto, T.; Nasu, H. *J. Jpn. Pet. Inst.* **2011**, *54* (3), 189.

Downloaded by CORNELL UNIV on May 31, 2012 | http://pubs.acs.org
Publication Date (Web): January 20, 2012 | doi: 10.1021/bk-2012-1092.ch004

Downloaded by PENNSYLVANIA STATE UNIV on May 31, 2012 | http://pubs.acs.org
Publication Date (Web): January 20, 2012 | doi: 10.1021/bk-2012-1092.ch005

Chapter 5

The Effect of Calcination Temperature on the Properties of MoP for the Hydrodeoxygenation of 4-Methylphenol

Victoria M. L. Whiffen and Kevin J. Smith*

**Department of Chemical and Biological Engineering,
University of British Columbia, 2360 East Mall,
Vancouver, British Columbia V6T 1Z3, Canada
*E-mail: kjs@interchange.ubc.ca**

Unsupported, high surface area MoP was prepared with the addition of citric acid (CA) to the precursor salt solutions. The MoP prepared with CA was calcined at 773, 823, 873, 923, and 973 K followed by reduction to 923 K in H_2. The C content of the reduced MoP-CA catalysts decreased from 13 to 4 wt% as the calcination temperature increased from 773 to 973 K, while the surface area decreased from 136 to 53 m^2/g and the MoP particle size increased from 5 to 9 nm, respectively. The C acted as a structural promoter of the calcined samples, limiting agglomeration of the metal crystallites during reduction so that nanoparticles of MoP were produced. The rate of hydrodeoxygenation, hydrogenation, and CO uptake was found to be dependent on the C content of the MoP-CA catalysts, reaching a maximum for the MoP-CA calcined at 823 K. The HDO of 4-methylphenol over the MoP-CA catalysts was found to be structure insensitive with an initial turn over frequency (TOF) of 0.079 s^{-1} at 623 K and 4.4 MPa H_2. It was found that the CO uptake correlated well to the site density based on the TEM and BET data.

In Nanocatalysis for Fuels and Chemicals; Dalai, A.;
ACS Symposium Series; American Chemical Society: Washington, DC, 2012.

Downloaded by PENNSYLVANIA STATE UNIV on May 31, 2012 | http://pubs.acs.org
Publication Date (Web): January 20, 2012 | doi: 10.1021/bk-2012-1092.ch005

Introduction

Bio-oils derived from the pyrolysis of bio-mass contain large amounts of oxygen (>10 wt%) that contribute to the low heating value, high viscosity, and instability of these oils (*1*). The oxygen can be removed by hydrodeoxygenation (HDO) using supported metal sulfide catalysts typically used for hydrodesulfurization (HDS) and hydrodenitrogenation (HDN) reactions (*2–4*). However, because bio-oils are S free, a sulfiding agent must be fed to the HDO reactor to maintain adequate sulfidation of the catalyst, and this is undesirable (*5*). Hence, there is an interest in non-sulfided catalysts for the HDO of bio-oil.

Catalysts such as metal phosphides, that are active and selective for HDS and HDN, are also candidates for HDO (*6–13*). Whiffen and Smith (*13*) have shown that unsupported, low surface area MoP has a lower activation energy and higher conversion for the HDO of 4-methylphenol compared to low surface area MoS_2, but the MoP activity was limited by low metal dispersion (*13*). Consequently, Wang and Smith (*14*) have shown that both the surface area and CO uptake of MoP can be increased by preparing the catalysts in the presence of citric acid (CA). In the present study, MoP prepared using CA, has been investigated for the HDO of 4-methylphenol, a refractory model compound present in pyrolysis bio-oils.

The objective of the present study was to investigate the effect of calcination temperature on the high surface area, unsupported MoP catalysts prepared with CA. The residual C content of the catalysts is shown to play an important role in determining the catalyst properties and the HDO activity.

Experimental

Catalyst Preparation

MoP was prepared following the method of Stinner et al. (*10*) and Wang and Smith (*14*) using precursor salts dissolved in water. A Mo:P molar ratio of 1:1 was obtained by dissolving 4 g of ammonium heptamolybdate (AHM) ($(NH_4)_6Mo_7O_{24}.4H_2O$) and a corresponding amount of diammonium hydrogen phosphate (AHP) ($(NH_4)_2HPO_4$) in 30 mL of de-ionized water (*10*, *13*, *14*). The precursor solution was aged for 24 h in a covered beaker held at 363 K in a water-bath, dried in an oven at 397 K for 24 h and calcined in air by heating to 773 K at 5 K/min with the final temperature held for 5 hours. The calcined catalyst precursor was ground to a powder (d_P < 53 μm) and converted to MoP by temperature-programmed reduction (TPR) in H_2 at a flow rate of 160 mL(STP)/min and a heating rate of 5 K/min to 573 K, followed by a heating rate of 1 K/min to 923 K. The final temperature was held for 2.5 h. The sample was then cooled to room temperature in a He flow and passivated in a flow of 1 mol% O_2/He for 3 h prior to removal from the quartz u-tube reactor for characterization purposes.

High surface area MoP was prepared in a similar manner, except for the addition of CA to the salt solution at a 2:1 CA:Mo molar ratio (*14*). The CA samples were calcined to 773, 823, 873, 923, or 973 K in air by heating to the desired temperature at 5 K/min, with the final temperature held for 5 hours, and then reduced in the same way as the MoP prepared without CA. The samples are identified as MoP-CA-ttt K, where ttt is the calcination temperature (K). The reduced MoP catalysts used for characterization were passivated as before prior to exposure to the atmosphere. The samples used for activity measurements were transferred directly from the quartz u-tube used for reduction, under a He flow (25 mL(STP)/min), into ~15 mL of decalin. They were then transferred to the reactor for activity measurements, without exposure to air.

Catalyst Characterization

Elemental C analysis was performed on the passivated MoP using a Perkin-Elmer 2400 Series II CHNS/O analyzer operated in the CHN mode. The C concentration was determined by measuring the production of CO_x using a thermal conductivity detector (TCD). The combustion temperature of the oven was held at 1248 K.

Powder x-ray diffraction (XRD) spectra of the passivated MoP was collected using a Rigaku diffractometer with a Cu Kα X-ray source of wavelength 1.54 Å. The analysis was performed using a 40 kV and 20 mA source and a scan range of 10-80° with a step size of 2°/min. Crystallite size (d_c) estimates were made using the Scherrer equation, $d_c = K\lambda/\beta \cos\theta$, where the constant K was taken to be 0.9, λ is the wavelength of radiation, β is the peak width in radians, and θ is the angle of diffraction.

Brunauer-Emmett-Teller (BET) surface areas of the calcined MoP precursors and the passivated MoP catalysts were measured by N_2 adsorption at 77 K using a volumetric unit (Micromeritics ASAP 2010). Prior to N_2 adsorption, the samples were degassed at 423 K in 30 mol% N_2/He (15 mL (STP)/min) for 2 h to remove moisture.

The CO uptake of the MoP catalysts was measured by pulsed chemisorption using a Micromeritics AutoChem II 2920. A known amount of calcined MoP precursor was pretreated in a flow of He (50 mL (STP)/min) at 923 K for 1 h to remove adsorbed species. Subsequently, the calcined MoP precursor was reduced in-situ in 9.5 mol% H_2/Ar (50 mL (STP)/min) by heating at 5 K/min to 573 K followed by a ramp of 1 K/min to 923 K with the final temperature held for 1.5 h. The sample was then cooled in 50 mL (STP)/min He to room temperature, replicating the standard reduction procedure of the calcined MoP precursors. After this treatment, 0.5 mL pulses of CO were injected into a flow of He (50 mL (STP)/min) and the CO uptake was measured using a TCD. CO pulses were repeatedly injected until no further CO uptake was observed after consecutive injections.

Transmission electron microscopy (TEM) images of the catalysts were obtained using a Hitachi H7600 operating at 120 kV with a tungsten filament. Passivated MoP samples were ground to a fine powder using an agate mortar and pestle, dispersed in ethanol and sonicated for 2 h. A drop of the catalyst suspension was placed on a 200 mesh copper grid coated with formvar carbon, and left to dry before analysis (*14*). Log-normal particle size distributions were obtained by editing the images in Pixcavator 4.0 Image Analysis software. Higher resolution TEM images were also generated using a FEI Tecnai transmission

Downloaded by PENNSYLVANIA STATE UNIV on May 31, 2012 | http://pubs.acs.org
Publication Date (Web): January 20, 2012 | doi: 10.1021/bk-2012-1092.ch005

electron microscope operating at 200 kV with a LaB_6 filament. These images were used to determine the d-spacing of the crystallites.

Catalyst Activity

HDO reactions were carried out in a 300 mL stirred-batch reactor operated at 623 K and 4.40 MPa H_2 with 2.96 wt% of 4-methylphenol (4-MP), used as a model reactant, in 100 mL decalin. The reactant solution was slurried with 2,930 ppm_w Mo catalyst, assuming pure MoP and the density of the solvent at ambient conditions (*15*). The reactor was sealed, purged in 55 mL (STP)/min N_2 for 1 h and pressurized with H_2 (UHP) to 2.41 MPa and then heated to the desired temperature at a ramp rate of 10.8 K/min and a stirrer speed of 1000 rpm. Subsequently, the H_2 pressure increased to 4.40 MPa following reactor heat-up to 623 K. The reactant and product concentrations were then analyzed and treated in a similar way to Whiffen and Smith (*13*). For all of the activity data reported herein, the carbon balance across the reactor was > 90 mol% and a number of the experiments were repeated to ensure repeatability of the data.

Results and Discussion

Catalyst Characterization

The properties of the reduced and passivated MoP catalysts, prepared with and without CA at various calcination temperatures, are summarized in Table I. The MoP-noCA was free of C whereas the CA samples contained significant amounts of C that decreased as the calcination temperature increased. Even upon calcination to 973 K and reduction to 923 K, 4 wt% carbon remained in the MoP-CA-973 K catalyst.

Table I also shows that the addition of CA to the catalyst precursors significantly increased the surface area of the MoP and this was a consequence of a reduced MoP particle size. Compared to the MoP-noCA calcined at 773 K, the surface area of the MoP-CA, calcined at the same temperature, increased by a factor of ~10. This was a consequence of Mo citrate formation as found by Cheng et al. (*16*), which prevented agglomeration of the Mo crystallites during calcination. As the calcination temperature of the CA samples increased, the surface area decreased due to the decomposition of the Mo citrate at high temperatures. The catalyst particle size was estimated from the BET surface area using the equation $d_{p(BET)} = 6/(S_{BET}\,\rho)$, assuming cubic or spherical geometry, where $d_{p(BET)}$ is the particle size calculated from the BET surface area, and ρ is the MoP density (7.5 g/cm^3) (*17*). The particle size of the MoP catalyst prepared without CA was estimated at 100 nm, significantly larger than the crystallite size calculated from the XRD data using Scherrer's equation (23 nm) for the (101) plane of MoP (Figure 1). This suggests significant agglomeration of the metal phosphide crystallites prepared without CA. In contrast, the calculated particle size of MoP-CA-773K was 6 nm, smaller than the crystallite size obtained from the XRD data (16 nm). The deviation between the calculated particle size and the XRD data was likely a consequence of the presence of MoP-CA nanoparticles (<

Downloaded by PENNSYLVANIA STATE UNIV on May 31, 2012 | http://pubs.acs.org
Publication Date (Web): January 20, 2012 | doi: 10.1021/bk-2012-1092.ch005

5nm) that were not detected by XRD line broadening (*18*). Similar differences were observed by Wang and Smith (*14*) for MoP-CA characterized by XRD and TEM. In the present study, TEM analysis showed a particle size that increased from 5.2 to 8.7 nm for the MoP-CA samples, as the calcination temperature increased from 773 to 973 K. The particle size, as calculated from the BET data, also increased as the calcination temperature increased. The increased particle size was likely due to the loss in carbon, thereby decomposing the metal citrate, that resulted in agglomeration of the crystallites as the calcination temperature increased. This suggests that the carbon from the CA acted as a structural promoter in the form of a metal citrate that limited agglomeration of the MoP crystallites.

The CO uptake of the MoP-CA-773 increased to 55 μmol/g_{MoP} compared to < 1 μmol/g_{MoP} for the MoP-noCA. The CO uptake values were corrected for the amount of C present in the reduced samples. MoP-CA calcined at 823 K displayed the highest CO uptake. However, as the calcination temperature increased above 823 K the CO uptake of the MoP-CA decreased, consistent with agglomeration of the MoP crystallites as shown from the TEM data. As the calcination temperature for the CA samples was increased above 823 K the Mo citrate was destroyed. This in turn resulted in larger MoP particles with low dispersions following reduction.

Downloaded by PENNSYLVANIA STATE UNIV on May 31, 2012 | http://pubs.acs.org
Publication Date (Web): January 20, 2012 | doi: 10.1021/bk-2012-1092.ch005

Table I. Physical and chemical properties of MoP prepared with and without CA

Catalyst	*MoP-CA*	*MoP-CA*	*MoP-CA*	*MoP-CA*	*MoP-CA*	*MoP-noCA*
Calcination T (K)	*773*	*823*	*873*	*923*	*973*	*773*
C (wt%)	13	9	6	5	4	0
S_{BET} (m^2/g_{cat})	136	112	75	63	53	8
$d_{p(BET)}$ (nm)	6	7	11	13	15	100
d_{101} (nm)	16	19	20	18	19	23
d_{TEM}[a] (STDev) (nm)	5 (0.5)	6 (0.2)	--	8 (3)	9 (1)	55 (5)
S_{TEM}[b] (m^2/g_{cat})	139	119	--	93	86	15
CO Uptake (μmol/g_{MoP})	54	60	34	22	19	<1

[a] average TEM particle size. [b] surface area calculated from TEM particle size.

Downloaded by PENNSYLVANIA STATE UNIV on May 31, 2012 | http://pubs.acs.org
Publication Date (Web): January 20, 2012 | doi: 10.1021/bk-2012-1092.ch005

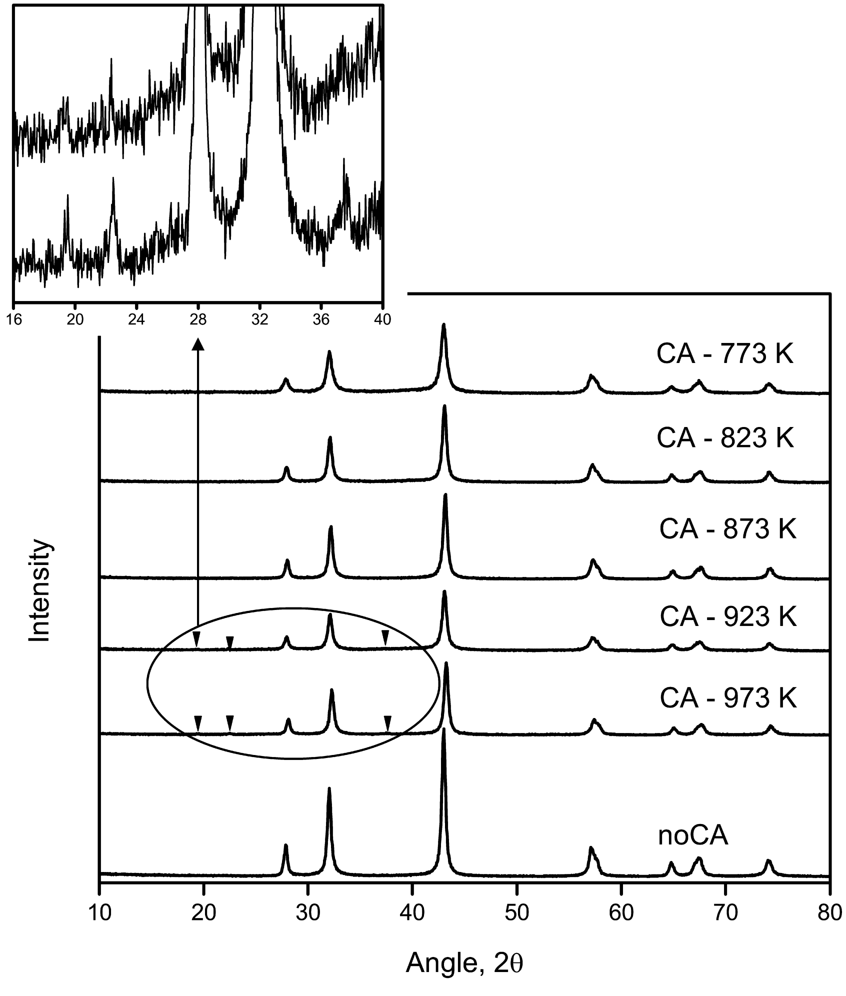

Figure 1. XRD diffractograms of MoP-CA and MoP-noCA catalysts.

The x-ray diffractograms, given in Figure 1, were used to estimate the crystallite sizes of the catalysts reported Table I. The XRD of all samples showed the (101) reflection at $2\theta = 43°$, characteristic of MoP (PDF#065-6487). Interestingly, MoP-CA-973 K and MoP-CA-923 K displayed additional diffraction peaks at $2\theta = 19.6°$, 22.5°, and 37.6°. These reflections are characteristic of $MoPO_4(OH)_3$ (PDF#00-011-0333). The formation of the unreduced phase could be a consequence of hydration from the production of water. The quantity of this species was less than 2%, as determined by the XRD peak intensity ratios.

TEM micrographs of the reduced and passivated samples are presented in Figure 2. In the case of the MoP catalyst prepared without CA (MoP–noCA, Figure 2 (a)), the particles aggregated to form large nanoclusters with a size of 50–60 nm, surrounded by a 20 nm passivation layer, similar to the morphology described by Wang and Smith (*14*), and Cheng et al. (*16*). Separate 6 nm particles were clearly evident for the MoP-CA calcined at 823 K (Figure 2 (b)) as observed by Wang and Smith (*14*), and Cheng et al. (*16*). These separate nanoparticles were also observed for MoP-CA-973 K (Figure 2 (c)). Most of the MoP-CA catalysts had particle sizes between 5-10 nm, although those calcined at higher temperature did display larger agglomerated particles, but still retained the phase of dispersed nanoparticles. The lognormal average size of these dispersed nanoparticles is given in Table I along with their associated STDev.

The small particles of MoP, identified via TEM, contributed to the high surface area encountered for the MoP-CA catalysts. This was shown by the reasonable agreement between the measured BET area and the area (S_{TEM}) calculated from the TEM particle size of the MoP-CA catalysts (Table I).

Downloaded by PENNSYLVANIA STATE UNIV on May 31, 2012 | http://pubs.acs.org
Publication Date (Web): January 20, 2012 | doi: 10.1021/bk-2012-1092.ch005

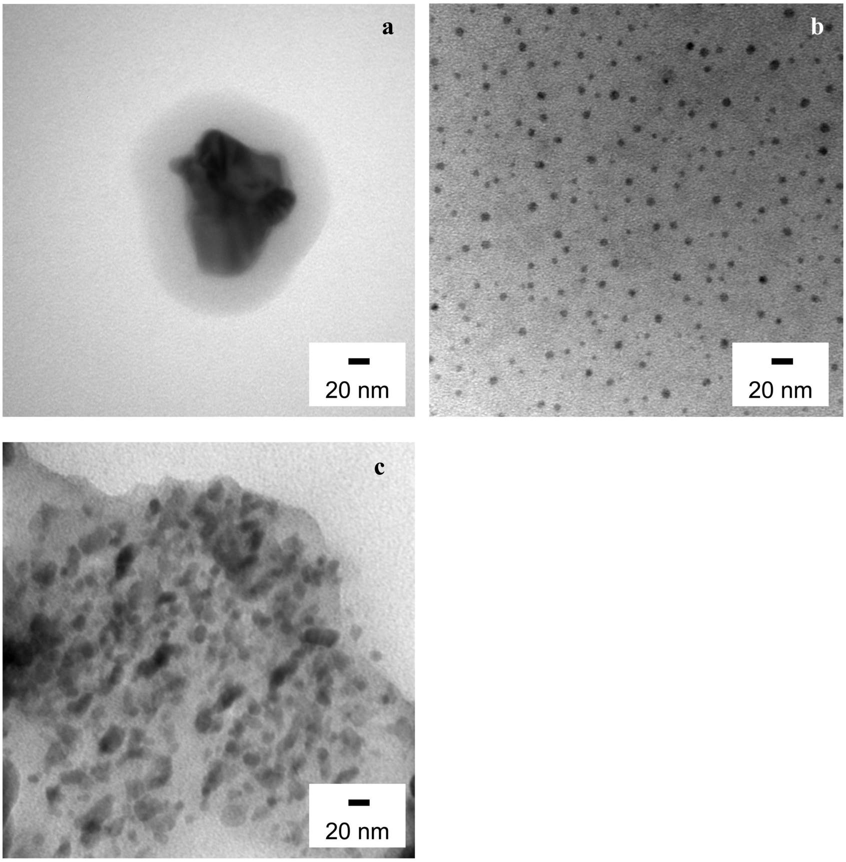

Figure 2. TEM images of reduced and passivated samples: (a) MoP–noCA with passivation layer; (b) MoP-CA-823 K; (c) MoP-CA-923 K.

Catalyst Activity and Product Distribution

Prior to reaction, the catalysts were reduced ex-situ and transferred in decalin to the reactor without exposure to air. The reactant, 4-methylphenol, was then added to the reactor. Toluene, methylcyclohexane, and small amounts of 1,3-dimethylcyclopentane were detected as products of the reaction. The error observed in the reactant conversion was approximately ±7% as determined from repeat experiments.

Table II reports the 4-methylphenol conversions and product selectivities after 5 h reaction at 623 K and 4.40 MPa over the MoP catalysts. The conversions are net of the thermal reaction, which resulted in 12% conversion after 5 h at the reaction conditions. The low surface area catalyst prepared in the absence of CA had a higher degree of hydrogenated products (50%) compared to MoP-CA-773 K (37%). As the calcination temperature of the MoP-CA catalysts increased to 823 K, the conversion and selectivity toward 4-methylcyclohexane increased. The conversion and selectivity towards 4-methylcyclohexane decreased as the aggregation of the MoP crystallites increased with increased calcination temperature above 823 K.

Downloaded by PENNSYLVANIA STATE UNIV on May 31, 2012 | http://pubs.acs.org
Publication Date (Web): January 20, 2012 | doi: 10.1021/bk-2012-1092.ch005

Table II. Conversion and product selectivity of 4-methylphenol over MoP Catalysts after 5 h reaction at 623 K and 4.40 MPa

Catalyst	*4-MP Conversion (%)*	*Product Selectivity (%)*		
		Toluene	*Methyl-cylcohexane*	*Dimethyl-cyclopentane*
MoP-CA-773 K	58	60	37	3
MoP-CA-823 K	71	51	47	2
MoP-CA-873 K	56	56	42	2
MoP-CA-923 K	40	56	43	1
MoP-CA-973 K	38	57	41	2
MoP-noCA	45	49	50	1

The 1st-order rate constant for the conversion of 4-methylphenol over the MoP-CA catalysts was calculated accounting for the thermal reaction, catalyst concentration, catalyst C content, and the solution volume. MoP-noCA had a rate constant of 1.10 ± 0.01 $mL.s^{-1}.mol_{Mo}^{-1}$. The MoP-CA-773K had a rate constant of 1.88 ± 0.09 $mL.s^{-1}.mol_{Mo}^{-1}$ and this reached a maximum at 2.28 ± 0.25 $mL.s^{-1}.mol_{Mo}^{-1}$ for the MoP-CA-823 K catalyst (Figure 3). The precursors calcined at lower temperatures had higher C content and lower rate constants, on a Mo basis. However, at higher calcination temperatures (above 873 K) the

C content was lower and the 1st-order rate constant was also reduced. This was due to agglomeration of the MoP crystallites at the high temperature. Overall, a maximum was found to exist between carbon content and observed activity of the MoP-CA catalysts. The maximum rate constant occurred for the catalyst with approximately 10 wt% carbon. A maximum in CO uptake for the MoP-CA samples occurred for the same catalyst (MoP-CA-823K).

The product selectivities as a function of 4-methylphenol conversion, are shown in Figure 4 for the MoP-CA-823 K catalyst. The results suggest three important reactions: hydrogenolysis of 4-methylphenol to produce toluene; hydrogenation to methylcyclohexane and isomerization to yield 1,3-dimethylcyclopentane a consequence of MoP surface acidity due to unreduced phosphate species (*6*). No methylcyclohexenes were detected over the MoP catalysts. All products were oxygen-free, confirming that HDO was successful.

Downloaded by PENNSYLVANIA STATE UNIV on May 31, 2012 | http://pubs.acs.org
Publication Date (Web): January 20, 2012 | doi: 10.1021/bk-2012-1092.ch005

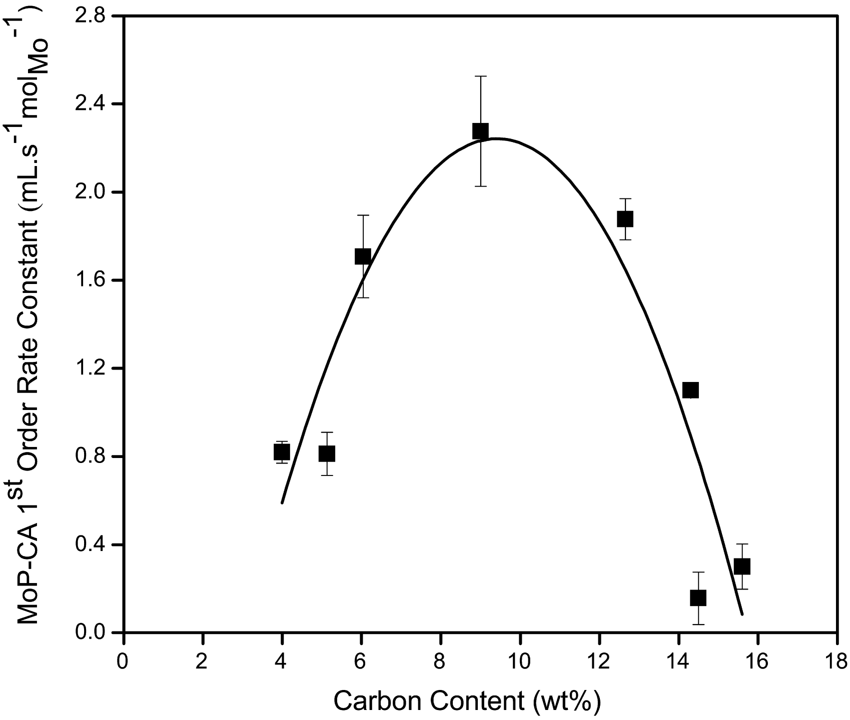

Figure 3. MoP-CA 1st-order rate constant versus carbon content of reduced MoP-CA catalysts.

Downloaded by PENNSYLVANIA STATE UNIV on May 31, 2012 | http://pubs.acs.org
Publication Date (Web): January 20, 2012 | doi: 10.1021/bk-2012-1092.ch005

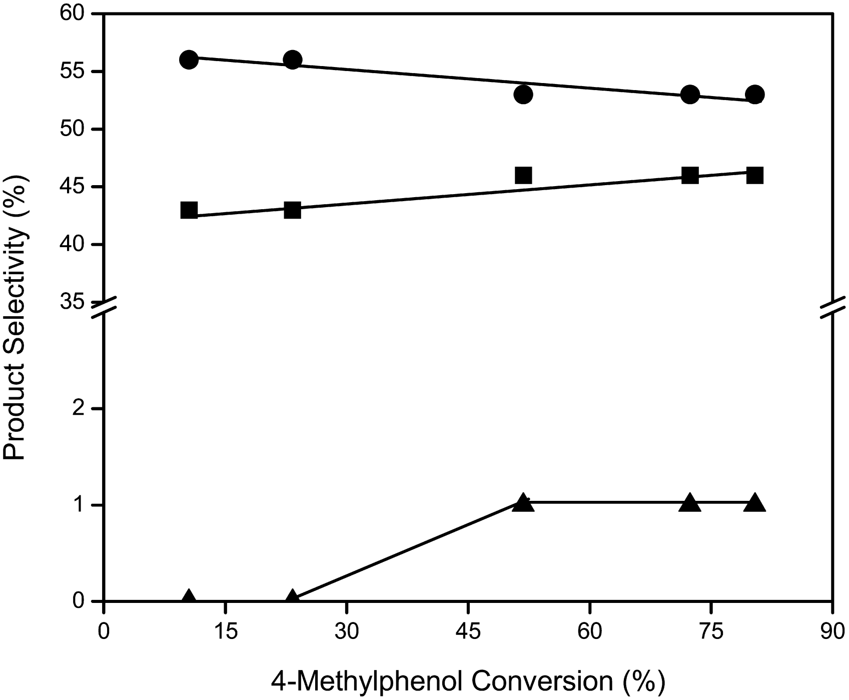

Figure 4. Product selectivity versus 4-methylphenol conversion over MoP-CA-823 K.

On the basis of the product distribution results, hydrogenolysis or direct deoxygenation (DDO) to produce toluene and the coupled ring saturation/rapid dehydration to produce 4-methylcyclohexene, were assumed to be the primary reactions for the HDO of 4-methylphenol. Toluene did not undergo further reaction whereas 4-methylcyclohexene was hydrogenated (HYD) to methylcyclohexane or isomerized to 1,3-dimethylcyclopentane (ISOM). This proposed reaction scheme is given in Figure 5 and is similar to that proposed by Laurent and Delmon (*19*).

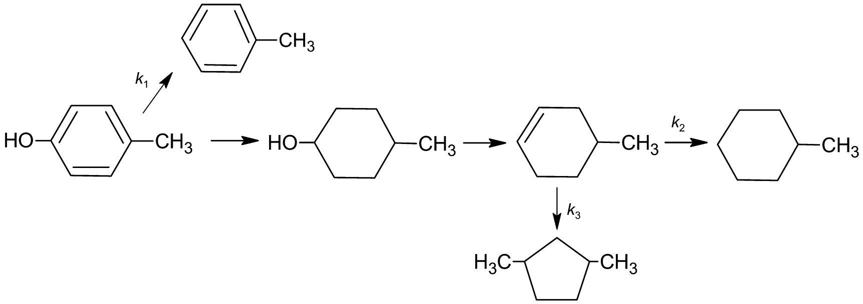

Figure 5. Proposed reaction scheme for the hydrodeoxygenation of 4-methylphenol over MoP catalysts.

Active Sites

The site density, calculated from the S_{BET} and TEM data, was well correlated with the measured CO uptake data (Table III) and therefore, it was assumed that the CO uptake was an appropriate measure of the number of active sites on the MoP catalyst. The total metal site density of the MoP-CA catalysts was calculated by assuming spherical MoP particles and a surface area to volume ratio of $6/\rho$, where ρ is the bulk density of MoP. The MoP site area, estimated at 9.71 atoms/nm^2, was calculated from the crystal structure of MoP and the average atom exposure of the low index planes (*10*, *17*). The calculated MoP site densities were much higher than the measured CO uptake data due to blockage of the active sites by phosphorous (*17*, *20*).

The initial HDO consumption rates per mol$_{Mo}$ of the MoP-CA catalysts prepared at different calcination temperatures, calculated from the initial reactant concentration and the 4-methylphenol decomposition 1st-order rate constant, are plotted as a function of CO uptake in Figure 6. The activity correlated with the CO uptake and from the slope of the linear regression plot, a TOF of 0.079 ± 0.0012 s^{-1} was calculated, assuming that one CO molecule adsorbs on one active site of the MoP catalyst (*9*). These results show that the hydrodeoxygenation of 4-methylphenol over MoP-CA catalysts is not structure sensitive. This result is expected as the particle size variation for MoP-CA catalysts was less than 5 nm and the 4-methylphenol reactant molecule likely adsorbs one site to one atom of the reactant molecule.

Table III. MoP site density based on BET, XRD, and TEM size versus CO uptake

Sample	*CO Uptake ($\mu mol/g_{cat}$)*	*Metal Site Density from BET ($\mu mol/g_{cat}$)*	*Metal Site Density from TEM ($\mu mol/g_{cat}$)*
MoP-CA-773 K	46	2239	2239
MoP-CA-823 K	55	1804	1916
MoP-CA-873 K	32	1208	--
MoP-CA-923 K	21	1015	1498
MoP-CA-973 K	18	854	1385
MoP-noCA	<1	129	234

Downloaded by PENNSYLVANIA STATE UNIV on May 31, 2012 | http://pubs.acs.org
Publication Date (Web): January 20, 2012 | doi: 10.1021/bk-2012-1092.ch005

Downloaded by PENNSYLVANIA STATE UNIV on May 31, 2012 | http://pubs.acs.org
Publication Date (Web): January 20, 2012 | doi: 10.1021/bk-2012-1092.ch005

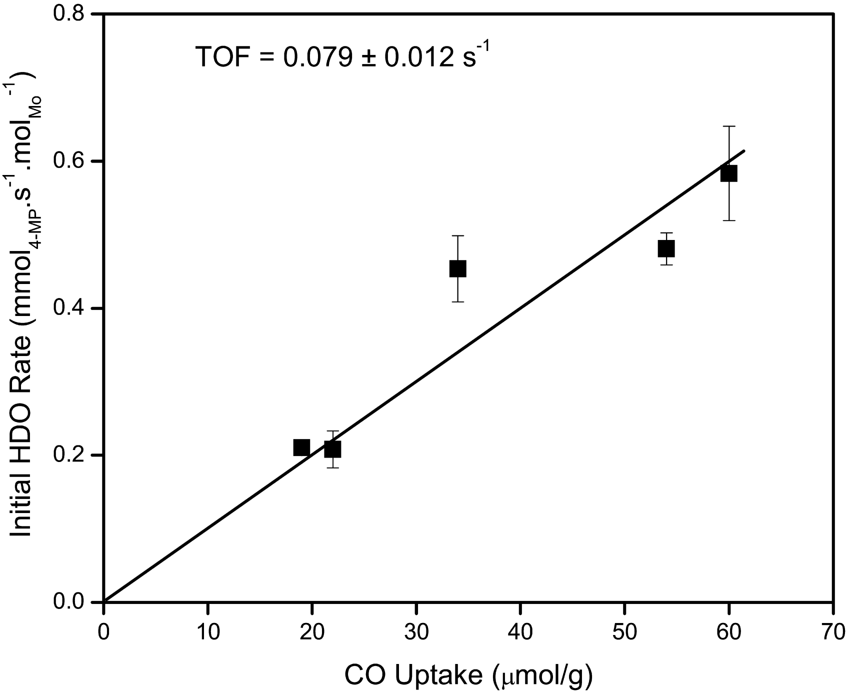

Figure 6. Initial HDO rate of 4-methylphenol versus CO uptake of MoP-CA catalysts.

Conclusions

Addition of CA prior to MoP increased the surface area, CO uptake, and HDO activity of 4-methylphenol. However, these CA samples were found to have significant amounts of C - 13 wt% residual C was present in the MoP-CA sample calcined at 773 K. This C acted as a structural support that limited agglomeration of the crystallites during calcination. A maximum initial hydrodeoxygenation rate and CO uptake was found for the MoP-CA catalyst containing 10 wt% carbon. Calcination of MoP-CA at temperatures above 823 K resulted in crystallite agglomeration, which reduced the CO uptake and initial hydrodeoxygenation rate. The hydrodeoxygenation of 4-methylphenol was found to be structure insensitive over all MoP-CA catalysts. The calculated TOF was approximately 0.079 s^{-1}.

References

1. Furimsky, E. *Appl. Catal., A* **2000**, *199*, 147–190.
2. Bunch, A.; Ozkan, U. *J. Catal.* **2002**, *206*, 177–187.
3. Yang, Y.; Tye, C.; Smith, K. *Catal. Commun.* **2008**, *9*, 1364–1368.
4. Tye, C.; Smith, K. *Catal. Today* **2006**, *116*, 461–468.
5. Wang, W.; Yang, Y.; Bao, J.; Luo, H. *Catal. Commun.* **2009**, *11*, 100–105.

6. Abu, I.; Smith, K. *J. Catal.* **2006**, *241*, 356–366.
7. Oyama, S.; Wang, X.; Requejo, F.; Sato, T.; Yoshimura, Y. *J. Catal.* **2002**, *209*, 1–5.
8. Yang, S.; Liang, C.; Prins, R. *J. Catal.* **2006**, *241*, 465–469.
9. Phillips, D.; Sawhill, S.; Self, R.; Bussell, M. *J. Catal.* **2002**, *207*, 266–273.
10. Stinner, C.; Prins, R.; Weber, T. *J. Catal.* **2000**, *191*, 438–444.
11. Li, K.; Wang, R.; Chen, J. *Energy Fuels* **2011**, *25*, 854–863.
12. Zhao, H.; Li, D.; Bui, P.; Oyama, S. *Appl. Catal., A* **2011**, *391*, 305–310.
13. Whiffen, V.; Smith, K. *Energy Fuels* **2010**, *24*, 4728–4737.
14. Wang, R.; Smith, K. *Appl. Catal., A* **2009**, *361*, 18–25.
15. Miyake, Y.; Baylaucq, A.; Zeberg-Mikkelsen, C.; Galliero, G.; Ushiki, H.; Boned, C. *Fluid Phase Equilib.* **2007**, *252*, 79–87.
16. Cheng, R.; Shu, Y.; Li, L.; Zheng, M.; Wang, X.; Wang, A.; Zhang, T. *Appl. Catal., A* **2007**, *316*, 160–168.
17. Clark, P.; Oyama, S. *J. Catal.* **2003**, *218*, 78–87.
18. Coughlan, B.; Keane, M. *Zeolites* **1991**, *11*, 854–857.
19. Laurent, E.; Delmon, B. *Ind. Eng. Chem. Res.* **1993**, *32*, 2516–2524.
20. Clark, P.; Li, W.; Oyama, S. *J. Catal.* **2001**, *200*, 140–147.

Downloaded by PENNSYLVANIA STATE UNIV on May 31, 2012 | http://pubs.acs.org
Publication Date (Web): January 20, 2012 | doi: 10.1021/bk-2012-1092.ch005

Downloaded by OHIO STATE UNIV LIBRARIES on May 31, 2012 | http://pubs.acs.org
Publication Date (Web): January 20, 2012 | doi: 10.1021/bk-2012-1092.ch006

Chapter 6

Catalytic Cracking of Heavy Oil over a Complex Metal Oxide Catalyst in a Steam Atmosphere

E. Fumoto,* S. Sato, and T. Takanohashi

Energy Technology Research Institute,
National Institute of Advanced Industrial Science and Technology,
16-1 Onogawa, Tsukuba 305-8569, Japan
***E-mail: e-fumoto@aist.go.jp**

Heavy oil upgrading to produce light oil from heavy oils such as petroleum residual oil and Canadian oil sand bitumen is necessary to meet fuel demands. Hydrocracking using hydrogen gas produces high-quality oil with low coke yield, but hydrogen is expensive. Therefore, this study investigated heavy oil upgrading using steam to produce light oil. Heavy oil was decomposed using a complex metal oxide catalyst consisting of iron, zirconium, and aluminum to produce light oil and carbon dioxide. After the lattice oxygen in iron oxide reacted with the heavy oil, oxygen species from steam were supplied to the iron oxide lattice and reacted with the heavy oil. The alkene/alkane ratio of the light oil produced by reaction in a steam atmosphere was low compared to that in a nitrogen atmosphere. Hydrogen generated from steam during the reaction of oxygen species from steam with heavy oil was incorporated into the light oil.

Introduction

Petroleum refineries use light oil to produce transportation fuels, and thus heavy oil upgrading is necessary to meet fuel demands. Heavy oil includes petroleum residual oil produced during refining processes and extra-heavy oil such as Canadian oil sand bitumen and Venezuelan orinoco tar, of which bountiful reserves exist. Table I shows the properties of typical heavy oils, atmospheric residual oil (AR), and Athabasca oil sand bitumen (*1*, *2*). These heavy oils have

Downloaded by OHIO STATE UNIV LIBRARIES on May 31, 2012 | http://pubs.acs.org
Publication Date (Web): January 20, 2012 | doi: 10.1021/bk-2012-1092.ch006

very high viscosity and low H/C ratios, and contain large amounts of high-boiling point components and impurities such as sulfur and heavy metals (vanadium, nickel, and iron).

To produce useful light oil from heavy oil, decomposition of heavy oil and an increase in the H/C ratio by addition of hydrogen are required. However, hydrogen is expensive, and thus heavy oil upgrading using steam as a source of hydrogen and oxygen appears to be a promising alternative. This chapter describes heavy oil upgrading over a catalyst in a steam atmosphere. Conventional upgrading processes are described, and an experimental investigation of heavy oil cracking using steam is discussed.

Table I. Properties of heavy oil

	AR [a]	*Bitumen* [b]
Composition (wt%)		
Light oil [c]	7	16
Vacuum gas oil [d]	49	39
Vacuum residue [e]	44	45
Density (g/cm^3)	0.944	1.01
Elemental analysis (wt%)		
C	85.7	83.5
H	11.6	10.6
N	0.16	0.47
S	2.48	4.17
O	-	1.00
H/C (mol/mol)	1.63	1.52
Conradson carbon residue (wt%)	5.8	11.3
Heavy metals (ppm)		
V	10	200
Ni	4	75
Fe	10	1

[a] AR was derived from Middle East crude. [b] Athabasca oil sand bitumen was recovered by steam-assisted gravity drainage (SAGD). [c] Light oil was defined as having a boiling point below 623 K. [d] Vacuum gas oil was defined as having a boiling point between 623 K and 773 K. [e] Vacuum residue was defined as having a boiling point above 773 K.

Heavy Oil Upgrading Process

Conventional Upgrading Processes

Conventional methods for upgrading heavy oil to produce light oil include thermal cracking (*3*, *4*), residue fluid catalytic cracking (RFCC) (*5*), and hydrocracking (*6–8*). Heavy oil is thermally cracked to produce gas, light oil, and coke in a coking process (*9*). Although the conversion of heavy oil to light oil increases with reaction temperature and residence time, large amounts of coke are produced.

The RFCC process combines a fluidized-bed reactor and a regenerator using zeolite catalysts (*9*). The catalyst is circulated continuously between the reactor and the regenerator. Heavy oil is cracked to produce light fractions, and coke is deposited on the catalyst in the reactor. The coke deposited on the catalyst is fed to the regenerator, and the spent catalysts are regenerated by combustion. Thus, the heat produced in the regenerator is supplied to the reactor using the catalyst as a heat carrier. However, deposition of heavy metals deactivates the catalysts (*5*).

In the hydrocracking process, coke generation decreases with increasing hydrogen consumption (*6*). Nickel–molybdenum and cobalt–molybdenum catalysts are often used. Several hydrocracking processes, such as H-Oil, LC-Fining, and T-Star, use an ebullated-bed reactor (*8*). This reactor is useful for mixing hydrogen, feed oil, and a catalyst because the catalyst is suspended in the upflow stream of feed oil.

Upgrading Process Using Water

Hydrocracking is useful for heavy oil upgrading because it produces light oil with low coke formation, but hydrogen is expensive. Thus, the use of water as a source for hydrogen and oxygen is a promising alternative for heavy oil upgrading. Several studies have reported the use of water for heavy oil upgrading by heavy oil treating (HOT), Aquaconversion®, and super critical water (*10–13*). In the HOT process (*10*), steam reacts with wüstite (FeO) catalysts to produce hydrogen and magnetite (Fe_3O_4). Heavy oil reacts with magnetite to produce light fractions, and coke is deposited on the magnetite. The coke/magnetite is burned to produce wüstite catalysts. Aquaconversion® is a mild process using two non-noble metal catalysts to transfer hydrogen from water to oil (*11*). Using supercritical water, heavy oil is decomposed to produce low-viscosity oil and coke (*12*, *13*).

This chapter describes the production of useful light oil from heavy oil with low coke formation through heavy oil upgrading over a complex metal oxide catalyst using steam. Catalysts for heavy oil upgrading must have a high capacity to decompose heavy oil, stable activity in a steam atmosphere at high temperatures, resistance to or lack of coke deposition, and resistance to sulfur and heavy metals contained in the heavy oil. Thus, an iron oxide-based catalyst was used for heavy oil upgrading in a steam atmosphere.

Downloaded by OHIO STATE UNIV LIBRARIES on May 31, 2012 | http://pubs.acs.org
Publication Date (Web): January 20, 2012 | doi: 10.1021/bk-2012-1092.ch006

Downloaded by OHIO STATE UNIV LIBRARIES on May 31, 2012 | http://pubs.acs.org
Publication Date (Web): January 20, 2012 | doi: 10.1021/bk-2012-1092.ch006

Experimental Procedure

Catalytic cracking of bitumen and AR was conducted using a complex metal oxide catalyst in a steam atmosphere. A typical complex metal oxide catalyst of iron, zirconium, and aluminum was prepared via coprecipitation by adding aqueous ammonia to an aqueous solution of iron(III) chloride, aluminum chloride, and zirconium oxychloride. The catalyst was treated in a steam atmosphere at 873 K for 1 h, pelletized without a binder, crushed, and sieved to give particles of 250–560 μm. The contents of iron oxide, zirconia, and alumina were 85, 9, and 7 wt%, respectively. Zirconium was added to the catalyst to promote steam decomposition (*14*), and alumina was added as a highly steam-tolerant material because iron oxide was alloyed with alumina homogeneously (*15*).

We used AR derived from Middle East crude and Athabasca oil sand bitumen recovered by steam-assisted gravity drainage (SAGD). The properties of these oils are given in Table I. As these heavy oils are viscous, they were diluted to 10 wt% using toluene and used as a feedstock. Toluene was chosen as the solvent because the ability of the catalyst to decompose toluene was negligible.

Approximately 1.5×10^{-3} kg of catalyst was loaded into a down-flow-type fixed-bed reactor (*1*). The feedstock and steam were fed to the reactor at flow rates of 1.1×10^{-3} and 1.0×10^{-3} kg/h, respectively. The reaction was carried out at 748 K, atmospheric pressure, and in a steam atmosphere. Gas and liquid products were separated through an ice trap. After 2 h, the reactor was cooled to room temperature, and product was collected. A comparative experiment was conducted under the same conditions using a nitrogen atmosphere.

Gas products were analyzed by gas chromatography using a thermal conductivity detector (GC-12A, Shimadzu Co. Ltd., Japan) equipped with Porapak Q and a flame ionization detector (GC-14A, Shimadzu Co. Ltd., Japan) equipped with Unibeads 3S columns. The boiling range distribution of the liquid products was measured by gas chromatographic distillation (HP6890, Agilent Technologies, Santa Clara, CA) with a wide-bore capillary column. The liquid products were defined as light oil (boiling point < 623 K) and heavy oil (boiling point > 623 K). The weight of coke was analyzed by combustion of spent catalyst using a thermogravimeter (TGA-50, Shimadzu Co. Ltd., Japan).

Production of Light Oil

Figure 1 shows photos of the bitumen feedstock solution and oil products, including the toluene solvent. Product oil was obtained by reacting bitumen over a complex metal oxide catalyst of iron, zirconium, and aluminum in a steam atmosphere. The heavy hydrocarbons of bitumen were decomposed, and the color of the oil changed from black to light brown during the reaction. Figure 2 shows distillation curves of bitumen and the product of the reaction of bitumen with the catalyst in a steam atmosphere. The curve of product shifted to right compared to that of bitumen, indicating that product included lower-boiling point component.

Heavy oil fractions of bitumen and AR were decomposed over a complex metal oxide catalyst of iron, zirconium, and aluminum to produce light fractions at reaction temperatures of 723–773 K in a steam atmosphere (*1*, *2*, *16–18*). Figure 3 shows the product yield for the AR reaction in nitrogen and steam atmospheres. The composition of AR is shown in Figure 3 for comparison. Heavy oil was decomposed using a catalyst to produce light oil, carbon dioxide, gaseous hydrocarbons (C_1–C_4), and coke. The yield of light oil generated by the reaction of AR for 2 h in a steam atmosphere was almost the same as that in a nitrogen atmosphere. Reaction of AR in a steam atmosphere resulted in a higher yield of carbon dioxide and less coke formation compared to the reaction in a nitrogen atmosphere. Oxygen species from steam reacted with heavy oil to produce large amounts of carbon dioxide and suppressed coke formation.

Downloaded by OHIO STATE UNIV LIBRARIES on May 31, 2012 | http://pubs.acs.org
Publication Date (Web): January 20, 2012 | doi: 10.1021/bk-2012-1092.ch006

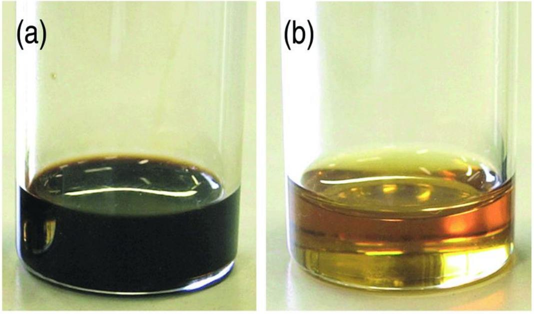

Figure 1. Photos of (a) the feedstock solution of bitumen and (b) product oil, including solvent. Product oil was produced by reacting bitumen over a complex metal oxide catalyst of iron, zirconium, and aluminum at 748 K in a steam atmosphere.

Downloaded by OHIO STATE UNIV LIBRARIES on May 31, 2012 | http://pubs.acs.org
Publication Date (Web): January 20, 2012 | doi: 10.1021/bk-2012-1092.ch006

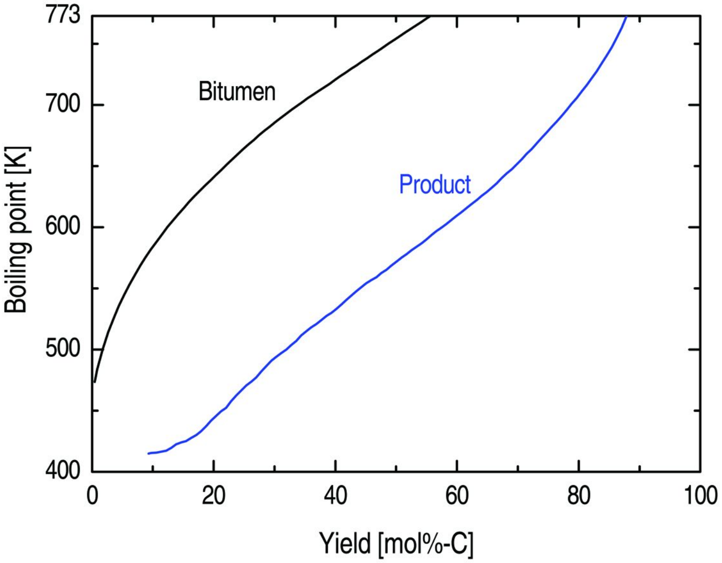

Figure 2. Distillation cureves of bitumen and product for the reaction of bitumen over a complex metal oxide catalyst of iron, zirconium, and aluminum at 748 K in a steam atmosphere.

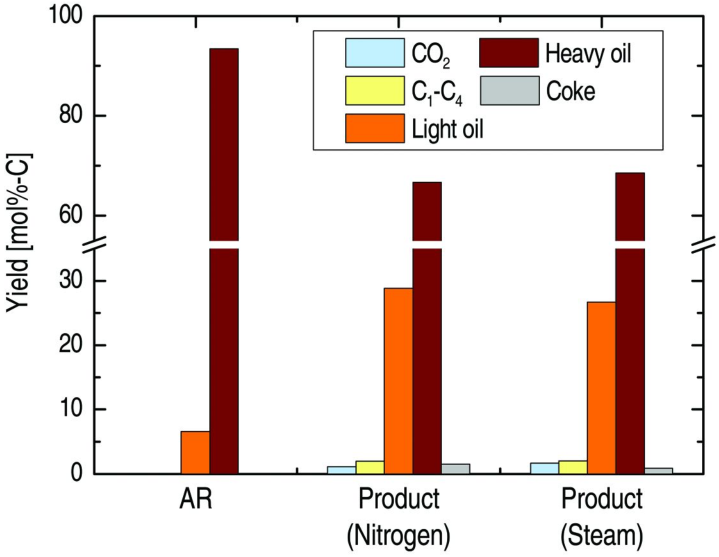

Figure 3. Product yield for the reaction of AR over a complex metal oxide catalyst of iron, zirconium, and aluminum at 748 K in nitrogen and steam atmospheres.

Downloaded by OHIO STATE UNIV LIBRARIES on May 31, 2012 | http://pubs.acs.org
Publication Date (Web): January 20, 2012 | doi: 10.1021/bk-2012-1092.ch006

Reaction Mechanism of Catalytic Cracking of Heavy Oil Using Steam

To elucidate the reaction mechanism of heavy oil cracking using a complex metal oxide catalyst of iron, zirconium, and aluminum in a steam atmosphere, the structure of the catalyst was characterized. Figure 4 shows X-ray diffraction (XRD) patterns of the catalyst before and after the reaction of AR in a steam atmosphere. The pattern before reaction corresponded to hematite (α-Fe_2O_3). A hematite domain size of 41 nm was calculated using Scherrer's equation. Peaks corresponding to hematite and magnetite appeared in the pattern of the catalyst after reaction in a steam atmosphere. The hematite structure changed to magnetite after reaction in a nitrogen atmosphere (*1*). These results suggested that heavy oil reacted with the lattice oxygen of iron oxide, and oxygen species from steam were supplied to the iron oxide lattice.

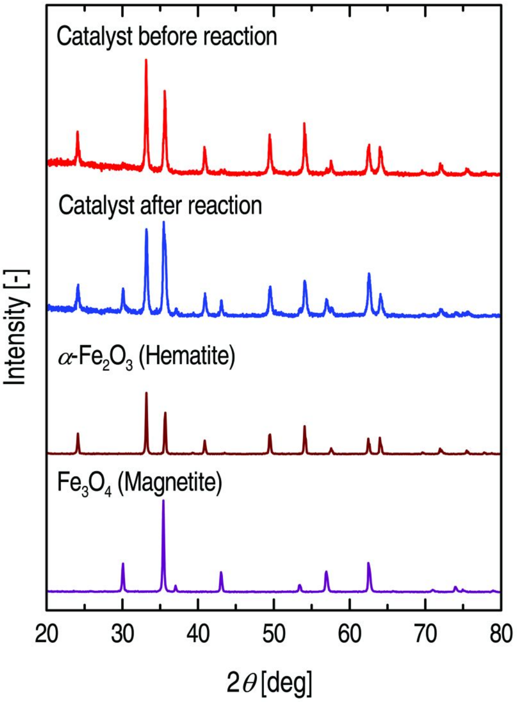

Figure 4. X-ray diffraction patterns of the complex metal oxide catalyst of iron, zirconium, and aluminum before and after reaction of AR at 748 K in a steam atmosphere.

Figure 5 shows the phase change of the metal oxide catalyst during the conversion of heavy oil to light fractions in a steam atmosphere. The proposed reaction mechanism is as follows. First, lattice oxygen in the metal oxide (MeO_X) reacts with heavy oil to produce light oil and carbon dioxide, and MeO_X is converted to $MeO_{X-\alpha}$. Next, oxygen species from steam are supplied to $MeO_{X-\alpha}$, reconstructing MeO_X. Thus, the hematite structure was maintained during the reaction of heavy oil when large amounts of oxygen species were supplied from steam to the iron oxide lattice of the catalyst after consumption of the lattice oxygen of hematite. The oxygen content of the liquid product generated by the catalytic cracking of AR with steam was approximately 0.7 wt% (*2*), while feedstock did not contain oxygen. The results indicated that the reaction of heavy oil and the oxygen species derived from steam produced a small amount of oxygen compounds in product oil. Approximately 10% of the oxygen species were incorporated into the product oil, and remaining 90% of the oxygen species were converted to carbon dioxide (*2*).

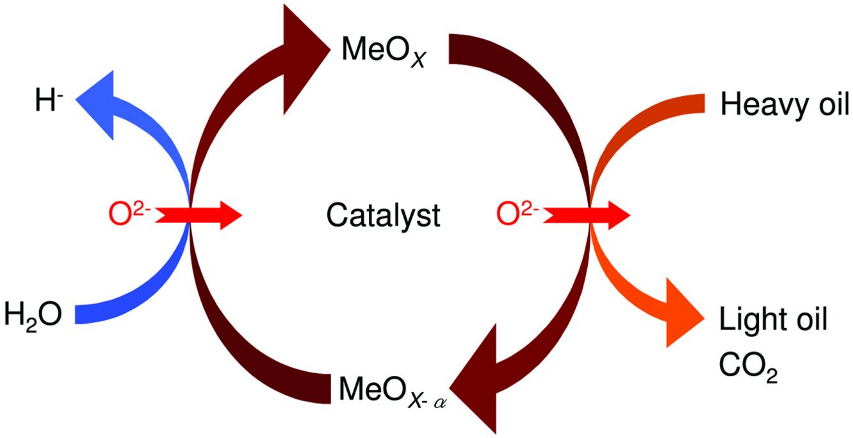

Figure 5. Phase change of the metal oxide catalyst during conversion of heavy oil to light fractions in a steam atmosphere.

The iron oxide content in the complex metal oxide catalyst of iron, zirconium, and aluminum prepared by coprecipitation maintained the hematite structure due to the addition of large amounts of oxygen species from steam (*1*, *18*). However, the structure of an iron oxide catalyst prepared from goethite (α-FeOOH) and a zirconia-supporting iron oxide catalyst prepared by impregnation changed from hematite to magnetite (*16*, *17*). Heavy oil was decomposed using these catalysts to produce light oil and carbon dioxide. The catalytic activity of the zirconia-supporting iron oxide catalyst toward the decomposition of heavy oil was higher than that of the iron oxide catalyst because zirconia promoted the generation of oxygen species from steam (*16*). After the structures of the iron oxide and zirconia-supporting iron oxide catalysts changed from hematite to magnetite during the reaction, the combustion of spent catalyst reconstructed the hematite structure. However, the activity of the zirconia-supporting iron oxide catalyst decreased with repeated reactions of heavy oil and regeneration of the catalyst because zirconia peeled away from the iron oxide during the phase change from hematite to magnetite (*17*). Addition of alumina to the iron oxide lattice prevented the peeling of zirconia (*17*), and the phase change of the complex metal oxide of iron, zirconium, and aluminum prepared by coprecipitation was

Downloaded by OHIO STATE UNIV LIBRARIES on May 31, 2012 | http://pubs.acs.org
Publication Date (Web): January 20, 2012 | doi: 10.1021/bk-2012-1092.ch006

suppressed when sufficient amounts of oxygen species from steam were supplied to the iron oxide (*18*). Thus, heavy oil was oxidatively cracked to produce light oil with no coke formation at a steam-to-feedstock flow rate ratio of 3 g/g (*1*).

Properties of Light Oil Produced from Heavy Oil

When oxygen species are supplied to iron oxide from steam and reacted with heavy oil, hydrogen species may be simultaneously generated from steam and be incorporated into products. To investigate the addition of hydrogen species into the product oil, the properties of product oil were examined. Figure 6 shows a proton nuclear magnetic resonance (^{1}H-NMR) spectrum of product oil generated by cracking AR over the complex metal oxide catalyst in a steam atmosphere. The product oil spectrum was measured using a Lambda-500 spectrometer (JEOL Ltd., Japan) after elimination of toluene using an evaporator. The ranges of 6.0–9.0, 4.2–6.0, and 0.1–4.2 ppm correspond to aromatic, alkenic, and other aliphatic protons, respectively. The percentage of aromatic, alkenic, and aliphatic protons are 8%, 1%, and 91%, respectively. Product oil was primarily composed of aromatic and aliphatic hydrocarbons, and the amount of alkene was small.

Downloaded by OHIO STATE UNIV LIBRARIES on May 31, 2012 | http://pubs.acs.org
Publication Date (Web): January 20, 2012 | doi: 10.1021/bk-2012-1092.ch006

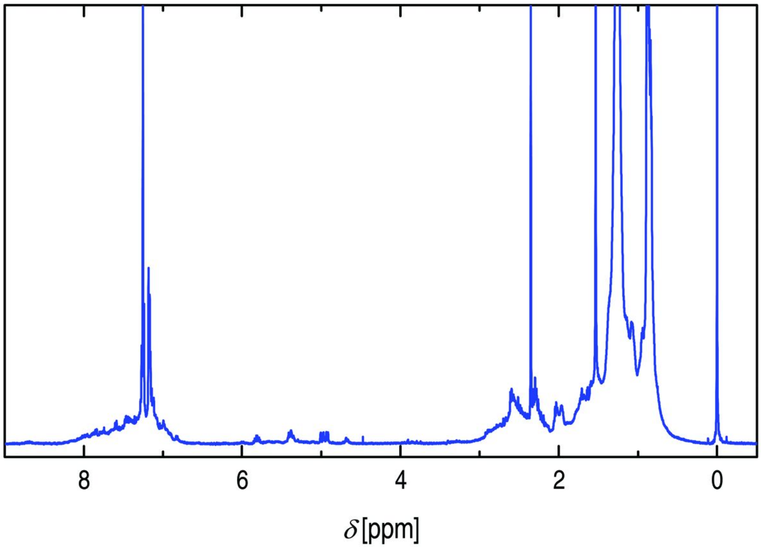

Figure 6. ^{1}H-NMR spectrum of product oil generated by cracking AR over a complex metal oxide catalyst of iron, zirconium, and aluminum in a steam atmosphere.

The alkene/alkane ratio of aliphatic hydrocarbons in the product oil was measured by gas chromatography with a flame ionization detector (HP6890, Agilent Technologies) equipped with a capillary column. Figure 7 shows the alkene/alkane ratio for light oil produced by AR cracking over the complex metal oxide catalyst in a steam atmosphere. The ratio was calculated from the gas chromatographic peak areas of aliphatic hydrocarbons. Gasoline + kerosene and gas oil were defined as aliphatic hydrocarbons with chains of 9–13 and 14–19 carbon atoms, respectively. Hydrocarbons with less than 9 carbon atoms were omitted because of interference from the toluene solvent peak. The alkene/alkane ratio of gasoline + kerosene and gas oil generated by the reaction in a steam atmosphere was less than that in a nitrogen atmosphere. This result suggests that hydrogen species derived from steam were incorporated into the hydrocarbons produced when oxygen species from steam were supplied to the iron oxide lattice and reacted with heavy oil over the catalyst. Consequently, the addition of hydrogen from steam to light hydrocarbons has the potential to produce valuable fuels.

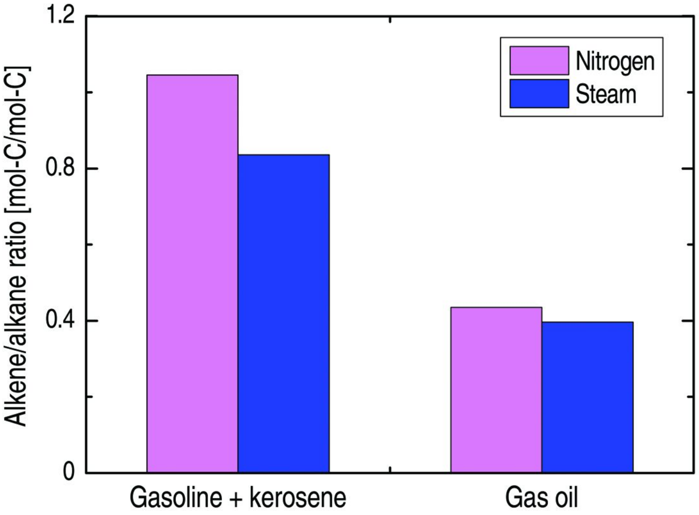

Figure 7. Alkene/alkane ratio of light aliphatic hydrocarbons produced by cracking AR at 748 K over a complex metal oxide catalyst of iron, zirconium, and aluminum in a steam atmosphere.

Conclusion

Catalytic cracking of heavy oil, such as petroleum residual oil and Canadian oil sand bitumen, using steam was investigated for the production of light oil. Heavy oil was decomposed over a complex metal oxide catalyst of iron, zirconium, and aluminum, producing light oil and carbon dioxide. Before the reaction, the structure of the catalyst was hematite. The hematite structure changed to magnetite after reaction in a nitrogen atmosphere, whereas the hematite structure was partially maintained after reaction in a steam atmosphere. Oxygen species from steam were supplied to the iron oxide lattice after the lattice oxygen of iron oxide reacted with heavy oil. The product oil contained lower amounts of alkenes. The alkene/alkane ratio of light aliphatic hydrocarbons produced by the reaction in a steam atmosphere was low compared to that in

Downloaded by OHIO STATE UNIV LIBRARIES on May 31, 2012 | http://pubs.acs.org
Publication Date (Web): January 20, 2012 | doi: 10.1021/bk-2012-1092.ch006

a nitrogen atmosphere. Hydrogen species were generated from steam when the oxygen species from steam were supplied to the iron oxide lattice, and the hydrogen species were incorporated into the light oil.

Acknowledgments

This work was partly supported by the Japan Petroleum Energy Center (JPEC) as a technological development project, supported financially by the Ministry of Economy, Trade, and Industry (METI).

References

1. Fumoto, E.; Matsumura, A.; Sato, S.; Takanohashi, T. *Energy Fuels* **2009**, *23*, 1338–1341.
2. Fumoto, E.; Sato, S.; Takanohashi, T. *Energy Fuels* **2011**, *25*, 524–527.
3. Rahmani, S.; McCaffrey, W.; Elliott, J. A. W.; Gray, M. R. *Ind. Eng. Chem. Res.* **2003**, *42*, 4101–4108.
4. Murugan, P.; Mahinpey, N.; Mani, T. *Fuel Process. Technol.* **2009**, *90*, 1286–1291.
5. Jeon, H. J.; Park, S. K.; Woo, S. I. *Appl. Catal., A* **2006**, *306*, 1–7.
6. Matsumura, A.; Kondo, T.; Sato, S.; Saito, I. *Fuel* **2005**, *84*, 411–416.
7. Galarraga, C. E.; Pereira-Almao, P. *Energy Fuels* **2010**, *24*, 2383–2389.
8. Martinez, J.; Sanchez, J. L.; Ancheyta, J.; Ruiz, R. S. *Catal. Rev. Sci. Eng.* **2010**, *52*, 60–105.
9. Moulijn, J. A.; Makkee, M.; Van Diepen, A. *Chemical Process Technology*; John Wiley & Sons, Ltd.: Hoboken, NJ, 2001; pp 32−78
10. Ozaki, H.; Murakami, T.; Suzuka, T. 32nd Conference of Canadian Society for Chemical Engineering, 1982.
11. Pereira, P.; Flores, C.; Zbinden, H.; Guitian, J.; Solari, R. B.; Feintuch, H.; Gillis, D. *Oil Gas J.* **2001**, *99*, 79–85.
12. Kishita, A.; Takahashi, S.; Kamimura, H.; Miki, M.; Moriya, T.; Enomoto, H. *J. Jpn. Pet. Inst.* **2002**, *45*, 361–367.
13. Watanabe, M.; Kato, S.; Ishizeki, S.; Inomata, H.; Smith, R. L., Jr. *J. Supercrit. Fluids* **2010**, *53*, 48–52.
14. Masuda, T.; Kondo, Y.; Niwa, M.; Shimotori, T.; Mukai, S. R.; Hashimoto, K.; Takano, M.; Kawasaki, S.; Yoshida, S. *Chem. Eng. Sci.* **2001**, *56*, 897–904.
15. Kubaschewski, O.; Schmid-Fetzer, R. In *Ternary Alloys*; Petzow, G., Effenberg, G., Eds.; VCH: Weinheim, Germany, 1992; Vol. 5.
16. Fumoto, E.; Tago, T.; Tsuji, T.; Masuda, T. *Energy Fuels* **2004**, *18*, 1770–1774.
17. Fumoto, E.; Tago, T.; Masuda, T. *Energy Fuels* **2006**, *20*, 1–6.
18. Fumoto, E.; Tago, T.; Masuda, T. *Chem. Lett.* **2006**, *35*, 998–999.

Downloaded by OHIO STATE UNIV LIBRARIES on May 31, 2012 | http://pubs.acs.org
Publication Date (Web): January 20, 2012 | doi: 10.1021/bk-2012-1092.ch006

Downloaded by UNIV OF GUELPH LIBRARY on May 31, 2012 | http://pubs.acs.org
Publication Date (Web): January 20, 2012 | doi: 10.1021/bk-2012-1092.ch007

Chapter 7

Hydrodesulfurization of 4,6-Dimethyldibenzothiophene Using Sol-Gel Alumina-Supported Cobalt−Molybdenum Catalysts with High Metal Loading

A. Ishihara,* N. Sato, S. Hayashi, T. Itoh, T. Hashimoto, and H. Nasu

Mie University, 1577 Kurima Machiyacho, Tsu-City 514-8507, Japan
***E-mail: ishihara@chem.mie-u.ac.jp**

In the present study, HDS of 4,6-dimethyldibenzothiophene (4,6-DMDBT) using sol-gel CoMo/Al_2O_3 catalysts with high metal loading were investigated. Aluminiumtri-*sec*-butoxide, ammonium heptamolybdate and cobalt nitrate hexahydrate were used in the preparation of catalysts. The molar ratio of Co:Mo:Al was 1:1:2 or 1:1:15. Surface area (SA), pore volume (PV) and pore diameter (PD) for CoMo/Al_2O_3 (1:1:15) were 437m^2/g, 1.02cm^3/g and 5.5nm, respectively. Those for CoMo/Al_2O_3 (1:1:2) were 213m^2/g, 0.82cm^3/g and 14nm, respectively. In HDS of 4,6-DMDBT using the conventional catalysts, the conversion decreased in the order CoMo/Al_2O_3 (1:1:2) > Co-Mo/ref.Al_2O_3 (prepared by conventional impregnation) > CoMo/Al_2O_3 (1:1:15). CoMo/Al_2O_3 (1:1:2) also showed the highest methylcyclohexyltoluene (MCHT) selectivity. Although CoMo/Al_2O_3 (1:1:2) had large metal contents, the higher SA, PV and PD were maintained, which resulted in the higher activity and selectivity. Further, it was thought that hydrogenation of an aromatic ring of 4,6-DMDBT, which is needed for HDS of 4,6-DMDBT, was promoted by the formation of the larger amount of active sites for hydrogenation of the aromatic ring which was caused by the larger amounts of active metals loaded into the catalyst.

In Nanocatalysis for Fuels and Chemicals; Dalai, A.;
ACS Symposium Series; American Chemical Society: Washington, DC, 2012.

Downloaded by UNIV OF GUELPH LIBRARY on May 31, 2012 | http://pubs.acs.org
Publication Date (Web): January 20, 2012 | doi: 10.1021/bk-2012-1092.ch007

Introduction

Sulfur concentrations of gasoline and gas oil have been regulated to less than 10 ppm. Such regulation may become severer in the near future because the regulation for NOx becomes severer. Further, if hydrogen for a fuel cell is prepared from naphtha, sulfur concentration in naphtha must be a ppb order. Thus the development of preparation methods for novel hydrodesulfurization (HDS) catalysts still has been required (*1*, *2*). In recent years, much attention has been focused on NEBULA catalysts for hydrotreating (*3*, *4*). However, the detail information for preparation has not been clarified. On the other hand, a sol-gel method enables us to make porous materials with fine structure and polycrystals with uniform composition and with more than one component at lower temperature (*5*). Active components Mo and Co in HDS catalysts were usually supported on Al_2O_3 by an impregnation method. In the case of the sol-gel method, since these active species can be added to an intermediate gel at the preparation of a support, very active catalysts with highly dispersed metal and with high metal loading may be obtained.

In the present study, HDS of 4,6-dimethyldibenzothiophene (4,6-DMDBT) using sol-gel $CoMo/Al_2O_3$ catalysts with high metal loading were investigated.

Experimental

Aluminium-sec-tributoxide ($Al(O\text{-}sec\text{-}C_4H_9)_3$, ASB) was dissolved in anhydrous ethanol. Then, aqueous solutions of ammonium heptamolybdate ($(NH_4)_6Mo_7O_{24}\cdot 4H_2O$) and cobalt nitrate hexahydrate ($Co(NO_3)_2\cdot 6H_2O$) were added to the ASB solution. Figure 1 shows the flow chart for the preparation of $CoMo/Al_2O_3$ with high metal loading by the sol-gel method. The molar ratio of Co:Mo:Al was 1:1:2 or 1:1:15. The obtained gel was dried and calcined at 500°C for 3h. The contents of MoO_3 and CoO for $CoMo/Al_2O_3$ (1:1:2) were 45 and 23wt%, respectively. Those for $CoMo/Al_2O_3$ (1:1:15) were 15 and 8wt%, respectively. For comparison, the reference alumina-supported conventional catalysts were also prepared using the impregnation methods. Ref. Al_2O_3 was supplied from a petroleum company in Japan. CoMo/ref.Al_2O_3 represents the catalyst where Mo and Co components were supported in impregnation simultaneously. Mo-Co/ref.Al_2O_3 represents the catalyst where Co component was supported first and Mo component was second in impregnation. Co-Mo/ref.Al_2O_3 represents the catalyst where Mo component was supported first and Co component was second in impregnation on ref.Al_2O_3. Each catalyst has 20wt% of MoO_3 and Co/Mo ratio 0.4. The measurement of XRD and N_2 adsorption for the prepared catalysts was performed. HDS of decalin solution of 4,6-DMDBT (0.01wt%) was performed using a fixed-bed reactor after presulfiding by H_2S/H_2 at 400°C. Reaction conditions were as follows: WHSV 28/h, 50 kg/cm^2, H_2 18 l/h. Products dimethylbiphenyl (DMBP) and methylcyclohexyltoluene (MCHT) were determined by GC-FID.

Downloaded by UNIV OF GUELPH LIBRARY on May 31, 2012 | http://pubs.acs.org
Publication Date (Web): January 20, 2012 | doi: 10.1021/bk-2012-1092.ch007

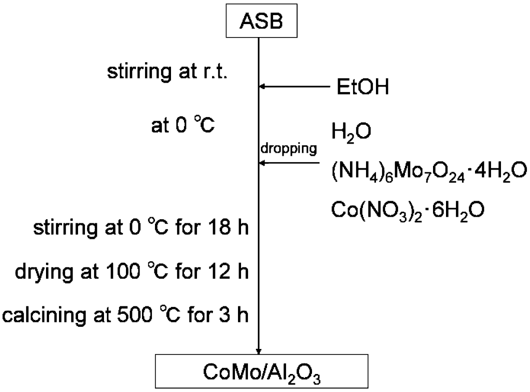
ASB
stirring at r.t.
EtOH
at 0 °C
dropping
H_2O
$(NH_4)_6Mo_7O_{24}\cdot 4H_2O$
$Co(NO_3)_2\cdot 6H_2O$
stirring at 0 °C for 18 h
drying at 100 °C for 12 h
calcining at 500 °C for 3 h
$CoMo/Al_2O_3$

Figure 1. Flow chart for preparation of $CoMo/Al_2O_3$ by the sol-gel method (Co:Mo:Al=1:1:2 or 1:1:15).

Results and Discussion

N_2 adsorption measurement was performed and the results are shown in Table 1. Surface area (SA), pore volume (PV) and pore diameter (PD) for $CoMo/Al_2O_3$ (1:1:15) were 437m^2/g, 1.02cm^3/g and 5.5nm, respectively. Those for $CoMo/Al_2O_3$ (1:1:2) were 213m^2/g, 0.82cm^3/g and 14nm, respectively. SA and PV for $CoMo/Al_2O_3$ (1:1:2) were smaller than that for $CoMo/Al_2O_3$ (1:1:15) but PD was larger. Figure 2 shows the BJH pore size distribution. $CoMo/Al_2O_3$ (1:1:2) with high metal content showed very broad distribution while that for $CoMo/Al_2O_3$ (1:1:15) was very sharp and relatively narrow. There may be a slight cohesion in particles of $CoMo/Al_2O_3$ (1:1:2) because its content of transition metal species was much larger than that of $CoMo/Al_2O_3$ (1:1:15). However, $CoMo/Al_2O_3$ (1:1:2) still maintained enough large surface area and pore volume to catalyze hydrodesulfurization and its larger pore would have an advantage for the diffusion of 4, 6-DMDBT.

According to XRD measurement in Figure 3, catalysts prepared by the conventional impregnation showed the peaks of gamma-alumina. Further CoMo/ref.Al_2O_3 revealed peaks of MoO_3. It is thought that since active species could not be supported uniformly for CoMo/ref.Al_2O_3 the HDS activity decreased in comparison with that for Co-Mo/ref.Al_2O_3.

In HDS of 4,6-DMDBT using the conventional catalysts, the conversion decreased in the order Co-Mo/ref.Al_2O_3 >CoMo/ref.Al_2O_3 >Mo-Co/ref.Al_2O_3 which is consistent with the order of surface area (Table 1 and Figure 4). When the performance of $CoMo/Al_2O_3$ (1:1:2) and $CoMo/Al_2O_3$ (1:1:15) was compared with that of Co-Mo/ref.Al_2O_3, $CoMo/Al_2O_3$ (1:1:2) showed the highest activity and MCHT selectivity (Figure 5). As shown in Figure 5, this catalyst exhibited the higher conversion than a typical commercial deep desulfurization catalyst supplied from a catalyst maker in Japan. Although $CoMo/Al_2O_3$ (1:1:2) had the larger metal contents, the higher SA, PV and PD were maintained, which resulted in the higher activity and selectivity. Further, it was thought that hydrogenation of an aromatic ring of 4,6-DMDBT, which is needed for HDS of 4,6-DMDBT, was promoted by the formation of the larger amount of active sites for hydrogenation of the aromatic ring which was caused by the larger amounts of active metals loaded into the catalyst. CoMo/Al_2O_3 (1:1:15) catalyst had higher surface area of 437m^2g^{-1}, but showed the lower activity. It is likely that the surface area is too high to be maintained under the hydrodesulfurization condition. Although chemisorption or N_2 adsorption experiments for catalysts after the reaction have not been performed at the present time, there might be a collapse of the structure which decreased the metal dispersion and surface area for CoMo/Al_2O_3 (1:1:15).

Downloaded by UNIV OF GUELPH LIBRARY on May 31, 2012 | http://pubs.acs.org
Publication Date (Web): January 20, 2012 | doi: 10.1021/bk-2012-1092.ch007

Table 1. BET surface area, BET pore volume and BJH pore diameter for each catalyst

Sample name	BET surface area (m^2g^{-1})	BET pore volume (cm^3g^{-1})	BJH pore diameter (nm)
CoMo/Al_2O_3	237	0.61	5.3
Co-Mo/Al_2O_3	263	0.46	6.1
Mo-Co/Al_2O_3	174	0.64	6.1
CoMo/Al_2O_3(1:1:2)	213	0.82	14
CoMo/Al_2O_3(1:1:15)	437	1.02	5.5

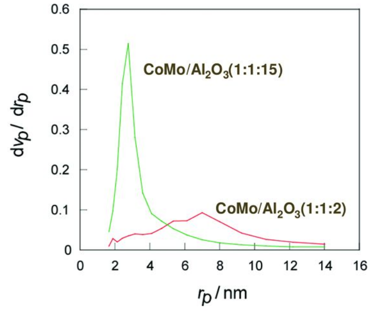

Figure 2. BJH pore size distribution of CoMo/Al_2O_3 (1:1:2) and CoMo/Al_2O_3 (1:1:15).

Downloaded by UNIV OF GUELPH LIBRARY on May 31, 2012 | http://pubs.acs.org
Publication Date (Web): January 20, 2012 | doi: 10.1021/bk-2012-1092.ch007

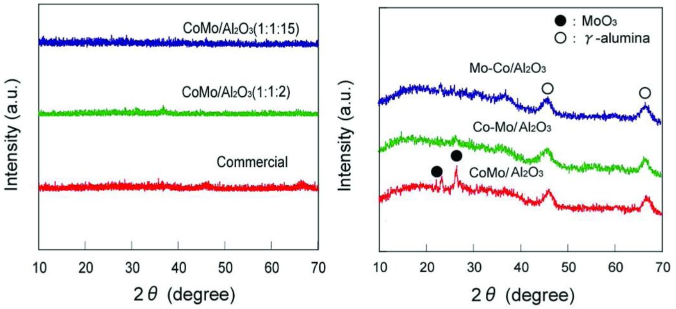

Figure 3. XRD patterns Commercial catalyst, CoMo/Al_2O_3(1:1:2), CoMo/Al_2O_3 (1:1:15) (left) and ref.Al_2O_3 supported catalysts (right).

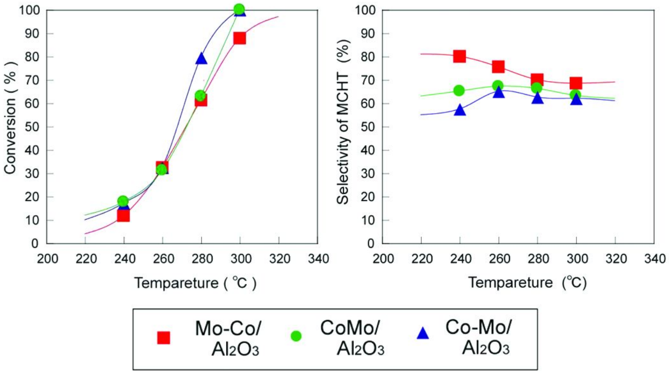

Figure 4. Effect of reaction temperature on conversion and selectivity for MCHT in HDS of 0.01 wt.% 4,6-DMDBT using catalysts prepared by the impregnation method.

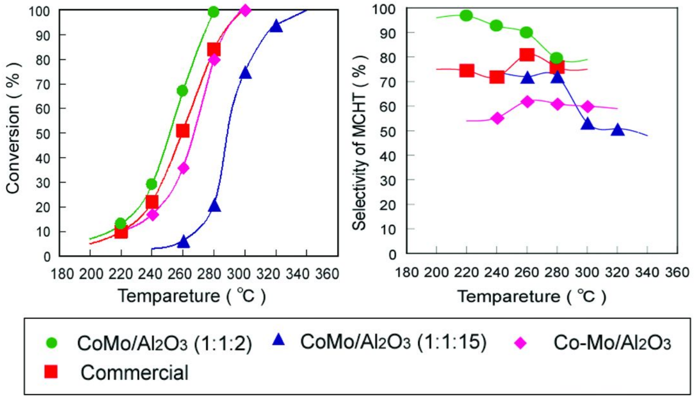

Figure 5. Effect of reaction temperature on conversion and selectivity for MCHT in HDS of 0.01 wt.% 4,6-DMDBT using catalysts prepared by the sol-gel method .

Downloaded by UNIV OF GUELPH LIBRARY on May 31, 2012 | http://pubs.acs.org
Publication Date (Web): January 20, 2012 | doi: 10.1021/bk-2012-1092.ch007

Conclusions

In impregnation catalysts, Co-Mo/Al_2O_3 catalyst which had the highest surface area showed the highest activity, while Mo-Co catalyst which had the least surface area showed the lowest activity. When CoMo/Al_2O_3 catalysts were prepared by the sol-gel method, CoMo/Al_2O_3 (1:1:2) catalyst, which contained larger amounts of active species, showed the highest activity. CoMo/Al_2O_3 (1:1:15) catalyst had higher surface area of $437 m^2 g^{-1}$, but showed the lower activity.

References

1. Kabe, T.; Ishihara, A.; Qian, W. *Hydrodesulfurization and Hydrodenitrogenation*; Kodansha Scientific; Wiley-VCH: Tokyo; Weinheim, Germany, 1999.
2. Ishihara, A. *J. Jpn. Petrol. Inst.* **2008**, *51* (2), 73–82.
3. Gochi, Y.; Ornelas, C.; Paraguay, F.; Fuentes, S.; Alvarez, L.; Rico, J. L.; Alonso-Nu´n˜ez, G. *Catal. Today* **2005**, *107–108* –536.
4. Eijsbouts, S.; Mayo, S. W.; Fujita, K. *Appl. Catal., A: Gen.* **2007**, *322*, 58–66.
5. Lebihan, L.; Mauchaussé, C.; Duhamel, L.; Grimblot, J. *J. Sol-Gel Sci. Technol.* **1994**, *2*, 837.

Chapter 8

TPA Supported on SBA-15 as Solid Acid Catalysts for the Biodiesel Production

Chinmoy Baroi and Ajay K. Dalai*

Catalysis and Reaction Engineering Laboratories,
Department of Chemical Engineering, University of Saskatchewan,
Saskatoon, Saskatchewan, Canada S7N5A9
***Phone: +1 306-966-4768. Fax: +1 306-966-4777.**
E-mail: ajay.dalai@usask.ca.

Downloaded by CORNELL UNIV on May 31, 2012 | http://pubs.acs.org
Publication Date (Web): January 20, 2012 | doi: 10.1021/bk-2012-1092.ch008

Biodiesel has gained worldwide recognition for many years due to its renewability, lubricating property and environmental benefits. This research is focused on synthesis of 12-Tungstophosphoric acid (TPA) supported on SBA-15 as acid catalysts for the biodiesel production from a model feedstock Triolein. A large number of 0-35% TPA supported on SBA-15 catalysts were synthesized by impregnation method and the catalysts were characterized using BET, XRD, FTIR, TEM and ICP-MS. The catalytic activity of these catalysts was tested by transesterification of Triolein using a stirred tank reactor. The effect of operating conditions such as catalyst conc. and methanol to Triolein molar ratio on the transesterification of Triolein was studied using response surface methodology (RSM). Based on the study, 25% TPA is identified as the optimum catalyst loading on SBA-15 by impregnation. From the optimization study of 25% TPA impregnated SBA-15 using RSM model, 4.15 wt% catalyst (based on Triolein) and 39:1 methanol to Triolein molar ratio is found to be the optimum reaction condition, when the reaction temperature is kept fixed at 200°C, stirring speed at 600 rpm and allowing 10-h of reaction time. Predicted ester yield at the above condition is 97.4 %, and the actual (experimental) yield is 97.2%.

Keywords: biodiesel; response surface methodology (RSM); impregnation; TPA

Downloaded by CORNELL UNIV on May 31, 2012 | http://pubs.acs.org
Publication Date (Web): January 20, 2012 | doi: 10.1021/bk-2012-1092.ch008

Introduction

The other name of transesterification is alcoholysis because in this process one alcohol is replaced by another i.e., the higher alcohol (glycerol) present in the triglyceride is replaced by a lower alcohol (e.g., methanol, ethanol) and the resultant monoalkyl esters of long chain fatty acids are called biodiesel. In the transesterification reaction, alcohols (e.g., methanol, ethanol) and oils or fats (edible and non edible) are used as reactants. Transesterification of triglycerides produces fatty acid alkyl esters (FAME) and glycerol. The glycerol phase settles down at the bottom of the reaction vessel. Diglycerides and monoglycerides are the intermediates in this process. The overall equation of transesterification is given in equation 1.

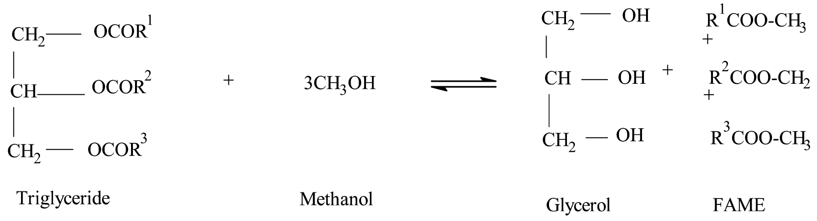

$$CH_2(OCOR^1)-CH(OCOR^2)-CH_2(OCOR^3) + 3CH_3OH \rightleftharpoons CH_2(OH)-CH(OH)-CH_2(OH) + R^1COO\text{-}CH_3 + R^2COO\text{-}CH_3 + R^3COO\text{-}CH_3 \quad [1]$$

Transesterification reaction can proceed either in presence of catalysts at lower temperature, pressure or in absence of catalysts at higher temperature and pressure in the supercritical state. Catalyzed transesterification reaction is preferred in biodiesel production because of the moderate reaction conditions. Most of the commercialtransesterification reaction is conducted with homogeneous alkaline catalysts, because homogeneous base catalyzed transesterification reaction is 4000 times faster than the homogeneous acid catalyzed reaction and are less corrosive to industrial equipments compared to the homogeneous acidic catalysts (*1*). One of the major problems associated with the base catalyzed reaction is formation of soap as an undesired reaction between free fatty acids (FFA) and bases, which consumes some of the base catalyst. Thus the base available for catalyzing the reaction is reduced. FFA content up to 3% in the oil or the feedstock doesn't affect the process significantly, but if the oil contains more than 5% FFA, the soap inhibits separation of glycerol from the biodiesels (*2*). The main drawback of commercial biodiesel production is the high cost of treated feedstock or pre-treatment of the feedstock which leads to high price of the biodiesel product. Estimation shows that approximately 88% of the total production cost is associated with the feedstock (*3*). This cost can be reduced by using cheaper feedstocks e.g., used cooking oil, yellow grease which contains large amounts of free fatty acids. Acid catalysts can catalyze esterification reaction along with transesterification reaction to produce similar type of ester from free fatty acids using alcohol, which is shown by equation 2.

$$\underset{\text{FFA}}{R^1COOH} + \underset{\text{Methanol}}{CH_3OH} \rightleftharpoons \underset{\text{FAME}}{R^1COOCH_3} + H_2O \quad [2]$$

Downloaded by CORNELL UNIV on May 31, 2012 | http://pubs.acs.org
Publication Date (Web): January 20, 2012 | doi: 10.1021/bk-2012-1092.ch008

Though homogeneous acid catalyst can serve this purpose, it causes severe corrosion problem to the equipment and also leads to environmental problem (*4*). Therefore, solid acid catalysts are now point of interests in producing biodiesel from different feedstocks. Among the solid acids, heteropoly compounds show strong and pure Brønsted acidity which are commonly known as heteropoly acids (HPA) (*5*, *6*), especially, $H_3PW_{12}O_{40}$ (TPA) possesses super acidity (Brønsted acidity) and higher thermal stability compared to other HPA (*7*). The major disadvantages of using this heteropolyacid are lower surface area (1 – 10 m^2/g) and solubility in polar media (*4*). These problems can be avoided by supporting $H_3PW_{12}O_{40}$ on various carriers. Silica based mesoporous materials fully satisfy all the desired criteria as a support for these types of reactions (*8*). Especially SBA-15, a silica based mesoporous material is an attractive support for its higher hydrothermal stability and low carbon deposition tendency compared to other silica based mesoporous supports (*9*). There is no literature available so far; on the TPA supported SBA-15 catalyzed transesterification. Thus, it can be considered as a base line study to understand the catalytic activity of TPA supported on SBA-15 in transesterification reaction for biodiesel production.

Experimental

Reagents

Triolein, Methanol (99.9%), P123 and TEOS (Tetraethyl orthosilicate) were purchased from Sigma-Aldrich, Oakville, Ontario, Canada. 12-Tungstophosphoric acid (TPA) of AR grade was purchased from Alfa-Aesar, MA, USA.

Catalyst Preparation

SBA-15 was synthesized using amphiphilictriblock copolymer poly (ethylene glycol)-block-poly (propylene glycol)-block- poly (ethylene glycol), which is commonly known as P123. The typical synthesis procedure for SBA-15 is as follows: 13.38 g of P123 was dissolved in 396 g water plus 25.11 g HCl solution by stirring for 2-3 hours at 40°C. Thereafter, 30 g of TEOS was added to the solution with stirring at 40°C. The resulting mixture was stirred at 40°C for 24h and thereafter, the mixture was aged in a Teflon bottle at 110°C for 24h. The solid product was recovered by filtration, washed several times with water and dried overnight at 100°C. Finally, the product was calcined in a flow of air at 550°C for 6h.

TPA impregnated on SBA-15 was prepared as follows: Calcined SBA-15 was added into the solution of calculated amount of TPA. After stirring at room temperature, the sample was oven dried at 110°C for 24 h and calcined at 300°C for 2h. TPA loading of 5, 15, 25 and 35 wt% supported on SBA-15 were prepared and used in the catalytic studies. These catalysts were designated as X%TPA/SBA-15 (Im), where X represents wt% loading.

Downloaded by CORNELL UNIV on May 31, 2012 | http://pubs.acs.org
Publication Date (Web): January 20, 2012 | doi: 10.1021/bk-2012-1092.ch008

Catalyst Characterization

BETsurface area and pore size measurements of the catalysts were performed using Micrometrics adsorption equipment (Model ASAP 2000) at -196°C using liquid nitrogen. Prior to the analysis the catalyst was evacuated at 200°C in a vacuum of 5×10^{-4} atm to remove all adsorbed moisture from the catalyst surface and pores. The surface area was calculated from the isotherms using Brunauer-Emmett-Teller (BET) method. The total pore volume and pore diameter was calculated using BJH method from desorption branch of the isotherms. For XRD analysis, a small amount of each sample was placed on a standard Goniometer head and the sample was set at the center of the Diffractometer. Diffraction data were collected with a Bruker Smart6000 CCD detector on a Goniometer. The X-ray radiation source was Cu-K_α (1.54 Å) X-ray tube fitted with pinhole Collimator. The sample to detector distance was 29.48 cm. The FTIR spectra of the catalysts were obtained using Perkin Elmer FTIR spectrum GX. Samples for the FTIR analysis were prepared by pelleting a well mixed 3 mg of catalyst powder with 200 mg of KBr. The nature of acid sites (Brønsted and Lewis) of the catalysts was distinguished by in situ infrared (FTIR) spectroscopy with chemisorbed pyridine. The catalyst sample was placed in a designed cell and heated in situ from room temperature to 300°C in a flowing stream of pure Helium. The sample was kept at 300°C for 2 h and then cooled to 100°C. Pyridine vapour was introduced in flowing helium and the spectra were recorded from 1400–1600 cm^{-1}. The W (Tungsten) content in the prepared catalysts and biodiesel were determined by inductivity coupled plasma-mass spectrometer (ICP-MS).

Transesterification of Triolein

Transesterification of Triolein (a model compound representing oil) using supported TPA was carried out in a 450 mL Parr reactor (Parr Instrument Co., ILL, USA) equipped with a temperature controller. Initially the reactor was charged with 100 g of Triolein and preheated to 60°C with stirring at 600 rpm. The stirring speed was optimized to eliminate the mass transfer limitation effect which are discussed in the results section. Methanol and catalysts were then added to the reaction vessel. Depending on the reaction temperature, the reactor was pressurized to ensure that at the desired reaction temperature the reactants are in the liquid phase. All the reactions were carried out for a reaction time of 10-h unless otherwise stated. Preliminary catalyst screening experiments were carried out using reaction conditions of 200°C, 4.14 MPa, 9:1 methanol to oil molar ratio, 1.5 wt% catalyst (based on the wt. of Triolein). These preliminary reaction conditions were chosen based on the previous research work by Kulkarni et al (*4*). Central Composite Design (CCD) was used to design the experiments for process optimization studies and Design Expert 6.1 software was used for this purpose. The ester phase (after separation of the catalyst by filtration and separation of the glycerol phase) was analyzed using High-performance liquid chromatography (HPLC). The ester yield (wt%) was calculated according to the equation 3.

Ester yield (wt%) = (wt. of the methyl ester in the ester phase)/ (wt. of the ester phase)×100 [3]

Water content in the produced biodiesel was determined by Karl-Fisher titration method and the acid value of the produced biodiesel was determined according to the AOCS-D6751 method.

Results and Discussion

Catalyst Characterization

The textural properties of the catalysts are summarized in Table I. The table shows that the introduction and increase in the loading of TPA decreases the BET surface area, total pore volume and pore size compared to that of pure SBA-15. Similar results were observed by A. I. Tropeceloet *et al.* (*10*).

Table I. Textural property of various catalysts

Catalyst	*Surface area[a] (m^2/g)*	*Pore[b] volume (cc/g)*	*Average pore[c] diameter (nm)*	*Theoretical loading*	*Actual loading[d]*
SBA-15	851	1.27	5.9	0	0
5% TPA/SBA-15 (Im)	796	1.10	5.7	5	5
15% TPA/SBA-15 (Im)	743	1.03	5.6	15	15
25% TPA/SBA-15 (Im)	594	0.76	5.5	25	25
35% TPA/SBA-15 (Im)	492	0.60	5.0	35	35

[a] Surface area calculated by BET method. [b] Pore volume obtained from the desorption branch of the isotherm by BJH method. [c] Mesopore diameter corresponding to the maximum of the pore size distribution obtained from the desorption branch of the isotherm by the BJH method. [d] Calculated based on the Tungsten (W) content of the catalyst using ICP-MS.

Downloaded by CORNELL UNIV on May 31, 2012 | http://pubs.acs.org
Publication Date (Web): January 20, 2012 | doi: 10.1021/bk-2012-1092.ch008

For the catalysts the hexagonal structure of SBA-15 is confirmed by a typical XRD pattern consisting of a strong peak (at 2θ around 0.8°) along with two weak peaks (at 2θ around 1.6° and 1.8°) (*10*, *11*). These weak peaks appear as broad peaks with the increase of the TPA loading on SBA-15, indicating the loss of long range order (Figure 1).

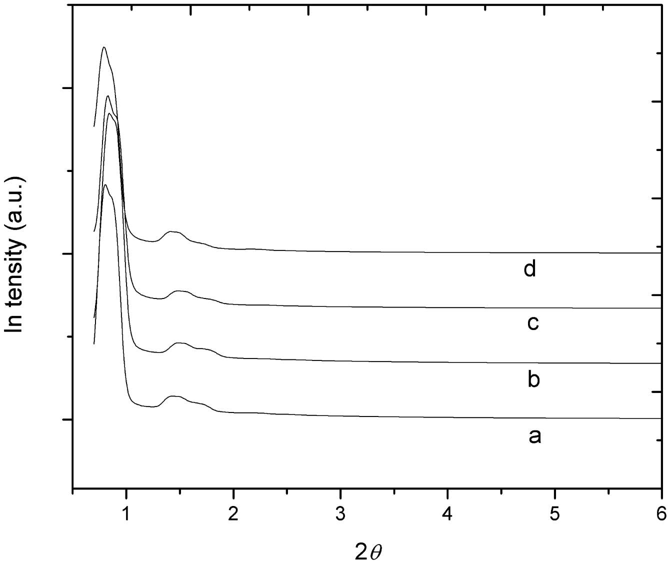

Figure 1. XRD patterns of (a) SBA-15, (b) 5% TPA/SBA-15 (Im), (c) 15% TPA/SBA-15 (Im) and (d) 25% TPA/SBA-15 (Im).

Downloaded by CORNELL UNIV on May 31, 2012 | http://pubs.acs.org
Publication Date (Web): January 20, 2012 | doi: 10.1021/bk-2012-1092.ch008

Pure TPA shows IR bands approximately at 1081 (P-O in the central tetrahedron), 989 (terminal W=O), 898 and 806 (W-O-W) cm^{-1} corresponding to asymmetric vibration associated with keggin ion (*10*, *12*, *13*). The IR bands at approximately 989, 898 and 806 cm^{-1} are observed and intensified significantly with the increase of TPA loading on SBA-15 (Figure 2).

The FTIR spectra of adsorbed pyridine were recorded from 1400 to 1600 cm^{-1} to distinguish the type of acid sites (Lewis or Brønsted) on the catalyst (Figure 3). The FTIR spectra of adsorbed pyridine on the catalysts show typically intense bands at 1533 and 1545 cm^{-1} characterized by Brønsted type acidity. The intense band at 1485 cm^{-1} is ascribed to both Lewis and Brønsted acid sites. Also, strong bands can be seen at 1441 cm^{-1} related to Lewis acidity (*4*).

The TEM images for 25%TPA/SBA-15 (Im) samples are presented in Figure 4. From the figures it is clear that when TPA is impregnated on SBA-15 (Figure 4), SBA-15 retains its structure and TPA enters into the pore.

Downloaded by CORNELL UNIV on May 31, 2012 | http://pubs.acs.org
Publication Date (Web): January 20, 2012 | doi: 10.1021/bk-2012-1092.ch008

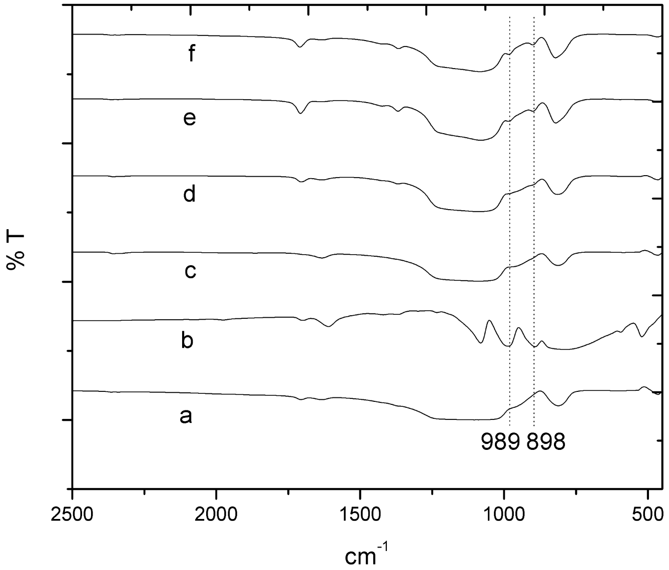

Figure 2. FTIR spectra of (a) SBA-15, (b) TPA, (c) 5% TPA/SBA-15 (Im), (d) 15% TPA/SBA-15 (Im), (e) 25% TPA/SBA-15 and (f) 35% TPA/SBA-15 (Im).

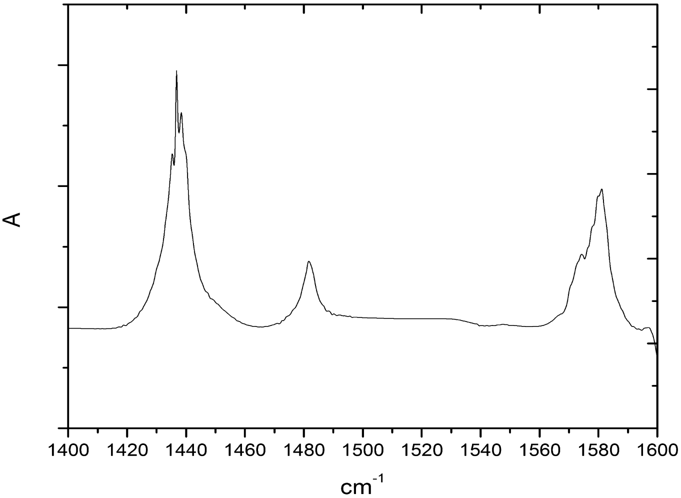

Figure 3. FTIR spectra of pyridine absorbed on supported TPA catalysts 25% TPA/SBA-15 (Im).

Downloaded by CORNELL UNIV on May 31, 2012 | http://pubs.acs.org
Publication Date (Web): January 20, 2012 | doi: 10.1021/bk-2012-1092.ch008

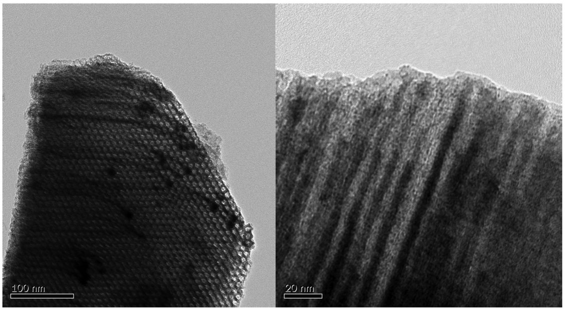

Figure 4. TEM images of 25% TPA/SBA-15(Im) (A&B).

Catalytic Activity

Figure 5 shows that 600 rpm is the optimum strring speed beyond which there is no increase in the ester yield (wt%). Thus 600 rpm is chosen as the optimum strring speed. Figure 6 shows that 25% TPA/SBA-15 (Im) produces the highest ester yield% (80.2 wt%) as compared to that using 35% TPA/SBA-15 (Im), when 1.5wt% catalyst (based on Triolein) and 9:1 methanol to Triolein molar ratio are used at 200°C, 4.14 MPa reaction pressure and 10-h reaction time as an initial reaction condition and further increase in loading results in almost same amount of ester formation. Thus 25% TPA/SBA-15 (Im) was considered as the optimum catalyst composition.

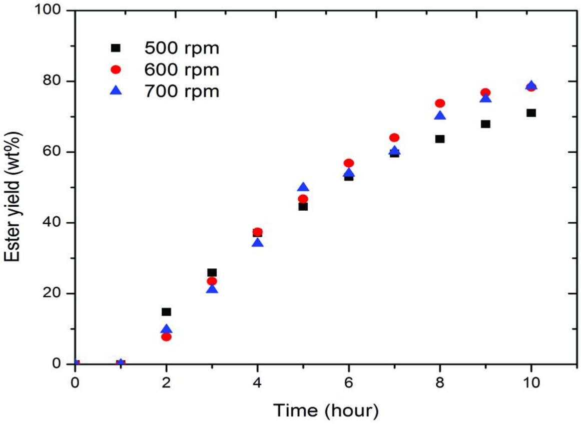

Figure 5. Optimization of stirring speed (1.5 wt% catalyst,25% TPA loading, 9:1 methanol to Triolein molar ratio, 200°C, 4.14 MPa and 10-h).

Downloaded by CORNELL UNIV on May 31, 2012 | http://pubs.acs.org
Publication Date (Web): January 20, 2012 | doi: 10.1021/bk-2012-1092.ch008

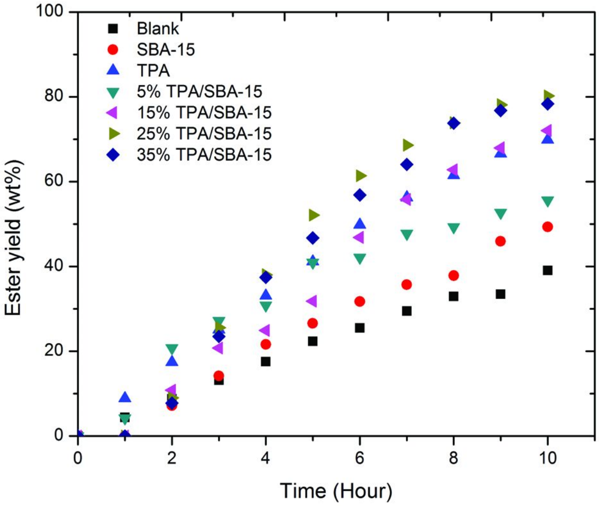

Figure 6. Catalyst loading screening (1.5 wt% catalyst, 9:1 methanol to Triolein molar ratio, 200°C, 4.14 MPa and 10-h).

Experimental Design, Statistical Analysis, and Optimization

The effects of various experimental parameters on transesterification of Triolein were studied. In the first stage the range studied are (1) catalyst wt: 1.5 -5 wt% (2) Methanol to oil molar ratio: 6:1-15:1 and (3) Reaction temperature: 100-200°C. A three factor 2 level design was used to perform 20 experiments. From the experiments, reaction temperature is found to be the most important factor, which affects the ester yield% positively without the interaction of other parameters. These experiments also show that ester yield% increases with the increase of other two parameters. Similar results were found using homogeneous acid catalyst in another study by Canakci and Gerpen (*14*). According to their study, reaction temperature dominates the rate of reaction, and the conversion increases with an increasing reaction temperature, increasing methanol to oil molar ratio and increasing acid catalyst concentration. The nitrogen pressure used in the experiments according to the reaction temperature and the pressure requirement increases exponentially with the reaction temperature (i.e. for reaction temperature 240°C, pressure requirement is 7.72MPa). Thus, the reaction temperature was kept fixed at 200°C for energy saving and minimizing formation of undesired product beyond 200°C as was found by Kulkarni et al. (*4*), to analyze the effects of catalyst wt% and methanol to Triolein molar ratio on the ester yield. Later in the second stage, the catalyst weight was varied from 1.5-8.5 wt% and the methanol to Triolein molar ratio from 19.4:1 to 40.6:1. A two factor two level design was used to perform the experiments. Figure 7 shows the effects of methanol to oil molar ratio on the ester yield (wt %). This figure shows the optimum region of parameter combinations for obtaining the highest ester yield.

From the experiments a second-order polynomial equation is developed to fit the experimental data.

$$\text{Ester yield\%} = 47.95+1.21\times\text{Cat.wt\%}+2.39\times\text{Methanol to Triolein molar ratio}-0.48331\times\text{Cat. wt\%}^2-0.034428\times\text{Methanol to Triolein molar ratio}^2 +.071761\times\text{Cat.wt\%}\times\text{Methanol to Triolein molar ratio}$$

From the above model, Cat.wt%, Methanol to Triolein molar ratio, Methanol to Triolein molar ratio^2 are found to be the significant factors.

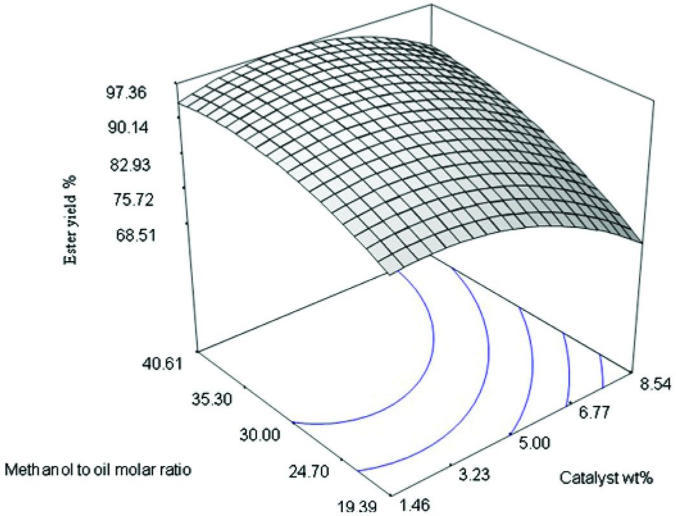

Figure 7. Response surface plot of ester yield% as a function of methanol to oil (Triolein) molar ratio and catalyst wt% (based on Triolein).

From the optimization, 4.15 wt% catalyst (based on Triolein) and 39:1 methanol to Triolein molar ratio are found to be the optimum reaction conditions, when the reaction temperature is kept fixed at 200°C, stirring speed at 600 rpm and allowing 10-h of reaction time. Predicted ester yield using the above condition is 97.4 % and the actual (experimental) yield is 97.2%, which indicates that the model prediction is validated well. The polynomial equation is valid for catalyst loading in the range of 1.46-8.54 wt% based on the Triolein and methanol to Triolein molar ratio in the range of 19.39-40.61 at 10-h reaction/residence time, 200°C, and 4.14 MPa. These three process variables (time, temperature and pressure) were kept fixed in the polynomial equation development. In the initial catalyst screening experiments reaction time of 10-h is found to be close enough to reach optimum ester yield. The reaction temperature was kept constant at 200°C, because, in a previous study by Kulkarni et al (*4*), it was found that

Downloaded by CORNELL UNIV on May 31, 2012 | http://pubs.acs.org
Publication Date (Web): January 20, 2012 | doi: 10.1021/bk-2012-1092.ch008

beyond 200°C undesired products are formed. The transesterification reaction is a constant molar volume reaction. Thus according to the Le Chatelier's principle, the reaction pressure has no effect on the reaction yield. The reaction pressure was chosen based on the reaction temperature to keep methanol in the liquid phase. Therefore, the reaction time, reaction temperature and reaction pressure were kept fixed throughout the optimization study.

Catalyst Deactivation and Reusability Study

In order to study the catalyst deactivation and reusability, the catalyst was filtered from the reaction mixture and then was washed with hexane to remove any non-polar compounds such as methyl esters present on the surface and dried at 100°C for 1-h. Finally, the catalyst was dried and used for transesterification. The study was done using the center point reaction condition of the optimization study. Table II shows the ester yield obtained using fresh and spent catalyst. It shows that the activity of the spent catalyst decreases with the usage.

Downloaded by CORNELL UNIV on May 31, 2012 | http://pubs.acs.org
Publication Date (Web): January 20, 2012 | doi: 10.1021/bk-2012-1092.ch008

Table II. Ester yield obtained using fresh and spent catalyst (5 wt%, 25% TPA/SBA-15 (Im) at 200°C, 4.14 MPa, 600 rpm, 10-h and using 30:1 methanol to Triolein molar ratio

Run no.	*Ester yield (wt%)*
1 (Fresh)	93.9
2	87.2
3	59.7
4	56.9

This loss in activity of the spent catalyst is due to the leaching of the active acid species, which is confirmed by pyridine adsorption study and ICP-MS analysis of W content of the biodiesel and the catalysts in the successive runs (Figure 8, Table III and IV).

Table III indicates that with higher yield, less TPA is present in the ester (biodiesel) phase, whereas at lower yield higher amount of TPA is present in the ester (biodiesel) phase. The surface area, pore volume and pore diameter of the spent catalyst (25% TPA/SBA-15 (Im)) are found to be 570 m^2/g, 0.73 cc/g and 5 nm respectively, which are almost same to those of fresh catalysts (Table I), which indicates that there is no structural change in the catalyst 25% TPA/SBA-15 (Im).

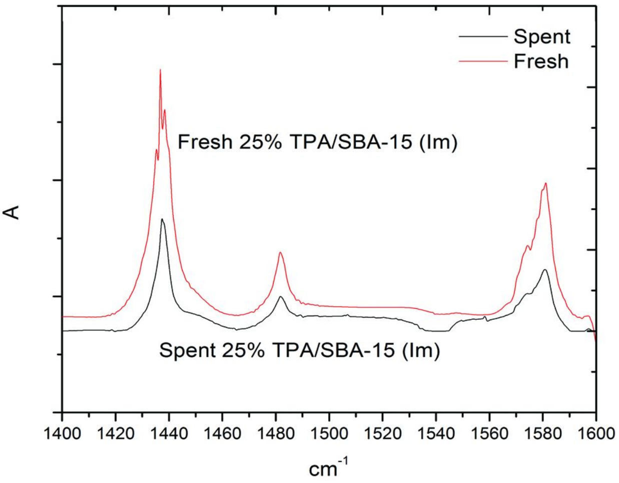

Figure 8. FTIR spectra of pyridine absorbed on fresh and spent 25%TPA/SBA-15 (Im) catalysts.

Table III. Metal content in Triolein and biodiesel samples in successive runs

Sample	*Metal (W) content/ppm*
Triolein	<0.03
Run 1	3.20
Run 2	18.6
Run 3	13.8
Run 4	2.60

Table IV. TPA content of the fresh and spent catalysts

Run no.	*TPA content in the catalyst (wt%)*[a]
1 (Fresh)	25
2	10.86
3	4.78
4	4.41

[a] Calculated based on the Tungsten content (W) of the catalyst using ICP-MS.

Downloaded by CORNELL UNIV on May 31, 2012 | http://pubs.acs.org
Publication Date (Web): January 20, 2012 | doi: 10.1021/bk-2012-1092.ch008

Downloaded by CORNELL UNIV on May 31, 2012 | http://pubs.acs.org
Publication Date (Web): January 20, 2012 | doi: 10.1021/bk-2012-1092.ch008

Effect of Presence of Water

For this study 0-2 wt% water was mixed with the Triolein. Figure 9 shows the effect of presence of water in the feedstock on the ester yield%. It shows that the ester yield % drops from 93.9% to 56.8% with the presence of 1wt% water and this ester yield decreases to 51.3% with the presence of 2wt% water in the feedstock.

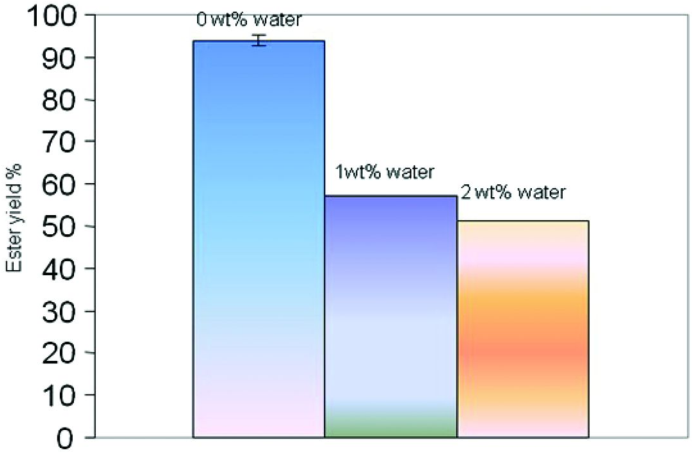

Figure 9. Effect of presence of water in Triolein on ester yield% (5wt% catalyst 25% TPA/SBA-15 at 200°C, 4.14 MPa, 600 rpm, 10-h and using 30:1 methanol to oil molar ratio).

Similar result was found using homogeneous catalyst by Canakci and Gerpen (*14*). Increasing concentration of water can give rise to water-rich clusters around protons and can shield it from hydrophobic triglyceride molecules, inhibiting reactions. On the other hand free fatty acid (FFA) with its polar carboxyl group can interact easily with the water molecules through hydrogen bond, and esterification reaction can continue in presence of water (*15*).

Effect of Free Fatty Acids (FFA)

For this study 0-35 wt% oleic acid was mixed with the Triolein. Figure 10 shows the effect of free fatty acid on the catalytic activity. It shows that the ester yield decreases from 93.9± 0.6 wt% (at initial 0% FFA content in the feed Triolein) to 64.7±3.21 wt% (at 95% confidence interval) with the presence of 5 wt% free fatty acid (FFA) in the Triolein, and again increases with the increase in the FFA content in the Triolein (for 15% FFA content in the feedstock Triolein, the ester yield increase to 71.94±1.58 wt% at 95% confidence interval). Figure 10 shows that the water content is the highest in the biodiesel (0.4±.01 wt% at 95% confidence interval) when the Triolein contains 5% FFA. Further increase in FFA, the water content in the biodiesel is less compared to that of 5% FFA and almost same, whereas the water contents of the Triolein (containing 0% FFA)

Downloaded by CORNELL UNIV on May 31, 2012 | http://pubs.acs.org
Publication Date (Web): January 20, 2012 | doi: 10.1021/bk-2012-1092.ch008

and corresponding biodiesel is .01 and .09 wt% respectively. Figure 11 shows that with the increase of the FFA in the feedstock Triolein, the acid value of the product biodiesel increases, whereas the acid value of the Triolein containing 0% FFA and corresponding biodiesel is 1.3 and .83±.02 mg KOH/g sample (at 95% confidence interval) respectively.

The sudden decrease of the ester yield in presence of 5% FFA can be explained based on the water content in the biodiesel and the acid catalyzed simultaneous esterification and transesterification reaction mechanism (Figure 10 and 12). The overall reaction mechanism of solid acid catalyzed transesterification and esterification reaction is shown in Figure 12. The esterification takes place between free fatty acids (RCOOH) and methanol (CH_3OH), whereas transesterification takes place between glycerides (RCOOR') and methanol adsorbed on acidic site (L^+) of the catalyst surface. The interaction of the carbonyl oxygen of free fatty acid or glyceride with acidic site of the catalyst forms carbocation. Then the nucleophillic attack of alcohol to the carbocation produces a tetrahedral intermediate.

In the esterification reaction, this tetrahedral intermediate eliminates one mole of water during rearrangement and formation of one mole of ester ($RCOOCH_3$) and in case of transesterification the tetrahedral intermediate only rearranges and forms one mole of ester similar to that of esterification reaction (*4*).

In studies it was found that esterification reactions are faster than transesterification reaction (*16*, *17*). Water is one of the products of esterification reaction. According to Loreto *et al.*'s findings, the water molecules affect the TG molecules accessibility to the catalyst and inhibit the reaction (*15*).

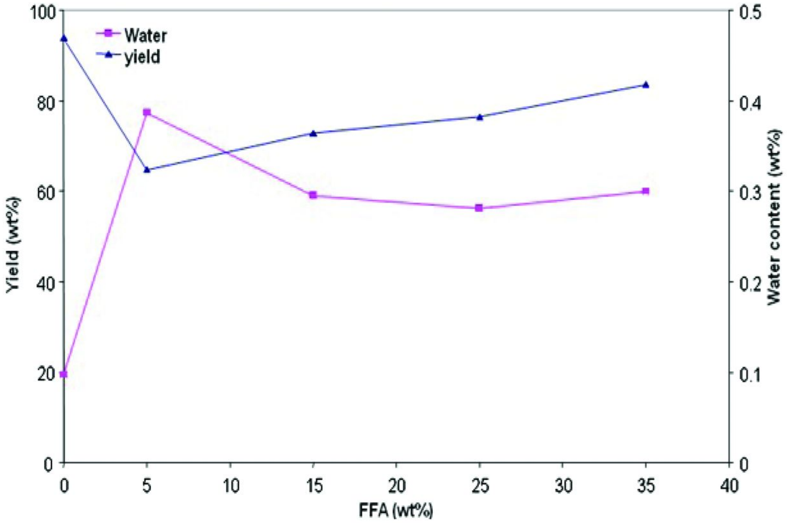

Figure 10. Effect of free fatty acids in Triolein on ester yield% and water content (5wt% catalyst 25% TPA/SBA-15 at 200°C, 4.14 MPa, 600 rpm, 10-h and using 30:1 methanol to oil molar ratio).

Downloaded by CORNELL UNIV on May 31, 2012 | http://pubs.acs.org
Publication Date (Web): January 20, 2012 | doi: 10.1021/bk-2012-1092.ch008

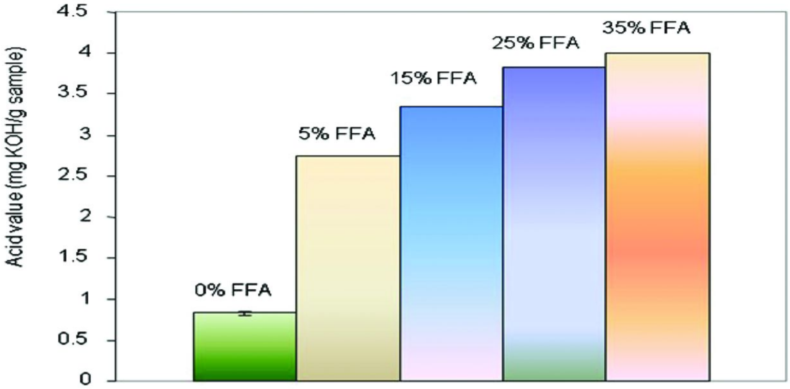

Figure 11. Effect of free fatty acids in Triolein on acid value (mg KOH/g sample) in the produced biodiesel.

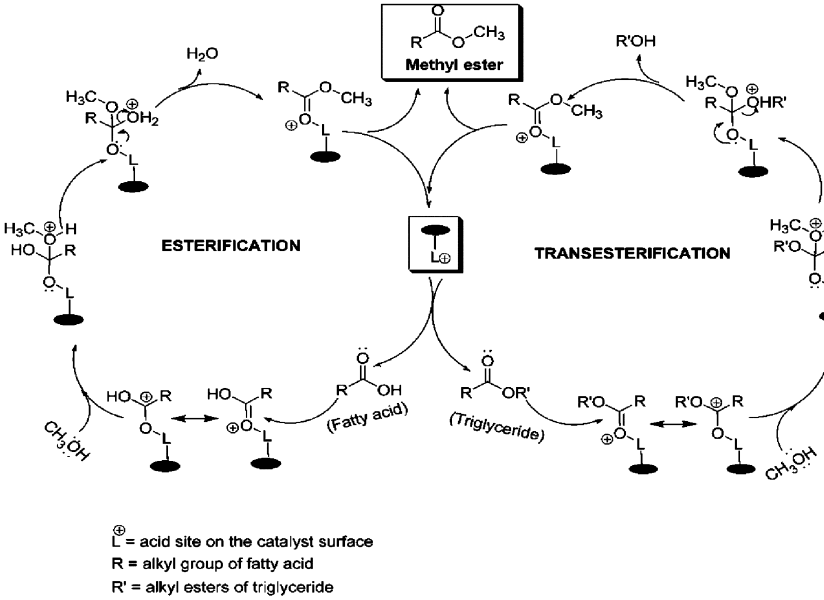
Methyl ester
H2O
R'OH
ESTERIFICATION
TRANSESTERIFICATION
(Fatty acid)
(Triglyceride)
CH3OH
CH3OH
L⊕ = acid site on the catalyst surface
R = alkyl group of fatty acid
R' = alkyl esters of triglyceride

Figure 12. Reaction mechanism of acid catalyzed simultaneous esterification and transesterification reaction (4).

The higher water content in the produced biodiesel from the feedstock containing 5% FFA indicates that, in that case, the catalyst initially catalyzes the esterification reaction than transesterification reaction. The esterification reaction product water later works as a poison for the transesterification reaction, which is already evident from the effect of presence of water study. The lower acid value of biodiesel in absence of FFA (Figure 10) indicates that 25% TPA/SBA-15 mainly catalyzes the transesterification reaction.

Conclusions

This research can be considered as a base line study to understand the catalytic activity of TPA supported on SBA-15 in the transesterification reaction for biodiesel production. Based on the study, 25% TPA is identified as the optimum catalyst loading on SBA-15 by impregnation method for biodiesel production from Triolein. From the optimization study using RSM model, 4.15 wt% catalyst (based on Triolein) and 39:1 methanol to Triolein molar ratio are found to be the optimum reaction conditions, when the reaction temperature is kept fixed at 200°C, stirring speed at 600 rpm and allowing 10-h of reaction time. Predicted ester yield at the above condition is 97.4 %, whereas the actual (experimental) yield is 97.2%. The catalyst suffers from poor reusability characteristics due to the leaching of the active species and the catalytic activity was reduced in presence of FFA and by-product water. Thus, the future detailed studies will be focused on improving the reusability and water tolerability of the catalyst.

Acknowledgments

The financial supports from the Natural Science and Engineering Council of Canada (NSERC), Agriculture and Biomass Innovation Network (ABIN) and Canada Research Chair (CRC) are acknowledged.

References

1. Srivastava, A.; Prasad, R. *Renewable Sustainable Energy Rev.* **2000**, *4*, 111–133.
2. Gerpen, J. V.; Knothe, G. *Biodiesel Handbook*; AOCS Press: New York, 2005; Chapter 4.
3. Marchetti, J. M.; Errazu, A. F. *Energy Convers. Manage.* **2008**, *49*, 2160–2164.
4. Kulkarni, M. G.; Gopinath, R.; Meher, L. C.; Dalai, A. K. *Green Chem.* **2006**, *8*, 1056–1062.
5. Busca, G. *Chem. Rev.* **2007**, *107*, 5366–5410.
6. Okuhara, T.; Watanabe, H.; Nishimura, T.; Inumaru, K.; Misono, M. *Chem. Mater.* **2000**, *12*, 2230–2238.
7. Kozhevnikov, I. V. *J. Mol. Catal.* **2007**, *262*, 86–92.
8. Wong, M. S.; Knowles, W. V. In *Nanoporous Materials: Science and Engineering*; Lu, G. Q., Zhao, X. S., Eds.; Series on Chemical Engineering, Imperial College Press: London, 2006; p125.
9. Herrera, J. E.; Kwak, J. H.; Hu, J. Z.; Wang, Y.; C. H. F. Peden, C. H. F. *Top. Catal.* **2008**, *49*, 259–267.
10. Tropecelo, A. I.; Casimiro, M. H.; Fonseca, I. M.; A.M. Ramos, A. M.; Vital, J.; J.E. Castanheiro, J. E. *Appl. Catal., A* **2010**, *390*, 183–189.
11. Yang, L.; Qi, Y.; Yuan, X.; Shen, J.; Kim, J. *J. Mol. Catal. A: Chem.* **2005**, *229*, 199–205.
12. Satishkumar, G.; Vishnuvarthan, M.; Palanichamy, M.; Murugesan, V. *J. Mol. Catal. A: Chem.* **2006**, *260*, 49–55.

Downloaded by CORNELL UNIV on May 31, 2012 | http://pubs.acs.org
Publication Date (Web): January 20, 2012 | doi: 10.1021/bk-2012-1092.ch008

13. Damyanova, S.; Dimitrov, L.; Mariscal, R.; Fierro, J. L. G.; Petrov, L.; Sobrados, I. *Appl. Catal., A* **2003**, *256*, 183–197.
14. Canakci, M.; Van Gerpen, J. *Trans. ASAE* **1999**, *42*, 1203.
15. Loreto, E.; Liu, Y.; Lopez, D. E.; Suwannakarn, K.; D. A. Bruce, D. A.; Goodwin, J. G. *Ind. Eng. Chem. Res.* **2005**, *44*, 5353–5363.
16. Ataya, F.; Dube, M. A.; Ternan, M. *Energy Fuels* **2007**, *21*, 2450–2459.
17. Lopez, D. E.; Goodwin, J. G., Jr.; D. A. Bruce, D. A.; Furuta, S. *Appl. Catal., A* **2008**, *339*, 76–83.

Downloaded by CORNELL UNIV on May 31, 2012 | http://pubs.acs.org
Publication Date (Web): January 20, 2012 | doi: 10.1021/bk-2012-1092.ch008

Downloaded by CORNELL UNIV on May 31, 2012 | http://pubs.acs.org
Publication Date (Web): January 20, 2012 | doi: 10.1021/bk-2012-1092.ch009

Chapter 9

Renewable Hydrogen Generation by Steam Reforming of Acetic Acid over Cu-Zn-Ni Supported Calcium Aluminate Catalysts

Madhumita Patel, K. K. Pant,* and Pravakar Mohanty

Indian Institute of Technology, New Delhi, India
***E-mail: kkpant@chemical.iitd.ac.in. Tel: 911126596172.**
Fax: 911126581120.

Catalytic steam reforming of biomass-derived-oil is one of the promising methods for the production of renewable hydrogen. Typically bio oil contains 12-14% by wt. acetic acid chosen as the model compound for the reforming reaction. In the present study performance of the Cu-Zn-Ni/CaO-Al_2O_3 catalyst was investigated for H_2 production in the range of 600-750 °C with an aim of minimization of CH_4 and CO formation. The calcium aluminate support was prepared by solid-solid reaction between calcium oxide and aluminium oxide (12/7 molar ratio) at 1250 °C for 24 hr. Cu, Zn and Ni were loaded on this support by wet impregnation method. For the preparation of catalyst, initial loadings of Cu, Zn and Ni were kept as 10%, 1% and 7% by wt. respectively. The catalyst was characterized by BET, XRD, SEM-EDX, TEM, TPD, TGA, TPO and TPR to understand the physico-chemical properties of the catalysts. The role of Ni metal was to break the C-C bond present in acetic acid and Cu metal promoted the steam reforming reaction on the surface of the catalyst. Incorporation of Zn enhanced the conversion, H_2 yield and also reduced deactivation of catalyst. The coke formation on the support surface was insignificant due to the presence of excess oxygen in the $12CaO.7Al_2O_3$ phase. At 700 °C, % H_2 yield was ≈94% and acetic acid conversion was ≈98%.

In Nanocatalysis for Fuels and Chemicals; Dalai, A.;
ACS Symposium Series; American Chemical Society: Washington, DC, 2012.

Keywords: H_2 production; acetic acid; steam reforming; Cu-Zn-Ni/Ca12Al7 catalyst

1. Introduction

Hydrogen (H_2) is identified to be an ideal energy carrier with high efficiency, since it possesses high heating value 121 MJ/kg (LHV) compared to any other known fuels and burns cleanly, without generating any environmental pollutants (*1*). H_2 production is an attractive subject of current interest for fuel cell applications which are considered to have the potential to provide a clean energy source for automobile as an alternative to gasoline or diesel engines. H_2 is also one of most important chemicals and is widely used for ammonia production, oil refineries, and methanol production etc. In view of growing environmental concerns, such as global warming and the depletion of fossil fuel, major efforts are being dedicated to develop the utilization of renewable energy sources. Bio oil produced from biomass has been proposed as an alternative to produce hydrogen; because this renewable rich energy resource does not contribute to a net increase in atmospheric CO_2. Bio-oil is a dark brown organic liquid. Bio-oil exhibits a complex composition with more than 200 different compounds including acids, alcohols, aldehydes, ketones as well as lignin derived oligomers, which are emulsified with water hence difficult to reform (*2*). In general, the steam reforming of bio-oil is simplified in terms of the oxygenated organic compounds ($C_nH_mO_k$) by the following reactions:

$$C_nH_mO_k+\left(n\text{-}k\right)H_2O=nCO+\left(n+m/2\text{-}k\right)H_2; \qquad (1)$$

The above reaction is followed by the water–gas shift reaction:

$$CO+H_2O \rightleftarrows CO_2+H_2 \;; \qquad (2)$$

The overall process can be represented as follows:

$$C_nH_mO_k+\left(2n-k\right)H_2O=nCO_2+\left(2n+m/2-k\right)\ H_2; \qquad (3)$$

Steam reforming of the main component in bio-oil such as acetic acid (12-14 by wt %) can offer the information for active catalyst preparation and the knowledge about the potential catalytic behaviour of bio-oil in steam reforming (*3*). Limited studies have been made on the steam reforming of acetic acid. Takanabe and co-workers studied the steam reforming of acetic acid over Pt/ZrO_2 catalyst for different process parameters like temperature, steam to carbon ratio and space velocity (*4*). Platinum helps in bond breaking of acetic acid to form H_2, CO, CH_4, and CO_2 into gas phase, and to form the carbonaceous residue (most probably CH_x species), which blocked Pt surface. But in presence of ZrO_2, H_2O can be activated to create supplementary surface hydroxyl groups, which react to gasify the residue on Pt to give chiefly steam-reforming/water–gas shift products (H_2, CO_2), and thus the catalytic cycles continue. Basagiannis and Verykios investigated the influence of metals (Ni and noble metals) and supports (Al_2O_3,

Downloaded by CORNELL UNIV on May 31, 2012 | http://pubs.acs.org
Publication Date (Web): January 20, 2012 | doi: 10.1021/bk-2012-1092.ch009

Downloaded by CORNELL UNIV on May 31, 2012 | http://pubs.acs.org
Publication Date (Web): January 20, 2012 | doi: 10.1021/bk-2012-1092.ch009

La_2O_3/Al_2O_3, MgO/Al_2O_3) on steam reforming of acetic acid (*5*). Result revealed that Ni based and Ru-based catalysts present high activity and selectivity toward H_2 production. Ru catalyst supported on La_2O_3/Al_2O_3 and MgO/Al_2O_3 carriers, showed good long-term stability as a function of time on stream. However, Ni catalysts were not as stable as Ru catalysts. The amount of carbon deposited on each catalyst was estimated, and it was found that it depends strongly on the nature of the catalyst. Vagia and Lemonidou studied the thermal decomposition and reforming in absence and presence of steam for different metal supported on the calcium aluminate supports (molar ratio of CaO to alumina were 12/7 and 1/2) (*6*). Coke formation was less compared to other support because of large oxygen content. In all these studies, it is observed that coke deposition on the catalyst surface is a serious problem. The rate of coke formation is higher in case of nickel catalyst in comparison to noble metal catalyst, however noble metal catalyst are too expensive. The catalyst preparation and selection of support are the two crucial factors for higher yield H_2, low CH_4 and CO formation and the low deactivation of catalyst. This paper focused on studying the effect of incorporation of Cu and Zn promoters on Ni metal supported on calcium aluminate for maximization of H_2 production. Calcium aluminate support was prepared in the laboratory.

2. Experimental

2.1. Catalyst Preparation

The carrier calcium aluminate support used (xCaO. yγ-Al_2O_3) with a molar ratio x/y =12/7, was prepared by solid state reaction between $CaCO_3$ and γ-Al_2O_3 at 1250 °C for 24 hour. Metals such as Cu, Zn and Ni were loaded on the support by the method of wet impregnation. The precursors used for Cu, Zn and Ni metals were $Cu(NO_3)_2.3H_2O$, $Zn(NO_3)_2.6H_2O$ and $Ni(NO_3)_2.6H_2O$ respectively (99.9% purity). Deionized water was used for the preparation of catalyst having pH of 6.8 ± 0.2. The aqueous solutions of the precursors were mixed with the support particles and dried in a vacuum rotary evaporator at 95 °C for 3 hour followed by overnight drying at 120 °C for 12 hour. The dried powder was calcined in air flow at 550 °C for 5 hour. Two batches of catalysts were prepared by varying the metal compositions as follows: (i) 10 wt% Cu and 1 wt% Zn and (ii) 10 wt% Cu, 1 wt% Zn and 7 wt% Ni. These were designated as CuZn and CuZnNi respectively whereas the support was designated as Ca12Al7.

2.2. Catalyst Characterization

The catalysts were characterized for final metal composition, surface areas and pore size, temperature programmed reduction (TPR), temperature programmed oxidation (TPO), NH_3 temperature programmed desorption (TPD), thermogravimetric analysis (TGA), X- ray diffraction (XRD), SEM-EDX and TEM methods. The details of the catalysts composition are presented in Table I.

Table I. Catalyst nomenclature and composition summary

Catalyst	*Composition (%)*						*Method of preparation*
	Ca	*Al*	*O*	*Cu*	*Zn*	*Ni*	
Ca12Al7	48.5	4.06	46.8	–	–	–	Solid-Solid reaction
CuZn	32.6	8.05	48.5	9.86	1.0	–	Wet impregnation method
CuZnNi	27.4	10.1	47.06	9.06	1.05	6.25	Wet impregnation method

2.3. Surface Area and Pore Size Analysis

The surface areas and pore volumes of the fresh and used catalyst were analyzed using N_2 adsorption-desorption isotherm. The BET surface area, total pore volume and pore size distribution of the catalyst was determined from nitrogen adsorption/desorption isotherms measured at –196 °C using Micromeritics ASAP 2010 apparatus. Prior to adsorption, the catalyst was degassed at 150 °C under vacuum for a period of 6 hour. The total pore volume was calculated at a relative pressure of $\cong$ 0.989.

2.4. Temperature-Programmed Reduction (TPR)

To quantify the amount of reducible zinc, copper, nickel phases and the reducibility of the catalyst has been followed by temperature programmed reduction (TPR), which was performed by taking a 0.25 gm of catalyst placed in a U-shaped quartz tube (6.6 mm i.d.). The TPR spectra was recorded using the Micromeritics Pulse Chemisorption Chemisorb 2720. The reducing gas mixture (H_2 = 0.15 Lh^{-1} and Ar = 2 Lh^{-1}) passed through the reactor heated from room temperature to 950 °C with a slope of 10 °C min^{-1} then maintained at desired temperature of 900 °C until the end of H_2 consumption showed by the baseline return. A thermal conductivity detector (TCD) was used to quantify H_2 consumption rate.

2.5. Temperature-Programmed Oxidation (TPO)

Temperature-programmed oxidation of post reaction catalysts was performed using a laboratory-made gas flow system (Micromeritics Pulse Chemisorption Chemisorb 2720). Typically about 10 mg of used catalyst was used in each measurement. In addition, the used catalysts were subjected to temperature programmed evaluation viz. TPR-TPO and TPO-TPR schemes. All the carbon gasification studies were carried out using the gas flow of 40 ml/min (having composition 4.5% O_2 and rest He). For each step, a ramp rate of 10 °C/min, from room to final temperature of 950 °C was employed, followed by holding time

Downloaded by CORNELL UNIV on May 31, 2012 | http://pubs.acs.org
Publication Date (Web): January 20, 2012 | doi: 10.1021/bk-2012-1092.ch009

of 1 h at 900 °C. All the gases were dehumidified prior to use. Used catalyst samples were dried in-situ under an Ar blanket at 160 ± 5 °C for 1 h prior to thermogravimetric analysis.

2.6. Temperature-Programmed Desorption (TPD-NH_3)

Acid sites density was evaluated by temperature programmed desorption (TPD) using mixture of of (4.9 vol % NH_3; balance He) preadsorbed at 35 °C. Previously to NH_3 adsportion, samples (300 mg) were reduced in H_2/Ar (2.4 L. h^{-1}) at 700 °C for 3 hour with a slope of 10 °C. min^{-1}. Samples were ammonia-saturated at room temperature in NH_3/He (4.9% vol) flow (2.1 L.h^{-1}) for 1 hour. Before TPD, weakly adsorbed NH_3 was removed by flowing He at 50 °C for 30 min. Ammonia was desorbed using a linear heating rate for 10 °C min^{-1} from 50 to 900 °C.

Downloaded by CORNELL UNIV on May 31, 2012 | http://pubs.acs.org
Publication Date (Web): January 20, 2012 | doi: 10.1021/bk-2012-1092.ch009

2.7. X-ray Powder Diffraction (XRD)

X-ray powder diffraction (XRD) patterns were obtained using a computerized IR Stage (PhiPsi X YZ) XRD having vertical diffractometer (Cu Kα radiation, $\lambda = 0.154$nm) equipped with a PW Bragg - Brentano (θ/2θ) goniometer, operated at 45 kV and 40 mA. X-ray diffractometer was equipped with an atmosphere and temperature control stage, where the samples were scanned with Bragg's angles between 10° and 90° using a step size (θ) 0.0501 sec per step having scan step time 12.15 sec and maintaining the goniometer at radius of 240 mm. Metal crystallites average diameters were estimated from XRD patterns using the Scherrer's equation. For phases and lattice structure identification International Diffraction Data (JCPDS) library was used.

$$d\,(Ni^0) = 0.75 \times d\,(NiO) \qquad (4)$$

The average size of (NiO) particle was calculated according to the Scherrer's equation.

$$d = [(0.89 \times \lambda / B\cos\theta) \times (180^0 / \pi) \qquad (5)$$

Where d is the average crystallite diameter, λ is the wave length of radiation, and B is the full width half in degrees. Then the Ni^0 metal dispersion was estimated from diameter of (Ni^0) by assuming a spherical geometry of the metal particles with uniform site density of 14.6 atoms per nm^2, using the following equation. $D = [96/d]$; where D is the (% Ni^0) dispersion and d is the mean particle size of Ni^0 in nm. The International Center for Diffraction Data (ICDD) library was used for phase identification.

2.8. Scanning Electron Microscope (SEM)

The morphology of the catalyst sample was investigated using SEM equipped with a new ZEISS EVO Series Scanning Electron Microscope EVO 50. The ZEISS EVO 50 is a versatile analytical microscope with a large specimen chamber.

Scanning Electron Microscope EVO 50 having the resolution 2.0 nm @ 30 kV (SE with LaB6 option) with magnification ranges up to 1,000,000X and at an acceleration voltage. Final metal loading on the catalyst was determined by SEM – EDX analysis using same Microscope EVO 50 and X-ray analysis. Metal loading percent on the catalyst was further conformed by UV-visible spectrophotometer.

2.9. Transmission Electron Microscope (TEM)

TEM was performed using PHILIPS CM12 microscope operated at an accelerating voltage of 100 kV. Both fresh and post-reaction samples were grounded in a mortar subsequently ultrasonically dispersed in ethanol-water solution. A drop of the suspension was then deposited on a Cu grid covered with a perforated carbon membrane for TEM observation (*7*).

Downloaded by CORNELL UNIV on May 31, 2012 | http://pubs.acs.org
Publication Date (Web): January 20, 2012 | doi: 10.1021/bk-2012-1092.ch009

3. Steam Reforming of Acetic Acid to Hydrogen

The experiments were performed at atmospheric pressure in a laboratory unit equipped with a mass flow controlled system, a fixed bed tubular reactor and an offline gas chromatograph. The details of the experimental set up are discussed elsewhere, used for glycerol reforming and only briefly presented here (*8*). A peristaltic pump was used for the feeding of the liquid reactants (a mixture of acetic acid and water) to the reactor through a preheater. The reactor was made of a cylindrical cup of 19 mm diameter and 30 mm length, perforated on the bottom with orifices of 0.5 mm diameter to enable the flow of gases. The experiments were performed in a temperature range from 600 to 750 °C at atmospheric pressure for a concentration of 10 wt% of acetic acid in distilled water. 3 gm of catalyst was taken inside the catalyst bed for every run and the flow rate was varied in the range of 0.38 to 1.3 ml/min. The catalyst used was in the form of pellet of particle size 0.5 ± 0.1 mm. Nitrogen was used as the carrier gas at a flow rate of 25 ml/min. Prior to the run of the catalyst, it was reduced at 550 °C in 50% H_2/N_2 flow for 3 hour before the reforming experiments. The hot gases exiting the reactor were passed through a condenser followed by a gas liquid separator. The liquid product was analysed by using a Nucon 5700 gas chromatograph and operated in FID mode. The gaseous product analysis was done using Nucon 5700 gas chromatograph and operated in TCD mode.

3.1. Reaction Involved in Steam Reforming of Acetic Acid

Reforming of acetic acid for H_2 production can be summarized as followes: First, Steam reforming of acetic acid reaction has discussed as stated below:

$$CH_3COOH \xrightarrow{H_2O} 2CO + 2H_2 \;;\; \Delta H^0_{298\ K} = 213.4\ kJ/mol \qquad (6)$$

This is followed by water gas shift reaction

$$CO + H_2O \xrightarrow{Catalyst} CO_2 + H_2 \;;\; \Delta H^0_{298\ K} = -\ 41\ kJ/mol \qquad (7)$$

The overall steam reforming reaction of acetic acid is

$$CH_3COOH+2H_2O \xrightarrow{\text{catalyst}} 2CO_2+4H_2\,;\ \Delta H^0_{298\,K}=131.4\text{kJ/mol} \qquad (8)$$

The maximum stoichiometric yield of H_2 from acetic acid reforming is 2 mole per mole of carbon. However due to some undesired reactions such as decomposition of acetic acid lower molecular weight oxygenates, lighter hydrocarbons (CH_4, C_2H_4) and coke also forms.

$$C_2H_4O_2 \rightarrow C_xH_yO_z\text{+Carbon+Gases}\left(H_2,CO,CO_2,CH_4,C_xH_{x+2}\right); \qquad (9)$$

Some amount of coke can also be formed from Boudouard reaction.

$$2CO \leftrightarrow CO_2 + C\,;\Delta H^0_{298\,K} = -172.4\text{kJ / mol}\,; \qquad (10)$$

Some of the hydrogen is lost because of the methanation and reverse water gas shift reaction.

$$CO + 3H_2 \rightleftarrows CH_4 + H_2O\,;\ \Delta H^0_{298\,K} = \text{-206.1 kJ/mol} \qquad (11)$$

$$CO_2 + 4H_2 \rightleftarrows CH_4 + 2H_2O\ ;\Delta H^0_{298\,K} = \text{-165.1 kJ/mol} \qquad (12)$$

$$H_2 + CO_2 \rightleftarrows H_2O + CO\,;\Delta H^0_{298\,K} = \text{41.1 kJ/mol} \qquad (13)$$

Small amount of acetone may be formed by ketonization reaction of acetic acid.

$$2CH_3COOH \rightleftarrows CH_3COCH_3\text{+}CO_2\text{+}H_2O;\ \Delta H^0_{298\,K}=\text{16.7 kJ/mol} \qquad (14)$$

The terms % H_2 yield, % acetic acid (acetic acid) conversion and % selectivity of gaseous product distribution were used to describe the catalytic results in reforming of the oxygenate. The definitions are given below.

$$\%\ H_2\ \text{yield} = \frac{\text{moles of } H_2 \text{ in gaseous product}}{4 \times \text{moles of acetic acid fed}} \times 100 \qquad (15)$$

$$\%\ \text{selectivity of } H_2 = \frac{\text{moles of } H_2 \text{ in gaseous product}}{\text{C atoms in gaseous phase}} \times \frac{1}{RR} \times 100 \qquad (16)$$

Where RR is H_2/CO_2 reforming ratio and RR = 4/2.

Downloaded by CORNELL UNIV on May 31, 2012 | http://pubs.acs.org
Publication Date (Web): January 20, 2012 | doi: 10.1021/bk-2012-1092.ch009

$$\%\text{ selectivity of 'i'} = \frac{\text{C atom in species 'i'}}{\text{C atoms in gaseous phase}} \times 100 \quad (17)$$

$$\%\text{ Acetic acid conversion} = \frac{\text{moles of Acetic acid in - moles of Acetic acid out}}{\text{moles of Acetic acid in}} \times 100 \quad (18)$$

3.2. Results and Discussion

The BET surface area and pore volume of the catalysts and support are shown in Table II.

Table II. BET surface areas and pore volume of the catalysts

Catalyst	*BET SA (m^2/g)*	*Pore Volume (cm^3/g)*	*Adsorption Pore width (Å)*
Ca12Al7	10.2 ± 1	0.012 ± 0.002	28 ± 4
CuZn	5.8 ± 1	0.017 ± 0.002	45 ± 4
CuZnNi	5.3 ± 1	0.015 ± 0.002	51 ± 4

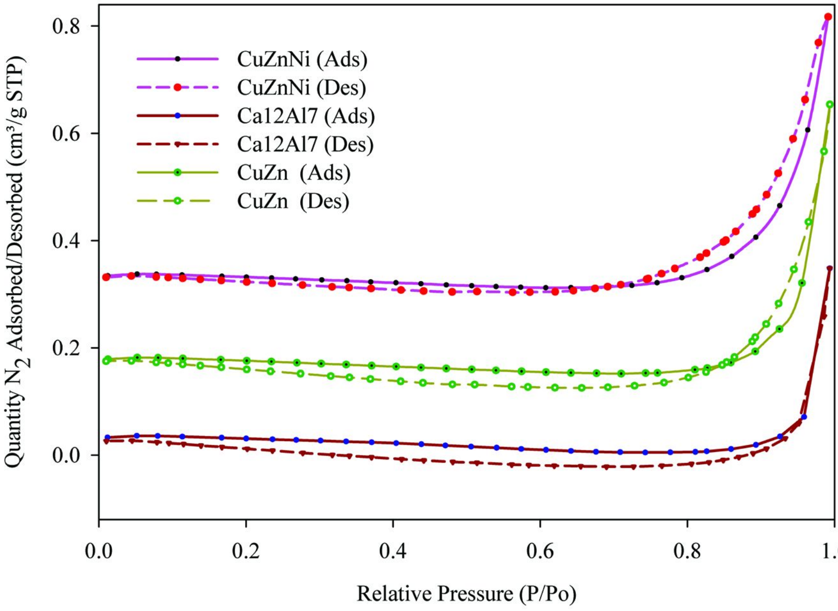

Figure 1. BJH isotherms of freshly prepared CuZnNi, Ca12Al7 and CuZn catalyst.

Downloaded by CORNELL UNIV on May 31, 2012 | http://pubs.acs.org
Publication Date (Web): January 20, 2012 | doi: 10.1021/bk-2012-1092.ch009

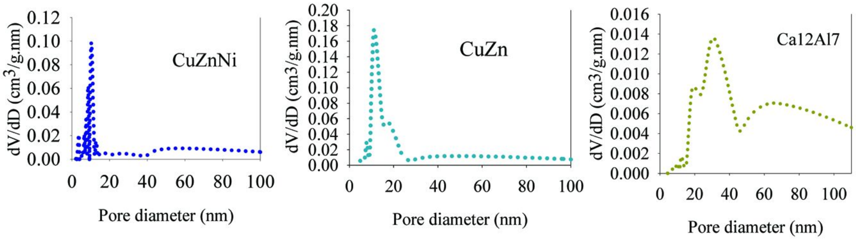

Figure 2. Pore-size distribution of freshly prepared CuZnNi, Ca12Al7 and CuZn catalyst.

The N_2 adsorption/desorption isotherms of the catalysts are are shown in Figure 1 and summerised in Table II. The p/p^o position of the inflection point corresponds to a diameter in the mesopore range. Type-IV adsorption with a combination of both H1 and H3 type hysteresis loops were observed in the N_2 adsorption isotherms which verified that the secondary inter particle aggregations possessed mesoporosity. Pore size distributions from BJH adsorption are presented in the Figure 2. The dV/dlogD values in the y-axis were calculated from BJH N_2 adsorption branch, where V is the adsorption volume (N_2) and D is the pore diameter (nm). Barrett-Joynes-Halenda (BJH) plots of pore size distribution suggested a wide range of pores, consistent with data obtained from XRD analysis. Each catalyst showed narrow uniform mesopore distribution (20 nm < width < 50 nm). The samples with different atomic ratios also showed similar pore size distributions which indicate the effectiveness of this method for preparing uniform mesoporous mixed oxide catalysts. For further characterization of the texture and structure of the samples, a transmission electron microscope observation was carried out for the support and (CuZnNi) catalyst sample. It was found that the crystallites were homogeneously distributed with highly disordered round-worm-like mesopores between the channels. The presence of large pores could be caused by collapse of layered structures or pore defects formed during catalyst synthesis. Here observed isotherms and pore size distribution were closely associated and dependent on catalyst synthesis. Also during catalyst calcination at high temperatures, a portion of small pores could collapse, which might lead to formation of large disordered pores and provided another dimension, explanation for experimental observations.

The reduction features of the catalysts were analyzed by TPR. The TPR plots of catalysts CuZnNi and Ca12Al7 support are shown in Figure 3. For sake of comparison, the TPR of CuZnNi with support clarified the phase formation of CuO and NiO after impregnation of Cu, Zn, and Ni on the support (Ca12Al7) material. The formation of prominent phases with higher Ca/Al ratio, kinetically favored for promoter metals to form stable phases for H_2 generation by WGS and reforming reactions. The TPR plot exhibited two overlapping reduction peak at 243 and 291 °C respectively breaking the CuO to Cu^{2+} ion (*9*). The other peak rounded at 490 °C associated with the reduction of NiO to Ni^0 strongly bonded to the support. Similarly TPR results have been presented for the reduction of $Ca_xAl_yO_z$ making different stable phases, for promotion of transition metal like Cu, Zn and Ni. For catalyst Ca12Al7, a broad peak was obtained at 685 °C, slightly higher

Downloaded by CORNELL UNIV on May 31, 2012 | http://pubs.acs.org
Publication Date (Web): January 20, 2012 | doi: 10.1021/bk-2012-1092.ch009

temperature side favours both WGS and reforming reaction in the reaction zones (600 – 750 °C) producing stable phases depicted in Figure 3, and it corresponded to the reduction of $Ca_xAl_yO_z$ phases enhancing a higher interaction with the support and the secondary metals. The TPR plot indicates that with Cu addition, the nickel oxide reduced at a lower temperature. Owing to the relatively small Zn with higher Ca-Al contents, no reduction of separate ZnO was observed. The shift of peak maximum to higher temperatures for the lower Ni-Cu content samples can be ascribed to the increase of the metal support interaction resulted from better dispersion of Ni and Cu in the Ca-Al spherical structures getting characterized from TEM analysis.

It is desirable that the better-dispersed Ni and an appropriate interaction between metal and support increase the Ni reducibility as both Cu and Ni are rich in *d*-electrons and Ni has unfilled *d* orbits. The unfilled *d*-orbits of Ni atoms can accept *d*-electrons from Cu (Cu – as a transition metal prefers filled *d* subshell, leaving *s* with one electron, resulting in an increase in *d*-electron density of Ni atom). It was observed that the H_2 consumption was very low for the used catalysts, indicating that metal oxide was not present in the catalysts after reaction and, therefore, it can be concluded that the catalysts were not deactivated by metal oxidation.

Downloaded by CORNELL UNIV on May 31, 2012 | http://pubs.acs.org
Publication Date (Web): January 20, 2012 | doi: 10.1021/bk-2012-1092.ch009

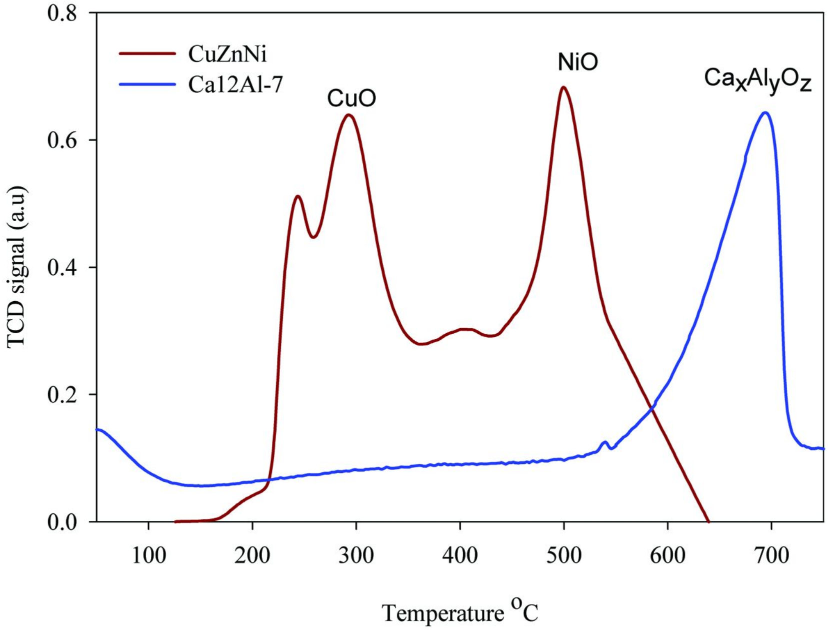

Figure 3. TPR curves of freshly prepared CuZnNi and Ca12Al7 catalysts.

Downloaded by CORNELL UNIV on May 31, 2012 | http://pubs.acs.org
Publication Date (Web): January 20, 2012 | doi: 10.1021/bk-2012-1092.ch009

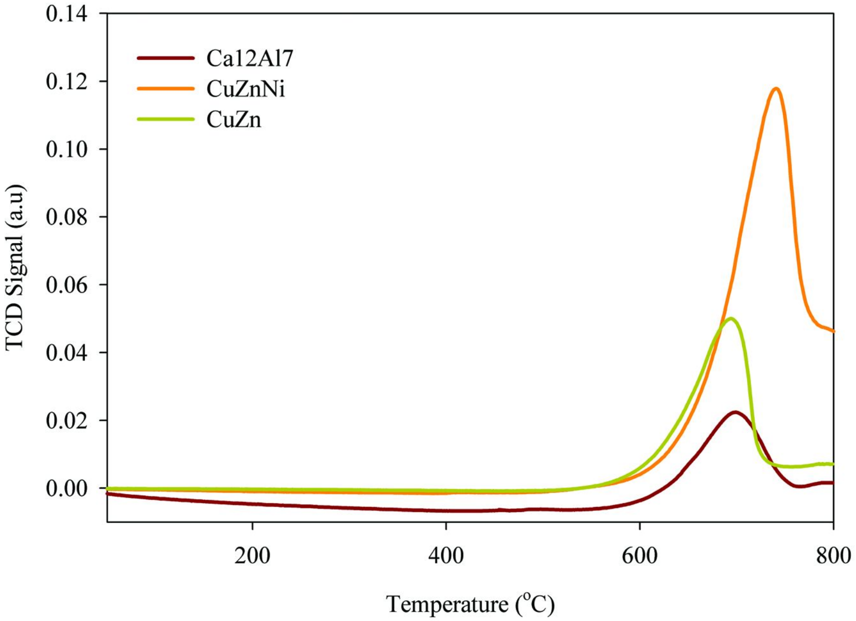

Figure 4. NH_3 TPD curves of freshly prepared CuZnNi, CuZn and Ca12Al7 catalysts.

The TPD spectra assigned a peak around 693 °C for CuZn to the desorption of ammonia from the strongest acid sites of the catalyst, where as the peak shifted towards higher temperature when Ni binding took place to the CuZnNi catalyst (Figure 4 and Table III). Because the calcium-aluminate is ultrastable or steamed and thus, possesses a considerable amount of non framework aluminum which exhibits acidity by ammonia method. This calcium oxide increases the thermal stability lowering to coking effect. Quantum mechanics calculation based on density functional theory (DFT) also predicted that the Ni (1 1 1) and Ni (1 0 0) planes raise an energetic barrier for CH_4 dissociation of 0.21 and 0.20 eV, respectively (*10*). Moreover calculation of dissociation of CH_4 transition state on these planes induced a dipole moment of 0.20 and 0.19 eÅ. Vagia and Lemonidou, reported that the characteristic of higher acidic sites with higher strength which may arise from the free Al_2O_3 as identified by XRD and total acidic sites also included the formation of calcium aluminates (*6*).

The open structure of the Ca12Al7 permits the easy diffusion of Ni to the bulk of the pellets as evidenced from the almost uniform distribution of the Ni (Figure 9B) and thus the dispersion of Ni with this catalyst was higher (*6*). Calculation of dispersion (D) based on particle size by Scherrer's equation provided an indication about the differential shape and lattice size are (~ 40 – 50 nm) summerised in Table IV.

Downloaded by CORNELL UNIV on May 31, 2012 | http://pubs.acs.org
Publication Date (Web): January 20, 2012 | doi: 10.1021/bk-2012-1092.ch009

Table III. NH_3 TPD and metal dispersion of freshly prepared catalyst

Catalyst	*Acidic site NH_3 Adsorption*		
	T (°C) NH_3 desorbed	*Total NH_3 adsorbed (m.ml/g) at STP*	*% Metal Dispersion*
Ca12Al7	701 °C	606	2.87
CuZn	693 °C	671	2.08
CuZnNi	735 °C	817	3.21

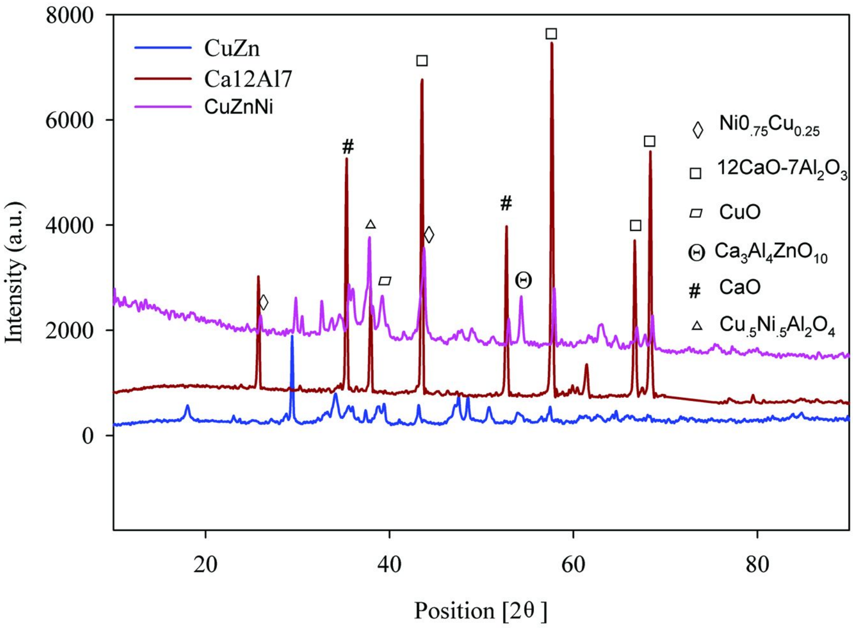

Figure 5. XRD spectra of freshly prepared CuZnNi, CuZn and Ca12Al7 catalysts.

Figure 5, shows the XRD pattern of catalyst samples. The XRD peaks correspond to fresh calcined samples of CuZn, Ca12Al7 and CuZnNi respectively, where $12CaO\text{-}7Al_2O_3$ phase was detected at 42.8°, 58.4°, 65.1° and 67.03° (JCPDS-780910) with cubic and body centered lattices (4 4 4). Phases like $CaAl_4O_7$, CaO and $CaCO_3$ were detected at 50.83° (JCPDS-720767), 37.1°, 54.4° respectively with monoclinic, end centered lattice revealed from JCPDS-461475. Other phases with the presence of Ni, Zn and Cu were formed with Ca-Al, detected as $Ni_{0.75}Cu_{0.25}$, $Cu_{0.5}Ni_{0.5}Al_2O_4$ and $Ca_3Al_4ZnO_{10}$. Most stable phases like $CaCO_3$ and $Ni_{0.75}Cu_{0.25}$ were hexagonal and rhombic centered (JCPDS-47-1743) and hexagonal f.c.c (JCPDS-780648) respectively. The lattice parameters (f.c.c) were calculated at (4 4 4) using the equation: $\alpha_{\text{f.c.c}} = \dfrac{\sqrt{2\lambda}}{\text{Sin}\theta}$; where, λ is the wave length of radiation and θ is Bragg's angle. Calcium and alumina were also found in form of $Ca_5Al_6O_{14}$ phases among which some were cubic, b.c.c, and some were end centered with orthorhombic or monoclinic in nature. It can be predicted for CuZnNi catalyst a single pattern corresponding to Ni-Cu phases were prominent, probably indicating either the higher dispersion or the amorphous nature of copper. XRD peaks are observed indicating particle size (d) = 3.6, 8.8 and 10.4 nm, which are in a good agreement with the standard XRD pattern and TEM analysis.

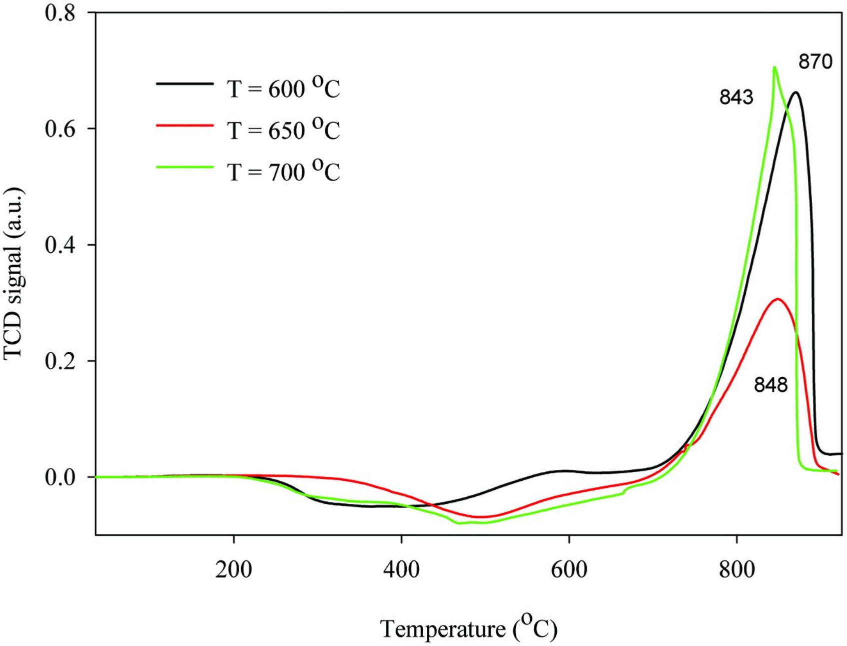

Figure 6. TPO analysis of used CuZnNi at different temperatures after 11 hours of time on stream (TOS).

From TPO spectra in Figure 6, typical carbonaceous species were found to exist on CuZnNi catalyst, analyzed in the temperature range of 840 – 875 °C. Figure 6, shows the mass loss due to the combustion, during the TPO experiments, of the carbon deposited on the used catalysts. First, it has to be mentioned that when the catalysts were heated in an oxygen containing atmosphere, metal oxidation took place and the spectra implied a sharp falling zone in the temperature range of 320 – 525 °C, indicating the decomposition of acetic acid in the mesopores (*11*). The addition of Ni and Cu to the catalyst resulted in a disappearance of crystalline carbon species, where as filamentous carbon species were decomposed at higher temperature reveled from TEM figures. Increase in temperature indicate higher O_2 requirement to decompose the deposited graphitic carbon species. High temperature reactions with calcium-aluminate species used as support indicated that catalyst with 7% Ni-10%Cu-1%Zn content was more susceptible to carbon formation and deactivation (*6*). It must be noted that the

Downloaded by CORNELL UNIV on May 31, 2012 | http://pubs.acs.org
Publication Date (Web): January 20, 2012 | doi: 10.1021/bk-2012-1092.ch009

coke accumulated in the catalyst is the result of two simultaneous processes: carbon formation reactions ($CH_4 \rightarrow C + 2H_2$) and ($2CO \rightarrow C + CO_2$) and carbon gasification through the inverse of the reactions indicated. Thus, the amount of deposited carbon depends on the relative rate of these processes that also determine the structure and reactivity of the deposited filamentous carbon (*11*). Coke, produced according to these two reactions, could cover the active centers and produced catalyst deactivation for a long thermal run.

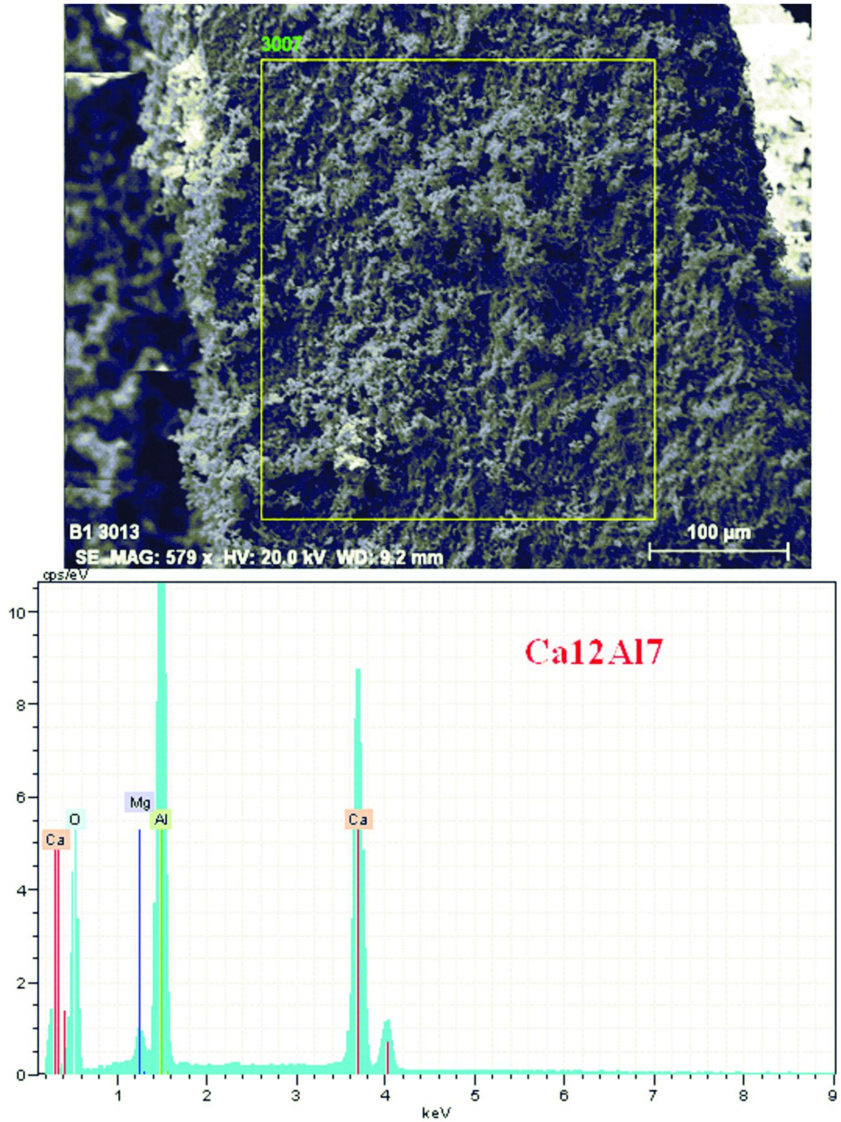

Downloaded by CORNELL UNIV on May 31, 2012 | http://pubs.acs.org
Publication Date (Web): January 20, 2012 | doi: 10.1021/bk-2012-1092.ch009

Downloaded by CORNELL UNIV on May 31, 2012 | http://pubs.acs.org
Publication Date (Web): January 20, 2012 | doi: 10.1021/bk-2012-1092.ch009

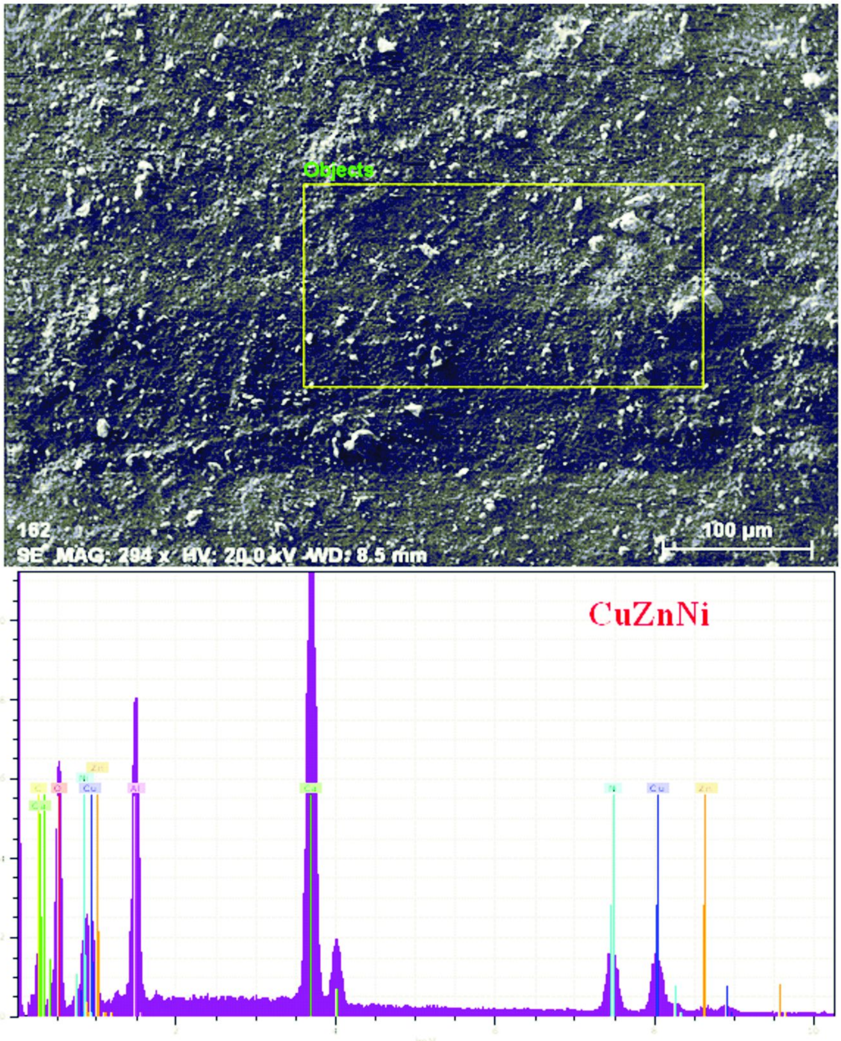

Figure 7. SEM-EDX image and peaks (A, left) freshly calcined Ca12Al7 (B, right) freshly calcined CuZnNi catalyst.

In Figure 7 (A and B), quantitative analysis by EDX and different peaks indicate the final weight % of metal loading for fresh calcined catalyst Ca12Al7 and CuZnNi. The SEM image indicates the uniform loading of transition metal particles on the support and uniformity of size and shape of the catalyst further characterized by TEM. The images were taken at 30,000 times magnification at 20 kV. The EDX pattern confirms the presence of Ca, Al and Cu w.r.t to each catalyst sample and no other undesired element such as chlorine or potassium was determined. Typically all sharp peaks indicate the atomic wt (%) of loaded metals on the support after physical synthesis (*12*). These EDX spectras indicate that the precursors were successfully handled for final loading with necessary physiochemical treatment of these samples, which are tabulated in Table I.

TGA plots are shown in Figure 8, as temperature vs. weight % for used CuZnNi catalyst. The final temperature was 800 °C to ensure all the carbon removed (*12*). The weight loss was prominent from 520 to 760 °C, due to oxidation of all filamentous carbon species deposited in the pores as well as on the external surface. BET analysis of these used samples also indicated relatively lower surface area due to the partial carbon blockage of the catalyst pore. A final loss of carboneous species, indicates the weight percentage of metal present in the catalyst. A small concentration of desorbed acetate and acetic acid compounds also decomposed in the catalyst in the temperature range between 240 to 420 °C. The total amount of filamenteous carbon deposited on the catalyst after a run time of 11 hours was 7 ± 0.5 species as obtained from TGA analysis.

Downloaded by CORNELL UNIV on May 31, 2012 | http://pubs.acs.org
Publication Date (Web): January 20, 2012 | doi: 10.1021/bk-2012-1092.ch009

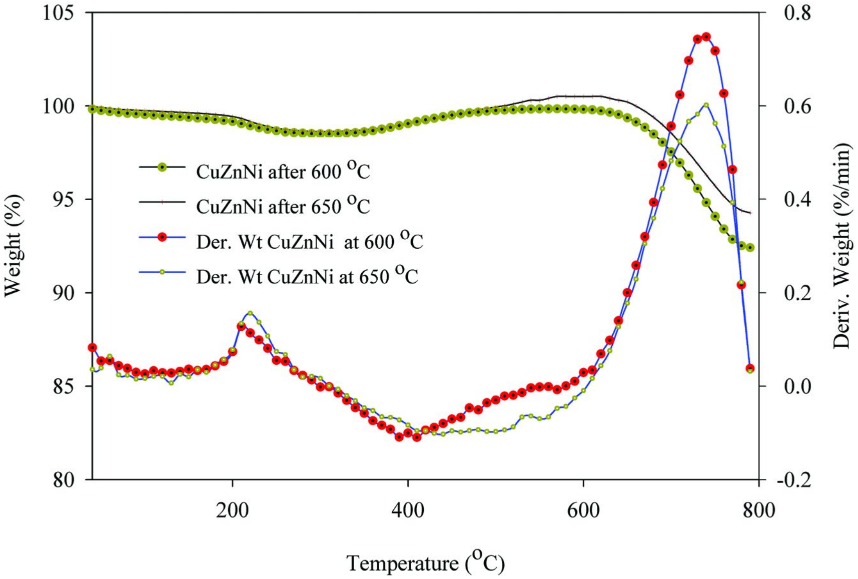

Figure 8. TGA-DTA graphs of used CuZnNi at different temperatures after 11 hours of time on stream (TOS).

The morphologies of metal particles and particle size distribution were investigated using TEM and the results are shown in Figure 9 (A and B). It is evident that Ca12Al7 had the most contrasted metal particles with around 20% particles larger than 10 nm (Figure 9A). Blackish particles are referred to calcium and the light shaded particles with spherical channelized modules are recognized as alumina particles. The metal particle size of the different catalysts had been estimated by measuring the size of at least 100 particles. Figure 9A, presenting the size distribution and the average metal particle size of Ca and Al distributed in scattered networking after solid-solid high temperature reaction. The largest particles and the most heterogeneous size distribution were observed for calcium particle in making the support where as the alumina had a lower average particle and homogeneous particle size distribution counted for making a catalyst, with particle sizes up to ~ 40 – 50 nm (*11*). Another observation was that the boundary between metals and support in cases of CuZnNi and Ca12Al7 became indistinct in comparison with the support only. With assumption that all the metals were present on the surface are spherical in nature; corresponding to sizes and distribution weight can be given by TEM, where metal dispersion (D_M) was calculated using the following equation given by (*13*). $D_M = 6\times10^7 \frac{V_M}{A_M}\left(\frac{1}{d(nm)}\right)$, where V_M is the bulk atomic volume of the metals (cm^3), A_M is the area of an atom (cm^2), and d is the metal particle size in nm. For Ni, Zn and Cu (as Ni, Cu and Zn having nearer atomic weight), their V_M is very close to one another, so average $V_M = 1.10 \times 10^{-23}$ cm^3 was taken; and their AM = 1×10^{-15} cm^2 was considered (*14*). The smaller Ni-Cu content catalysts had larger metal dispersion than that of the f.c.c. crystals, indicating more metal site existing on the surface, as f.c.c structures were confirmed from XRD (JCPDS) lattice data.

Downloaded by CORNELL UNIV on May 31, 2012 | http://pubs.acs.org
Publication Date (Web): January 20, 2012 | doi: 10.1021/bk-2012-1092.ch009

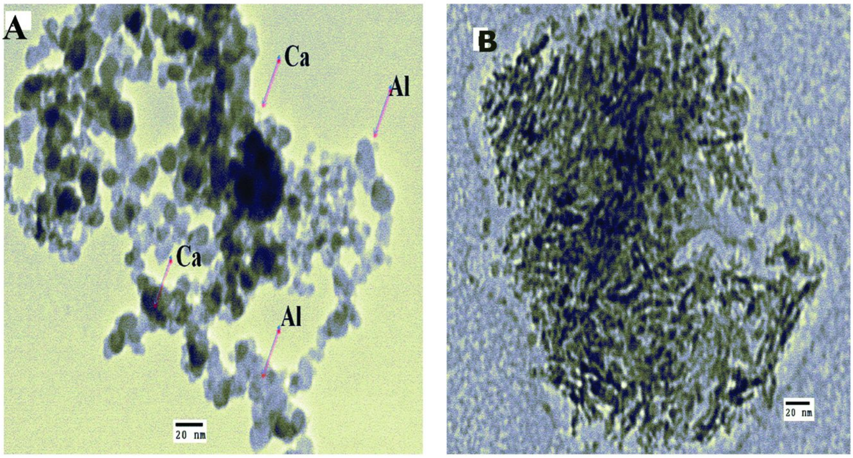

Figure 9. (A) TEM image of freshly prepared Ca12Al7 (B) Freshly calcined CuZnNi catalyst.

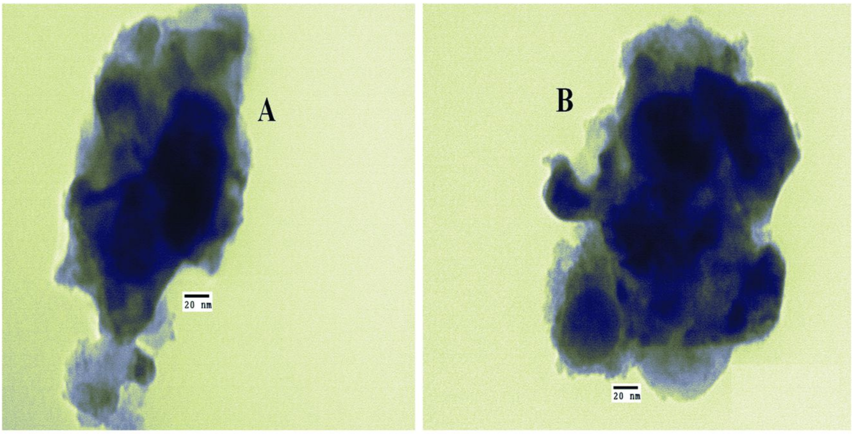

Figure 10. TEM images of used CuZnNi catalysts; reaction temperature: (A) 650 °C , (B) 700 °C.

The metal particles location is very important for the catalyst stability and longer activity because when the particle is at the top of the carbon filament, it is accessible to the reactant vapors hence, keeping steady catalytic activity; on the contrary, upon encapsulation the metal particles lose their activity because they are not accessible to reactants (*15*). In this work TEM images of used CuZnNi catalyst after 650 °C and 700 °C has shown in Figure 10 (A and B). Most of the particles were found at the top of the filament, although there were some metal particles encapsulated in the filaments which help in simultaneously water shift gas reaction and carbon formation with auto consumption process (*16*). Thus, as small metal particles (≥10nm) generate carbon filaments with a short diameter and a thermodynamically unfavourable growth due to higher (S/C) ratio. Moreover, carbon gasification towards CO_2 (a structure-sensitive reaction) is favored in small particles (*14*). Only minor differences in the mean particle size were observed comparing the XRD and TEM analysis shown in Table IV.

N_2-physisorption has revealed that CuZnNi had lower surface area and fewer low mesoporous pores (<10 nm), less small-pore volume than other catalysts with lower Ni-Cu content shown in Table IV. This may be attributed to its relatively high content of aluminum-calcium oxides, which suppose to facilitate porous structures and high thermal stability for surface area (*14*). It is indicated that the CuZnNi catalysts with prominent BET surface area can provide large contact area for the (acetic acid) reactants, thus resulting in high reaction activity. However, the precipitates will not have any activity until they are reduced in H_2-contaning gas. In other words, the active sites on the catalysts must be the metallic Ni, Zn and Cu that have been formed during reduction. It is apparent that catalyst activity depends not only on metal sites but also on other factors such as metal crystalline structure and metal support environment, which was revealed from XRD and TEM characterization. Lower metal density and better metal dispersion on catalyst surface may lead to more active sites on the catalyst surface. The particle size distribution indicates that the portion of smaller particles increases

Downloaded by CORNELL UNIV on May 31, 2012 | http://pubs.acs.org
Publication Date (Web): January 20, 2012 | doi: 10.1021/bk-2012-1092.ch009

with the decrease in Ni-Cu content in terms of activity and yield. Phases like $Ni_{0.75}Cu_{0.25}$, $Cu_{0.5}Ni_{0.5}Al_2O_4$ and Cu remained intact after reforming reaction which was confirmed from the XRD spectra of the used catalyst shown in Figure 11. Evidence of the presence of more than one phases of Ca and Al could be attributed to the stringent conditions (1250 °C for 24h) which had been used for the solid-solid phase interaction of the support. Such high thermal treatment are generally recommended for the formation of monophasic calcium aluminates, confirmed from the XRD spectra.

In conclusion, even though CuZnNi contained the lower amount of Ni among the other three catalysts, synergy of larger surface area, less metal density, better metal dispersion, and smaller metal particles gave rise to more active sites and led to higher catalytic activity, which is shown in Table V.

Downloaded by CORNELL UNIV on May 31, 2012 | http://pubs.acs.org
Publication Date (Web): January 20, 2012 | doi: 10.1021/bk-2012-1092.ch009

Table IV. (%) of metal dispersion and particle size distribution

Catalyst	*O_2 chemisorbed T (°C) and (ml O_2/g) at STP*	*Main Phases identification*	*Particle size (nm)*	
			XRD	*TEM*
Ca12Al7	_	$12CaO\text{-}7Al_2O_3$	15-26	10-34
CuZn/CaAl	_	_	16-24	12-32
CuZnNi/CaAl (F)	_	CuO and $Ni_{0.75}Cu_{0.25}$	14-22	10-30
CuZnNi (U) at 600°C	(870°C)-3.98	CuO	16-28	13-36
CuZnNi (U) at 650°C	(848°C)-3.02	$Cu_{0.5}$Ni0.5Al_2O4	14-30	12-35
CuZnNi (U) at 700°C	(843°C)-4.32	CuO and $Ni_{0.75}Cu_{0.25}$	15-30	11-37

Table V. Screening of catalyst

Catalyst	*CuZn*			*CuZnNi*		
Temperature (°C)	600	650	700	600	650	700
% H_2 yield	23	30	44	67	78	95
% Acetic Acid conversion	10	17	22	70	84	99

Downloaded by CORNELL UNIV on May 31, 2012 | http://pubs.acs.org
Publication Date (Web): January 20, 2012 | doi: 10.1021/bk-2012-1092.ch009

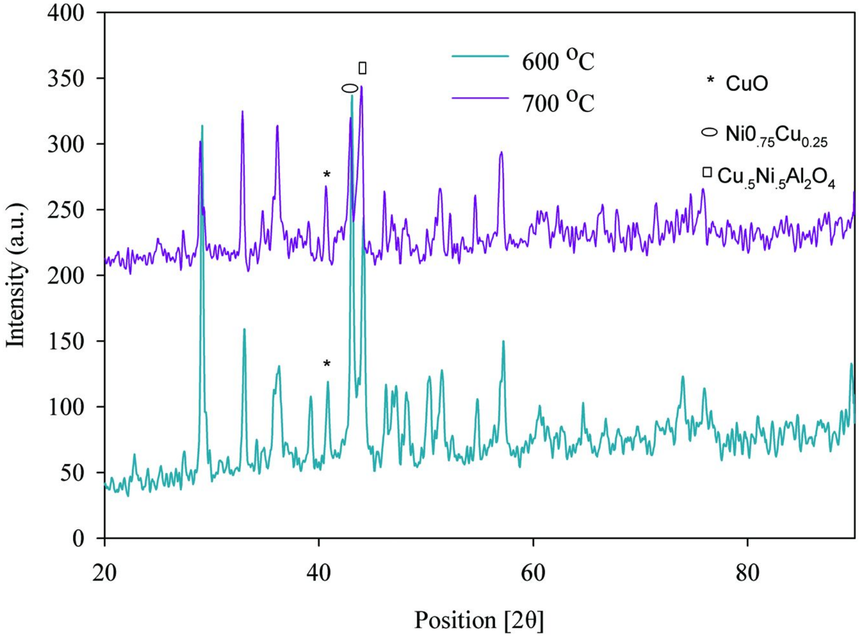

Figure 11. XRD spectra of used CuZnNi catalyst with reaction 600 °C and 700 °C.

4. Screening of the Catalysts for Acetic Acid Reforming

For selection of best suitable catalyst for steam reforming of acetic acid among the two prepared catalysts, they were tested at three different temperatures i.e. 600, 650 and 700 °C and at one atmospheric pressure, 3 gm of catalyst, 10 wt% acetic acid concentration and feed rate of 0.38ml/min.

From Table V, it is observed that CuZn catalyst resulted lowest % H_2 yield and % acetic acid conversion compared to the CuZnNi catalyst. This is due to the addition of Ni to CuZn catalyst. The role of Ni was to promote the scission of C-C bond present in acetic acid and it also favored steam reforming reaction at relatively low temperature. Cu helped in water gas shift reaction to increase the formation of H_2 from hydration carnon monoxide. Zn metal was used as promoter to accelerate the steam reforming reaction. The disadvantage of Ni was that it favored coke formation on the active sites of the catalyst. Coke formation on Ni catalyst was minimized due to the presence of calcium aluminate ($12CaO\text{-}7Al_2O_3$) phase in the support that provided large amount of oxygen in its lattice structure. CuZnNi was chosen as suitable catalyst for further study of different process parameters for steam reforming of acetic acid. The reforming activity of the CuZnNi catalyst was tested at different temperature, runtime, flow rate of feed and acetic acid concentration to evaluate the H_2 selectivity, and acetic acid conversion. These results are discussed below.

Downloaded by CORNELL UNIV on May 31, 2012 | http://pubs.acs.org
Publication Date (Web): January 20, 2012 | doi: 10.1021/bk-2012-1092.ch009

4.1. Effect of Temperature

Temperature is the one of the important process parameter for steam reforming reaction. The % yield of H_2 was measured as the function of the reformer temperature ranging from 600 to 750 °C for an acetic acid concentration of 10 wt%. The thermodynamic analysis of selectivity (CO, CO_2, CH_4) and yield (H_2) for steam reforming of acetic acid was also done at different temperature, pressure and concentration of acetic acid. From this analysis it was found that % H_2 yield increased with temperature and reached to maxima 96% at 680 °C, 1 atm pressure and 10 wt% acetic acid concentration. Further increased in temperature favoured methanation reaction which decreased the % H_2 yield. CO selectivity increased with temperature because of reverse water gas shift reaction, but CH_4 selectivity decreased with temperature as steam reforming of methanation suitable at high temperature (*17*).Selectivity of CO_2 decreased with increased in temperature. So at 680 °C selectivity of CO and CH_4 was minimum that is 9% and 0.01% respectively and selectivity of CO_2 was 90% for 1 atm pressure and 10 wt% acetic acid concentration. Therefore based on thermodynamics result it is found that at 680 °C the % H_2 yield obtained was maximum. As temperature increased beyond 680 °C, % H_2 yield decreased approximately 5-6% from the maximum value (which was obtained at 680 °C) and no change was observed up to 1000 °C. Figure 12 shows the variation of the % H_2 yield at different temperatures for the typical steam reforming condition. The % H_2 yield was approximately 68% at 600 °C and it increased to 94% as the temperature reached 700 °C. When the temperature was further increased to 750 °C the % H_2 yield decreased to 85 which is in agreement to the thermodynamics results.

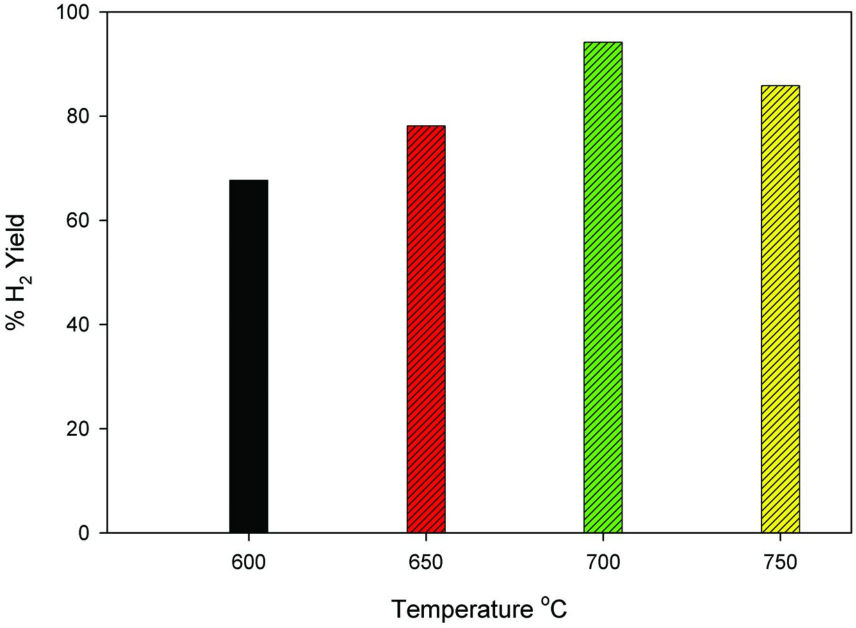

Figure 12. Effect of temperatures on % H_2 yield (Pressure,1 atm; acetic acid concentration, 10 wt % at a flow rate of 0.38 ml/min; 3 gm of catalyst).

Figure 13 shows the variation of % acetic acid conversion with temperature at one atmospheric pressure for 10 wt% acetic acid. As the temperature increased from 600 to 700 °C, acetic acid conversion increased from 70 to 98%. But at 750 °C, acetic acid conversion was only 96%. It can be observed that there is no significant effect of temperature on acetic acid conversion beyond 700 °C rather it decreased to 96% from 98%. Variation of % selectivity of gaseous products shown in Figure 14, is with temperature. From figure it can be observed that % H_2 selectivity increased from 38 to 67% as the temperature increased from 600 to 650 °C. At 750 °C % H_2 selectivity dropped to 60%. CO_2 selectivity increased from 78 to 91% as temperature increased from 600 to 700 °C. The reason behind this could be the presence of $12CaO\text{-}7Al_2O_3$ phases in the support which contains large amount of oxygen. CO selectivity decreased from 7 to 3% as temperature increased from 600 to 750 °C due to water gas shift reaction. CH_4 selectivity decreased from 15 to 6% as temperature increased from 600 to 750 °C due to steam reforming of methane reaction which was favourable at high temperature. Thermodynamically CO_2 and CH_4 selectivity decreased with temperature and results were according to the thermodynamic analysis. From this figure it can be seen that there is no such variation of selectivity of products at 700 °C and 750 °C.

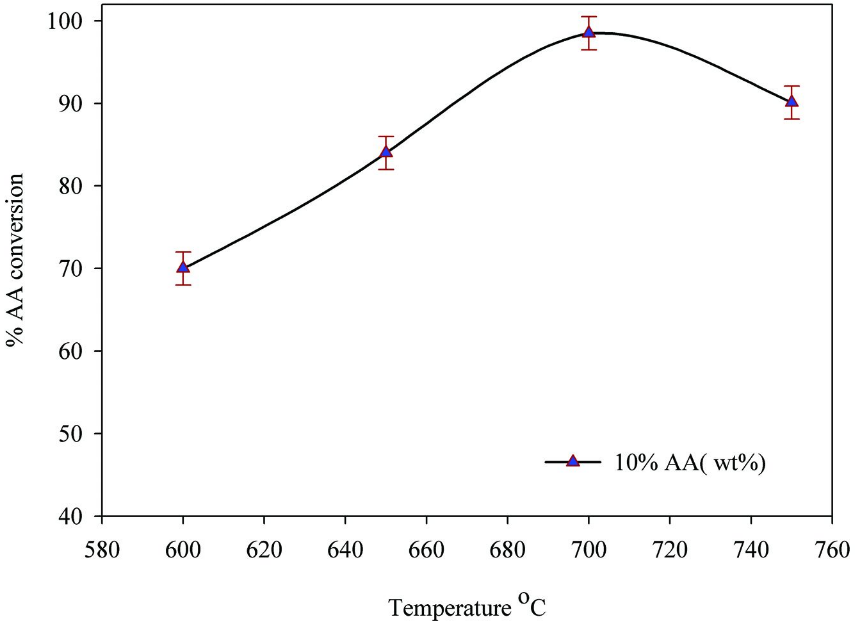

Figure 13. Effect of temperature on % acetic acid conversion (Pressure,1 atm; acetic acid concentration, 10 wt % at a flow rate of 0.38 ml/min; 3 gm of catalyst).

Downloaded by CORNELL UNIV on May 31, 2012 | http://pubs.acs.org
Publication Date (Web): January 20, 2012 | doi: 10.1021/bk-2012-1092.ch009

Downloaded by CORNELL UNIV on May 31, 2012 | http://pubs.acs.org
Publication Date (Web): January 20, 2012 | doi: 10.1021/bk-2012-1092.ch009

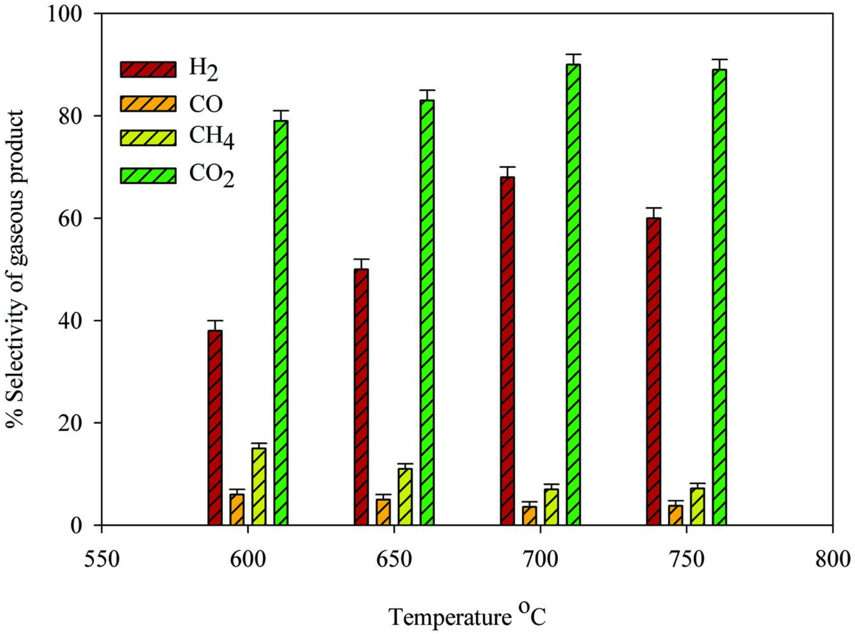

Figure 14. Effect of temperature on % selectivity of gaseous products (Pressure,1 atm; acetic acid concentration, 10 wt % at a flow rate of 0.38 ml/min; 3 gm of catalyst).

4.2. Effect of Time on Stream (Run Time) on Conversion and Yield

To investigate the effects of time on stream, experiments were carried out at four different temperatures ranging from 600 to 750 °C with feed containing 10 wt% of acetic acid. Duration of run time was kept at 11h. Figure 15 and Figure 16, show the % H_2 yield and % acetic acid conversion with the run time. As the temperature increased from 600 to 700 °C, % H_2 yield and acetic acid conversion increased and was maximum at approximately 700 °C. From run time it was concluded that deactivation rate of the catalyst is low at all temperatures indicating that active sites were not blocked due to the coke formation on the catalyst surface.

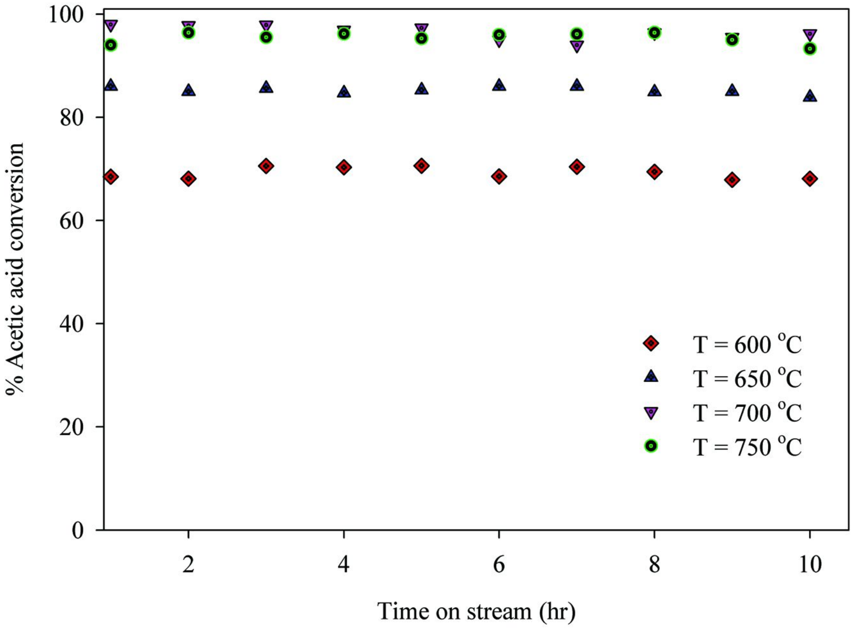

Figure 15. Effect of time on stream on % acetic acid conversion (Pressure,1 atm; acetic acid concentration, 10 wt % at a flow rate of 0.38 ml/min; 3 gm of catalyst).

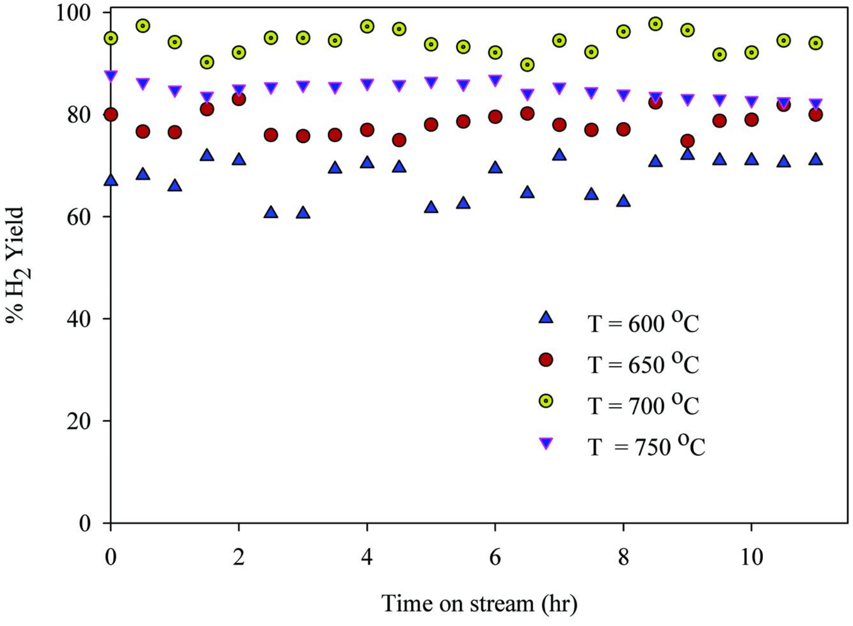

Figure 16. Effect of time on stream on % H_2 yield (Pressure,1 atm; acetic acid concentration, 10 wt % at a flow rate of 0.38 ml/min; 3 gm of catalyst).

Downloaded by CORNELL UNIV on May 31, 2012 | http://pubs.acs.org
Publication Date (Web): January 20, 2012 | doi: 10.1021/bk-2012-1092.ch009

4.3. Effect of Acetic Acid Concentration

Acetic acid concentration was varied by adding water. Figure 17 shows the variation of acetic acid concentration i.e. 10 wt% and 20 wt% on H_2 yield and acetic acid conversion. As concentration of acetic acid increased, there was significant decreased in H_2 yield i.e. from 95 to 58%. Therefore low acetic acid concentration with high water contain favoured the % H_2 yield. Also for acetic acid conversion decreased from 98 to 55% as acetic acid concentration was increased from 10 to 20%.

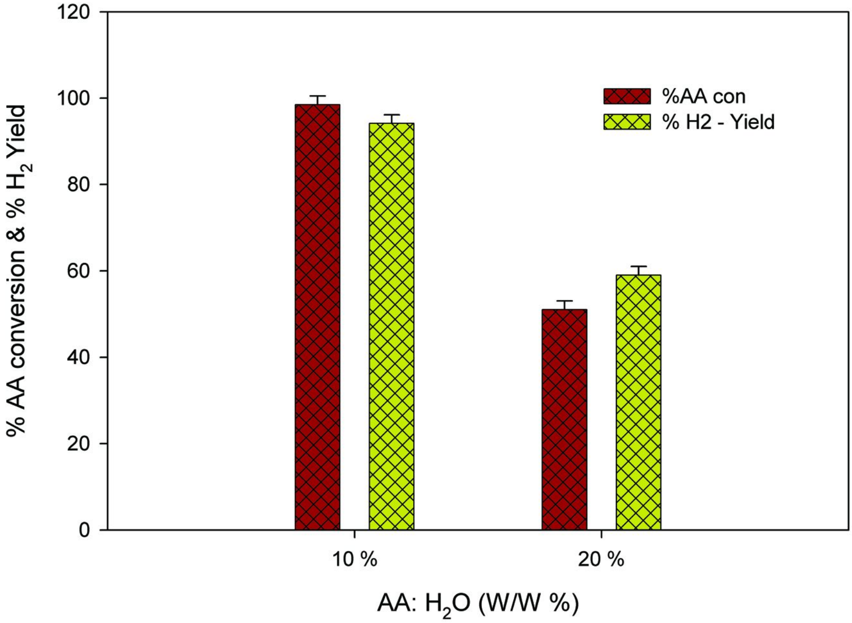

Figure 17. Effect of acetic acid concentration on % H_2 yield and % acetic acid conversion (Pressure,1 atm; acetic acid concentration, 10 wt % at a flow rate of 0.38 ml/min; 3 gm of catalyst, T = 700 °C).

4.4. Effect of Feed Flow Rate

Figure 18 shows the variation of acetic acid conversion with W/F_{A0} (weight of catalyst to molar flow rate of acetic acid) at three different temperatures. Maximum acetic acid conversion was obtained at 700 °C at lower initial acetic acid flowrate (high residence time). As flow rate increased from 0.38 to 1.3ml/min at 700 °C, acetic acid conversion decreased to 36%. At 650 °C, acetic acid conversion decreased from 85 to 30% as acetic acid flowrate increased from 0.38 to 1.3 ml/min. At 600 °C, acetic acid conversion decreased from 71% to 20% as acetic acid flowrate increased from 0.38 to 1.3 ml/min. When flow rate of acetic acid was

Downloaded by CORNELL UNIV on May 31, 2012 | http://pubs.acs.org
Publication Date (Web): January 20, 2012 | doi: 10.1021/bk-2012-1092.ch009

increased, the contact time between the reactant and catalyst bed decreased due to lower residence time, hence acetic acid conversion decreased with increase in acetic acid flow rate.

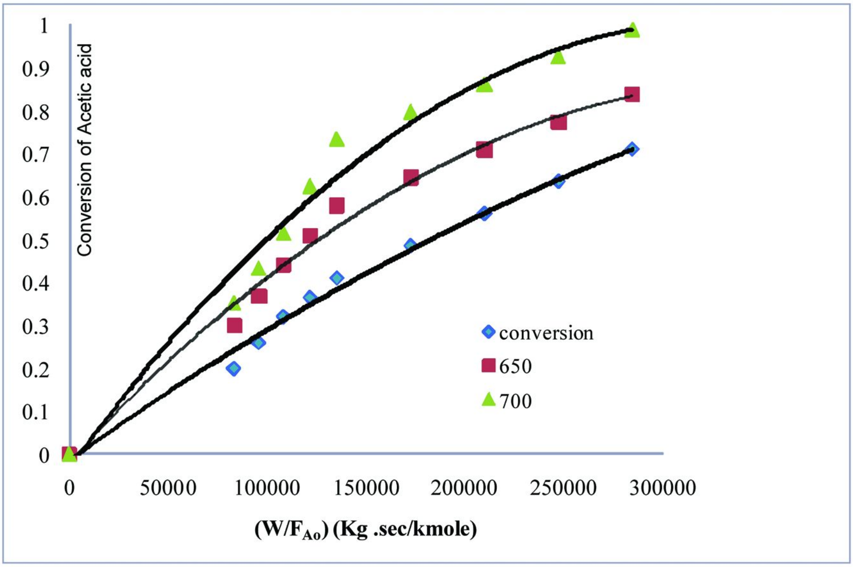

Figure 18. Effect of Wt. of catalyst/F_{A0} on % acetic acid conversion (Pressure, 1 atm; acetic acid concentration, 10 wt %; 3 gm of catalyst).

5. Conclusions

Steam reforming of a model biooil compound, acetic acid was investigated in a fixed bed in the presence of a CuZnNi catalyst using 10 wt% of acetic acid with water. Catalyst 10%Cu/1%Zn/7%Ni (CuZnNi) was prepared by wet impregnation method on a calcium aluminate support with $12CaO\text{-}7Al_2O_3$ as the major phase. Yield of H_2 over CuZnNi catalyst was maximum at 700 °C (94%), where as CH_4 and CO were in negligible quantity. It implies that steam reforming reaction was the dominant reaction than side reactions like methanation or reverse water gas shift reactions over CuZnNi. The effect of coking was negligible which can be further studied in next work plan and kinetic analysis of acetic acid is in progress. CuZnNi catalyst was found effective for hydrogen production with significant environmental benefits.

Acknowledgments

The authors wish to thank the Defence Research Development Organization (DRDO) Government of India, for providing financial support for this project.

Downloaded by CORNELL UNIV on May 31, 2012 | http://pubs.acs.org
Publication Date (Web): January 20, 2012 | doi: 10.1021/bk-2012-1092.ch009

References

1. Hou, T.; Yuan, L.; Ye, T.; Gong, L.; Tu, J.; Yamamoto, M.; Torimoto, Y.; Li, Q. *Int. J. Hydrogen Energy* **2009**, *34*, 9095–9107.
2. Marquevich, M.; Czernik, S.; Chornet, E.; Montane, D. *Energy Fuels* **1999**, *13* (6), 1160–6.
3. Hu, X.; Lu, G. *Appl. Catal., B* **2010**, *99*, 289–297.
4. Takanabe, K.; Aika, K.; Seshanb, K.; Lefferts, L. *J. Catal.* **2004**, *227*, 101–108.
5. Basagiannis, A. C.; Verykios, X. E. *Int. J. Hydrogen Energy* **2007**, *32*, 3343–3355.
6. Vagia, E. C.; Lemonidou, A. A. *Appl. Catal., A* **2008**, *351*, 111–121.
7. Wierczyn'ski, D. S.; Libs, S.; Courson, C.; Kiennemann, A. *Appl. Catal., B* **2007**, *74*, 211–222.
8. Dave, C. D.; Pant, K. K. *Renewable Energy* **2011**, *36*, 3195–3202.
9. Patel, S. S. Ph.D. Thesis, Indian Institute of Technology, Delhi, India, 2008.
10. Bevy, L. P. *Focus on Catalysis Research*; Nova Science Publishers, Inc.: Hauppauge, NY, 2006.
11. Alonso, D. S.; Juan-Juan, J.; Illa´n-Go´ mez, M. J.; Roma´ n-Martı´nez, M. C. *Appl. Catal., A* **2009**, *371*, 54–59.
12. Mohanty, P.; Pant, K. K.; Parikh, J.; Sharma, D. K. *Fuel Process. Technol.* **2011**, *92* (3), 600–608.
13. Vannice, M. A. *Kinetics of Catalytic Reactions*; Springer, New York, 2005; pp 23–33.
14. Zhang, J.; Wang, H.; Dalai, A. K. *Appl. Catal., A* **2008**, *339*, 121–129.
15. Guell, B. M.; Torres da Silva, I. M.; Lefferts, L. *Appl. Catal., B* **2009**, *88*, 59–65.
16. Segner, J.; Campbell, C. T.; Doyen, G.; Ertl, G. *Surf. Sci.* **1984**, *138*, 505.
17. Vagia, E. C.; Lemonidou, A. A. *Int. J. Hydrogen Energy* **2007**, *32*, 212–223.

Downloaded by CORNELL UNIV on May 31, 2012 | http://pubs.acs.org
Publication Date (Web): January 20, 2012 | doi: 10.1021/bk-2012-1092.ch009

Downloaded by UNIV OF GUELPH LIBRARY on May 31, 2012 | http://pubs.acs.org
Publication Date (Web): January 20, 2012 | doi: 10.1021/bk-2012-1092.ch010

Chapter 10

Influence of Different Supports on Hydrosulfurization and Hydrodenitrogenation of Heavy Gas Oils Using FeW Catalysts

Philip E. Boahene, Kapil Soni, Ajay. K. Dalai,* and J. Adjaye

Catalysis and Chemical Reaction Engineering Laboratories,
Department of Chemical Engineering, University of Saskatchewan,
Saskatoon, Saskatchewan, Canada S7N 5A9
***E-mail: ajay.dalai@usask.ca. Tel. +1-306-966-4771. Fax +1-306-966-4777.**

The application of Fe-W catalysts supported on commercial γ-Al_2O_3 and mesoporous SBA-15 supports have been investigated in the present study. Catalysts were prepared using the aqueous impregnation technique and thoroughly characterized by N_2 physisorption, powder XRD, FTIR-pyridine adsorption, ICP/MS, DRIFT spectroscopy of CO adsorption, TEM, HRTEM, and SEM. The nominal contents of Fe and W impregnated were 2 and 15 wt.%, respectively. At these metal loadings, small-angle X-ray scattering analysis revealed that the hexagonal structural ordering of the parent SBA-15 material remained intact after the impregnation procedure. Furthermore, powder XRD analysis evidenced homogeneous metal dispersion on both supports. Hydrotreating experiments were conducted in a downward flow micro-trickle bed reactor at temperature, pressure, liquid hourly space velocity (LHSV), and gas/oil ratio of 375-400°C, 8.8 MPa, $1h^{-1}$, and 600 mL/mL, respectively. The HDS and HDN catalytic activities were measured using heavy gas oil derived from Athabasca bitumen as feedstock. Catalytic activity results have been correlated with characterization data and are discussed on the basis of surface acidic groups (Lewis and Bronsted acidity) on these supports.

Keywords: HDS; HDN; FeW; SBA-15; HGO; FTIR-pyridine; Lewis; Bronsted

Downloaded by UNIV OF GUELPH LIBRARY on May 31, 2012 | http://pubs.acs.org
Publication Date (Web): January 20, 2012 | doi: 10.1021/bk-2012-1092.ch010

Introduction

The global energy consumption trends depict a scenario of great concern since oil inevitably remains the most important and abundant source of energy worldwide. The World Energy Outlook (WEO) presents a picture of higher future demands for oil, which envisages increase from 85 million bbl/day in 2008 to 106 million bbl/day by 2030 (*1*). As a result of the increasing demand of energy derived from conventional petroleum feedstocks to facilitate transportation and also to foster industrialization, energy resources other than the conventionally available have become the necessary option. With the anticipated decline in conventional oil production, unconventional oil such as oil shale and oil sands have become important resources if future global oil demands are to be met. However, in comparison, unconventional feedstocks are of degraded quality resulting in very high contents of pollutant heteroatomic species such as sulfur, nitrogen, and polyaromatic compounds (*2*). Meanwhile, more and more stringent environmental regulations that limit the amount of sulfur and aromatics in fuel are being put into effect to help curb emissions of noxious pollutants resulting from their combustion in internal combustion engines (*3*). As a result, the challenging task on refineries and researchers is to explore novel ideas and technologies of producing lighter hydrocarbons of high quality from crude feedstocks of unconventional origin. Moreover, due to difficulty in the treatment of these crude feedstocks, the catalysts and process technology employed are of crucial importance.

Catalytic hydrotreatment is the industrially recognized technology used over the years to reduce levels of sulfur, nitrogen and polyaromatic species in petroleum feedstocks so as to yield clean gasoline and diesel products. Hydrodesulfurization (HDS) and hydrodenitrogenation (HDN) of refinery streams are two of the most important reactions in petroleum refining processes for removing sulfur and nitrogen components in the feedstock using γ-Al_2O_3 supported MoS_2 or WS_2 active phase, promoted by 2-5wt. % Ni or Co (*4*). Generally, whereas NiMo sulfide catalysts are excellent in HDN and hydrogenation (HYD) reactions, CoMo sulfides are effective for HDS reactions (*5*). However, the removal of organic sulfur (HDS) and nitrogen (HDN) species from petroleum distillates represents a great challenge due to the competive inhibiting effects among these compounds during the high temperature (300-450 °C) and pressure (6-10 MPa) hydrotreatment reactions. As a result, the improvement of catalysts used therein have being of great interest to research scientists in the field of catalysis. Among the many ways explored to improve HDT catalysts performance, changing of the catalyst support is one of the most effective ways (*6–13*). Principally, the nature of the catalyst support plays a vital role to achieve high dispersion of metal nanoparticles and high levels of promotion of the active sulfided phases by the promoters.

Downloaded by UNIV OF GUELPH LIBRARY on May 31, 2012 | http://pubs.acs.org
Publication Date (Web): January 20, 2012 | doi: 10.1021/bk-2012-1092.ch010

Over the years, supports other than the commercial γ-Al_2O_3 studied for potential HDT applications include clays (*6*), carbon (*7*), oxides (*8*), mixed oxides (*9*), zeolites (*10*) and mesoporous materials like MCM-41 (*11*), HMS (*12*), SBA-15 (*13*), and KIT-6 (*14*). These studies on the influence of catalyst supports on hydrotreating functionalities using model compounds and real feedstocks are consistent with the fact that development of better HDT catalyst is predicated on the characteristic design of the catalyst support. It is known that by means of an adequate support design it is possible to increase significantly the HDS, HYD and HDN activities of hydrotreating catalysts via metal-support interactions (*5*). The support and catalyst may bond together in such a way to enhance the reactivity of the catalyst; however, the support may also be inactive and provide a high surface area substrate to increase the collisions of the reactants with the catalysts (*15*).

In an attempt to elucidate the role of catalyst supports via metal-support interactions, Topsoe et al. (*5*, *16*) concluded that the catalytic activity depends on the form, orientation and growth of MoS_2 species on the surface support. Moreover, Prins et al. (*17*) reported that the MoS_2 has a layered lattice with weak sulfur-sulfur interactions between sandwiched domains of MoS_2 layers on the surface support. Other authors (*18*, *19*) have found that the MoS_2 clusters are controlled by the surface orientation and crystalline phase of the alumina. However, W-based catalysts applied for hydrotreating processes are more useful especially when increased hydrogenation activity is required; like for HDN and dearomatization reactions (*20*). By means of XPS and electron microscopy, Breysse et al. (*21*) have observed tungsten atoms in WS_2-like form during the sulfidation studies of Ni-W/$A1_2O_3$ catalysts at 400 °C. They concluded that the HYD activity of biphenyl does not vary with the sulfidation temperature in the same way as HDS reactions; giving an indication of the existence of two different WS_2-like catalytic sites responsible for hydrogenolysis and hydrogenation reactions. Kameoka et al (*22*) also reported that Ni promoted W/$A1_2O_3$ catalysts showed a much higher HDN and HYD activities for the upgrading of coal-derived liquids as compared to Ni and Co-promoted W/$A1_2O_3$ catalytic systems. Even though very limited studies have been reported in the open literature using Fe as a promoter for HDT reactions, a study conducted by Linares et al. (*23*) on Fe and Ni promoted Mo/MCM-41 for the HDS of dibenzothiophene (DBT) and HYD of 2-methylnaphthalene reactions indicated that the incorporation of Fe possibly induced Bronsted acidity that enhanced the performance of such a catalyst. That notwithstanding, in the comparison of typical promoters employed in the preparation of HDT catalysts, it well known that the cost of Fe per kilogram is less expensive as compared to Ni and Co counterparts. Hence, one has to consider the economical benefits to be derived when Fe is used as a promoter in the hydrotreating catalyst system formulation.

Regarding applications of different support materials for HDT reactions, reported studies have attempted to correlate catalytic performance to physicochemical properties of the support. Some studies concentrated on the acidic and basic nature of the support and its effect on the nature of interaction with the active metal (*24–26*). Reported studies using model compounds as feedstocks are conclusive that an enhanced catalytic performance is attainable by changing the nature of the catalyst support. Due to their desirably attractive textural

Downloaded by UNIV OF GUELPH LIBRARY on May 31, 2012 | http://pubs.acs.org
Publication Date (Web): January 20, 2012 | doi: 10.1021/bk-2012-1092.ch010

properties, SBA-15 materials have been considered as potential catalyst supports for hydrotreating applications (*13*). In this regard, Dhar et al. (*27*) evaluated the catalytic functionalities of sulfided SBA-15-supported Mo, CoMo, and NiMo catalysts viz HDS and HYD reactions and found mesoporous SBA-15 support to be suitable for the catalysts studied. The catalytic activities of these catalysts were also compared with γ-Al_2O_3 and SiO_2-supported catalysts. Furthermore, the findings of Vradman et al. (*28*) also evidenced the excellent potential of high loading SBA-15-supported NiW catalysts for deep hydrotreatment of petroleum feedstocks, following their application in the HDS of dibenzothiophene and HYD of toluene. The activity of the optimized NiWS/SBA-15 catalyst was found to be 1.4 and 7.3 times higher, respectively, than that of a sulfided commercial CoMo/Al_2O_3. In our previous work on real feedstock (*29*), we investigated the effect of different pore diameter FeW/SBA-15 catalysts for the hydrotreatment of bitumen-derived heavy gas oil. It was concluded that the catalyst pore diameter plays a critical role in the mass transfer of reactant molecules to catalytic active sites and a pore diameter of 10 nm was found to be most effective in the HDS and HDN activities for the span of catalyst pore sizes studied.

In the present work, we investigated how the textural properties of different supports may affect the HDS and HDN activities of supported FeWS catalytic systems. A mesoporous SBA-15 supports of desirable textural properties was synthesized and thoroughly characterized by N_2-adsorption/desorption isotherms, small-angle X-ray scattering, scanning electron microscopy, transmission emission microscopy and high resolution transmission emission microscopy. For the purpose of supports comparison, a commercial γ-Al_2O_3 of similar average pore diameter as that of the large pore diameter SBA-15 material was used to benchmark performance at similar Fe and W metals loading.

2.0. Experimental

2.1. Synthesis of SBA-15 Supports

Mesoporous silica SBA-15 supports were synthesized in acidic medium using hexanes as micelle swelling agent. The two different SBA-15 materials obtained were prepared following the procedure described elsewhere (*30*, *31*). The triblock copolymer Pluronic P123 (M_{av} = 5800, $EO_{20}PO_{70}EO_{20}$, Aldrich) was used as the structure-directing agent (SDA) and tetraethyl orthosilicate (TEOS) as the silica source. The nominal molar ratio of the chemicals used in the synthesis mixture was 1.0 TEOS:0.0168 P123:4.02 C_6H_{14}:0.0295 NH_4F:4.42 HCl:186 H_2O. The two SBA-15 materials with different pore diameters were synthesized by varying the molar ratio of C_6H_{14} and NH_4F. In a typical synthesis procedure, 9.8 g P123 and 0.109 g NH_4F were dissolved in 335 mL of 1.3 M aqueous HCl solution at room temperature. This solution was transferred to a constant temperature bath (CTB) maintained at 15°C. After 1 h of mechanical stirring, a mixture of 20.8 g TEOS and 34.6 g C_6H_{14} was added. The reaction was allowed to proceed under mechanical agitation for 24 h in the CTB, after which the gel formed was isolated and subjected to hydrothermal treatment in a teflon-lined autoclave for 3 days. The solid product was filtered, washed with deionized water, and dried for 24 h at room temperature.

Downloaded by UNIV OF GUELPH LIBRARY on May 31, 2012 | http://pubs.acs.org
Publication Date (Web): January 20, 2012 | doi: 10.1021/bk-2012-1092.ch010

To remove the organic template, the sample was calcined at 550°C for 5 h using a heating rate of 2°C/min.

2.2. Preparation of SBA-15 and γ-Al_2O_3 Supported FeW Catalysts

SBA-15-supported FeW catalysts were prepared by the aqueous impregnation method. The dried and calcined SBA-15 supports were impregnated successively using aqueous solutions of ammonium metatungstate (AMT), $(NH_4)_6H_2W_{12}O_{40}$ (Fluka) and iron nitrate, Fe $(NO_3)_3.9H_2O$ (Aldrich) as W and Fe sources, respectively. Following each impregnation, the catalyst samples were dried at 120°C for 24 h. In a typical synthesis procedure, 0.514 g AMT was dissolved in 15 mL de-ionized water until a homogenous solution was formed. 2.55 g siliceous SBA-15 was added to this solution to obtain the required 15 wt.% W/SBA-15. This mixture was dried in an oven at 100°C for 3h. 2 wt. % Fe was also loaded by using same approach. The prepared low pore diameter (lpd) and high pore diameter (hpd) FeW/SBA-15 catalysts were subsequently calcined at 550 °C for 5h. These catalysts are designated as FeW/SBA-15 (lpd) and FeW/SBA-15 (hpd) with pore diameters 5 and 10 nm, respectively.

For the preparation of FeW/γ-Al_2O_3 catalyst, a similar successive incipient wetness impregnation technique was used to load 15 wt.% W and 2 wt.% Fe onto the extruded commercial γ-Al_2O_3 support. Prior to impregnation, the γ-Al_2O_3 support (obtained from Sud Chemical India Ltd., New Delhi) was dried at 120ºC overnight to remove any moisture. The procedure adapted for the impregnation of aqueous metal precursor solutions onto the commercial γ-Al_2O_3 support was similar to that described for the SBA-15 supports, only that 0.514g AMT was dissolved in 4.3 mL (i.e. total pore volume of γ-Al_2O_3 support used is 0.8623 mL/g) in deionized water for the impregnation of 5g γ-Al_2O_3 support. Following the final impregnation of the Fe precursor, the catalyst was dried overnight at 120ºC and then calcined at 500°C for 4 h. All the prepared catalysts were characterized by N_2-adsorption/desorption, inductively coupled plasma (ICP), powder X-ray diffraction (XRD), CO uptake and other characterization techniques.

2.3. Characterization

The crystal structures of calcined FeW/SBA-15 catalysts were determined using a Bruker Smart equipment with step sizes of 0.02° in 2θ by the small-angle X-ray scattering technique. Diffraction patterns were recorded with a Bruker Smart 6000 CCD detector on a 3-circle D8 goniometer using a Rigaku RU 200 Cu rotating anode generator fitted with parallel focusing cross-coupled mirrors and a 0.5 mm pinhole collimator. Data was obtained using a still data collection (Bruker Software: SMART) with an exposure time of 300 seconds in the 0 to 10.0° range. Broad angle XRD patterns of the SBA-15 and γ-Al_2O_3 supported catalysts were recorded on a Rigaku diffractometer using Cu Kα radiation.

The characterization of textural properties was performed with a Micromeritics ASAP 2000 analyzer at liquid nitrogen temperature of 77 K. The fully computerized analysis allowed the estimation of the specific surface areas of the samples, through the Brunauer–Emmett–Teller (BET) method in the standard pressure range 0.05-0.30 P/P_o. Prior to sample analysis, the catalyst was degassed in vacuum at 200°C until the static pressure remained less than $6.6x10^{-4}$ Pa. The value of 0.1620 nm^2 was taken for the cross-section of the physically adsorbed N_2 molecule. The pore diameter and pore size distributions were calculated from the adsorption and desorption branches of the isotherms using the Barrett-Joyner-Halenda (BJH) method. The mesopore volume was determined from the N_2 adsorbed at a $P/P_0 = 0.4$. The total pore volume was calculated from the amount of nitrogen adsorbed at $P/P_0 = 0.95$, assuming that adsorption on the external surface was negligible compared with adsorption in pores. In all cases, correlation coefficients above 0.999 were obtained.

The morphology of the oxidic FeW/SBA-15 catalysts was ascertained by the transmission electron microscopy (TEM) obtained with a Tecnai F20 under an accelerating voltage of 200 kV. The powder samples were grounded smoothly in an agate mortar and dispersed in heptane in an ultrasonic bath for several minutes. A few drops were then deposited on 200 mesh Cu grids covered with a holey carbon film. The electron micrographs were recorded in electron negative films and in a digital PC system attached to the electron microscope. Scanning electron microscopy (SEM) micrographs were observed on a Hitachi-S4700 microscope.

Diffuse reflectance infrared fourier transform spectroscopy (DRIFTS) experiments were performed using a Perkin Elmer Spectrum GX instrument equipped with DTGS detector and KBr beam splitter. Carbon monoxide (CO) was used as a probe molecule to determine the number of accessible surface metal atoms present on the sulfided catalysts. Approximately 10 mg of powdered catalyst sample was loaded into a sample cup inside a Spectrotech diffuse reflectance in situ cell equipped with ZnSe windows. A mounted thermocouple apparatus allowed the direct measurement of sample surface temperature. Spectra for each experiment were averaged over 64 scans in the region 4000-1000 cm^{-1} with a nominal 4 cm^{-1} resolution. Prior to the CO adsorption, the catalyst was in situ sulfided in the Spectrotech diffuse reflectance cell using 10% (v/v) H_2S/H_2 (50 cm^3/min) at 400 °C for 2 h. At this temperature, the flow was switched to helium (He) at a flow rate of 50 mL/min and the temperature decreased to 30°C. The background spectrum was then recorded. The adsorption process was carried out at 30°C by introducing CO (30 mL/min) into the system for 30 min. After adsorption, the system was subsequently purged with He for 30 min at a flow rate of 50 cm^3/min. Spectra were then recorded under He flow. The background spectrum was subtracted from the post adsorption spectra.

The carbon monoxide uptake by sulfided catalysts was also measured using the Micromeritics ASAP 2000 instrument. Prior to the CO chemisorption measurement, 0.2 g of sample was in situ sulfided using 10 mol. % H_2S in H_2 at 400°C for 4 h, and then the sample was evacuated at 120°C until the static pressure remained less than 6.6×10^{-4} Pa. The chemisorption was performed by passing pulses of CO over the sample to measure the total gas uptake at 35°C.

Inductive coupled plasma-mass spectroscopic (ICP/MS) analysis was utilized to quantify the metal composition in the catalysts. Approximately 0.05 g of the catalyst sample was dissolved in hydrofluoric acid (48-51%) at a temperature of 100-150°C for 3 days. Following cooling to room temperature, samples were further dissolved in concentrated HNO_3 to ensure the complete dissolution of the

Downloaded by UNIV OF GUELPH LIBRARY on May 31, 2012 | http://pubs.acs.org
Publication Date (Web): January 20, 2012 | doi: 10.1021/bk-2012-1092.ch010

Downloaded by UNIV OF GUELPH LIBRARY on May 31, 2012 | http://pubs.acs.org
Publication Date (Web): January 20, 2012 | doi: 10.1021/bk-2012-1092.ch010

metals. The final solution was prepared using 0.2 N HNO_3 and analyzed with a mass spectrometer. Furthermore, an energy-dispersive X-Ray (EDX) analysis was also used for local compositional analysis using a system attached to the electron microscope which was operated at 25 kV. The chemical composition determination was based on the average analytical data of individual particles.

2.4. Catalytic Activity

The HDN and HDS activities of all the prepared FeW supported catalysts were tested using HGO derived from Athabasca bitumen. The feed stock was supplied by Syncrude Canada Ltd and its properties can be found in Table 1.

Table 1. Characteristics of Heavy Gas Oil derived from Athabasca bitumen

Characteristic	*Heavy Gas Oil*
Nitrogen (wppm)	3615
Sulfur (wppm)	42,302
Density (g/ml)	0.99
Aromatic content (wt.%)	31.4
Asphaltene content (wt. %)	1.55
Boiling point distribution	
IBP (°C)	210.8
FBP (°C)	597.3
Boiling range (°C)	***(wt%)***
IBP–205 (Gasoline)	0
205–260 (Kerosene)	1
260–315 (Light gas oil)	5
315–425 (Heavy gas oil)	39
425–600 (Vacuum gas oil)	55

Hydrotreating experiments were conducted in a downward flow micro-trickle bed reactor system (10 mm ID; 285 mm length) using 5 mL of catalyst under typical industrial process conditions. This reactor system is a high pressure and temperature reaction set-up whose operation mimics industrial hydrotreaters. The set-up consists of liquid and gas feeding sections, a high pressure reactor, a heater with temperature controller, a scrubber for removing the ammonium sulfide from the reaction products, and a high pressure gas-liquid separator. Details of catalyst loading into the reactor are described elsewhere (*32*, *33*). Typically, the catalyst

Downloaded by UNIV OF GUELPH LIBRARY on May 31, 2012 | http://pubs.acs.org
Publication Date (Web): January 20, 2012 | doi: 10.1021/bk-2012-1092.ch010

bed was packed using 5 mL of catalyst (~1.5 g) and silicon carbide (SiC) particles as diluents. Dilution of the catalyst bed with SiC particles was necessary to enhance the heat and mass transfer along the length of the reactor. SiC particle size selection was based on earlier published work by Bej et al. (*33*).

Activation of the oxidic FeW catalysts was carried out for a period of 48 h at temperatures of 193°C for 24 h and then 343°C for another 24 h during a sulfidation step. In this procedure, 2.9 vol. % butanethiol was used as a sulfiding agent in straight run gas oil (VOLTESSO 35). An initial catalyst pre-wetting protocol was necessary prior to catalytic activity study. This procedure was carried out by pumping ~100 mL of the sulfiding solution at a high flow rate of 2.5 mL/min into the reactor. The high oil flow rate was subsequently adjusted to 5 mL/h and maintained to obtain a liquid hourly space velocity (LHSV) of 1 h^{-1}. Furthermore, the hydrogen gas flow was operated at a rate that corresponds to a gas/oil ratio of 600 mL/mL.

To achieve steady state catalytic activity, the catalyst was first precoked (stabilized) at temperature and pressure of 375°C and 8.8 MPa, respectively, for 5 days with the real feed (HGO) at a flow rate of 5 mL/h. After precoking, HDN and HDS activity studies were conducted for 3 days each at temperatures of 375°C, 388°C, and 400°C. The pressure, gas/oil ratio and LHSV were maintained constant at 8.8 MPa, 600 mL/mL and 1 h^{-1}, respectively. The liquid hydrotreated products collected after 24 h were purged with nitrogen gas to remove dissolved ammonia and hydrogen sulfide gases. A transient period of 24 h was allowed within experiments whenever a process condition was to be studied; and liquid products taken within these transient periods were not analyzed. Samples were analyzed for total nitrogen and sulfur contents using an Antek 9000 NS analyzer. Total nitrogen content of the liquid product was measured by the combustion/chemiluminence technique following ASTM D4629 method and the sulfur content was measured using the combustion/fluorescence technique following ASTM 5463 method. The instrumental error in N and S analysis was 3%.

3.0. Results and Discussion

3.1. Support and Catalyst Characterizations

3.1.1. Elemental Analysis

All calcined supported FeW catalysts were analyzed for their respective elemental compositions. Fe and W were identified using inductively coupled plasma - mass spectrometer (ICPMS). The results of ICP-MS of FeW/SBA-15 and FeW/γ-Al_2O_3 with targeted compositions are presented in Table 2. The elemental compositions obtained from ICP-MS and EDX correlate well with each other, as well as with targeted values.

Downloaded by UNIV OF GUELPH LIBRARY on May 31, 2012 | http://pubs.acs.org
Publication Date (Web): January 20, 2012 | doi: 10.1021/bk-2012-1092.ch010

Table 2. Elemental Composition, CO uptake, and HDS/HDN steady-state activities of SBA-15 supported FeW catalysts with different pore diameter at various reaction temperatures (Catalyst = 5 cm^3, P = 8.8 MPa, LHSV = 1 h^{-1} and H_2/oil ratio = 600 (v/v))

Sample ID	*Composition*		*CO uptake (μmol/g)*	*Sulfur/nitrogen removal at each reaction temperature (wt %)*					
				375°C		*388°C*		*400°C*	
	Fe (wt %)	*W (wt %)*		*S*	*N*	*S*	*N*	*S*	*N*
FeW/ SBA-15 (lpd)	2* (1.86)	15* (14.28)	14	39	11	50	13	59	21
FeW/ SBA-15 (hpd)	2* (1.91)	15* (14.07)	25	45	17	53	17	66	33
FeW/γ-Al_2O_3	2* (1.87)	15* (13.89)	39	69	26	80	32	89	49

* Targeted.

3.1.2. Small-Angle X-ray Scattering Analysis

The small-angle X-ray scattering (SAXS) patterns of FeW/SBA-15 materials in their oxide form are presented in Figure 1. The SAXS measurements were carried out to ascertain the mesoporous structure of the FeW/SBA-15 catalysts investigated. The crystalline phases of the calcined catalysts can also be obtained by this technique.

The SAXS patterns of Fe-W catalysts supported on SBA-15 of different pore diameters are reported in our previous work (*29*) for 2θ values of 0.5-10°. The optimum pore diameter catalyst reported from this work (*31*) was selected and compared with the γ-Al_2O_3 supported FeW catalyst at similar metal loadings of 2 wt.% Fe and 15 wt.% W, respectively. As shown in Figure 1, the small-angle XRD pattern of these catalysts exhibited three well-resolved peaks, characteristic of pure SBA-15 materials (*34*). These XRD peaks are indexable as (d_{100}), (d_{110}) and (d_{200}) reflections associated with the p6mm symmetry of the hexagonal ordered pore structure. This is indicative of the fact that the hexagonal structure order of the material was not significantly affected after loading of 2 wt.% Fe and 15 wt.% W on the support. However, minor changes are observable with peaks corresponding to d_{110} and d_{200} planes; giving indication of a slight structural change of the siliceous SBA-15 material as a result of metals loading.

For the mesoporous FeW/SBA-15 catalysts, estimation of the unit-cell parameter (a_0) from the position of the (d_{100}) diffraction line was evaluated using the equation $a_0 = d_{100} \times 2 / \sqrt{3}$; and given in Table 3.

Downloaded by UNIV OF GUELPH LIBRARY on May 31, 2012 | http://pubs.acs.org
Publication Date (Web): January 20, 2012 | doi: 10.1021/bk-2012-1092.ch010

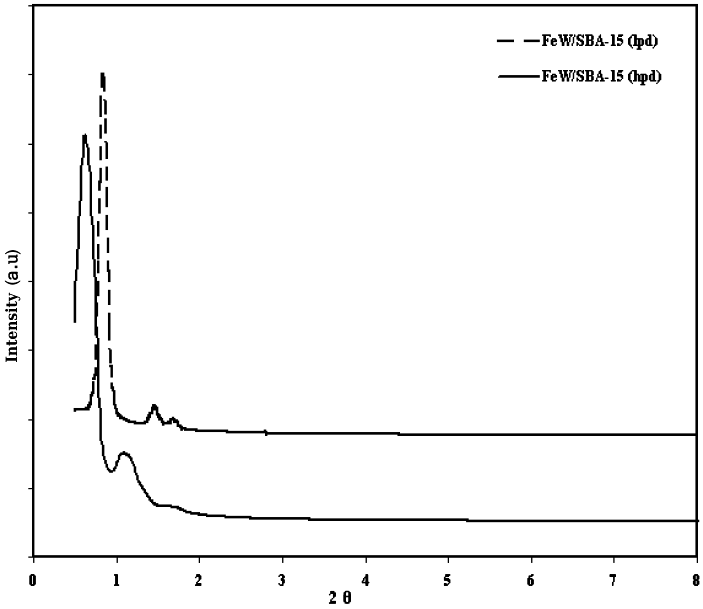

Figure 1. Small-angle X-ray scattering patterns of FeW/SBA-15 (lpd) and FeW/SBA-15 (hpd) catalysts.

Pore wall thickness (φ) was assessed by subtracting D_{ads} from the unit-cell parameter (a_0), which corresponds to the distance between centers of adjacent mesopores. It is noteworthy that the pore wall thickness of the pure SBA-15 support is similar to that of the FeW/SBA-15 catalyst; indicating that anchoring of metal species via surface silanol groups during the impregnation of metal precursors did not significantly alter the pore wall thickness of the pristine SBA-15 material. Also, the effect of swelling agent on the SBA-15 materials produced is quite evident by noticing the observable changes 2θ values. From Figure 1, it can be seen that the diffraction peak of SBA-15 support synthesized with swelling agent is shifted to lower 2θ values as compared to support synthesized without the incorporation of swelling agent. This is indicative of an increase in unit-cell size (a_0), which corresponds to increase in pore diameter of the siliceous SBA-15 materials (*35*) as shown in Table 3.

3.1.3. Wide-Angle X-ray Diffraction

The wide angle X-ray diffraction patterns of the pristine SBA-15 support and Fe-W/SBA-15 catalysts are shown in Figure 2 for 2θ values in the interval of 10° to 80°.

Downloaded by UNIV OF GUELPH LIBRARY on May 31, 2012 | http://pubs.acs.org
Publication Date (Web): January 20, 2012 | doi: 10.1021/bk-2012-1092.ch010

Table 3. Physical properties of SBA-15 (lpd and hpd) and γ-Al_2O_3-supported FeW catalysts determined from N_2 sorption and XRD analyses

Sample ID	S_{BET} $(m^2/g)_{Sup}$	S_{BET} $(m^2/g)_{Cat}$	NS_{BET}	*PV* (cm^3/g)	PD_{ads} *(nm)*	d_{100} *(nm)*	a_0 *(nm)*	φ *(nm)*
FeW/ SBA-15 (lpd)	867	642	0.89	0.66	5.1	10.3	11.8	6.7
FeW/ SBA-15 (hpd)	636	498	0.94	0.89	10.1	12.4	14.4	4.3
FeW/γ-Al_2O_3	276	154	0.67	0.42	10.8	-	-	-

S_{BET}, specific surface area calculated by the BET method. **NS_{BET}** (Normalized surface area) were calculated by using the equation, NS_{BET} = (S_{BET} of the catalysts)/(1-x). S_{BET} of the support **PV**, pore volume determined by nitrogen adsorption at a relative pressure of 0.98. **PD_{ads}**, mesopore diameter corresponding to the maximum of the pore size distribution obtained from the adsorption isotherm by the BJH method. **a_0**, unit-cell parameter determined from the position of the (1 0 0) diffraction line as $a_0 = d_{100} \times 2 / \sqrt{3}$ **φ**, pore wall thickness calculated as $\varphi = a_0 - D_{ads}$.

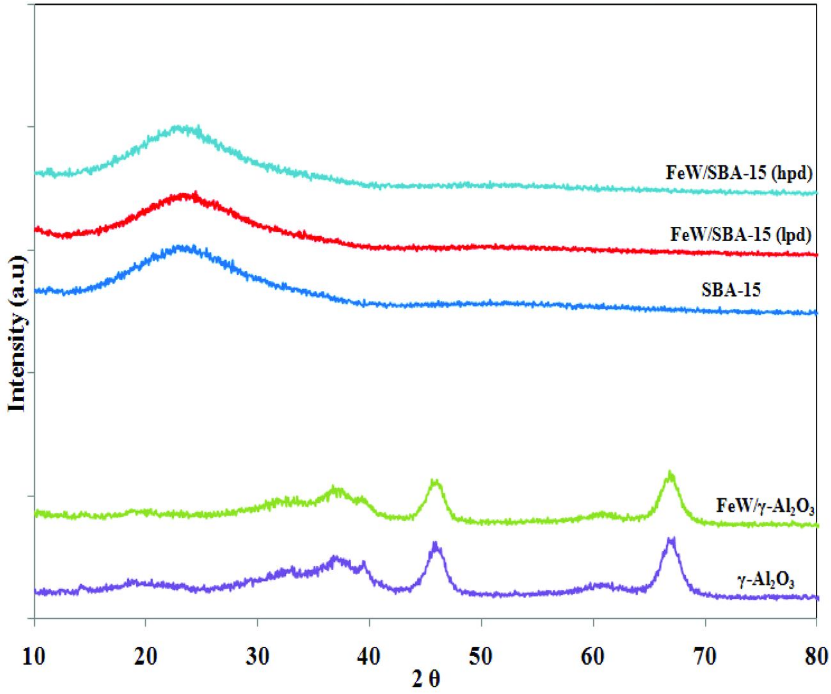

Figure 2. Wide-angle X-ray diffraction patterns of FeW/SBA-15 and FeW/γ-Al_2O_3 catalysts.

Also shown in Figure 2 is the profile for FeW/γ-Al_2O_3 catalyst of similar metals loading (2 wt.% Fe and 15 wt.% W). At this metal loading, crystalline phases were not detectable by X-ray signals; which is indicative of the fact that either metal species were homogeneously dispersed on the support or their compositions were below the detection limit of the X-ray signals. The absence of XRD signals in wide angle region indicates that the particle size of metals is below the coherence length of X-ray scattering i.e., smaller than ~4 nm; suggesting that metals are well dispersed on the support due to the absence of any crystalline oxidic phase. However, a characteristic single broad hump centered at 2θ values of 15-40º is observable for all the SBA-15 materials analyzed, which is due to the siliceous nature of these materials (*36*). The high surface area of silica supports favor dispersion of the active phases. Obviously, the relatively higher surface area of the SBA-15 support (636 m^2/g) may have played a significant role by enhancing great dispersion of catalytic phases. That notwithstanding, at this metal loading, the moderately high surface area of the γ-Al_2O_3 support (276 m^2/g) investigated was sufficiently high enough for the homogeneous distribution of dispersed oxidic metal phases formed as a result of catalyst calcination in air flow.

3.1.4. N_2 Adsorption-Desorption Isotherms Measurement

Measurement of textural properties of materials can be examined by N_2 adsorption-desorption isotherms at liquid nitrogen temperature of -196°C. Figure 3A shows the nitrogen adsorption-desorption isotherms for the pure SBA-15 materials and the supported FeW catalysts.

For the mesoporous SBA-15 materials, the textural and structural characteristics (surface area S_{BET}, total pore volume V_P, pore diameter D_P, unit-cell parameter a_0 and pore wall thickness) have been provided in Table 3.

All catalysts exhibited the type IV isotherm with H1 hysteresis loop, which is characteristic of a well-formed SBA-15 material. The shape of the loop is unchanged after the Fe and W metals loading indicating that support and catalysts exhibit uniform textural porosity, which is also in agreement with XRD results. The height of the hysteresis loop is decreased after metals loading into SBA-15 due to a decreased pore volume indicating the introduction of metal species within the mesopores of the support. Moreover, the surface area and pore volume of the SBA-15 decreased significantly after metal loading. For the SBA-15 support synthesized with swelling agent, one could observe a decrease in the pore wall thickness (d) with increasing unit cell parameter (a_o). A decrease in the pore wall thickness suggests an increase in the pore diameter of the support due to the incorporation of hexane into the synthesis medium (*35*). As can be seen from Table 3, the calculated pore wall is thick enough to survive pore collapse under the rather severe hydrotreating reaction conditions. The results from N_2 adsorption-desorption analysis correlates well with that obtained from XRD analysis. The pore size distributions of the pure SBA-15 support and FeW/SBA-15 catalysts are given in Figure 3B.

Downloaded by UNIV OF GUELPH LIBRARY on May 31, 2012 | http://pubs.acs.org
Publication Date (Web): January 20, 2012 | doi: 10.1021/bk-2012-1092.ch010

Downloaded by UNIV OF GUELPH LIBRARY on May 31, 2012 | http://pubs.acs.org
Publication Date (Web): January 20, 2012 | doi: 10.1021/bk-2012-1092.ch010

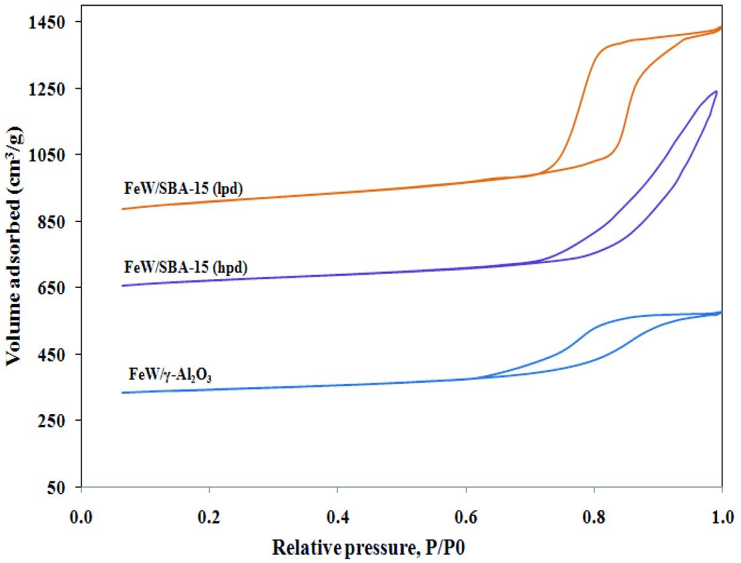

Figure 3A. N_2-adsorption isotherms of FeW/SBA-15(lpd), FeW/SBA-15(hpd), and FeW/γ-Al_2O_3.

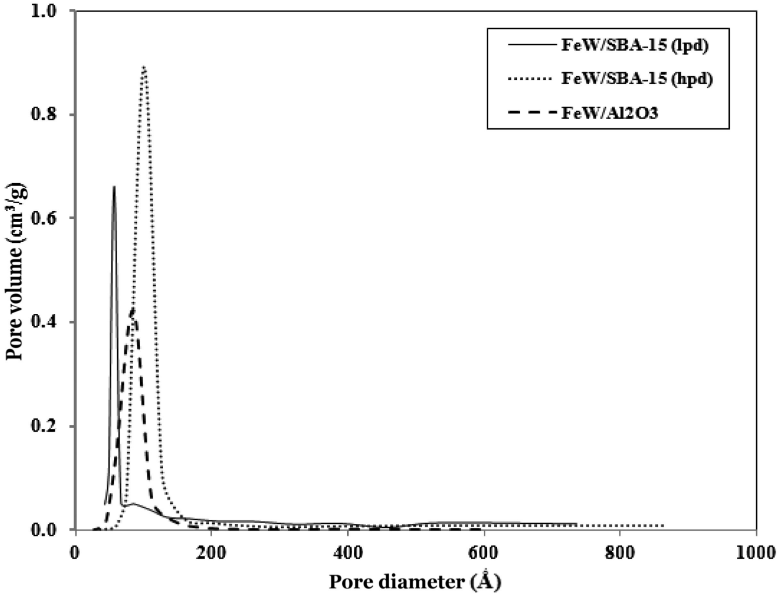

Figure 3B. Pore size distribution of FeW/SBA-15(lpd), FeW/SBA-15(hpd), and FeW/γ-Al_2O_3.

Downloaded by UNIV OF GUELPH LIBRARY on May 31, 2012 | http://pubs.acs.org
Publication Date (Web): January 20, 2012 | doi: 10.1021/bk-2012-1092.ch010

The sharpness of the desorption branches is indicative of the narrow mesopore size distribution. In the case of the γ-Al_2O_3 support and supported FeW catalyst, the pore size distribution profile as can be seen from Figure 3B are comparatively broader, with other smaller pore channels in the lower pore regions. This characteristic broad pore size distribution contributes to the prevalent diffusional limitation experienced by γ-Al_2O_3 supports during the hydroprocessing of feedstocks of heavier hydrocarbon fractions (*37*). It is noteworthy to mention that for an enhanced hydrotreating activity for heavier feedstock applications, the pore size distribution of the catalyst support should be narrow and the pore diameter must be large enough to overcome most diffusional restrictions (*38*). Such desirably high specific surface area, large pore diameter and narrow pore size distribution were characteristic of the all SBA-15 materials prepared. The presence of dispersed metal species inside the mesopores of the SBA-15 support was confirmed by estimating the normalized S_{BET} values of the catalyst using an equation proposed by Vradman et al. (*39*):

$$NS_{BET} = (S_{BET}\text{ of the catalysts})/\ (1\text{-}x).\ S_{BET}\text{ of the support}$$

where NS_{BET} is the normalized S_{BET} and x is the weight fraction of the phases. The values of normalized NS_{BET} are given in Table 3. As a measure of the extent of pore blockage experienced by the catalyst support during the metals loading procedure, values of NS_{BET} of catalysts close to unity suggest less pore blockage. For instance, NS_{BET} of FeW/SBA-15 (lpd) was computed to be 0.89, which is < 1; indicating that the introduction of the FeO and WO_3 nanoparticles caused a minimal reduction in pore volume resulting in an insignificant decrease in the normalized surface area. Furthermore, these results also give an indication that impregnation of metal species on a catalyst support plays a vital role in the overall catalytic surface area required for a given chemical reaction.

3.1.5. TEM, HRTEM, and SEM Analyses

Figure 4 presents the morphological features of calcined FeW/SBA-15 catalysts. The micrograph for the FeW/SBA-15 (hpd) catalysts is obtained by from our previous work with this catalyst (*29*).

A well-ordered cylindrical channel-like pore morphology with a 2D hexagonal (p6mm) mesostructure can be seen in all materials prepared (*35*). The TEM images provide a pictorial evidence of an ordered meso-structured SBA-15 silicate material. These images confirmed that the mesoporous and well-ordered structure of the SBA-15 was preserved even after metals loading. The absence of patches of metal aggregates or agglomerates suggests a homogeneous dispersion of metal nanocrystallites on the supports as confirmed by XRD results of samples analyzed. The distance between two consecutive centers of hexagonal pores estimated from the TEM images are in ranges of 5 to 6 and 10 to 11 nm for the low and high-pore diameter catalysts, respectively, which are consistent with N2 physisorption results.

Downloaded by UNIV OF GUELPH LIBRARY on May 31, 2012 | http://pubs.acs.org
Publication Date (Web): January 20, 2012 | doi: 10.1021/bk-2012-1092.ch010

HRTEM analyses performed on sulfided FeW/SBA-15 and FeW/γ-Al_2O_3 catalyst samples are shown in Figure 5, respectively. Layered structures of the WS_2-like slabs are observable. Random sampling of various unit square regions of respective figures yielded in an estimated average slab height of 2 nm. Such measurements were repeated several times on distinct catalyst samples, giving an indication of the presence of WS_2 phase on all catalyst samples investigated.

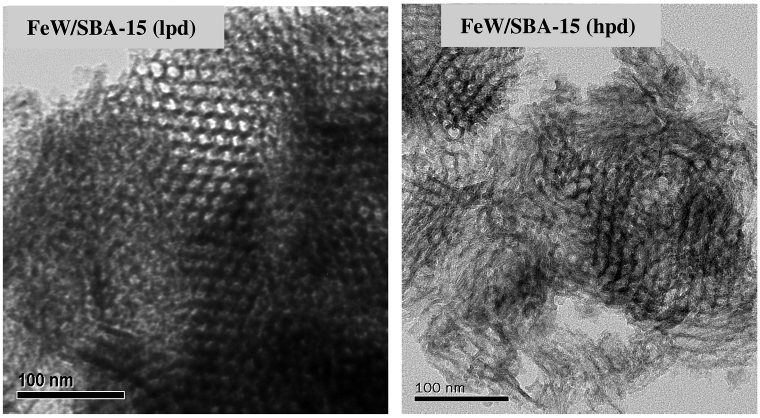

Figure 4. Transmission electron micrographs of FeW/SBA-15 (lpd) and FeW/SBA-15 (hpd) catalysts.

For the SBA-15 supported FeWS catalysts, average slab length and stacking layers of 3 to 4 nm and 2, respectively, were found as opposed to similar values of 4 to 5 nm and about 3 to 4 stacking layers for the sulfided FeW/γ-Al_2O_3 catalyst. This variation in slab length and layers of WS_2 stacks formed on the different supports could be attributed to their respective surface chemical properties, which has a direct interplay on metal-support interactions. One can attribute the rather weak interaction between the sulfide species and the SBA-15 support to the relatively low number of Si-OH groups and low support acidity (*40*) as compared to the γ-Al_2O_3 counterpart. This probably might have contributed to the relatively poor dispersion of the active WS_2 phase generated as a result of catalyst sulfidation. Daage et al. (*41*) concluded from their study that the morphology of the MoS_2 or WS_2 crystal structure formed during catalyst sulfidation affects the reaction pathway selectivity (hydrogenation versus direct desulfurization route) of the overall HDT reaction. The selectivity of the HDT process is dependent on the stack height of the metal sulfide slabs of a given diameter *d*, which is attainable by varying the ratio of rim sites to edge sites. The theory suggests the rim sites are active in hydrogenation and C-S bond breaking, while edge sites participate only in C-S bond breaking. The basal plane consists entirely of sulfur atoms and is considered dormant (*41*). On a study conducted by Topsøe et al. (*42*) using a commercial CoMo/Al_2O_3 catalysts, the authors proposed two main structures for the CoMoS phase present on CoMo/Al_2O_3 namely: type I phase (i.e. CoMoS I) and type II phase (CoMoS II). The type I is mostly thought to be incompletely sulfided and to consist mainly of MoS_2 monolayers interacting with the support via Mo-O-Al bonds. CoMoS II phases are thought to be fully sulfided and consist often of stacked MoS_2 particles that are only weakly interacting with the support via van der Waals interactions.

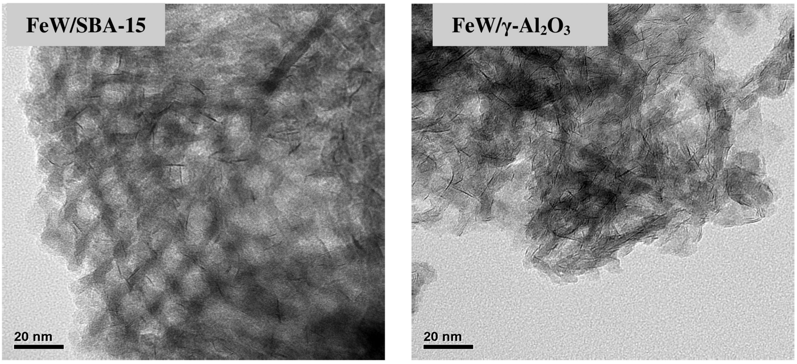

Figure 5. High resolution transmission electron micrographs of FeW/SBA-15 and FeW/γ-Al_2O_3 catalysts.

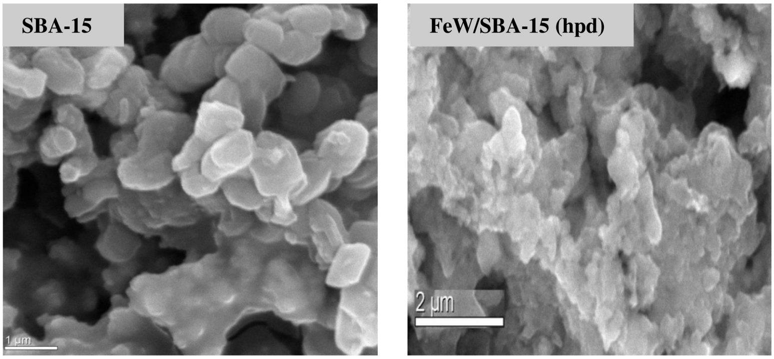

Figure 6. Scanning electron micrographs of SBA-15 and FeW/SBA-15 (hpd).

In the case of FeW/γ-Al_2O_3 catalyst system, the greater number of stacks formed may be considered desirable for the creation of the type-II Fe-promoted WS_2 phase, resulting in weaker interaction between the interface of the γ-Al_2O_3 support and the topmost layers in the stack. It is noteworthy that the topmost layers are more facile for the HYD and HDS reactions; thus, the farther away a layer in a stack is located from the support, the easier will it be made available during the HDT reaction, since slabs formed close to the support surface are literally fused to the support; rendering it inactive. Thus, one can concluded that albeit the high dispersion provided by the SBA-15 support by reason of its high surface

Downloaded by UNIV OF GUELPH LIBRARY on May 31, 2012 | http://pubs.acs.org
Publication Date (Web): January 20, 2012 | doi: 10.1021/bk-2012-1092.ch010

Downloaded by UNIV OF GUELPH LIBRARY on May 31, 2012 | http://pubs.acs.org
Publication Date (Web): January 20, 2012 | doi: 10.1021/bk-2012-1092.ch010

area, the relatively stronger interaction between Fe-promoted WS_2 layers distance away from the support made the strongly bounded sulfur difficult to participate in the HDS; thus, explaining the lower HDT activities observed for the FeW/SBA-15 catalyst.

The SEM images of the pure SBA-15 support and supported FeW catalysts showed that all samples contained fibre-like particles of several tens of micrometers in length (Figure 6). Similar morphology of mesoporous SBA-15 materials has been reported by other researchers (*43*).

3.1.6. DRIFT Spectroscopy for CO Adsorption

A well-known fact for heterogeneous catalytic reactions is that the nature of the surface sites governs the dispersion of the supported active phases (*44*). Thus, the nature of active species present on the sulfided FeW catalysts was studied by DRIFT spectroscopy of adsorbed carbon monoxide. DRIFT spectroscopy of CO adsorption on the sulfided FeW catalysts supported on both SBA-15 and γ-Al_2O_3 was performed at 30 °C to characterize the surface active sites. Figure 7 shows DRIFT spectra of catalysts studied around C-O stretching region. Strong bands at 2106 and 2070 cm^{-1} were observed for all catalyst samples analyzed.

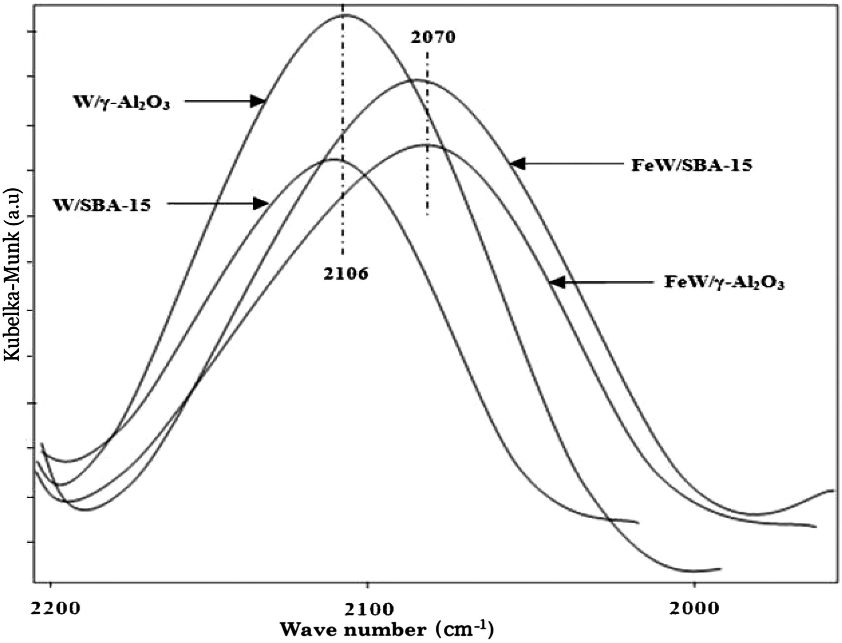

Figure 7. DRIFTS of CO adsorption profiles of unpromoted (W/SBA-15 and W/SBA-15) and Fe-promoted (W/SBA-15 and W/SBA-15) catalysts.

Similarity in adsorption profiles suggests similar adsorption patterns of the probe CO molecules on both SBA-15 and γ-Al_2O_3 supported FeW catalysts. For the sulfided FeW/SBA-15 catalyst, the intensity of the peak observed at 2106 cm^{-1} corresponds to unpromoted tungsten sulfides, which is indicative of a higher number of WS_2 phase. Nonetheless, the intensity of the peak observed for the FeW/γ-Al_2O_3 catalyst at 2070 cm^{-1} was distinctively prominent, giving an indication of significantly more CO molecules adsorbed at Fe-W-S sites of this catalysts. The occurrence of a greater number of FeWS centres exhibited by the sulfided FeW/γ-Al_2O_3 catalyst may be attributable to the higher number of active Fe and W sulfide species generated on the γ-Al_2O_3 support. This is probably due to its higher surface functional groups available for metal species anchorage. By contrast, one can deduce from the DRIFT studies that the γ-Al_2O_3 support enhanced the formation of more active FeW-S species; making it more labile for the creation of a higher number of co-ordinatively unsaturated sites generally required for hydrotreating reactions.

Another characterization technique generally used to probe the nature of catalytically active sites responsible for the adsorption reactant species prior to surface reaction of the adsorbed species is the CO uptake analysis. The amount of CO uptake (µmol/g of cat.) by the sulfided catalysts gives a quantitative measure of the fraction of exposed surface metal atoms. The CO uptake measured from CO chemisorption is equivalent to the number of active metal atoms that are accessible to the reactant molecules present in the feedstock. As can be seen in Table 2, the amount of CO species adsorbed by the sulfided FeW/γ-Al_2O_3 catalyst is more than that absorbed by the FeW/SBA-15 counterpart. This could be due to the relatively greater number of accessible metal species present on the former catalyst; probably due to its highly dispersed metal phases and greater number of Fe-promoted WS_2 stacks formed by this catalyst as revealed by the HRTEM analysis.

3.2. Acidity Determination by FTIR-Pyridine Adsorption Studies

Studies on the spectra of pyridine complexes and the amount of pyridine adsorbed on various solid catalysts are commonly used as tools to distinguish between the various types of species (sites) present on the surface of heterogeneous catalysts (*45*, *46*). Whereas the protonated form of pyridine is best characterized by a band near 1540 cm^{-1}; the co-ordinately bound pyridine formed by interaction with Lewis type sites has a band near 1450 cm^{-1} (*47*). In lieu of this, the distribution of acid sites (Lewis and Bronsted) generated on the surface of the FeW catalyst samples, the pure SBA-15 and γ-Al_2O_3 supports were characterized by the fourier transform infra-red spectroscopic analysis using pyridine as a probe molecule. This technique also helps to distinguish the various acid sites (Bronsted or Lewis) present on the supports as well as the FeW catalysts prepared. It is known that pyridine interacts with acidic sites in specific way to form the coordinated species PyL on Lewis acid sites and the pyridinium ion PyH^+ on protonic sites (*48*, *49*). Due to its relatively weaker basic nature as compared to ammonia, pyridine can effectively titrate stronger acid sites (*45*). Furthermore, it is able to neutralize both Brønsted and Lewis acid sites. The bands at 1545 cm^{-1} and 1440 cm^{-1} are assigned

Downloaded by UNIV OF GUELPH LIBRARY on May 31, 2012 | http://pubs.acs.org
Publication Date (Web): January 20, 2012 | doi: 10.1021/bk-2012-1092.ch010

to pyridine adsorbed on the Brønsted and Lewis acid sites, respectively. However, the band at 1483 cm^{-1} is associated with both Lewis and Brønsted acid sites (*45*). It can be seen from Figure 8A that the IR spectra of adsorbed pyridine on pure γ-Al_2O_3 support after 1 h evacuation of physisorbed pyridine at 150°C yielded IR peaks at 1440 and 1584 cm^{-1}.

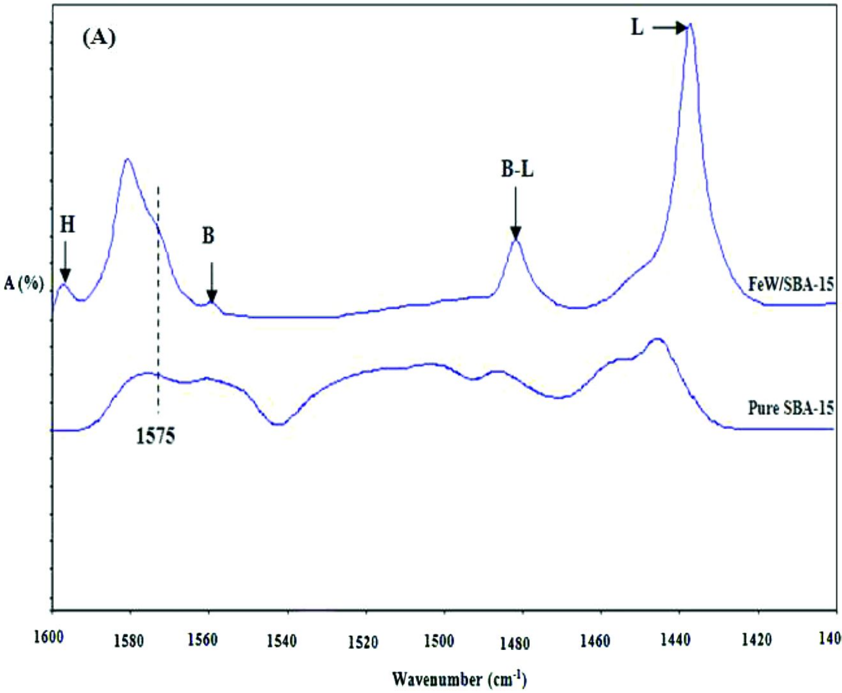

Figure 8A. Pyridine-adsorption spectra of pure SBA-15 and FeW/SBA-15.

These peaks can be attributed to the coordination of pyridine molecules to the Lewis acid sites present on the γ-Al_2O_3 support (*46*, *50*). However, the adsorption band at 1594 cm^{-1}, which appeared as a shoulder is associated with hydrogen bonding between pyridine and surface silanol groups (*51*). This is evident in the FeW/SBA-15 catalyst. The pyridine adsorption spectra of FeW/γ-Al_2O_3 catalyst evidenced additional peaks at 1550 and 1640 cm^{-1} (Figure 8B). These peaks could be assigned to the protonation of pyridine (PyH^+), indicating the presence of Bronsted acidic sites, probably due to the introduction of metal cations onto the support. Nonetheless, adsorption of pyridine on the pure SBA-15 support evidenced only two weakly developed IR humps at 1457 and 1580 cm^{-1}, which are associated with the relatively weak interactions via hydrogen bonding existing between pyridine molecules and surface silanol groups of the SBA-15 support (*52*). As in the case of the alumina support, the incorporation of Fe and W metals on the SBA-15 support resulted in a slight shift of the 1550 cm^{-1} band to 1560 cm^{-1}

Downloaded by UNIV OF GUELPH LIBRARY on May 31, 2012 | http://pubs.acs.org
Publication Date (Web): January 20, 2012 | doi: 10.1021/bk-2012-1092.ch010

respectively. However, the intensities of these bands on the γ-Al_2O_3-supported catalyst is higher as compared to the FeW/SBA-15 catalyst. Moreover, it can be seen from pyridine adsorption profiles that the loading of FeW catalyst on the γ-Al_2O_3-support led to the generation of more Bronsted and Lewis acid sites as compared to the SBA-15 counterpart, suggesting that the higher numbers of these acid sites may be responsible for its better performance for both HDS and HDN activities.

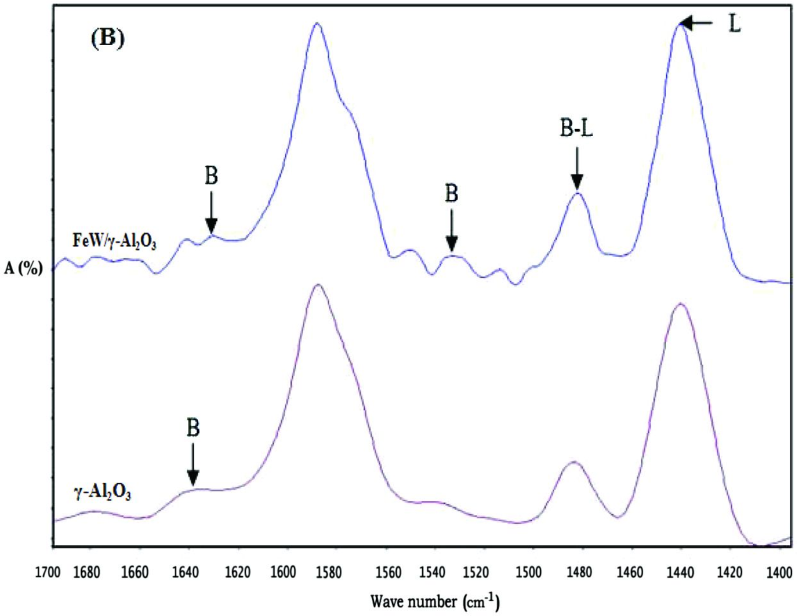

Figure 8B. Pyridine-adsorption spectra of γ-Al_2O_3 support and FeW/γ-Al_2O_3.

Downloaded by UNIV OF GUELPH LIBRARY on May 31, 2012 | http://pubs.acs.org
Publication Date (Web): January 20, 2012 | doi: 10.1021/bk-2012-1092.ch010

3.3. Catalytic Performance Tests of SBA-15 and γ-Al_2O_3-Supported FeW Catalysts

To evaluate the HDS and HDN activities of prepared catalysts, the FeW/SBA-15 (lpd), FeW/SBA-15 (hpd), and FeW/γ-Al_2O_3 were subjected to screening using bitumen-derived heavy gas oil under typical industrial conditions of pressure, temperature, LHSV and gas/oil of 8.8 MPa, 375-400°C, 1 h-1, and 600 mL/mL, respectively. The intended Fe and W loadings for these catalysts was consistent with most commercial NiMo/γ-Al_2O_3 catalysts at 2.5 and 13.0 wt %, respectively.

Downloaded by UNIV OF GUELPH LIBRARY on May 31, 2012 | http://pubs.acs.org
Publication Date (Web): January 20, 2012 | doi: 10.1021/bk-2012-1092.ch010

3.3.1. Effect of Precoking on Sulfur and Nitrogen Conversion

It is a general knowledge that at the start-of-run (SOR) of the hydrotreating reactions, the sulfided catalysts undergo a decline in activity from its initially very high activity as a result of time-on-stream (TOS). Catalyst precoking is the common practice mostly performed to stabilize this initial high activity. The effect of precoking on HDS and HDS activities of SBA-15 (lpd and hpd) and γ-Al_2O_3-supported FeW catalysts are shown in Figure 9.

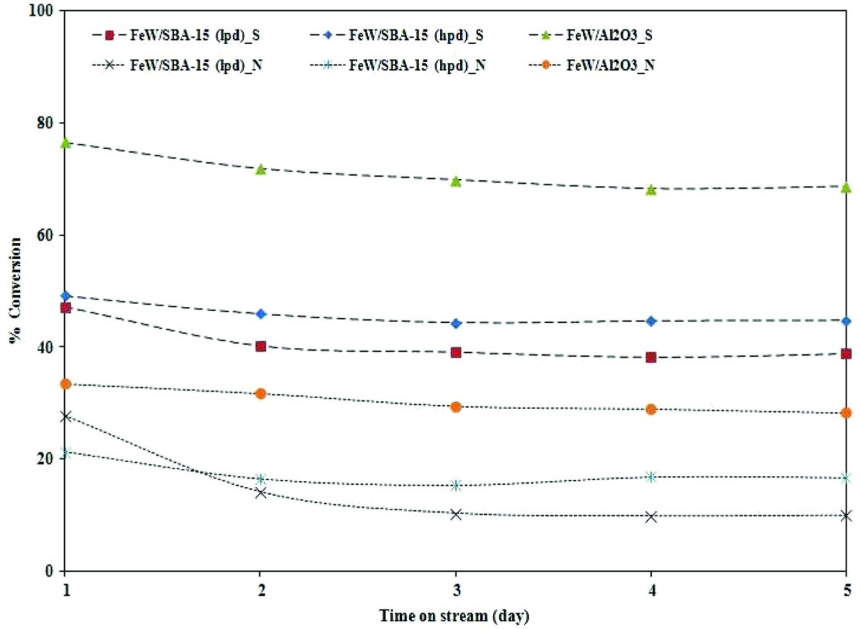

Figure 9. Hydrodesulfurization (HDS) and Hydrodenitrogenation (HDN) activities of SBA-15 and γ-Al_2O_3-supported FeW catalysts during pre-coking with HGO at 375 °C (catalyst = 5 mL, P = 8.8 MPa, LHSV = 1 h^{-1} and H_2/oil ratio = 600 (v/v)).

As can be seen, the FeW/SBA-15 (lpd) showed the highest initial HDS and HDN activity on the 1st day, which significantly dropped on the 2nd day, which became stable after the 3rd day. For the SBA-15 (hpd) and γ-Al_2O_3-supported FeW catalysts, the drop in HDS and HDN activities from 1st to 2nd days was smooth and stabilized after the 3rd day. A possible explanation to this observation could be due to the variable pore diameters of catalysts investigated. It worth mentioning that the pore diameter of catalysts play significant role by controlling the diffusion of reactant molecules to the catalytically active sites within the pore; thus, affecting the rates and conversions of the hydrotreating reactions. That notwithstanding, the choice of catalyst pore diameter is a crucial parameter that deserves special consideration in parallel with feedstock to be processed. In view of this, one can conclude from Figure 9 that HDT activity would be more stable for catalyst with pore diameters of 10 nm as opposed to that of 5 nm. Furthermore, the smaller pore catalyst might have suffered severe hindered diffusion due to the typical bulky sulfur and nitrogen molecules present in the heavy gas oil; consequently, resulting in the sharp decrease in HDT activity as reaction progressed (within 48 h period). The small nature of the catalyst pore may necessitate an accelerated pore-mouth blockage by the low-molecular-size asphaltenes and other heteroatom-containing species; thus, restraining the diffusion of relatively reactive organosulfur and nitrogen species that can easily be hydrotreated. Even though there may be differences in surface chemistry of the SBA-15 and γ-Al_2O_3 materials, the precoking activity profile observed for the γ-Al_2O_3-supported FeW catalyst was similar to that of SBA-15 (hpd); probably due to similitude in their pore diameter.

Downloaded by UNIV OF GUELPH LIBRARY on May 31, 2012 | http://pubs.acs.org
Publication Date (Web): January 20, 2012 | doi: 10.1021/bk-2012-1092.ch010

3.3.2. Pore Size Effect on Sulfur and Nitrogen Conversions

For hydroprocessing of heavy gas oils, it has been indicated that the catalyst pore size may have a significant effect on activity, because intra-pore diffusion in this situation is an important factor (*53*, *54*). The ability of feedstock molecules to easily diffuse to the active catalyst centers would help to determine how efficient a catalyst would be in accomplishing a specific HDT reaction. Thus, a catalyst with large pore size would facilitate diffusion of bulkier molecules from the bulk fluid to the active sites. However, one should be mindful of the fact that extremely large pore diameter may not necessarily mean that diffused molecules actually participated in the surface reaction. Table 2 and Figure 9 show the two main catalyst pore sizes (5 and 10 nm) studied in this work. For the FeW/SBA-15 catalysts, the results in Table 2 and Figure 9 show that at similar metals loading (2 wt. % Fe and 15 wt. % W), the HDS and HDN activities increased as the pore diameter of the support was increased from 5 to 10 nm by varying the C_6H_{14} to NH_4F ratio of the synthesis medium. Though the recorded HDS activity was similar for the two different pore diameter FeW/SBA-15 catalysts, the marginal increment in both HDS and HDN activities observed at all levels of temperatures studied could be attributed to the differences in pore channel opening, which undoubtedly contributed in the removal of these heteroatomic species from the feedstock. Moreover, the higher CO uptake by the FeW/SBA-15 (hpd) catalyst (see Table 2) suggests a greater number of accessible metal sites on this catalyst; even though the surface area decreased with increasing catalyst pore size. This gives an indication that the dispersion of active metals increased with pore size; probably due to an increase in pore volume. It is important to note that even though the FeW/SBA-15 (lpd) catalyst had the highest surface area and should generally be considered as the one that could provide the sufficient surface for metal dispersion, it is a sound argument that not all dispersed metals on the high surface area support (Cat-A) might have been involved in the adsorption process; probably due to their widely dispersed nature on the support. A widely dispersed active species on the support may result in wide spacing between adjacent surface adsorbed species, which could present significant difficulty in the interaction of these species. It can also be noted from Table 2 that the amount of CO uptake by the γ-Al_2O_3-supported FeW catalyst was higher as compared to the FeW/SBA-15 (hpd) catalyst with similar pore diameter. This disparity could be explained due to differences in surface properties of these supports. As confirmed by the HRTEM studies of these two supports, the nature of the γ-Al_2O_3 support enhanced the formation of greater number of stacks of shorter lengths, resulting in a higher stack height. The converse was the case for the SBA-15 support. This result gives an indication that a good recipe for the formulation of an effective HDS catalyst should not consider the pore diameter in isolation but also the surface chemical properties of the support material.

Thus, on the basis of the two different catalyst pore sizes (5 and10 nm) investigated and their hydrotreating activity results, it can be suggested that an optimum pore diameter of approximately 10 nm was effective for both HDS and HDN of the HGO. This corroborates our findings in our previous investigations on the role catalyst pore diameter plays in the hydrotreatment reaction (*29*). For the HDS activity, a study conducted by Inoguchi et al. (*55*) on the control of pore size of supports concluded that an optimal pore diameter of 10 nm is recommended for the HDS of petroleum distillates. Thus, it may be noted that the present results in Figures 10A and 10B for the HDS and HDN of heavy gas oil fractions are consistent with that reported in the investigation by Inoguchi et al. (*55*) using γ-Al_2O_3-supported NiMo catalyst.

3.3.3. Temperature Effect on Sulfur and Nitrogen Conversions

Temperature effect on hydrotreating conversions is a crucial parameter that needs to be seriously considered. Practical speaking, an easy and cost-efficient way of increasing sulfur and nitrogen conversions is by manipulating process temperature. However, it should be noted that an excessively high operating temperature may lead to activity loss and shortening of catalyst life (*56*). It is also worth mentioning that during hydrotreating reactions, rapid catalyst deactivation (or ageing) may occur as a result of agglomeration (sintering) of nanocrystallite metal particles into larger less active phases; and also the potential coverage of active phases initiated by coke precursor deposition on the catalyst surface (*57*). Hence, the general practice to maintain a stable catalyst activity and desired product quality is to gradually increase the operating temperature so as to compensate for catalyst deactivation. Thus, the effect of temperature on catalytic hydrotreatment using heavy gas oil feedstock was evaluated for the FeW/SBA-15 catalyst systems investigated; and results are presented in Figures 10A and 10B.

Temperature was varied from 375 to 400 °C; while pressure, H_2 to oil ratio, and LHSV conditions were maintained at 8.8 MPa, 600 mL/mL and 1 h^{-1}, respectively. The displayed results show that maximum HDS activity was observed at 400°C. It may be noted that the HDS activities for all catalysts increased with increasing temperature; indicating that the reaction rate of heteroatom removal was accelerated by high temperature. As aforementioned, significant temperature increments may risk further cracking of products and

Downloaded by UNIV OF GUELPH LIBRARY on May 31, 2012 | http://pubs.acs.org
Publication Date (Web): January 20, 2012 | doi: 10.1021/bk-2012-1092.ch010

subsequently lead to the generation of hydrocarbon precursors responsible for coke formation. Thus, the choice of an appropriate temperature in commercial units is very important.

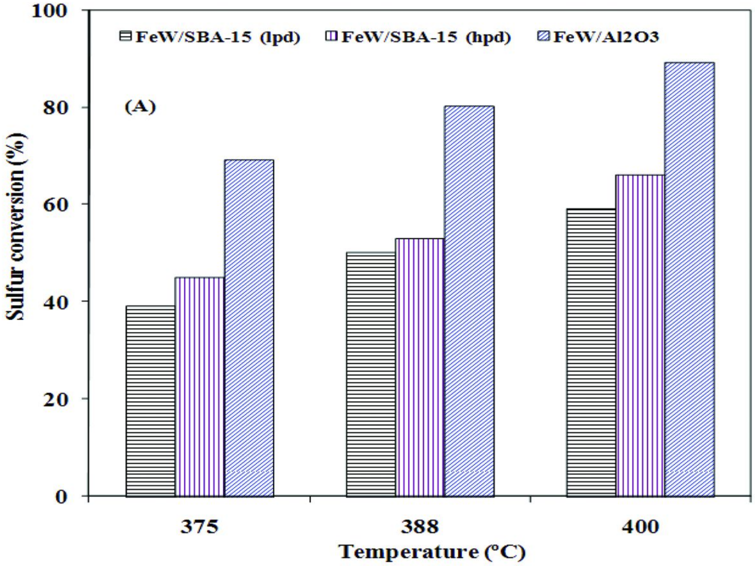

Figure 10A. Hydrodesulfurization (HDS) activities of SBA-15 and γ-Al_2O_3-supported FeW catalysts during screening with HGO as a function of temperature (catalyst = 5 mL, P = 8.8 MPa, LHSV = 1 h^{-1} and H_2/oil ratio = 600 (v/v)).

From the results presented in Table 2, it can be seen that increasing temperature did not result in any significant improvement in nitrogen conversion for the FeW/SBA-15 catalysts studied. However, the HDN activity for the γ-Al_2O_3-supported FeW catalyst significantly increased with temperature increase from 388 to 400°C. A possible explanation to this observation could be due to the greater number of Bronsted acid sites present on this catalyst in comparison to the FeW/SBA-15 counterpart as revealed by the pyridine adsorption studies. These protonated Bronsted sites are known to generally facilitate the hydrogenation pathway during hydrotreating reaction. For the HDN reaction over the conventional NiMo/γ-Al_2O_3 catalyst, the preferred pathway is the pre-hydrogenation of the N-containing ring prior to C-N bond scission (*16*); hence, a catalyst showing characteristics of Bronsted acidity would be a plausible candidate for reactions involving the saturation of olefin bonds. A study conducted by Gounder et al. (*58*) on the catalytic hydrogenation of alkenes on acidic zeolites revealed that the reactivity of Brønsted acid sites played a vital role in the catalysis of alkene hydrogenation with H_2. Nonetheless, it is generally agreed upon that the effect of hydrogenation reaction is more significant in HDN reaction than HDS (*59*); and this fact is often explained on the basis of HDS and HDN reaction mechanisms. Thus, the HDN rate can be affected by the

Downloaded by UNIV OF GUELPH LIBRARY on May 31, 2012 | http://pubs.acs.org
Publication Date (Web): January 20, 2012 | doi: 10.1021/bk-2012-1092.ch010

equilibrium of N-ring hydrogenation because N-ring hydrogenation occurs before nitrogen removal (hydrogenolysis). HDS does not always require hydrogenation since it can proceed via two possible mechanisms, namely; ring hydrogenation followed by hydrogenolysis or (ii) direct hydrogenolysis (*60*).

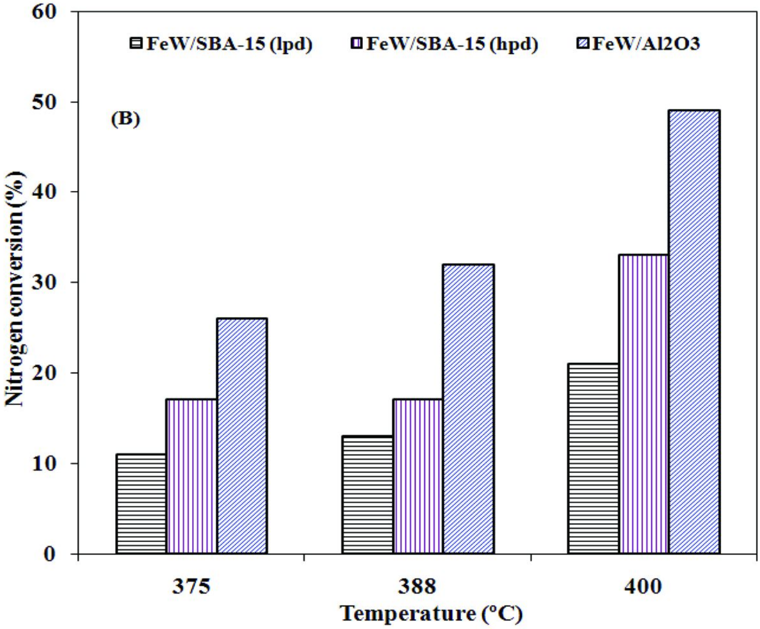

Figure 10B. Hydrodenitrogenation (HDN) activities of SBA-15 and γ-Al_2O_3-supported FeW catalysts during screening with HGO as a function of temperature (catalyst = 5 mL, P = 8.8 MPa, LHSV = 1 h^{-1} and H_2/oil ratio = 600 (v/v)).

4.0. Conclusions

In this work, a highly ordered mesoporous SBA-15 supports were synthesized under acidic conditions using hexane as a pore swelling agent. SBA-15 (low and high pore diameters) and commercial γ-Al_2O_3-supported FeW catalysts were prepared by the aqueous impregnation technique using aqueous solutions of the same amount metal (2 wt.% Fe and 15 wt.% W) precursors.

Profiles from small-angle X-ray scattering for the FeW/SBA-15 catalysts exhibited three well-resolved peaks characteristic of the parent SBA-15 material. TEM analysis of catalysts studied suggested a well-ordered cylindrical pore structure of the SBA-15 samples, which was preserved even after loading of 2 wt.% Fe and 15 wt.% W. At these metals loading, broad angle XRD patterns evidenced a homogenously dispersed oxide metal species for all catalysts. The shape of the N_2 adsorption–desorption isotherms confirmed the synthesis of a well-formed SBA-15 material; however, a broad pore size distribution profile was obtained for the FeW/γ-Al_2O_3 catalyst.

Downloaded by UNIV OF GUELPH LIBRARY on May 31, 2012 | http://pubs.acs.org
Publication Date (Web): January 20, 2012 | doi: 10.1021/bk-2012-1092.ch010

At constant pressure, LHSV, and gas-oil ratio of 8.8 MPa, 1 h^{-1}, and 600 mL/mL, the FeW/γ-Al_2O_3 catalyst recorded the maximum HDS and HDN activities at all levels of temperatures studied as compared to the FeW/SBA-15 counterpart. Surface characterization techniques namely pyridine adsorption, CO uptake and DRIFTS of CO employed to probe the catalytically active species confirmed that the former catalyst has an enhanced surface chemical properties, which might be responsible for its superior performance to the texturally desirable SBA-15-supported catalysts.

Acknowledgments

The authors acknowledge the Natural Science and Engineering Research Council of Canada, as well as Syncrude Canada Ltd. for financing this research.

References

1. Gautier, C. *Oil, Water, Climate: An Introduction*; Cambridge University Press: New York, 2008.
2. Angelic, R. J. *Polyhedron* **1997**, *16*, 3073–3088.
3. Okamoto, Y.; Breysse, M.; Dhar, G. M.; Song, C. *Catal. Today* **2003**, *86*, 1–3.
4. Scheffer, B.; Mangnus, P. J.; Moulijn, J. A. *J. Catal.* **1990**, *121*, 18–30.
5. Topsøe, H.; Clausen, B. S.; Massoth, F. E. *Hydrotreating Catalysts in Catalysis: Science and Technology*; Anderson, J. R., Boudart, M., Eds.; Springer-Verlag: Berlin, Heidelberg, 1996; Vol. 11.
6. Maity, S. K.; Srinivas, B. N.; Prasad, V. V. D. N.; Singh, A.; Dhar, G. M.; Prasada Rao, T. S. R. *Stud. Surf. Sci. Catal.* **1998**, *113*, 579−590.
7. Prins, R.; de Beer, V. J. H.; Somorjai, G. A. *Catal. Rev.: Sci. Eng.* **1989**, *31*, 1–41.
8. Maity, S. K.; Rana, M. S.; Srinivas, B. N.; Bej, S. K.; Dhar, G. M.; Prasada Rao, T. S. R. *J. Mol. Catal. A: Chem.* **2000**, *153*, 121–127.
9. Damyanova, S.; Petrov, L.; Centeno, M. A.; Grange, P. *Appl. Catal., A* **2002**, *224*, 271–284.
10. Li, D.; Nishijima, A.; Morris, D. E. *J. Catal.* **1999**, *182*, 339–348.
11. Klimova, T.; Calderon, M.; Ramirez, J. *Appl. Catal., A* **2003**, *240*, 29–40.
12. Boahene, P. E.; Soni, K.; Dalai, A. K.; Adjaye, J. *Appl. Catal., B* **2011**, *101*, 294–305.
13. Dhar, G. M.; Kumarana, G. M.; Kumara, M.; Rawat, K. S.; Sharma, L. D.; Raju, B. D.; Rao, K. S. R. *Catal. Today* **2005**, *99*, 309–314.
14. Soni, K.; Rana, B. S.; Sinha, A. K.; Bhaumik, A.; Nandi, M.; Kumar, M.; Dhar, G. M. *Appl. Catal., B* **2009**, *90*, 55–63.
15. Luck, F. *Bull. Soc. Chim. Belg.* **1991**, *100*, 781–800.
16. Knudsen, K. G.; Cooper, B. H.; Topsøe, H. *Appl. Catal., A* **1999**, *189*, 205–215.
17. Prins, R.; de Beer, V. J. H.; Somorjai, G. A. *Catal. Rev.: Sci. Eng.* **1989**, *31*, 1–41.

Downloaded by UNIV OF GUELPH LIBRARY on May 31, 2012 | http://pubs.acs.org
Publication Date (Web): January 20, 2012 | doi: 10.1021/bk-2012-1092.ch010

Downloaded by UNIV OF GUELPH LIBRARY on May 31, 2012 | http://pubs.acs.org
Publication Date (Web): January 20, 2012 | doi: 10.1021/bk-2012-1092.ch010

18. Lauritsen, J. V.; Helveg, S.; Laegsgaard, E.; Clausen, B. S.; Topsøe, H.; Besenbacher, F. *J. Catal.* **2001**, *97*, 1–5.
19. Shimada, H.; Sato, T.; Yoshimura, Y.; Hiraishi, J.; Nishijima, A. *J. Catal.* **1988**, *110*, 275–284.
20. Benitez, A.; Ramirez, J.; Fierro, J. L. G.; Agudo, A. L. *Appl. Catal., A* **1996**, *144*, 343–364.
21. Breysse, M.; Cattenot, M.; Decamp, T.; Frety, R.; Gachet, C.; Lacroix, M.; Leclercq, C.; de Mourgues, L.; Portfaix, J. L.; Vrinat, M.; Houari, M.; Grimblot, J.; Kasztelan, S.; Bonelle, J. P.; Housini, S.; Bachelier, J.; Duchet, J. C. *Catal. Today* **1988**, *4*, 39–55.
22. Kameoka, T.; Yanase, H.; Nishijima, A.; Sato, T.; Yoshimura, Y.; Shimada, H.; Matsubayashi, N. *Appl. Catal., A.* **1995**, *123*, 217–228.
23. Linares, C. F.; Amezqueta, P.; Scott, C. *Energy Fuels* **2008**, *87*, 2817–2823.
24. Pratt, K. C.; Sanders, J. V.; Chritov, V. *J. Catal.* **1990**, *124*, 416–432.
25. Qu, L.; Zhang, W.; Kooyman, P. J.; Prins, R. *J. Catal.* **2003**, *215*, 7–13.
26. Ji, Y.; Afanasiev, P.; Vrinat, M.; Li, W.; Li, C. *Appl. Catal., A* **2004**, *257*, 157–164.
27. Dhar, G. M.; Kumaran, G. M.; Kumar, M.; Rawat, K. S.; Sharma, L. D.; Raju, B. D.; Rao, K. S. R. *Catal. Today* **2005**, *99*, 309–314.
28. Vradman, L.; Landau, M. V.; Herskowitz, M.; Ezersky, V.; Talianker, M.; Nikitenko, S.; Koltypin, Y.; Gedanken, A. *J. Catal.* **2003**, *213*, 163–175.
29. Boahene, P. E.; Soni, K. K.; Dalai, A. K.; Adjaye, J. *Appl. Catal., A* **2011**, *402*, 31–40.
30. Sun, J.; Zhang, H.; Ma, D.; Chen, Y.; Bao, X.; Klein-Hoffmann, A.; Pfaender, N.; Su, D. S. *Chem. Commun.* **2005**, 5343–5345.
31. Kruk, M.; Cao, L. *Langmuir* **2007**, *23*, 7247–7254.
32. Sundaramurthy, V.; Eswaramoorthi, I.; Dalai, A. K.; Adjaye, J. *Microporous Mesoporous Mater.* **2008**, *111*, 560–568.
33. Bej, S. K.; Dalai, A. K.; Maity, S. K. *Catal. Today* **2001**, *64*, 333–345.
34. Zhao, D.; Feng, J.; Huo, Q.; Melosh, N.; Fredrickson, G. H.; Chmelka, B. F.; Stucky, G. D. *Science* **1998**, *279*, 548–552.
35. Cao, L.; Man, T.; Kruk, M. *Chem. Mater.* **2009**, *21*, 1144–1153.
36. Zepeda, T. A.; Pawelec, B.; Fierro, J. L. G.; Halachev, T. *J. Catal.* **2006**, *242*, 254–269.
37. Chen, Y.-W.; Lin, C.-S.; Hsu, W.-C. *Catal. Lett.* **1989**, *3*, 99–102.
38. Gary, J. H.; Handwerk, G. E.; Kaiser, M. J. *Petroleum Refining*, 5th ed.; 2004; Chapter 9, pp 195−197.
39. Vradman, L.; Landau, M. V.; Kantorovich, D.; Koltypin, Y.; Gedanken, A. *Microporous Mesoporous Mater.* **2005**, *70*, 307–318.
40. Huang, Z. D.; Bensch, W.; Kienle, L.; Fuentes, S.; Alonso, G.; Ornelas, C. *Catal. Lett.* **2008**, *122*, 57–67.
41. Daage, M.; Chianelli, R. R. *J. Catal.* **1994**, *149*, 414–427.
42. Topsøe, H.; Clausen, B. S.; Massoth, F. E. *Hydrotreating Catalysis - Science and Technology*; Springer-Verlag: New York, 1996.
43. Zepeda, T. A.; Pawelec, B.; Fierro, J. L. G.; Halachev, T. *J. Catal.* **2006**, *242*, 254–269.

44. Digne, M.; Sautet, P.; Raybaud, P.; Euzen, P.; Toulhoat, H. *J. Catal.* **2002**, *211*, 1–5.
45. Parry, E. P. *J. Catal.* **1963**, *2*, 371.
46. Basila, M. R.; Kantner, T. R.; Rhee, K. H. *J. Phys. Chem.* **1964**, *68*, 3197.
47. Eberly, P. E., Jr. *J. Phys. Chem.* **1968**, *72*, 1042–1046.
48. Knozinger, H.; Stolz, H. *Bunsenges Phys. Chem.* **1970**, *74*, 1056.
49. Al-Shalabi, M. A.; Abdel-Aal, H. K. *Prepr. Pap.-Am. Chem. Soc., Div. Pet. Chem.* **2005**, *50* (4) (1&2), 351−352.
50. Xiaohong, L.; Wang, Y. M.; Wu, P. *ChemCatChem* **2010**, *2*, 1303.
51. Hughes, T. R.; White, H. M. *J. Phys. Chem.* **1967**, *71*, 2192–2201.
52. Rajagopal, S.; Marzari, J. A.; Miranda, R. *J. Catal.* **1995**, *151*, 192–203.
53. Ohtauka, T. *Catal. Rev: Sci. Eng.* **1977**, *16*, 291–325.
54. Green, D. C.; Broderick, D. H. *Chem. Eng. Prog.* **1981**, *77*, 33–39.
55. Inoguchi, M. *Shokubai* **1978**, *20*, 144–154.
56. Moschopedis, S. E.; Parkash, S.; Speight, J. G. *Energy Fuel* **1978**, *57*, 431–434.
57. Speight, J. G. *The Desulfurization of Heavy Oils and Residual*; Marcel Dekker: New York, 2000.
58. Gounder, R.; Iglesia, E. *J. Catal.* **2011**, *277*, 36–45.
59. Botchwey, C.; Dalai, A. K.; Adjaye, J. *Energy Fuels* **2003**, *17*, 1372–1381.
60. Mapiour, M.; Sundaramurthy, V.; Dalai, A. K.; Adjaye, J. *Energy Fuels* **2009**, *23*, 2129–2135.

Downloaded by UNIV OF GUELPH LIBRARY on May 31, 2012 | http://pubs.acs.org
Publication Date (Web): January 20, 2012 | doi: 10.1021/bk-2012-1092.ch010

Downloaded by PENNSYLVANIA STATE UNIV on May 31, 2012 | http://pubs.acs.org
Publication Date (Web): January 20, 2012 | doi: 10.1021/bk-2012-1092.ch011

Chapter 11

Insights into Structural and Chemical Properties of Activated Montmorillonite for Fischer-Tropsch Synthesis over Supported Cobalt Catalysts

**Qing-Qing Hao, Guang-Wei Wang, Zhao-Tie Liu,
and Zhong-Wen Liu***

**Key Laboratory of Applied Surface and Colloid Chemistry, MOE, and
School of Chemistry & Materials Science, Shaanxi Normal University,
Xi'an 710062, China**
***Tel: +86-29-8530-3200. Fax: +86-29-8530-7774.
E-mail: zwliu@snnu.edu.cn.**

A Na-type montmorillonite (Na-MMT) activated with HNO_3 at elevated temperatures for different times was investigated for the selective synthesis of liquid fuels via the Fischer-Tropsch synthesis over 20 wt.% Co-supported catalysts under the conditions of 1.0 MPa, 235 °C, $H_2/CO=2$, and W/F=5.02 $g{\cdot}h{\cdot}mol^{-1}$. Although Co/Na-MMT is not a suitable catalyst for the FT synthesis, high CO conversion was achieved over Co/activated MMT catalysts, which is similar to that of typical Co/SiO_2 catalyst of the FT synthesis. Moreover, the product selectivity over Co/activated MMT, i.e., clearly higher selectivity of C_4-C_{12} hydrocarbons and obviously lower selectivity of C_{21}^+ hydrocarbons than those over Co/SiO_2, was significantly deviated from the Anderson-Schulz-Flory distribution of the FT synthesis. Among the catalysts tested, Co/Acid-MMT-12/80 was the best catalyst to control the product distribution of the FT synthesis. The materials were characterized by XRD, FTIR, SEM, N_2 adsorption-desorption at low temperature, H_2-TPR, and NH_3-TPD techniques. Depending on the activation conditions, the acidity and textural properties of the activated MMT were significantly changed due to the following events occurred in different degrees:

In Nanocatalysis for Fuels and Chemicals; Dalai, A.;
ACS Symposium Series; American Chemical Society: Washington, DC, 2012.

Downloaded by PENNSYLVANIA STATE UNIV on May 31, 2012 | http://pubs.acs.org
Publication Date (Web): January 20, 2012 | doi: 10.1021/bk-2012-1092.ch011

the leaching of the substituted cations, the exchanging of H^+ with the interlayer Na^+, and the destruction of the MMT interlayer structure. Ultimately, the MMT laminar structure was completely destructed after activation of Na-MMT at 100 °C for 24 h. The reaction results were well explained based on these characterization data. The content of Na^+ was revealed as the main factor to control the FT activity, and the acidity of the activated MMT was responsible for the narrowed product distribution. Considering the simple procedure for the activation of MMT, Co/activated MMT is a promising catalyst for selectively synthesizing liquid fuels via the FT route provided the MMT is activated under suitable conditions.

Introduction

Although clay has been known and industrially utilized for a long history, it is a relatively young discipline of scientific study since the emergence of the generally accepted concept of clay mineral in mid-1930s (*1*). Because of its abundance, cheapness, environmental compatibility, and more importantly, the versatile and facile tailoring in porosity, acidity, hydrophilicity, etc., clay is recognized as a material of the 21st century (*1*, *2*). Thus, in recent years, an increased attention spanning from physics, chemistry, environmental and materials science has been paid on the development of clay science and its applications (*3*).

Montmorillonite (MMT), a 2:1 layered dioctahdedral aluminosilicate of smectite-type clay, is one of the most investigated clay minerals. The primary structure of MMT is composed of two tetrahedral sheets with Si in cationic sites sandwiching an octahedral Al sheet. The junction plane between tetrahedral and octahedral sheets consists of the shared apical oxygen atoms of the tetrahedrons and the unshared hydroxyls that lie at the centre of each hexagonal ring of tetrahedrons. The partial substitution of Al^{3+} for the tetrahedral Si^{4+} and Mg^{2+} for the octahedral Al^{3+} makes the layers negatively charged, and is neutralized by the exchangeable cations in the interlayer space. Based on these structural properties, MMT can be modified via covalent bonding of molecules to the atom at the MMT layer or replacing the interlayer exchangeable cations in the gallery region with different molecules (*4*, *5*). These modifications create wide ranges of possible changes in surface area, porosity, and acidity besides the functions effected by introduced molecules (*2*, *3*). Since these changes are closely pertinent to catalysis, MMT in its natural or modified form has been extensively applied for catalyzing a variety of chemical reactions (*4*–*8*). Moreover, new methods on the modification of MMT are still pursued thanks to its amazing amenability in tailoring (*5*).

Among the available modification methods, acid activation, i.e., treatment with inorganic liquid acids, e.g., H_2SO_4, HCl, is one of the most simple and efficient routes to adjust the acidity and porosity of MMT (*3*, *8*–*11*). Indeed, activated MMT has long been used as a catalyst in petroleum refining, and renewed interest as a catalyst or catalyst support in organic synthesis is extensively

Downloaded by PENNSYLVANIA STATE UNIV on May 31, 2012 | http://pubs.acs.org
Publication Date (Web): January 20, 2012 | doi: 10.1021/bk-2012-1092.ch011

explored in recent years (*3*, *5*, *11*). Although the detailed mechanism of the acid activation of MMT is not thoroughly understood, following changes of physical and chemical properties are generally observed (*8–15*): (1) Replacing the interlayer exchangeable cations of Na^+, Ca^{2+}, etc. with protons; (2) Dissolving the extraframework mineral impurities; (3) Delamination or destruction of the laminar MMT platelet; (4) Leaching of Al^{3+}, Mg^{2+}, etc., in octahedral and tetrahedral sheets; (5) Formation of free and amorphous silica. These changes are strongly dependent on the extent of the acid activation, and the final product is essentially amorphous or poorly crystallized, protonated, and porous silica (*9*, *16*). Thus, the activated MMT with desirable porosity and acidity can be obtained under appropriate activation conditions.

Being a well-established technology to convert syngas ($CO+H_2$) into high-value added fine chemicals and super clean fuels, Fischer-Tropsch (FT) synthesis is receiving considerable worldwide attention because of the recently increased concern on the energy supply security and the implementation of more stringent environmental legislations on liquid fuels (*17*). However, the FT reaction is a polymerization process following the Anderson-Schulz-Flory (ASF) kinetics. Accordingly, the reaction product is a very complicated mixture, composed mainly of normal paraffins with varied carbon numbers and nonselective to any specific hydrocarbon (*18*, *19*). To improve the efficiency of the FT process, it is desirable to selectively synthesize liquid fuels by minimizing the selectivity of gaseous (C_1-C_3) and solid (C_{21}^+) hydrocarbons. However, it is still one of the most challenges for the FT synthesis.

To break the ASF polymerization kinetics, several strategies have been practiced to improve the selectivity of the targeted groups of hydrocarbons such as olefins, gasoline, and diesel (*20–25*). As indicated in our previous analyses on the possible strategies (*26*), the best method is to make an efficient bifunctional catalyst, in which an FT active metal is integrated with a solid acid having suitable acidity and meso porosity. In this case, cracking of long-chain FT hydrocarbons together with the confinement of nano-sized pores can effectively increase the selectivity of liquid hydrocarbons (*26*). Moreover, some technical aspects of the feasible bifunctional catalyst, e.g., matching of the optimal temperatures for the FT synthesis and cracking reactions of the long-chain FT hydrocarbons, no detrimental mutual effect of different active centers, must be deliberately considered. Although much work has been done on this purpose (*21–26*), efficient solid acids with adjustable acidity and easily tailored porosity are still rare for selectively synthesizing liquid fuels via the FT synthesis.

The above analyses indicate that the activated MMT is a solid acid characterized in high surface area, adjustable porosity and acidity. Moreover, cobalt has been proved to be one of the most effective and industrially important active metals for the FT synthesis. These properties make the Co/activated MMT a promising bifunctional catalyst for controlling the product distribution of the FT synthesis. However, to the best of our knowledge, this is not reported in the open literature.

Thus, in this work, MMT was treated with HNO_3 for different extents of activation, and the Co/activated MMT was comparatively studied for the FT synthesis. Remarkably, the distribution of FT products over Co-supported

MMT catalysts was significantly deviated from the ASF kinetics. Moreover, the Co-supported MMT with a suitable extent of activation showed both high CO conversion and low selectivity of C_{21}^+ hydrocarbons. These prominent results are well correlated with acidic and textural properties of activated MMTs based on the characterization results of XRD, FTIR, H_2-TPR, NH_3-TPD, and N_2 adsorption at low temperature.

Experimental

Materials and Methods

Materials

The Na-type MMT (Na-MMT, Zhejiang Sanding Group Co., Ltd.) was used as a starting material without further purification. To 20 wt.% HNO_3 aqueous solution (200 mL), a desired amount of Na-MMT was added under vigorous stirring, and a 2 wt.% Na-MMT suspension was obtained. To adjust the extent of the activation, the thus prepared slurry was magnetically stirred at 60-100 °C for 4-36 h, respectively. After activation, the slurry was centrifugated, sufficiently washed with de-ionized water. Finally, activated MMT was obtained by drying the solid at 80 °C for 12 h. The MMT activated under different conditions was abbreviated as Acid-MMT-t/T, where t and T are time and temperature during the acid treatment, respectively.

The cobalt-supported MMT was prepared by the incipient wetness impregnation method. Cobalt nitrate ($Co(NO_3)_2{\cdot}6H_2O$, 99.0%,) was used as the cobalt precursor, and the metallic cobalt loading was kept at 20 wt.% for all the catalysts. The catalysts were dried at 120 °C for 12 h, and calcined in air at 200 °C for 2 h by increasing the temperature at a controlled heating rate of 2 °C/min.

Characterization Techniques

Textural properties of the samples were determined based on N_2 adsorption-desorption isotherms measured with BelSorp-Max (Bel Japan Inc.) at -196 °C. Each sample of 150 mg was degassed at 350 °C for 5 h. The surface area was calculated by the BET method, and the pore size distribution was determined based on the BJH method using the data of desorption branches.

X-ray diffractograms were obtained on a Rigaku D/Max 2550VB+/PC equipment (Cu/K_α radiation, 40 kV, 50 mA). Based on the Scherrer formula, the crystal size of the Co_3O_4 over the calcined catalysts was estimated using the 440 diffraction (2θ at about 65.5°). The crystal size of the metallic cobalt in the reduced catalysts was calculated according to $d(Co^0) = 0.75d(Co_3O_4)$.

The study of Fourier Transform Infrared Spectroscopy (FTIR) was carried out on a Nicolet Avatar 360 spectrometer. FTIR spectra in the transmittance mode were recorded in the range of 400-4000 cm^{-1} at a resolution of 4 cm^{-1} using the KBr pressed disk technique.

Downloaded by PENNSYLVANIA STATE UNIV on May 31, 2012 | http://pubs.acs.org
Publication Date (Web): January 20, 2012 | doi: 10.1021/bk-2012-1092.ch011

The reduction behavior of the catalysts was studied by hydrogen temperature-programmed reduction (H_2-TPR) using a Micromeritics Autochem 2920 instrument. The amount of the loaded catalyst was accurately weighed at 50.05± 0.5 mg. Priori to H_2-TPR, the system was flushed with an Ar flow at room temperature for 30 min. After this, it was switched to 10 vol.% H_2 in Ar. H_2-TPR was performed at a heating rate of 10 °C/min until 900 °C. A downstream 2-propanol/liquid N_2 trap was used to retain the water generated during the reduction. The H_2 consumption rate was monitored with a thermal conductivity detector (TCD) previously calibrated using the reduction of CuO as a reference.

The NH_3-TPD of the MMTs was measured with a Micromeritics Autochem 2920 instrument. 50.0±0.5 mg of sample was applied to the test. After flushing with a He flow at 550 °C for 60 min, NH_3 adsorption was started at 120 °C for 30 min. Subsequently, it was purged for 2 h in a flow of helium at the same temperature. Finally, NH_3-TPD was carried out from 120 to 550 °C with a heating rate of 10 °C /min under a helium flow of 30 mL/min.

The morphology of different samples was observed on an environmental scanning electron microscope (Philips-FEI model Quanta 200). To determine the content of Na^+, 0.02000 g of each MMT samples was dissolved in a mixed solution of HNO_3 and HF under a microwave irradiation. The content of Na+ in the solution was measured by atomic absorption spectrometer (AAS).

Reaction Procedure

FT Reaction

The FT reaction was performed in a stainless steel fixed bed reactor (i. d. = 10 mm) by loading 0.5 g catalyst (40-60 mesh) diluted with the same amount of quartz sands. Prior to reaction, the catalyst was reduced at atmospheric pressure in a flow of pure H_2 (50 cm^3/min) at 400 °C for 4 h. After reduction, the catalyst was evaluated for the FT reaction under the conditions of H_2/CO=2 (4 % Ar as internal standard), T=235 °C, W/F=5.05 g h/mol, P=1.0 MPa.

Product Analysis

To prevent condensation of the products, the line between the outlet of the reactor and the inlet of the gas chromatograph (GC) column was heated at or above 180 °C. The effluent products were analyzed by on-line GC (GC-9560, Shanghai Huaai chromatographic analysis Co., Ltd) equipped with an HP-PONA capillary column (0.20 mm×50 m, 0.5 μm) and an FID detector. The CO, CH_4 and CO_2 in the effluent after cooling in an ice-water trap were on-line analyzed with a packed active carbon column and a TCD detector. The selectivity of hydrocarbons was calculated on the basis of carbon number.

Downloaded by PENNSYLVANIA STATE UNIV on May 31, 2012 | http://pubs.acs.org
Publication Date (Web): January 20, 2012 | doi: 10.1021/bk-2012-1092.ch011

Downloaded by PENNSYLVANIA STATE UNIV on May 31, 2012 | http://pubs.acs.org
Publication Date (Web): January 20, 2012 | doi: 10.1021/bk-2012-1092.ch011

Results and Discussion

Structural Properties

Long Range Order

The XRD patterns of the Na-MMT and the activated MMTs are given in Figure 1. From the characteristic (001) diffraction, structural changes of the MMT activated under different conditions were clearly observed. The (001) diffraction of Na-MMT was at 2θ of about 7.4°, corresponding to a d_{001} spacing of 1.20 nm. However, the d_{001} spacing of Acid-MMT-4/60 was slightly increased to be 1.52 nm (2θ of about 5.8°). Further increasing the severity of the activation conditions, the d_{001} spacing was kept constant (1.59 nm). This indicates that the MMT interlayer was expanded after the activation, which is agreeable with the recent results on the activation of bentonite (*10*). Based on the structural information of the MMT, the expanded interlayer space must be originated from the exchangeable cations in the interlayer region. During the activation, protons entered into the interlayer region via ion-exchanging with the interlayer Na^+. This was clearly reflected from the continuously decreased content of Na^+ over MMTs with increasing the severity of the activation conditions (Table 1). Additionally, as revealed from the FTIR results in the next section, leaching of Al^{3+} from MMT layers during the activation was clearly occurred. Thus, the leached Al^{3+} may also be exchanged into the interlayer region, and partially hydrolyzed due to its high charge to radius ratio. The d_{001} spacing of MMT is reported to be changed with its hydration state induced by the exchangeable cations, i.e., 0.96-1.01 nm for dehydrated layers, 1.23-1.27 nm for monohydrated layers, and 1.51-1.58 nm for bi-hydrated layers (*27*, *28*). In our case, the d_{001} spacing of the raw Na-MMT and the activated MMT was highly consistent to that of monohydrated layers and bi-hydrated layers, respectively. Based on these, the higher hydration state of the activated MMT may be explained as the substitution of protons and Al^{3+} for Na^+, which is agreeable with the constant d_{001} spacing of the MMT activated at 80 °C for 4 - 36 h.

As indicated in Figure 1, the X-ray active quartz as an impurity (2θ of about 20.8 and 26.5°, PDF No. 46-1045) was present in the raw Na-MMT. Moreover, the impure quartz was not removed even under the severest activation conditions, which is consistent to the reported results (*10*, *13*). Increasing the severity of the activation conditions, decomposition of the MMT interlayer structure was enhanced as revealed from the progressively decreased intensity of the (001) diffraction. Moreover, a broad peak at 2θ of about 22° due to amorphous silica appeared for Acid-MMT-24/80, and its intensity was clearly increased with further increasing the severity of the activation conditions. Under the severest activation conditions, i.e., Acid-MMT-24/100, all the diffractions of MMT were disappeared, and only the XRD peaks for amorphous silica and impure quartz were observable. This indicated a complete decomposition of the MMT interlayer structure.

Downloaded by PENNSYLVANIA STATE UNIV on May 31, 2012 | http://pubs.acs.org
Publication Date (Web): January 20, 2012 | doi: 10.1021/bk-2012-1092.ch011

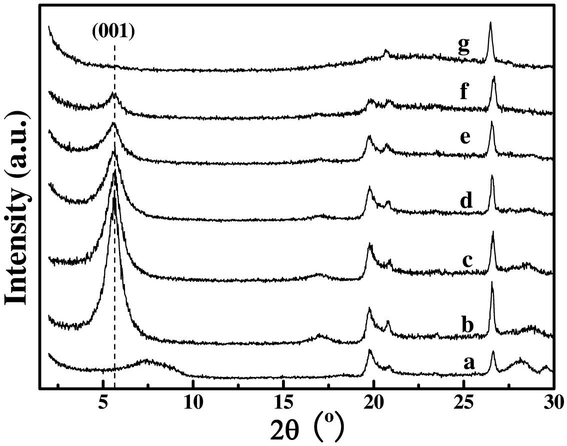

Figure 1. XRD patterns for Na-MMT (a), Acid-MMT-4/60 (b), Acid-MMT-4/80 (c), Acid-MMT-12/80 (d), Acid-MMT-24/80 (e), Acid-MMT-36/80 (f), and Acid-MMT-24/100 (g).

Short Range Order

FTIR spectroscopy has been proved to be a powerful and sensitive tool to probe the chemical and structural changes of clays during the activation. To further determine the chemical and structural variations, FTIR studies were performed, and the results are given in Figure 2. For the raw Na-MMT, the characteristic bands originated from hydroxyl groups, silicate anions, and octahedral cations can be identified based on reference results (*12*, *29–32*). The broad band at about 3450 cm^{-1} and the intense absorption near 1640 cm^{-1} were assigned to the stretching and bending vibrations of the hydroxyl groups in molecular water presented in MMT. The IR absorption band for the stretching of hydroxyl groups coordinated to octahedral Al^{3+} was appeared at about 3623 cm^{-1}, and the substitution of the octahedral Al^{3+} by Fe^{3+} or Mg^{2+} was indicated from its broadness (*29*, *32*). The most intensive band centered at about 1040 cm^{-1} was attributed to the stretching vibrations of the Si-O in tetrahedral sheets. The bending vibrations of the Si-O-Al (Al in octahedral) and Si-O-Si were clearly observed at about 523 and 465 cm^{-1}, respectively. The hydroxyl bending bands for Al-OH-Al, Al-OH-Fe, and Al-OH-Mg were observed at 915, 875, and 845 cm^{-1}, respectively, indicating the presence of substituted octahedral cations of Al, Fe, and Mg. Moreover, a much lower content of Mg^{2+} than that of Al^{3+} in Na-MMT was revealed from the intensity of these IR bands. The weak IR absorption at about 625 cm^{-1} was related to the perpendicular vibration of the octahedral cations (*29*). The presence of quartz was indicated from the inflection at about 692 cm^{-1} and the weak doublet at 796 and 777 cm^{-1}, which is agreeable with the XRD results.

The structural and compositional changes of the activated MMTs, e.g., substitution of interlayer cations with protons, delamination, leaching of octahedral cations, can be determined based on the variation of the IR spectra. During the activation, OH groups were attacked by the exchanged and penetrated protons, leading to the successive dissolution of the central atoms via dehydroxylation (*30*). This was clearly revealed from the IR absorptions of the OH groups. Increasing the severity of the activation conditions, the intensity of the IR bands for OH groups (3623, 915, 875, and 845 cm^{-1}) was gradually decreased or disappeared, indicating the progressively increased leaching of the octahedral cations of Al, Fe, and Mg, etc. Correspondingly, the amount of the water coordinated to the octahedral cations was decreased, leading to the decreased intensity of the vibrations of the hydroxyl groups in molecular water (3450 and 1640 cm^{-1}). This was further reflected from the intensified Si-O-Si bending vibrations (465 cm^{-1}) with increasing the severity of the activation conditions. Moreover, the decreased intensity for the 625 cm^{-1} band with increasing the severity of the activation conditions is also agreeable with this explanation.

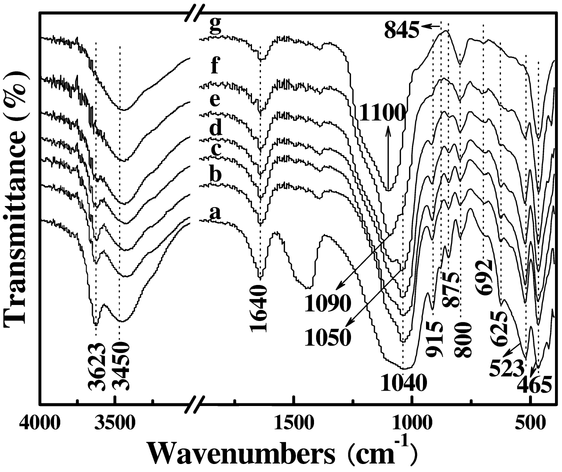

Figure 2. FTIR spectra of Na-MMT (a), Acid-MMT-4/60 (b), Acid-MMT-4/80 (c), Acid-MMT-12/80 (d), Acid-MMT-24/80 (e), Acid-MMT-36/80 (f), and Acid-MMT-24/100 (g).

In comparison with Na-MMT, a narrowed Si-O vibration and its slight shift towards higher frequency (1050 cm^{-1}) were observed for Acid-MMT-4/60, indicative of a slight change of the layered MMT structure. Moreover, the Mg^{2+} was completely removed as indicated from the disappearance of the 845 cm^{-1} IR band. For the MMT activated at 80 °C, pronounced changes with increasing activation time from 4 to 24 h were as follows: (1) A shoulder absorption at about 1100 cm^{-1} assigned to the Si-O vibrations of amorphous silica with a three-dimensional framework was appeared, and its intensity was increased; (2) The characteristic band of amorphous silica at 800 cm^{-1} was gradually overlapped the doublet of quartz and its intensity was enhanced. For Acid-MMT-36/80, the 1040 cm^{-1} band was diminished as an inflection together with the dominated

Downloaded by PENNSYLVANIA STATE UNIV on May 31, 2012 | http://pubs.acs.org
Publication Date (Web): January 20, 2012 | doi: 10.1021/bk-2012-1092.ch011

Downloaded by PENNSYLVANIA STATE UNIV on May 31, 2012 | http://pubs.acs.org
Publication Date (Web): January 20, 2012 | doi: 10.1021/bk-2012-1092.ch011

Si-O band for amorphous silica, indicative of a severe depletion of the layered MMT structure. However, as revealed from the most sensitive band (520 cm^{-1}) to the presence/absence of residual Al in octahedral sheet (*12*), the layered MMT structure was still not completely depleted.

In the case of Acid-MMT-24/100, besides the IR absorptions of quartz (692 cm^{-1}), only IR peaks due to amorphous silica (1100, 800, and 465 cm^{-1}) and molecular water (1640 and 3450 cm^{-1}) were observed, indicative of the complete destruction of the layered MMT structure. This is agreeable with the XRD results. In summary, under the selected activation conditions, the activated MMT with different extents of structural destruction was obtained.

The Co-Supported Catalysts

The XRD patterns of the cobalt-supported MMTs are given in Figure 3. After loading 20 wt.% cobalt, the (001) diffraction of MMT was still clearly seen although its intensity was significantly decreased. Moreover, diffractions of the cubic Co_3O_4 (JCPDS 65-3103) at 2θ of 19.1, 31.4, 36.9, 44.9, 59.6, and 65.5° were observed for all the catalysts, indicating that the same phase of cobalt is formed independent of the specific MMT. Moreover, the crystal size of Co_3O_4 was in the ranges of 10-30 nm (Table 1), and clearly decreased with increasing the extent of the activation of MMT. Depending on the MMT support, the crystal size of metallic cobalt over the reduced catalysts was in the ranges of 10-20 nm.

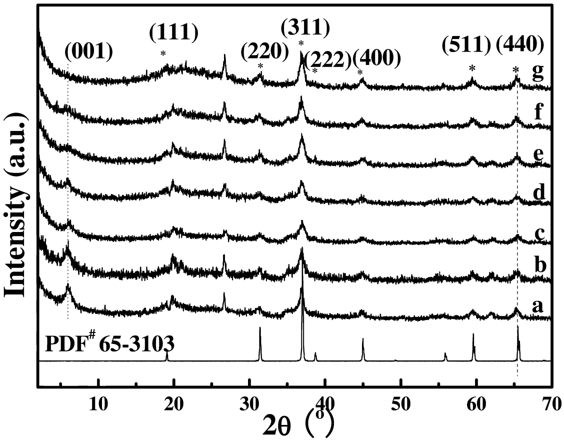

Figure 3. XRD patterns for 20 wt.% Co loaded on Na-MMT (a), Acid-MMT-4/60 (b), Acid-MMT-4/80 (c), Acid-MMT-12/80 (d), Acid-MMT-24/80 (e), Acid-MMT-36/80 (f), and Acid-MMT-24/100 (g).

Textural Properties

Morphology

A flake-like morphology is generally observed for MMT due to a regular pile of its plates. To evaluate the effect of the activation on the morphologic changes, various MMT samples were subjected to SEM observations. The typical SEM images of MMTs are shown in Figure 4. In the case of Na-MMT, irregular flakes with small patches of platelets were clearly seen. For Acid-MMT-4/80, however, clumps of agglomerated particles attached on MMT flakes were observed, reflecting the destruction of the MMT laminar structure. Further increasing the severity of the activation conditions, more agglomerates and much fewer flakes were found for Acid-MMT-24/80. Under the severest activation conditions, Acid-MMT-24/100 showed big clumps of amorphousness-like agglomerates. Thus, the destruction of the MMT laminar structure during the activation was clearly ascertained from the SEM observations, which are agreeable with the results of XRD and FTIR.

Downloaded by PENNSYLVANIA STATE UNIV on May 31, 2012 | http://pubs.acs.org
Publication Date (Web): January 20, 2012 | doi: 10.1021/bk-2012-1092.ch011

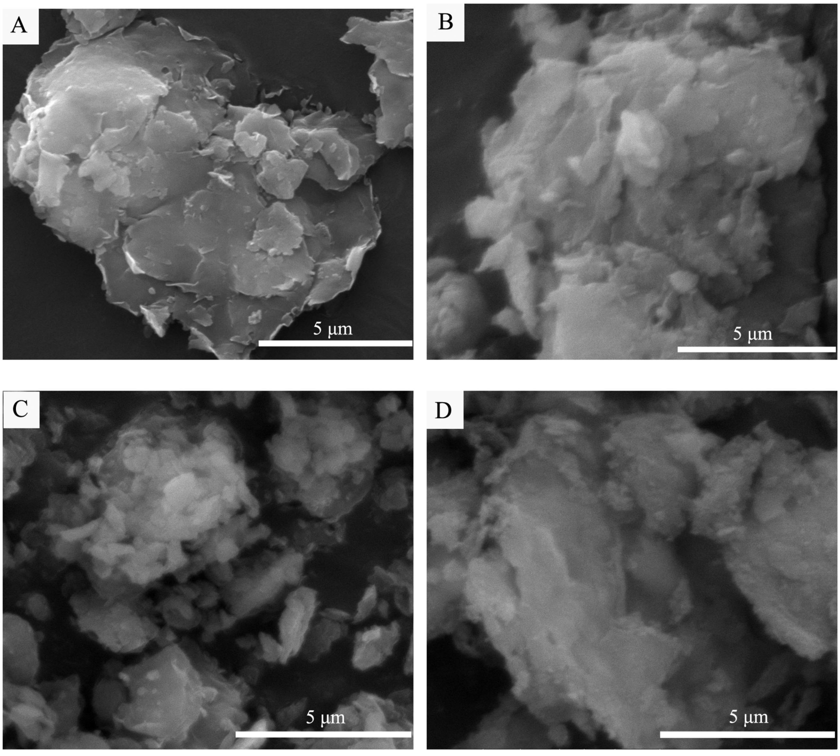

Figure 4. SEM images of Na-MMT (A), Acid-MMT-4/80 (B), Acid-MMT-24/80 (C), and MMT-24/100 (D).

Downloaded by PENNSYLVANIA STATE UNIV on May 31, 2012 | http://pubs.acs.org
Publication Date (Web): January 20, 2012 | doi: 10.1021/bk-2012-1092.ch011

Table 1. Textural and crystal properties of the MMTs and the 20 wt.% Co loaded samples

	BET Surface area (m^2/g)	*Pore volume ($cm^3 \cdot g^{-1}$)*	*Pore size (nm)*	*Na^+ (wt.%)*	*d (Co_3O_4) (nm)*	*d (Co^0) (nm)*
Na-MMT	10.7	0.09	33.0	4.31	---	---
Acid-MMT-4/60	133.6	0.18	5.3	3.81	---	---
Acid-MMT-4/80	141.3	0.24	6.8	3.73	---	---
Acid-MMT-12/80	188.3	0.33	7.0	3.37	---	---
Acid-MMT-24/80	227.4	0.52	9.1	3.13	---	---
Acid-MMT-36/80	244.8	0.70	11.5	3.04	---	---
Acid-MMT-24/100	185.6	0.90	19.3	2.84	---	---
Co/Na-MMT	18.6	0.08	17.6	---	26.7	20.2
Co/Acid-MMT-4/60	105.1	0.14	5.3	---	27.8	20.9
Co/Acid-MMT-4/80	129.5	0.18	5.4	---	23.2	17.4
Co/Acid-MMT-12/80	153.8	0.22	5.4	---	17.2	12.9
Co/Acid-MMT-24/80	162.0	0.29	7.2	---	17.0	12.7
Co/Acid-MMT-36/80	182.3	0.38	8.3	---	13.4	10.1
Co/Acid-MMT-24/100	180.6	0.29	6.4	---	13.1	9.8

Surface Area

The BET surface areas of different samples are summarized in Table 1. In the case of Na-MMT, its surface area was only about 10 m^2/g. On the contrary, a mild activation of the raw Na-MMT, i.e., Acid-MMT-4/60, produced a sharply increased BET surface area (133 m^2/g). For the MMT activated at 80 °C, the surface area was nonlinearly increased with increasing the activation time from 4 to 36 h. In comparison with Acid-MMT-36/80, the surface area of Acid-MMT-24/100 was significantly decreased. According to the results of XRD and FTIR, the delamination of the MMT laminar structure, i.e., decreasing the number of layers per stack, was occurred depending on the activation conditions. Moreover, the formation of amorphous silica for the MMT activated at 80 °C was enhanced with increasing the activation time, and Acid-MMT-24/100 was essentially amorphous silica. These facts suggest that the delaminated MMT has a higher surface area than amorphous silica. Following this deduction, changes of the surface area with the activation conditions are well explained.

Surface areas of the cobalt-loaded sample versus the corresponding MMT were strongly related to the specific sample. The surface area of Co/Na-MMT was slightly higher than that of Na-MMT, which can be reasonably attributed to the contribution from the cobalt oxide. However, in comparison with Acid-MMT-4/60, Co/Acid-MMT-4/60 showed a clearly decreased surface area. Moreover, more pronounced decrease in surface area was observed for Co/Acid-MMT-24/80 and Co/Acid-MMT-36/80. If pore volumes are examined (Table 1), this can be reasonably explained as the pore-blocking effect of the cobalt oxide. Contrary to this, comparable surface areas but significantly varied pore volumes were found for Acid-MMT-24/100 and Co/Acid-MMT-24/100. This can be explained as its different pore structures as revealed in the next section.

Evolution of Pore Structure

The N_2 adsorption-desorption isotherms of MMTs are given in Figure 5. As indicated from the isotherm, Na-MMT was essentially a nonporous material. On the contrary, the volume of the adsorbed N_2 over the activated MMTs was steeply increased with increasing p/p_0 in the ranges of 0-0.1, indicative of the presence of micropores. Moreover, the formation of mesopores was revealed from the gradual increase of the amount of N_2 adsorbed above the medium ranges of p/p_0. This was clearly indicated from the calculated pore volume (Table 1), which is significantly increased with increasing the severity of the activation conditions. Thus, both micropores and mesopores were created after the activation of Na-MMT. Based on the IUPAC classification (*33*), all the activated MMTs showed a type-IV isotherm. However, the hysteresis loop was strongly dependent on the activation conditions. In the cases of Acid-MMT-4/60, Acid-MMT-4/80, and Acid-MMT-12/80, a typical H4 hysteresis loop, in which the branches of the adsorption and the desorption are nearly horizontal and parallel in a wide ranges of p/p_0, was observed, indicative of the narrow slit-like pores (*33*). Moreover, a triangular shape with an almost horizontal desorption branch falling steeply close to the lower limit of the hysteresis loop was appeared. This phenomenon has widely been observed for pillared clays, which is explained as the presence of disordered domains from the collapsed laminar structure (*6*). This explanation is well supported by our XRD and FTIR results. Acid-MMT-24/80 exhibited a transition from an H4 to an H3 type hysteresis, and more similar to an H3 type hysteresis loop was observed for Acid-MMT-36/80. Generally, the slit-shaped pores originated from loosely coherent plate-like particles are interpreted for an H3 type hysteresis loop (*33*). As revealed from XRD and FTIR, Acid-MMT-36/80 showed a higher extent of delamination than Acid-MMT-24/80, which is agreeable with the explanation on the observed hysteresis loops. Although a typical H3 type hysteresis was observed for Acid-MMT-24/100, the branches of adsorption and desorption were nearly parallel at p/p_0 greater than 0.8, which is interpreted as the presence of open cylindrical mesopores (*34*). Considering that Acid-MMT-24/100 was amorphous silica in nature, cylindrical pores were more reasonable. Thus, the size and shape of the hysteresis loops indicated the evolution and transformation of slit-like, slit-shaped to cylindrical pores with increasing the severity of the activation conditions.

As shown in Table 1, the average pore size was continuously increased with increasing the severity of the activation conditions. Based on the isotherms

Downloaded by PENNSYLVANIA STATE UNIV on May 31, 2012 | http://pubs.acs.org
Publication Date (Web): January 20, 2012 | doi: 10.1021/bk-2012-1092.ch011

(Figure 5), the pore size distribution was calculated to get more information on the pore property. In the case of micropores, very similar patterns determined by the Horvarth-Kawazoe equation were observed for all the MMTs (data not shown). However, as shown in Figure 6, great differences were present for the mesopore size distribution based on the BJH method. The pore size distributions of Acid-MMT-4/60, Acid-MMT-4/80, and Acid-MMT-12/80 were essentially the same, i.e., a narrow pore size distribution centered at about 3.7 nm. On the contrary, a bimodal pore structure centered at about 3.7 and 5.5 nm was developed for Acid-MMT-24/80. In the cases of Acid-MMT-36/80 and Acid-MMT-24/100, the pore size distributions were very broad, and the peak maxima were located at about 10.5 and 15.6 nm, respectively. Thus, increasing the severity of the activation conditions, the peak pore size was increased, and the pore size distribution became wider. This is nicely agreeable with the events occurred during the activation, i.e., destruction of the MMT laminar structure, leaching of Al^{3+}, etc., as revealed from XRD and FTIR studies.

Acidity and Reduction Behavior

Acidic Properties

The acidic properties of the MMTs were evaluated by NH_3-TPD method, and the results are shown in Figure 7. The acidity of materials based on the NH_3-TPD profile is broadly classified as weaker acidic sites (the temperature at peak maximum of about 210 °C) and stronger acidic sites (the temperature at peak maximum of about 380 °C). The raw Na-MMT was basically non acidic. On the contrary, significant amounts of weaker and stronger acidic sites were created after the acid activation of Na-MMT. During the activation of clays, two main factors are reported to be responsible for the increased acidity (*13*): (1) The exchange of interlayer cations with protons; (2) The formation of the tetrahedral Al^{3+} originated from leaching one of the pair of the octahedrally coordinated Al^{3+}. Moreover, a further leaching of the tetrahedral Al^{3+} under the severer activation conditions leads to a decreased acidity (*13*). Thus, a maximum acidity is generally observed with increasing the degree of the activation. By examining the NH_3-TPD profiles in Figure 7, a maximum amount of acidic sites was observed for Acid-MMT-12/80. Additionally, a slightly decreased amount of acidic sites over Acid-MMT-24/80 than that over Acid-MMT-12/80 was coincided with the starting of the obvious leaching of the tetrahedral Al^{3+}, as indicated from the clear IR shoulder adsorptions at 1100 cm^{-1} (Figure 2). Moreover, a further decrease in the amount of acidic sites and an increase in the maximum temperature of the NH_3-TPD peak for Acid-MMT-36/80 were reasonably ascribed to the obvious leaching of the tetrahedral Al^{3+}. It should be noted that the acidic differences for those activated MMTs were very limited as revealed from the NH_3-TPD profiles. On the contrary, significantly lower acidity was found for Acid-MMT-24/100 due to the complete leaching of the isomorphous substituted cations as revealed from FTIR results. Moreover, the acidity of Acid-MMT-24/100 can be reasonably assigned to the protonated amorphous silica.

Downloaded by PENNSYLVANIA STATE UNIV on May 31, 2012 | http://pubs.acs.org
Publication Date (Web): January 20, 2012 | doi: 10.1021/bk-2012-1092.ch011

Downloaded by PENNSYLVANIA STATE UNIV on May 31, 2012 | http://pubs.acs.org
Publication Date (Web): January 20, 2012 | doi: 10.1021/bk-2012-1092.ch011

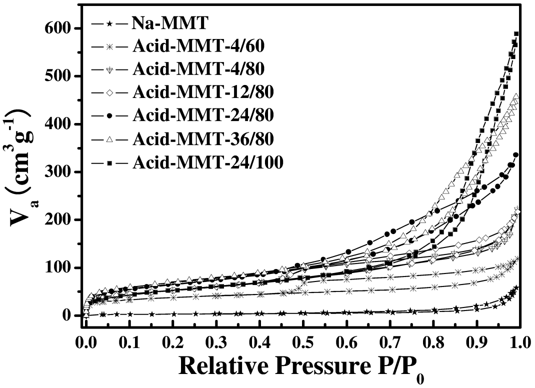

Figure 5. N_2 adsorption-desorption isotherms of MMTs.

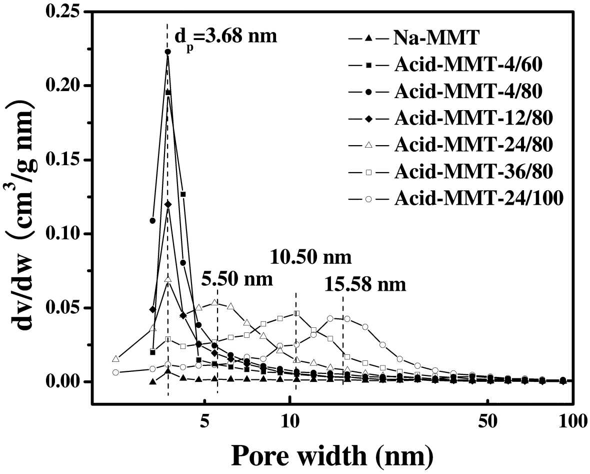

Figure 6. Mesopore size distribution calculated by the BJH method using desorption branch.

Downloaded by PENNSYLVANIA STATE UNIV on May 31, 2012 | http://pubs.acs.org
Publication Date (Web): January 20, 2012 | doi: 10.1021/bk-2012-1092.ch011

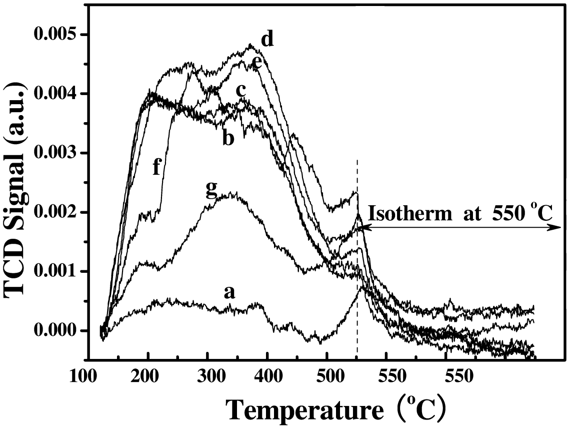

Figure 7. NH_3-TPD profiles of Na-MMT (a), Acid-MMT-4/60 (b), Acid-MMT-4/80 (c), Acid-MMT-12/80 (d), Acid-MMT-24/80 (e), Acid-MMT-36/80 (f), and Acid-MMT-24/100 (g).

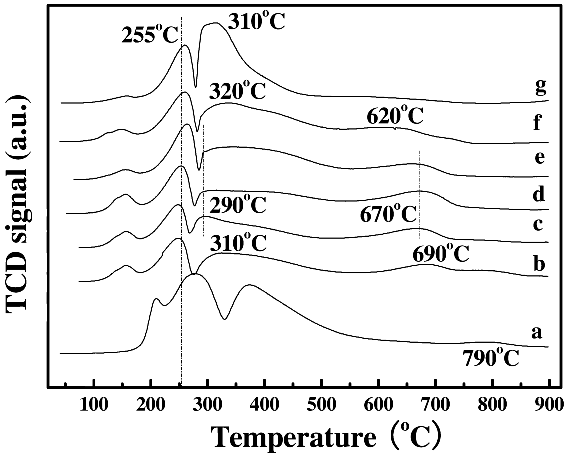

Figure 8. H_2-TPR profiles for the 20 wt.% Co loaded on Na-MMT (a), Acid-MMT-4/60 (b), Acid-MMT-4/80 (c), Acid-MMT-12/80 (d), Acid-MMT-24/80 (e), Acid-MMT-36/80 (f), and Acid-MMT-24/100 (g).

Reduction of Cobalt Oxides

The H_2-TPR profiles of the Co-supported catalysts are given in Figure 8. All the catalysts showed a small peak at a maximum temperature of about 160 °C (a shoulder peak at about 210 °C for Co/Na-MMT). This may be ascribed to the reduction of Co_3O_4 having bigger particle sizes or the decomposition of the residual $Co(NO_3)_2$, which may not be totally decomposed during calcining the catalyst at 200 °C (*35*). The reduction of Co_3O_4 to metallic Co over the supported catalysts is well established to occur in two consecutive steps via CoO intermediate. In the case of Co/Na-MMT, the temperature at peak maximum for the reduction of Co_3O_4 and CoO was at about 273 and 375 °C, respectively. It is noteworthy that a small but clear reduction peak at about 790 °C was observed. Commonly, the reduction of the cobalt ions entrapped into zeolite framework is significantly retarded (*36*). Thus, the high temperature at peak maximum of 790 °C can be reasonably ascribed to the reduction of the cobalt oxide located in the MMT interlayer, indicating that ion-exchange of Co^{2+} is occurred during impregnation of $Co(NO_3)_2$. In comparison with Co/Na-MMT, the temperatures at peak maxima for the reduction of Co_3O_4 and CoO were clearly decreased for all the Co/activated MMT catalysts. Moreover, almost identical temperature (~255 °C) and shape of the peak for the reduction of Co_3O_4 were observed. On the contrary, the reduction of CoO was strongly dependent on the specifically activated MMT, which may be induced from the varied pore properties and chemical compositions. This was supported by comparing the small H_2-TPR peaks at higher temperature above 600 °C due to the reduction of the cobalt oxide located in the MMT interlayer region. The decreased peak temperature from 690 °C (Co/Acid-MMT-4/60) to 620 °C (Co/Acid-MMT-36/80) was well agreeable with the increased average pore size from 5.3 to 8.3 nm. Moreover, the clear impact of the MMT interlayer structure on the reduction behavior of the catalysts was unambiguously revealed from the disappearance of the high temperature peak for Co/Acid-MMT-24/100, in which the MMT interlayer structure is completely destructed.

FT Performance

Activity

Co/Na-MMT was essentially non-active for the FT synthesis (less than 5% CO conversion). Moreover, CH_4 was the main product, and its selectivity was over 40% at a time on stream (TOS) of 10 h. Thus, Co/Na-MMT is not a suitable catalyst for the FT reaction. On the contrary, a significantly increased CO conversion was obtained over the Co/activated MMT catalysts (Figure 9a). Moreover, CO conversion was stable after a TOS of about 3 h. The CO conversion at steady state was decreased in the order of Co/Acid-MMT-24/100 >> Co/Acid-MMT-36/80 ≈ Co/Acid-MMT-24/80 > Co/Acid-MMT-12/80 ≈ Co/Acid-MMT-4/80 > Co/Acid-MMT-4/60. For a comparison purpose, 20 wt.% cobalt impregnated on silica (Fujisilicia Q-15, surface area=200 m^2/g, average pore size=15 nm, pore volume=1.0 mL/g) was investigated for the FT

Downloaded by PENNSYLVANIA STATE UNIV on May 31, 2012 | http://pubs.acs.org
Publication Date (Web): January 20, 2012 | doi: 10.1021/bk-2012-1092.ch011

reaction under the same conditions. From the summarized results of the FT reaction (Table 2), the CO conversion over Co/Q-15 was obviously lower than that over Co/Acid-MMT-24/100 although the supports were essentially silica. Thus, the FT activity was strongly dependent on the activation conditions of Na-MMT. The reason will be discussed in the next section in combination with the characterization results.

Downloaded by PENNSYLVANIA STATE UNIV on May 31, 2012 | http://pubs.acs.org
Publication Date (Web): January 20, 2012 | doi: 10.1021/bk-2012-1092.ch011

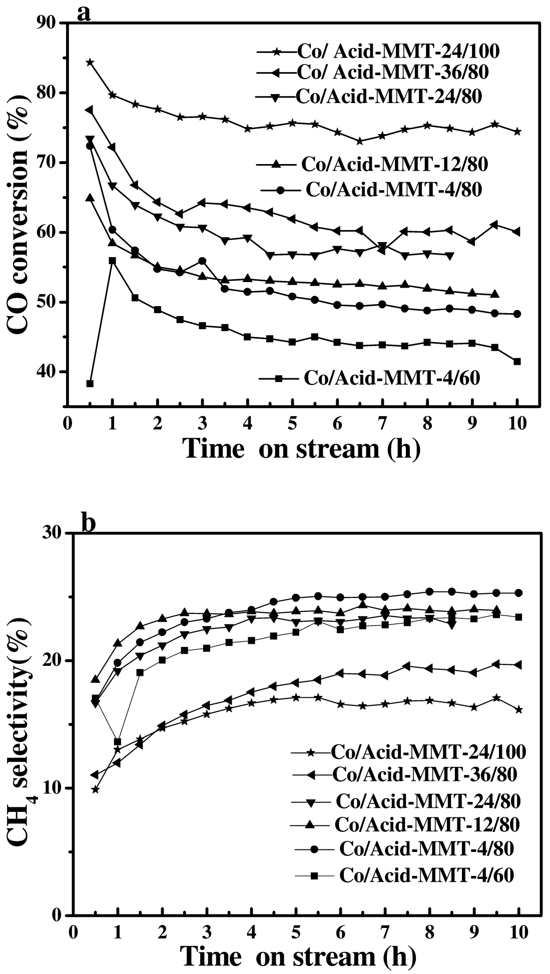

Figure 9. Time-on-stream CO conversion (a) and CH_4 selectivity (b) over 20 wt.% Co loaded on MMT derived materials.

Downloaded by PENNSYLVANIA STATE UNIV on May 31, 2012 | http://pubs.acs.org
Publication Date (Web): January 20, 2012 | doi: 10.1021/bk-2012-1092.ch011

Table 2. Main results of the FT synthesis over different catalysts*

Catalyst	*CO conv. (%)*	*CO_2 sele. (%)*	*Hydrocarbon distribution (%)*				
			C_1	C_2~C_3	C_4~C_{12}	C_{13}~C_{20}	C_{21}^+
Co/Q-15#	54.9	1.5	10.07	3.78	34.47	13.69	37.99
Co/Acid-MMT-4/60	44.2	1.1	22.21	7.30	37.55	6.48	26.46
Co/Acid-MMT-4/80	50.8	2.7	24.92	7.84	39.12	6.51	21.61
Co/Acid-MMT-12/80	52.9	1.3	23.86	7.88	41.02	6.68	20.56
Co/Acid-MMT-24/80	56.9	1.5	23.06	7.84	38.12	3.58	27.40
Co/Acid-MMT-36/80	61.9	1.0	18.27	7.36	41.69	6.65	26.04
Co/Acid-MMT-24/100	75.7	1.7	17.11	6.02	38.22	5.43	33.22

* Operating conditions: W/F = 5.05 g h/mol, P = 1 MPa, T = 508 K, TOS = 5 h. # SiO_2, Fujisilicia Q-15.

Product Distribution

As shown in Table 2, all the catalysts showed a low CO_2 selectivity due to the low catalytic activity of cobalt for the water-gas-shift reaction. The CH_4 selectivity over MMT-based catalysts was generally higher than that over Co/Q-15, and a decreasing order was observed with increasing the severity of the activation conditions. Significantly, in comparison with the results over Co/Q-15, all the MMT-based catalysts showed a higher selectivity of C_4~C_{12} and a lower selectivity of C_{21}^+ hydrocarbons, which is clearly deviated from the ASF distribution. Moreover, increasing the degree of the activation of Na-MMT, the maximum selectivity of C_4~C_{12} and the minimum selectivity of C_{21}^+ hydrocarbons were observed over Co/Acid-MMT-12/80. Thus, the Co-supported activated MMT is a promising catalyst for selectively synthesizing liquid hydrocarbons via the FT route provided the activation conditions are suitably optimized. In addition, all the MMT-based catalysts showed quite similar selectivities of C_2~C_3 hydrocarbons, which is almost doubled than that over Co/Q-15. On the contrary, the selectivity of C_{13}~C_{20} hydrocarbons over the MMT-based catalysts, which slightly depends on the activation conditions, was only about half of that over Co/Q-15.

Downloaded by PENNSYLVANIA STATE UNIV on May 31, 2012 | http://pubs.acs.org
Publication Date (Web): January 20, 2012 | doi: 10.1021/bk-2012-1092.ch011

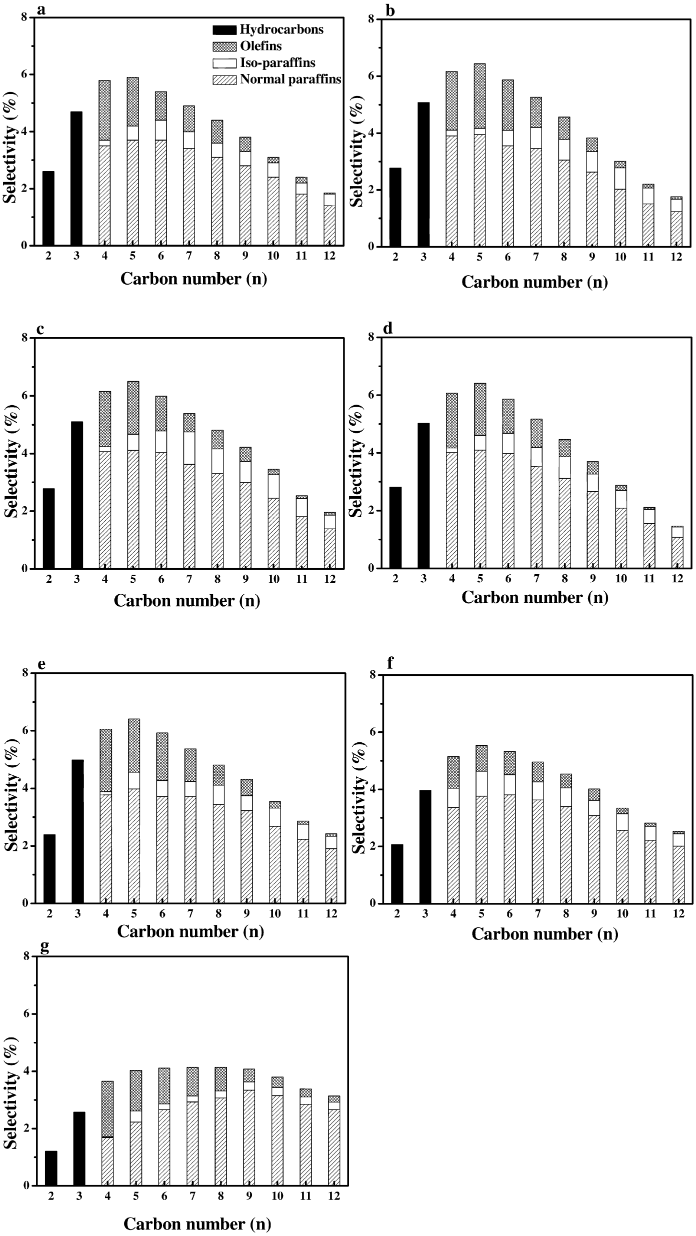

Figure 10. The carbon number distribution of FT hydrocarbons at TOS of 5 h over 20 wt.% Co loaded on Acid-MMT-4/60 (a), Acid-MMT-4/80 (b), Acid-MMT-12/80 (c), Acid-MMT-24/80 (d), Acid-MMT-36/80 (e), Acid-MMT-24/100 (f), and Co/Q-15 (g).

Downloaded by PENNSYLVANIA STATE UNIV on May 31, 2012 | http://pubs.acs.org
Publication Date (Web): January 20, 2012 | doi: 10.1021/bk-2012-1092.ch011

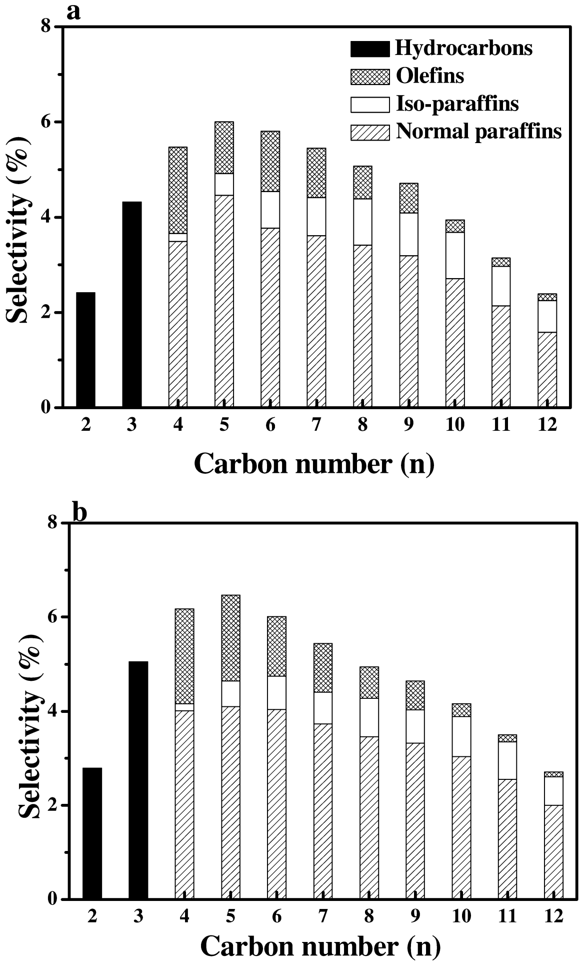

Figure 11. The carbon number distribution of FT products at TOS of 2 h (a) and 10 h (b) over 20 wt.% Co/Acid-MMT-24/80.

The detailed carbon number distribution is very helpful to understand the reaction mechanism. Thus, detailed carbon number distributions of C_2 to C_{12} hydrocarbons at steady state were calculated, and the results are given in Figure 10. The most significant observation for the MMT-based catalysts was as follows: (1) Normal paraffins were the main product irrespective of carbon numbers and catalysts; (2) The selectivity of branched alkanes was very low, and almost independent of the specific catalyst. In comparison with Co/Q-15, Co/Acid-MMT-4/60 showed much higher selectivity of C_2-C_3 hydrocarbons and C_4-C_7 paraffins, and obviously lower selectivity of C_{10}-C_{12} paraffins. Moreover, the carbon number distributions over Co/Acid-MMT-4/60 and Co/Acid-MMT-4/80 were very similar, and only a slight difference in the selectivity of C_2-C_7 hydrocarbons was observable. Comparing the results over Co/Acid-MMT-4/80, Co/Acid-MMT-12/80, and Co/Acid-MMT-24/80, almost identical distributions of C_2-C_{12} hydrocarbons were found. Co/Acid-MMT-36/80 showed a slightly lower selectivity of C_2 hydrocarbons and higher selectivity of C_7-C_{12} hydrocarbons than those over Co/Acid-MMT-24/80. However, a clearly decreased selectivity of C_2-C_8 hydrocarbons contributed mainly from olefins was perceived over Co/Acid-MMT-24/100.

To evaluate the stability of the product composition, the detailed carbon number distributions of C_2-C_{12} hydrocarbons over Co/Acid-MMT-24/80 at TOS of 2 and 10 h were determined, and the results are given in Figure 11. Comparing the results in Figure 10d and Figure 11, there were only very tiny variations in the carbon number distributions with increasing TOS from 2 to 10 h, indicating a very stable product composition.

Downloaded by PENNSYLVANIA STATE UNIV on May 31, 2012 | http://pubs.acs.org
Publication Date (Web): January 20, 2012 | doi: 10.1021/bk-2012-1092.ch011

Structure and Catalytic Performance

Main Factors for Activity

Although Co/Na-MMT showed bad performance for the FT reaction, CO conversion over the Co/Activated MMTs was significantly increased. The crystal size of Co is believed to be a key factor to determine the activity of the FT reaction over Co-supported catalysts. However, the recent work indicates that the cobalt-time-yield is essentially constant with increasing the crystal size of Co from 10.4 to 141 nm (*37*). In our case, the crystal size of Co over all the catalysts is less than 21 nm, and is only slightly dependent on the specific support (Table 1). Thus, the great differences in CO conversion over different catalysts cannot be induced from the slight variation of the crystal size of Co.

In recent years, the presence of Na^+ over Co-supported catalysts has been reported to significantly decrease the activity of the FT synthesis (*38*, *39*). Thus, the CO conversion against the content of Na^+ over different catalysts is plotted. As indicated in Figure 12, there exists a strong negative correlation between the CO conversion and the content of Na^+. This indicates that the content of Na^+ is a key factor to determine the activity of the FT synthesis over the MMT-based catalysts. For the FT synthesis over Co-based catalysts, reports on the effect of alkali metal ions as either impure or added promoters are fewer, and its mechanism is not clear (*38–40*). However, to explain the FT results over alkali cations-especially Na^+, K^+, promoted group VIII metals-mainly Fe (*41*), the following models are postulated as: (1) Site blocking; (2) The metal electronic interactions; (3) The direct chemical interactions; (4) The alkali-induced surface reconstructions; (5) The electrostatic interactions. In our case, to balance the negative charges of the MMT layer, Na^+ is a natural component in the MMTs. Moreover, except Co/Acid-MMT-24/100, Na^+ is mainly located in the interlayer region of the MMTs, and cobalt species are principally present on the external surfaces of the MMT interlayer. Thus, the former four models cannot be applied to explain our results. In fact, as revealed from Table 1 and Figure 2, the decreasing of the content of Na^+ is accompanied with the increasing of the destruction of the MMT laminar structure. Moreover, the reduction extent of cobalt is clearly increased with the destruction of the MMT laminar structure (Figures 2, 8). After complete destruction of the MMT laminar structure, Co/Acid-MMT-24/100 shows the highest CO conversion among the tested catalysts. Based on these facts and the reasoning, the poisoning effect of Na^+ on the FT synthesis over Co/MMT catalysts may be originated from the electrostatic interactions of Na^+ and cobalt species via the MMT interlayer structure.

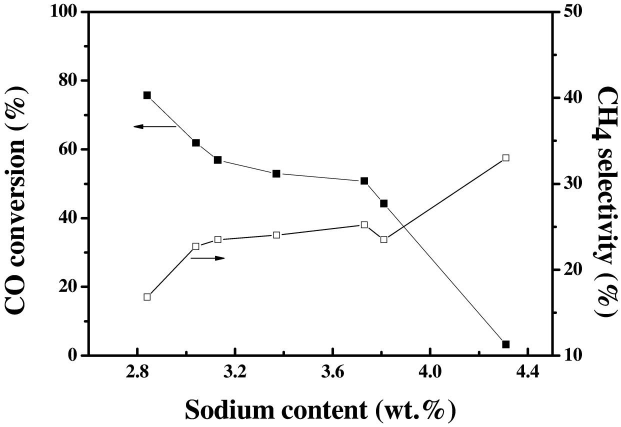

Figure 12. The steady-state CO conversion and CH_4 selectivity versus the content of Na^+ over different MMT-based catalysts.

It is noteworthy that the chemical compositions of the activated MMTs are clearly dependent on the activation conditions due to the leaching of the substituted cations of Al, Fe, and Mg. Consequently, the interaction between Co and the activated MMT may be varied, leading to some changes in the reduction behavior of the catalysts. This cannot be excluded based on the available data.

Reasons for the Deviation of ASF Distribution

After treatment of Na-MMT with HNO_3, acidic sites are created depending on the activation conditions (Figure 7). As reported in many works, depending on the acidity of the catalysts, cracking/isomerization reactions of long-chain FT hydrocarbons are occurred in different extents (*42*, *43*). In our case, the comparable selectivies of iso-paraffins over Co/Acid-MMT and Co/Q-15 indicate that isomerization reactions are negligibly occurred (Figure 10). This phenomenon has been observed in our previous studies on the FT synthesis over Co/pillared MMT (*26*) and Co/ion-exchanged MMT catalysts (*44*). It has been reported that the isomerization reaction is significant only above 277 °C for the hydroconversion of normal heptane over 1 wt.% Pt-supported MMT pillared with alumina or silica (*45*), which is consistent with our observations. Moreover, higher selectivity of iso-paraffins over Co/ZSM-5 and Co/MCM-22 than Co/MMT at 230 °C is explained as the stronger acidity of zeolite than the clay (*46*). A recent work on the hydroisomerization of long-chain n-alkanes over Pt/zeolite catalysts reveals that the zeolite structure, especially the porosity, plays an important role in determining the product selectivities, which extensive cracking are occurred

Downloaded by PENNSYLVANIA STATE UNIV on May 31, 2012 | http://pubs.acs.org
Publication Date (Web): January 20, 2012 | doi: 10.1021/bk-2012-1092.ch011

over Pt/MCM-22 and Pt/ZSM-5 due to the blockage of the reaction intermediates inside the porosity of these zeolites (*47*). Thus, in the present case, the low degree of isomerization can be reasonably attributed to the relatively low reaction temperature, the weak acidity and the microporosity of the activated MMTs. However, much higher selectivities of C_2-C_{12} hydrocarbons and significantly lower selectivities of C_{21}^+ hydrocarbons over Co/Acid-MMT catalysts than over Co/Q-15 are obtained (Table 2). Thus, cracking of the long-chain FT hydrocarbons over acidic sites of activated MMTs is significantly occurred, and is responsible for the deviation of the product selectivity from the ASF distribution. The highest amount of acidic sites over Acid-MMT-12/80 (Figure 7) versus the highest selectivity of C_4-C_{12} hydrocarbons and the lowest selectivity of C_{21}^+ hydrocarbons (Table 2) over the corresponding catalyst supports this explanation. Moreover, the change in the acidity of Acid-MMT-4/60, Acid-MMT-4/80, and Acid-MMT-12/80 is agreeable with the variation in the selectivity of C_{21}^+ and C_4-C_{12} hydrocarbons over the respective Co-supported catalysts. If the distribution of the acidic sites over Acid-MMT-24/80 and Acid-MMT-36/80 are considered, the catalytic results in Table 2 over the corresponding catalysts are easily understandable. Because of the significantly lower amount of acidic sites and the clearly higher CO conversion (more long-chain FT hydrocarbons produced), the comparable selectivities of C_4-C_{12} and C_{21}^+ hydrocarbons over Co/ Acid-MMT-24/100 and Co/Q-15 are reasonable.

Due to the presence of metallic Co and acidic sites, Co/Acid-MMT is essentially a bifunctional catalyst, which may catalyze hydrocracking reactions. Indeed, in comparison with the results over Co/Q-15, significantly higher selectivities of C_4-C_7 normal paraffins and only slightly higher selectivities of C_4-C_6 olefins are observed over Co/Acid-MMT catalysts except Co/Acid-MMT-24/100 (Figure 10). This indicates that both hydrocracking and cracking reactions are occurred although the former is dominant. On the contrary, significantly increased selectivities of C_4-C_7 normal alkanes and clearly decreased selectivities of C_4-C_8 alkenes over Co/Acid-MMT-24/100 than those over Co/Q-15 rule out the occurring of the cracking reaction, and only hydrocracking reactions are responsible for the observed product distribution. This is reasonable if the structure of the catalyst and the spillover mechanism of hydrocracking reactions (*48*) are taken into account. As revealed from the characterization results (Figures 1-2), the layered MMT structure is only partially destructed from Acid-MMT-4/60 to Acid-MMT-36/80. Moreover, Co is mainly located on the external surfaces of the MMTs, and the acidic sites are originated from the sheet and interlayer regions of the MMTs. Thus, due to the long distance, the spillover of hydrogen from Co to the acidic sites over these catalysts may be weakened, leading to the occurrence of both hydrocracking and cracking reactions. On the contrary, Acid-MMT-24/100 is essentially a protonated amorphous silica (Figures 1-2) due to the complete destruction of the layered MMT structure, in which the inhibition on the spillover of hydrogen is disappeared. Consequently, only hydrocracking reaction is occurred over Co/Acid-MMT-24/100. In accordance with this explanation, the specific product distribution of the FT reaction over different catalysts is understandable by taking account of the CO conversion, and the acidic and structural characteristics of the materials.

Downloaded by PENNSYLVANIA STATE UNIV on May 31, 2012 | http://pubs.acs.org
Publication Date (Web): January 20, 2012 | doi: 10.1021/bk-2012-1092.ch011

As shown in Table 2 and Figure 9b, the selectivity of CH_4 over Acid-MMT-based catalysts is clearly higher than that over Co/Q-15. According to the generally accepted carbonium mechanism for cracking/hydrocracking reactions (*49*), the formation of CH_4 is much less favored. This is supported by the clearly different selectivities of C_{21}^+ hydrocarbons but similar selectivities of CH_4 over Co/Acid-MMT-4/60 and Co/Acid-MMT-12/80. Thus, considering the lower reaction temperature and the lower acidity of the Acid-MMT, higher selectivity of CH_4 over Co/Acid-MMT catalysts should not be originated from the cracking of the long-chain FT hydrocarbons. Although the FT reaction over a Co-based catalyst with a smaller pore size is reported to give a higher selectivity of CH_4 (*50*), this is not valid in our case because of the comparable pore sizes but clearly varied selectivities of CH_4 over Co/Acid-MMT-24/80, Co/Acid-MMT-36/80, and Co/Acid-MMT-24/100. Thus, the higher selectivity of CH_4 over the Acid-MMT-based catalysts must be caused by other factors.

As shown in Figure 12, an almost linear correlation between the content of Na^+ and the selectivity of CH_4 over different catalysts is disclosed, indicating that the content of Na+ is an important factor to determine the selectivity of CH_4. Moreover, combining the selectivities of CH_4 over Co/Na-MMT, Co/Acid-MMT-36/80, and Co/Acid-MMT-24/100 (Table 2) with the structural information of the Acid-MMT (Figures 1-2), effect of the MMT interlayer structure on the selectivity of CH_4 cannot be excluded. For the FT synthesis over Co-based catalysts, a high selectivity of CH_4 has been assigned to the presence of unreduced cobalt oxides (*51*). Indeed, as revealed from the H_2-TPR patterns and the reduction peak above 600 °C (Figure 8), the unreduced cobalt oxides are clearly present over the MMT-based catalysts after reduction at 400 °C. Thus, the higher selectivity of CH_4 over the MMT-based catalysts can be reasonably attributed to the higher content of Na^+, the MMT interlayer structure, and the presence of unreduced cobalt oxides. Since the thus mentioned factors are inter-correlated to each other, the essence of these factors influencing the selectivity of CH_4 cannot be conclusively revealed based on the available data.

Downloaded by PENNSYLVANIA STATE UNIV on May 31, 2012 | http://pubs.acs.org
Publication Date (Web): January 20, 2012 | doi: 10.1021/bk-2012-1092.ch011

Conclusions

In summary, depending on the activation conditions of Na-MMT, significant amounts of acidic sites and mesopores were created for the activated MMTs. Although Co/Na-MMT is a bad catalyst for the FT synthesis, a high CO conversion similar to that over Co/SiO_2 was achieved over the Co/activated MMT catalysts. More importantly, ~41% C_4-C_{12} hydrocarbons and less than 21% C_{21}^+ hydrocarbons were obtained over Co/Acid-MMT-12/80, which is significantly deviated from the ASF distribution over Co/SiO_2. We demonstrated for the first time that the Co/activated MMT is a promising catalyst for selectively synthesizing liquid fuels via the FT route provided the suitable activation conditions are applied for Na-MMT. The content of Na^+ was revealed to be the main factor to control the FT activity, and the acidity of the activated MMT was responsible for the narrowed product distribution. Thus, a further detailed optimization of the activation conditions of the Na-MMT based on the present work may create a more efficient catalyst for improving the selectivity of the liquid FT hydrocarbons, and is worthy to be investigated. One more necessary study is to reveal the mechanistic nature for the effect of Na^+ on the FT activity. Considering the complex composition of the natural MMT, a synthetic material with a layered structure may be a better choice.

Acknowledgments

The financial support provided by National Natural Science Foundation of China (20876095) is highly acknowledged. The partial financial support from the Program for New Century Excellent Talents in University (NCET-08-0799), and the Fundamental Research Funds for the Central Universities (2010ZYGX012, GK201002043) and the SRF for Returned Overseas Chinese Scholars by MOE is also acknowledged.

Downloaded by PENNSYLVANIA STATE UNIV on May 31, 2012 | http://pubs.acs.org
Publication Date (Web): January 20, 2012 | doi: 10.1021/bk-2012-1092.ch011

References

1. Bergaya, F.; Lagaly, G. In *Handbook of Clay Science*; Bergaya, F., Theng, G. K. G., Lagaly, G., Eds.; Developments in Clay Science; Elsevier: Amsterdam, 2006; Vol. 1, pp 1−19.
2. Annabi-Bergaya, F. *Microporous Mesoporous Mater.* **2008**, *107*, 141–148.
3. Bergaya, F.; Theng, G. K. G.; Lagaly, G. *Handbook of Clay Science*; Bergaya, F., Theng, G. K. G., Lagaly, G., Eds.; Developments in Clay Science; Elsevier: Amsterdam, 2006; Vol. 1, pp 499−752.
4. Stefanis, A. D.; Tomlinson, A. A. G. *Catal. Today* **2006**, *114*, 126–141.
5. Nagendrappa, G. *Appl. Clay Sci.* **2011**, in press, DOI: 10.1016/j.clay.2010.09.016.
6. Gil, A.; Korili, S. A.; Vicente, M. A. *Catal. Rev. Sci. Eng.* **2008**, *50*, 153–221.
7. Centi, G.; Perathoner, S. *Microporous Mesoporous Mater.* **2008**, *107*, 3–15.
8. Vaccari, A. *Appl. Clay Sci.* **1999**, *14*, 161–198.
9. Wallis, P. J.; Gates, W. P.; Patti, A. F.; Scott, J. L.; Teoh, E. *Green Chem.* **2007**, *9*, 980–986.
10. Steudel, A.; Batenburg, L. F.; Fischer, H. R.; Weidler, P. G.; Emmerich, K. *Appl. Clay Sci.* **2009**, *44*, 105–115.
11. Chitnis, S. R.; Sharma, M. M. *React. Funct. Polym.* **1997**, *32*, 93–115.
12. Breen, C.; Madejova, J.; Komadel, P. *Appl. Clay Sci.* **1995**, *10*, 219–230.
13. Kumar, P.; Jasar, R. V.; Bhat, T. S. G. *Ind. Eng. Chem. Res.* **1995**, *34*, 1440–1448.
14. Hart, M. P.; Brown, D. R. *J. Mol. Catal. A: Chem.* **2004**, *212*, 315–321.
15. Kooli, F. *Thermochim. Acta* **2009**, *486*, 71–76.
16. Komadel, P.; Madejova, J. In *Handbook of Clay Science*; Bergaya, F., Theng, G. K. G., Lagaly, G., Eds.; Developments in Clay Science; Elsevier: Amsterdam, 2006; Vol. 1, pp 263−287.
17. Leckel, D. *Energy Fuels* **2009**, *23*, 2342–2358.
18. Dry, M. E. *Catal. Today* **2002**, *71*, 227–241.

Downloaded by PENNSYLVANIA STATE UNIV on May 31, 2012 | http://pubs.acs.org
Publication Date (Web): January 20, 2012 | doi: 10.1021/bk-2012-1092.ch011

19. Dry, M. E. *Appl. Catal., A* **2004**, *276*, 1–3.
20. Tsubaki, N.; Fujimoto, K. *Fuel Process. Technol.* **2000**, *62*, 173–186.
21. Bi, Y.; Dalai, A. K. *Can. J. Chem. Eng.* **2003**, *81*, 230–242.
22. Bessel, S. *Appl. Catal., A* **1995**, *126*, 235–244.
23. Botes, F. G.; Bohringer, W. *Appl. Catal., A* **2004**, *267*, 217–225.
24. Liu, Z.-W.; Li, X.; Asami, K.; Fujimoto, K. *Ind. Eng. Chem. Res.* **2005**, *44*, 7329–7336.
25. Liu, Z.-W.; Li, X.; Asami, K.; Fujimoto, K. *Appl. Catal., A* **2006**, *300*, 162–169.
26. Hao, Q.-Q.; Wang, G.-W.; Liu, Z.-T.; Lu, J.; Liu, Z.-W. *Ind. Eng. Chem. Res.* **2010**, *49*, 9004–9011.
27. Ferrage, E.; Lanson, B.; Malikova, N.; Plancon, A.; Sakharov, B. A.; Drits, V. A. *Chem. Mater.* **2005**, *17*, 3499–3512.
28. Oueslati, W.; Rhaiem, H. B.; Lanson, B.; Amara, A. B. H. *Appl. Clay Sci.* **2009**, *43*, 224–227.
29. Tyagi, B.; Chudasama, C. D.; Jasra, R. V. *Spectrochim. Acta, Part A* **2006**, *64*, 273–278.
30. Madejova, J.; Bujdak, J.; Janek, M.; Komadel, P. *Spectrochim. Acta, Part A* **1998**, *54*, 1397–1406.
31. Breen, C.; Zahoor, F. D. *J. Phys. Chem. B* **1997**, *101*, 5324–5331.
32. Vicente-Rodriguez, M. A.; Suarez, M.; Banares-Munoz, M. A.; Lopez-Gonzalez, J. de Dios *Spectrochim. Acta, Part A* **1996**, *52*, 1685–1694.
33. Sing, K. S. W.; Everett, D. H.; Haul, R. A. W.; Moscou, L.; Pierotti, R. A.; Rouquerol, J.; Siemieniewska, T. *Pure Appl. Chem.* **1985**, *57*, 603–619.
34. de Jong, K. P.; Zecevic, J.; Friedrich, H.; de Jongh, P. E.; Bulut, M.; van Donk, S.; Kenmogne, R.; Finiels, A.; Hulea, V.; Fajula, F. *Angew. Chem., Int. Ed.* **2010**, *49*, 10074–10078.
35. Borg, Ø.; Eri, S.; Blekkan, E. A.; Storsæter, S.; Wigum, H.; Rytter, E.; Holmen, A. *J. Catal.* **2007**, *248*, 89–100.
36. Resini, C.; Montanari, T.; Nappi, L.; Bagnasco, G.; Turco, M.; Busca, G.; Bregani, F.; Notaro, M.; Rocchini, G. *J. Catal.* **2003**, *214*, 179–190.
37. Prieto, G.; Martinez, A.; Concepcion, P.; Moreno-Tost, R. *J. Catal.* **2009**, *266*, 129–144.
38. Borg, Ø.; Hammer, N.; Enger, B. C.; Myrstad, R.; Lindvag, O. A.; Eri, S.; Skagseth, T. H.; Rytter, E. *J. Catal.* **2011**, *279*, 163–173.
39. Balonek, C. M.; Lillebo, A. H.; Rane, S.; Rytter, E.; Schmidt, L. D.; Holmen, A. *Catal. Lett.* **2010**, *138*, 8–13.
40. de la Osa, A. R.; Lucas, A. D.; Romero, A.; Valverde, J. L.; Sanchez, P. *Fuel* **2011**, *90*, 1935–1945.
41. Uner, D. O. *Ind. Eng. Chem. Res.* **1998**, *37*, 2239–2245.
42. Bao, J.; He, J.; Zhang, Y.; Yoneyama, Y.; Tsubaki, N. *Angew. Chem., Int. Ed.* **2008**, *47*, 353–356.
43. Liu, Z.-W.; Li, X.; Asami, K.; Fujimoto, K. *Catal. Today* **2005**, *104*, 41–47.
44. Wang, G.-W.; Hao, Q.-Q.; Liu, Z.-T.; Liu, Z.-W. *Appl. Catal., A* **2011**, in press, DOI: 10.1016/j.apcata.2011.07.032.
45. Monlina, M. F.; Molina, R.; Moreno, S. *Catal. Today* **2005**, *107*, 426–430.

46. Ngamcharussrivichai, C.; Imyim, A.; Li, X.; Fujimoto, K. *Ind. Eng. Chem. Res.* **2007**, *46*, 6883–6890.
47. Soualah, A.; Lemberton, J. L.; Pinard, L.; Chater, M.; Magnoux, P.; Moljord, K. *Appl. Catal., A* **2008**, *336*, 23–28.
48. Kusakari, K.; Tomishige, K.; Fujimoto, K. *Appl. Catal., A* **2002**, *224*, 219–228.
49. Akhmedov, V. M.; Al-Khowaiter, S. H. *Catal. Rev. - Sci. Eng.* **2007**, *49*, 33–139.
50. Liu, Y.; Fang, K.; Chen, J.; Sun, Y. *Green Chem.* **2007**, *9*, 611–615.
51. Xiong, H. F.; Zhang, Y. H.; Liew, K. Y.; Li, J. L. *J. Mol. Catal. A: Chem.* **2005**, *231*, 145–151.

Downloaded by PENNSYLVANIA STATE UNIV on May 31, 2012 | http://pubs.acs.org
Publication Date (Web): January 20, 2012 | doi: 10.1021/bk-2012-1092.ch011

Downloaded by STANFORD UNIV GREEN LIBR on May 31, 2012 | http://pubs.acs.org
Publication Date (Web): January 20, 2012 | doi: 10.1021/bk-2012-1092.ch012

Chapter 12

Design and Preparation of Ni-Co Bimetallic Nanocatalyst for Carbon Dioxide Reforming of Methane

Jianguo Zhang,[†] Hui Wang,[*] Chunyu Xi,[#] Mohsen Shakouri, Yongfeng Hu,[a] and Ajay K. Dalai

**Department of Chemical and Biological Engineering,
University of Saskatchewan, 57 Campus Drive, Saskatoon,
Saskatchewan S7N 5A9, Canada
[a]Canadian Light Source, 101 Perimeter Road, Saskatoon,
Saskatchewan S7N 0X4, Canada
[†]Current affiliation: Saskatchewan Research Council, Saskatoon,
Saskatchewan S7N 2X8, Canada
[#]Current affiliation: Jilin University, Changchun, Jilin, China
[*]Fax: 1-306-966-4777. Tel: 1-306-966-2685. E-mail: Hui.Wang@usask.ca.**

Catalyst design and preparation for an ultra stable and highly active catalyst for CO_2 reforming of CH_4 is presented in this work. The objective was to develop a catalyst of inexpensive and commonly available materials that is able to overcome the long standing carbon formation and thermal sintering problems. The catalyst design began with a thorough investigation of the target reaction as well as possible side reactions, followed by the fundamental stoichiometric analysis, thermodynamic analysis, surface reaction mechanism discussion, and ended up with a list of desired properties of the to-be-developed catalyst, suggested catalyst components, and proposed preparation method. Based on the outcome of the design, cheap transition metal nickel (Ni) was proposed for the active metal, a mixture of mangnisium oxide (MgO) and aluminium oxide (Al_2O_3) was used as support, and other transition metals close to Ni in the periodic table were chosen to modify the properties of the Ni sites. The co-precipitation preparation method was suggested so as to give rise to strong metal-support interaction (MSI)

In Nanocatalysis for Fuels and Chemicals; Dalai, A.;
ACS Symposium Series; American Chemical Society: Washington, DC, 2012.

Downloaded by STANFORD UNIV GREEN LIBR on May 31, 2012 | http://pubs.acs.org
Publication Date (Web): January 20, 2012 | doi: 10.1021/bk-2012-1092.ch012

and thus, grow small metal particles in the subsequent catalyst reduction. It turned out that Ni-Co bimetallic catalyst of small metal loading in the frame of MgAlOx perfomed the best in catalyzing a stable and high throughput of syn-gas from the CO_2 reforming of CH_4. Characterizations indicated that the synergy of Ni and Co, strong SMI, high metal dispersion, nano-scale particle sizes, and formation of spinel-type thermal stable solid solutions structures, which are ensential to the suppression of carbon formaton and thermal sintering, are made not only with a certain composition of the catalyst but also the catalyst preparation procedures. The latter is even more important.

Keywords: carbon dioxide reforming of methane; Ni-Co bimetallic catalyst; catalyst design; coprecipitation method

1. Introduction

As early as 1928, Fischer and Tropsch tested CO_2 reforming of CH_4 on various base metals (*1*). Earlier research on CO_2 reforming of CH_4 was focused on producing synthesis gas, or syn-gas in short, with suitable H_2/CO ratios to synthesize hydrocarbons and related products from materials other than petroleum (*2*). In 1980s, efforts were made to use the CO_2 reforming of CH_4 - methanation cycle for the storage of solar energy (*3*, *4*). Since 1990s, there are increasing interests in utilizing this reaction to explore a new source of energy while to mitigate greenhouse gas emissions. The application of this reaction requires a catalyst to make the reaction to proceed toward its desired direction in economical way. Therefore, the research and development of catalysts for CO_2 reforming of CH_4 have signified the evolution of the technology. Hundreds of reforming catalysts have been developed and tested since 1928. However, industrially applicable catalysts have yet been developed. It is well known that deactivation has been a long-standing problem for the reforming catalysts and carbon deposition, thermal sintering, and metal oxidation are the major causes of catalyst deactivation (*5*).

Our previous work has obtained an excellent catalyst which is able to conduct the carbon dioxide reforming of methane reaction for 2000 h without significant deactivation (*6*). Later we found out that to make small enough metal particles on a thermostable support material is a key to the successful mitigation or suppression of carbon formation during the catalytic reaction (*7*). This work resulted in a US patent (*8*). Although the catalyst we developed uses very common raw materials and contains very common elements that are frequently used in catalyst preparation, the catalyst design work, the very initial work that leads to a proper catalyst preparation method which is able to establish the catalyst with desired properties and performance, is worthy being reported. However, due to the long-term process of patent application, this part of work has not been published. This paper will mainly discuss the catalyst design procedure and how it leads to a successful formulation of catalyst preparation method. Recent results of the XANES (X-ray absorption near edge spectroscopy), EXAFS (extended X-ray absorption fine structure spectroscopy), and TEM (transmittance electron microscopy) analysis are briefly used to confirm the conclusions that the catalyst design and our previous work have led to.

2. Catalyst Design

2.1. Objectives of Catalyst Design

The objectives of catalyst design are: 1) to identify desired properties of catalysts for CO_2 reforming of CH_4; 2) to propose catalyst composition; 3) to select catalyst percursor materials; and 4) to determine catalyst preparation method. The catalyst design procedure is shown in Figure 1, beginning with the target reaction.

Downloaded by STANFORD UNIV GREEN LIBR on May 31, 2012 | http://pubs.acs.org
Publication Date (Web): January 20, 2012 | doi: 10.1021/bk-2012-1092.ch012

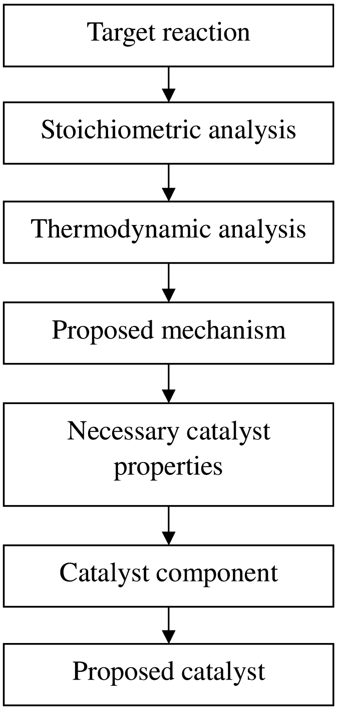
Target reaction
Stoichiometric analysis
Thermodynamic analysis
Proposed mechanism
Necessary catalyst properties
Catalyst component
Proposed catalyst

Figure 1. General procedures of catalyst design (9).

2.2. Target Reaction

CO_2 reforming of CH_4 is the target reaction and expressed by Eq. 1. In this reaction, CH_4 and CO_2 are converted to CO and H_2 on a catalyst. The mixture of CO and H_2 is called synthesis gas.

$$CO_2 + CH_4 \xrightarrow{\text{Catalyst}} 2CO + 2H_2 \tag{1}$$

At a temperature lower than 916 K, Gibbs free energy change of the target reaction is positive, i.e., $\Delta G^{o}_{r,T<916K} > 0$. The reaction is not thermodynamically favourable at lower temperatures. A temperature higher than 916 K is required to convert the feed into product. On the other hand, the reaction temperature needs to be as low as possible to either suppress the side reactions or lower the thermal stress on the reactor. Therefore, a reaction temperature of 1023 K, which is slightly lower than the temperatures commonly found in literature (Reference (*10*)) was chosen to be the working temperature for the catalyst to be designed.

2.3. Stoichiometric Analysis

Stoichiometrically possible reactions are listed as: 1) primary reactant reactions, 2) reactant self-interactions, 3) reactant cross-interactions, 4) reactant-product reactions, and 5) product-product reactions (*11*). However, only the reactions involving chemically stable compounds at 1023 K are considered to be physically realistic. As well, Gibbs free energy change of reaction at 1023 K was calculated using the third law method (*12*). Following simple thermodynamic principles, reactions with positive Gibbs free energy change are excluded in further thermodynamic analysis.

2.3.1. Primary Reactant Reaction

CO_2 and CH_4 are the primary reactants involved in the reaction. The primary reactant reactions are hereby defined as the ones involving only one primary reactant molecule and are shown in Table 1. One can see that the CH_4 decomposition is the only primary reactant reaction in CO_2 reforming of CH_4. CH_4 decomposition is thermodynamically favourable while a CO_2 self reaction does not occur at 1023 K.

Table 1. Primary reactant reaction

Reaction	$\Delta G^{0}_{r,1023K}$ *(kJ)*
Single CO_2 does not react at 1023 K	Not appliable
$CH_4 \leftrightarrow C + 2H_2$	-22

2.3.2. Reactant Self-Interaction Reaction

The reactant self-interaction reactions are those involving two molecules of the same reactant. As presented in Table 2, C_2 hydrocarbons can be produced through the interaction between two CH_4 molecules, while there is no reaction between two CO_2 molecules. At 1023 K, the Gibbs free energy changes of the

In Nanocatalysis for Fuels and Chemicals; Dalai, A.;
ACS Symposium Series; American Chemical Society: Washington, DC, 2012.

Downloaded by STANFORD UNIV GREEN LIBR on May 31, 2012 | http://pubs.acs.org
Publication Date (Web): January 20, 2012 | doi: 10.1021/bk-2012-1092.ch012

CH_4 self-interaction reactions are all positive. From a thermodynamic perspective, these reactions are not favourable. Therefore, at 1023 K, their existence in CO_2 reforming of CH_4 reaction system can be neglected.

Table 2. Reactant self-interaction reaction

Reaction	$\Delta G^0_{r,1023K}$ *(kJ)*
No reaction between two CO_2 at 1023 K	Not applicable
$2CH_4 \leftrightarrow C_2H_6 + H_2$	71
$2CH_4 \leftrightarrow C_2H_4 + 2H_2$	77
$2CH_4 \leftrightarrow C_2H_2 + 3H_2$	126

2.3.3. Reactant Cross-Interaction Reaction

The reactions between different reactant molecules are defined as reactant cross-interaction reactions which include the target reaction (Eq. 1) and other parallel cross-interaction reactions as listed in Table 3. They are thermodynamically favourable.

Table 3. Reactant self interaction reaction

Reaction	$\Delta G^0_{r,1023K}$ *(kJ)*
$CH_4 + CO_2 \leftrightarrow 2CO + 2H_2$	-31
$CH_4 + 2CO_2 \leftrightarrow 3CO + H_2O + H_2$	-31
$CH_4 + 3CO_2 \leftrightarrow 4CO + 2H_2O$	-27

2.3.4. Reactant-Product Reaction

One type of side reactions are those taking place between the reactant and the product molecules as shown in Table 4. Reverse water-gas shift reaction (RWSR) is a major side reaction in CO_2 reforming of CH_4 (*10*, *13*). It consumes H_2 and produces H_2O. RWSR has a positive change of Gibbs free energy at 1023 K. However, it will not be ruled out due to its being widely reported in literature. The side product H_2O can further react with CH_4 leading to more reactions. The reaction between CO_2 and C from CH_4 decomposition (see Table 1) is likely as well.

Downloaded by STANFORD UNIV GREEN LIBR on May 31, 2012 | http://pubs.acs.org
Publication Date (Web): January 20, 2012 | doi: 10.1021/bk-2012-1092.ch012

Table 4. Reactant-product reactions

Reaction	$\Delta G^0_{r,\ 1023K}$ *(kJ)*
$CH_4 + 2H_2O \leftrightarrow CO_2 + 4H_2$	-35
$CH_4 + H_2O \leftrightarrow CO + 3H_2$	-33
$CO_2 + C \leftrightarrow 2CO$	-9
$CO_2 + H_2 \leftrightarrow CO + H_2O$	2
$CO_2 + 2H_2 \leftrightarrow C + 2H_2O$	13
$CO_2 + 4H_2 \leftrightarrow CH_4 + 2H_2O$	35

Downloaded by STANFORD UNIV GREEN LIBR on May 31, 2012 | http://pubs.acs.org
Publication Date (Web): January 20, 2012 | doi: 10.1021/bk-2012-1092.ch012

2.3.5. Product-Product Reaction

Side reactions can also occur between product molecules as shown in Table 5. However, from a thermodynamic point of view, only the reactions between H_2O and C deposit are likely to occur while other reactions between CO and H_2 are not thermodynamically favorable at 1023 K.

Table 5. Product-product reaction

Reactions	$\Delta G^0_{r,1023K}$ *(kJ)*
$H_2O + C \leftrightarrow H_2 + CO$	-11
$CO + H_2 \leftrightarrow HCHO$	122
$CO + 2H_2 \leftrightarrow CH_3OH$	150
$nCO + mH_2 \leftrightarrow C_nH_{2(m-n)} + nH_2O$	>0

2.3.6. Network of Reaction

From above stoichiometeric analysis, in addition to the target reaction (Eq. 1), the side reactions include RWSR (Eq. 2) and steam reforming of CH_4 (Eq. 3) in Table 4, CH_4 decomposition (Eq. 4) in Table 1, carbon removal reactions (Eq. 5 and 6) in Table 4 and 5, reactant cross reactions (Eq. 7 and 8) in Table 3. They are listed as follows:

$$CO_2 + CH_4 \xleftrightarrow{K_1} 2CO + 2H_2 \qquad (1)$$

$$CO_2 + H_2 \xleftrightarrow{K_2} CO + H_2O \qquad (2)$$

$$H_2O + CH_4 \xleftrightarrow{K_3} CO + 3H_2 \tag{3}$$

$$CH_4 \xleftrightarrow{K_4} C + 2H_2 \tag{4}$$

$$C + CO_2 \xleftrightarrow{K_5} 2CO \tag{5}$$

$$C + H_2O \xleftrightarrow{K_6} CO + H_2 \tag{6}$$

$$CH_4 + 2CO_2 \xleftrightarrow{K_7} 3CO + H_2O + H_2 \tag{7}$$

$$CH_4 + 3CO_2 \xleftrightarrow{K_8} 4CO + 2H_2O \tag{8}$$

To simplify thermodynamic analysis in the following section, the number of independent reactions was determined by obtaining the rank of the stoichiometric coefficient matrix (*14*). It turned out that three independent equations, for example, Eqs. 1, 2, and 4, can be selected to describe the reaction system sufficiently. It is also noticed that any group of independent reactions would include one reaction involving carbon species such as any of Eqs. 4, 5 or 6.

2.4. Thermodynamic Analysis

2.4.1. Equilibrium Composition as a Function of Temperature

The variation of equilibrium composition with temperatures can be determined by solving a group of nonlinear equations relating the moles of each component to the equilibrium constant of independent reactions. The equilibrium composition as a function of reaction temperature is calculated based on two independent reactions without considering the one involving carbon formation. The reaction involving carbon formation is not considered due to its small magnitude (6.3×10^{-4} %) in comparison with the total carbon element involved in CO_2 reforming of CH_4 (*6*). Figure 2 shows the effects of reaction temperature on the equilibrium composition at 1 atm and an initial $CH_4/CO_2/N_2$ ratio of 1/1/0.

Downloaded by STANFORD UNIV GREEN LIBR on May 31, 2012 | http://pubs.acs.org
Publication Date (Web): January 20, 2012 | doi: 10.1021/bk-2012-1092.ch012

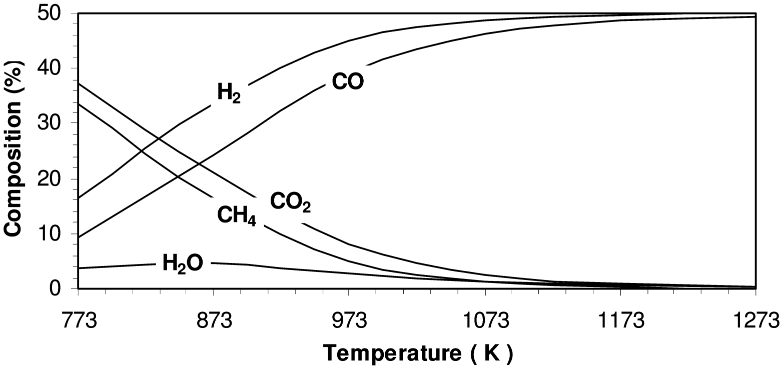

Figure 2. Variation of equilibrium composition with temperatures.

It can be seen that the equilibrium compositions of H_2 and CO increase while those of H_2O, CH_4, and CO_2 drop with increase in the reaction temperature. The effects of the reaction temperature on the equilibrium composition can be ascribed to the change of the RWSR with temperature. Due to its moderately endothermic property in comparison with the strong endothermic property of CO_2 reforming of CH_4 (Eq. 1) and CH_4 decomposition (Eq. 4), the increase in the reaction temperature would mitimize RWSR, and therefore, render the molecule ratio of H_2 to CO closer to unity at higher temperatures (Figure 2). Based on this discussion, it is preferable to use a higher temperature, such as 1023 K, to increase the conversion of the reactants and, as a result, to increase the CO and H_2 concentrations in the reaction products.

2.4.2. Equilibrium Composition as a Function of Total Pressure

Figure 3 shows the effects of total pressure on the equilibrium composition. One can see that with increase in the total pressure of reaction, the reactant compositions increase while those of the products drop. As a reaction of increasing volume, the equilibrium of CO_2 reforming of CH_4 (Eq. 1) tends to shift to the left-hand side at higher total pressures while the equilibrium of RWSR (Eq. 2), as a volume-constant reaction, is not affected by the total pressure change.

Using the equilibrium composition data, the CH_4 conversion and H_2 selectivity can be calculated. Figures 4 and 5 show the variation of CH_4 conversion and H_2 selectivity with reaction temperatures and pressures at initial $CH_4/CO_2/N_2$ ratio of 1/1/0. The observations from the two figures are the same: conversion and selectivity increase with temperature increase while droping with the increase in pressures. Therefore, higher temperatures and lower pressures are thermodynamically perfered for CO_2 reforming of CH_4.

Downloaded by STANFORD UNIV GREEN LIBR on May 31, 2012 | http://pubs.acs.org
Publication Date (Web): January 20, 2012 | doi: 10.1021/bk-2012-1092.ch012

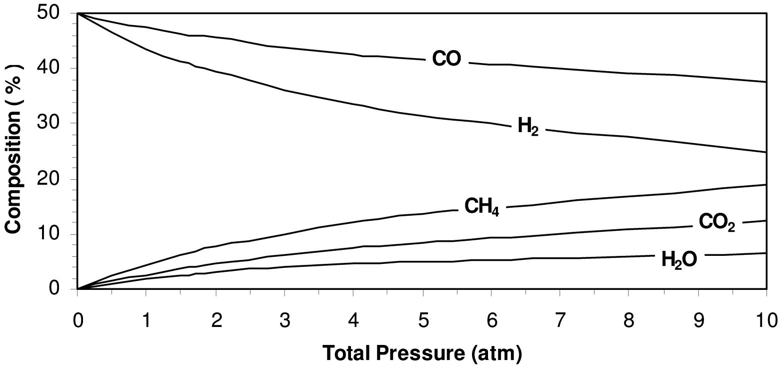

Figure 3. Effects of total pressure on equilibrium composition at 1023 K and initial $CO_2/CH_4/N_2$ ratio of 1/1/0.

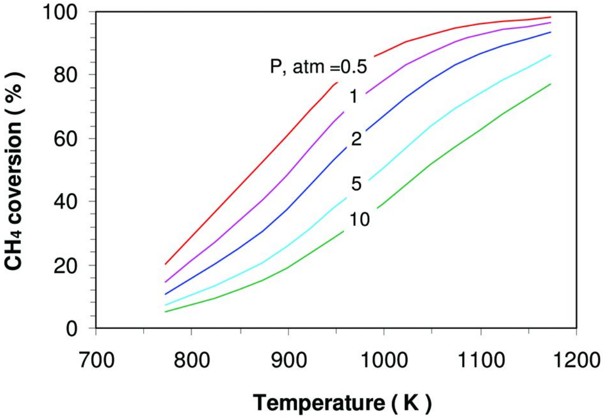

Figure 4. Effects of temperatures and pressures on CH_4 conversion.

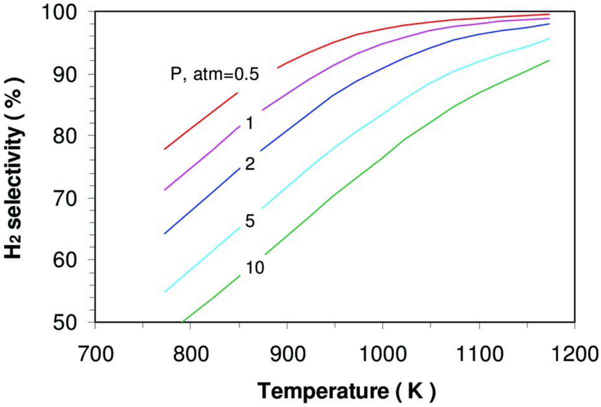

Figure 5. Effects of temperatures and pressures on H_2 selectivity.

Downloaded by STANFORD UNIV GREEN LIBR on May 31, 2012 | http://pubs.acs.org
Publication Date (Web): January 20, 2012 | doi: 10.1021/bk-2012-1092.ch012

2.4.3. Equilibrium Composition as a Function of Initial CO_2/CH_4 Molar Ratio

The equilibrium composition as a function of initial CO_2/CH_4 molar ratio is shown in Figure 6. It can be seen that the composition of CH_4 decreases quickly with the increase in CO_2 ratio. At a CO_2 to CH_4 ratio of 3, most of CH_4 is reacted. At a CO_2 to CH_4 ratio of 1, H_2 reaches its maximum composition in the reaction mixture. When CO_2 to CH_4 ratio is higher than 1, product H_2 is consumed by reacting with CO_2 through RWSR, resulting in decrease in H_2 compposition and increase in both CO and H_2O compositions. After H_2O composition reaches its maximum level, reactions would stop due to the depletion of CH_4. The product concentrations drop gradually due to the dilution effect of CO_2.

Downloaded by STANFORD UNIV GREEN LIBR on May 31, 2012 | http://pubs.acs.org
Publication Date (Web): January 20, 2012 | doi: 10.1021/bk-2012-1092.ch012

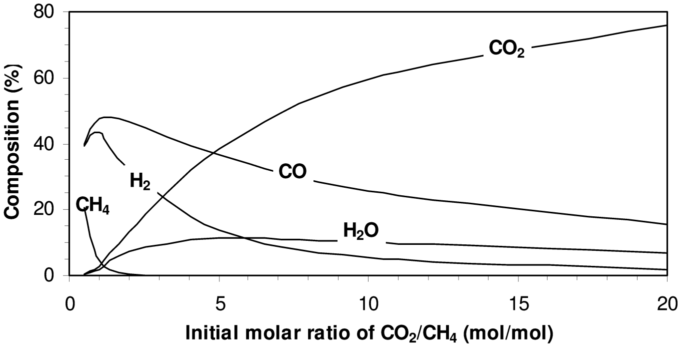

Figure 6. Effect of initial CO_2/CH_4 on equilibrium composition at 1023 K and 1 atm.

2.4.4. Effects of Inert N_2

It is a common practice to use nitrogen as an internal standard for GC analysis in the research of CO_2 reforming of CH_4. The effect of N_2 on CH_4 conversion and H_2 selectivity at 1 atm, various temeratures, and initial CH_4/CO_2 ratio of 1/1 were calculated and the results are shown in Figure 7. The figure shows that the existence of N_2 can enhance both CH_4 conversion and H_2 selectivity at various temperatures. The higher the N_2 concentration, the higher the degree of enhancement on CH_4 conversion and H_2 selectivity.

Downloaded by STANFORD UNIV GREEN LIBR on May 31, 2012 | http://pubs.acs.org
Publication Date (Web): January 20, 2012 | doi: 10.1021/bk-2012-1092.ch012

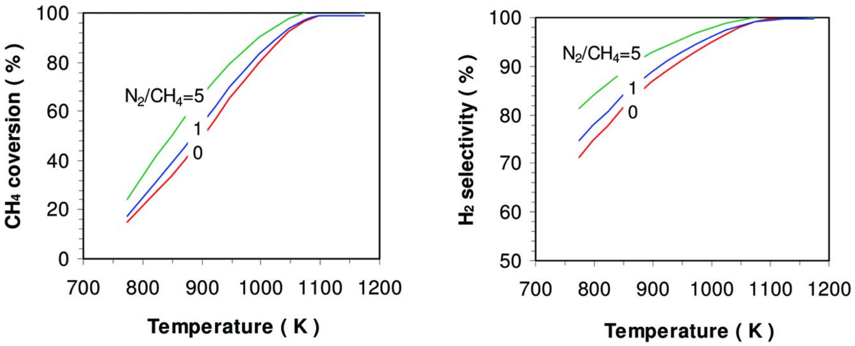

Figure 7. Effects of inert N_2 gas on CH_4 conversion and H_2 selectivity.

2.4.5. Carbon Formation

As carbon formation has been recognized as one of the major causes of catalyst deactivation, it is evaluated using a thermodynamic analysis method (*15*). The reactions involving carbon speces are those represented by Eqs. 4, 5, and 6. The equilibrium constants of these three reactions can be expressed by Eqs. 9-11:

$$CH_4 \xleftrightarrow{K_4} C + 2H_2 \qquad K_4 = \left(\frac{p^{e}_{H_2}}{\hat{f}^{o}_{H_2}}\right)^2 \Big/ \left(\frac{p^{e}_{CH_4}}{\hat{f}^{o}_{CH_4}}\right) \qquad (9)$$

$$C + CO_2 \xleftrightarrow{K_5} 2CO \qquad K_5 = \left(\frac{p^{e}_{CO}}{\hat{f}^{o}_{CO}}\right)^2 \Big/ \left(\frac{p^{e}_{CO_2}}{\hat{f}^{o}_{CO_2}}\right) \qquad (10)$$

$$C + H_2O \xleftrightarrow{K_6} CO + H_2 \qquad K_6 = \left(\frac{p^{e}_{CO}}{\hat{f}^{o}_{CO}}\right)\left(\frac{p^{e}_{H_2}}{\hat{f}^{o}_{H_2}}\right) \Big/ \left(\frac{p^{e}_{H_2O}}{\hat{f}^{o}_{H_2O}}\right) \qquad (11)$$

where, superscript e is used to indicate the partial pressure at equilibrium state.

$\hat{f}_j^o$ is the standard fugacity of species j. At any state including equilibrium state, three parameters *α*, *β*, and *γ* are defined accordingly as shown by Eqs. 12-14:

$$\alpha = \left(\frac{p_{H_2}}{\hat{f}_{H_2}^o}\right)^2 \Bigg/ \left(\frac{p_{CH_4}}{\hat{f}_{CH_4}^o}\right) \quad (12)$$

$$\beta = \left(\frac{p_{CO}}{\hat{f}_{CO}^o}\right)^2 \Bigg/ \left(\frac{p_{CO_2}}{\hat{f}_{CO_2}^o}\right) \quad (13)$$

$$\gamma = \left(\frac{p_{CO}}{\hat{f}_{CO}^o}\right)\left(\frac{p_{H_2}}{\hat{f}_{H_2}^o}\right) \Bigg/ \left(\frac{p_{H_2O}}{\hat{f}_{H_2O}^o}\right) \quad (14)$$

When the system is at equilibrium conditions, we have:

$$\alpha = K_4,\ \beta = K_5,\ \text{and}\ \gamma = K_6 \quad (15)$$

If $\alpha < K_4$, $\beta > K_5$, and $\gamma > K_6$, all the reactions move toward the direction of carbon formation. Carbon formation is favourable. However, if $\alpha > K_4$, $\beta < K_5$, and $\gamma < K_6$, carbon formation is not thermodynamically favourable. At a certain initial $CO_2/CH_4/N_2$ ratio and 1 atm, trial and error method was used to solve a group of non-linear equations to find a certain border temperature above which carbon formation is not thermodynamically favourable, i.e. $\alpha > K_4$, $\beta < K_5$, and $\gamma < K_6$. As shown in Figure 8, carbon formation zone and carbon free zone are obtained. The presence of inert gas, N_2, can slightly affect the border between carbon formation zone and carbon free zone. However, at the ideal feed ratio of CO_2/CH_4=1/1, carbon formation is seen inevitable from Figure 8. The increase of CO_2 in feed may inhibit carbon formation. However, it is not practical to use excess CO_2 to inhibit carbon formation from an industrial point of view due to the high cost of product separation. Therefore, at the industrially practical conditions, i.e. CO_2/CH_4 = 1/1 and 923 K < T < 1323 K, the only way to suppress carbon formation is to seek carbon resistant catalysts on which the extent of carbon formation does not cause deactivation.

Downloaded by STANFORD UNIV GREEN LIBR on May 31, 2012 | http://pubs.acs.org
Publication Date (Web): January 20, 2012 | doi: 10.1021/bk-2012-1092.ch012

Downloaded by STANFORD UNIV GREEN LIBR on May 31, 2012 | http://pubs.acs.org
Publication Date (Web): January 20, 2012 | doi: 10.1021/bk-2012-1092.ch012

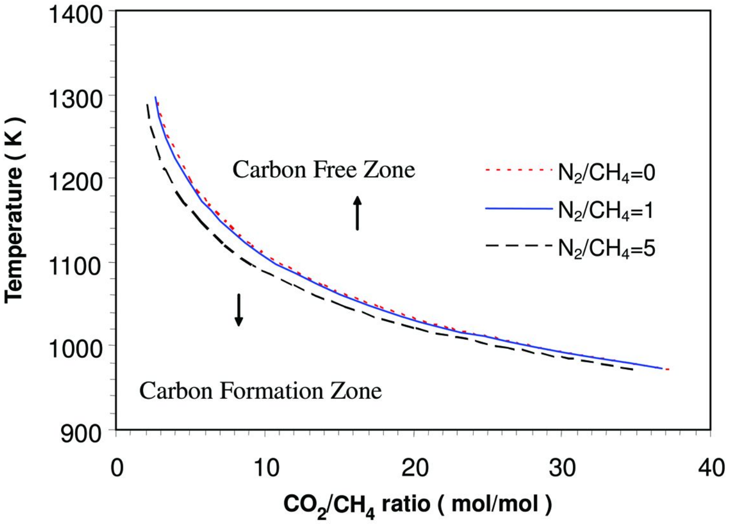

Figure 8. Effects of CO_2/CH_4 ratio and inert gas N_2 on limiting temperatures below which carbon formation occurs at 1 atm.

2.5. Proposed Reaction Mechanism

The dissociation of CH_4 is believed as one of the initial steps for the methane reforming reaction (*16*). Two H_2 molecules and one CO molecule are formed via H and CH_x (x = 0-3) species originated from the dissociation of CH_4. The presence of CH_x species on the surface of catalysts have been confirmed through pulsing experiments (*17*, *18*) and transient isotopic studies (*19*, *20*). It is reported that the nreversible adsorption of CH_4 on the surface of catalyst leads to cracking of CH_4 and the cracking is a rate determining step (RDS) while CH_4 adsorption is at equilibrium (*21–23*).

$$CH_4 + M \leftrightarrow CH_4 - M \qquad \text{Equilibrium} \qquad (16)$$

$$CH_4 - M \rightarrow C - M + 2H_2 \qquad \text{RDS} \qquad (17)$$

where, M is the active sites on metals.

The participation of CO_2 molecules is through its dissociative chemisorption. Infrared spectroscopy has indicated that CO_2 can dissociate to carbon monoxide and adsorbed O (*24*, *25*). The carbon monoxide formed is released to the gas phase immediately (*26*).

$$CO_2 + 2S \leftrightarrow CO\text{-}S + O - S \qquad (18)$$

$$CO\text{-}S \rightarrow CO + S \qquad (19)$$

where, S is the active sites on oxide support.

Rostrup-Nielsen (*27*) and Kim et al. (*28*) assumed the dissociative chemisorption of CO_2 as the rate-limiting step. However, Hei et al. (*29*) reported that both dissociation of CH_4 and CO_2 may be rate-limiting steps based on the same magnitude of the activation barrier. Kroll et al. (*30*, *31*) suggested that the surface oxidation step, as represented by Eq. 20, should be the rate-limiting step due to the lack of kinetic isotopic effect for the formation of CO during the CO_2 reforming of CH_4.

$$C - M + O - S \rightarrow CO + M + S \qquad (20)$$

where, C-M originated from the dissociation of CH_4 and O-S from the dissociation of CO_2. The participation of CO_2 may also be through directly reacting with the C-M species in the form of intact activated molecule (Eq. 21) (*21*, *32*, *33*).

$$CO_2 + C - M \rightarrow 2CO + M \qquad (21)$$

Based on above discussion, a surface reaction mechanism is proposed for defining the necessary properties of catalysts for CO_2 reforming of CH_4. As shown in a schemastic of Figure 9, the dissociative chemisorption of CH_4 occurs on the active metal centers of the metallic state of catalysts is believed to be responsible for the CH_4 activation (*18*). The absorption of CO_2 is supposed to take place on the surface of oxide support part since the carbon in CO_2 molecule as a Lewis acid centre tends to react with Lewis base centre of an oxide. The reaction between M-C species and activated S-CO_2 (Eq. 21) is assumed as the rate determining step based on the following rationale and fact: 1) if the dissociation of CH_4 is RDS, carbon accumulation is unlikely to occur; and 2) carbon accumulation has been a well-known challenge for CO_2 reforming of CH_4, which means carbon species formation rate is higher than carbon species removal rate.

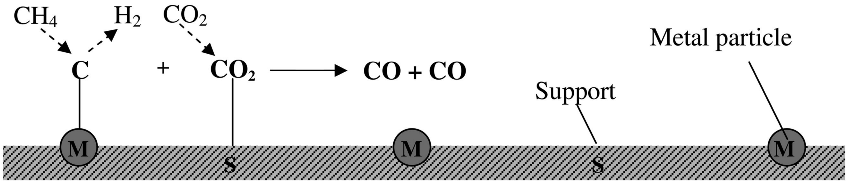

Figure 9. Proposed surface mechanism of CO_2 reforming of CH_4.

In Nanocatalysis for Fuels and Chemicals; Dalai, A.;
ACS Symposium Series; American Chemical Society: Washington, DC, 2012.

Downloaded by STANFORD UNIV GREEN LIBR on May 31, 2012 | http://pubs.acs.org
Publication Date (Web): January 20, 2012 | doi: 10.1021/bk-2012-1092.ch012

Downloaded by STANFORD UNIV GREEN LIBR on May 31, 2012 | http://pubs.acs.org
Publication Date (Web): January 20, 2012 | doi: 10.1021/bk-2012-1092.ch012

2.6. Desired Catalyst Properties

It is recognized that the major causes of catalyst deactivation for CO_2 reforming of CH_4 are carbon formation, sintering, and metal oxidation (*10*, *34*). In addition to having excellent thermal stability to resist sintering, based on the above proposed mechanism, catalysts should facilitate the rate determining step (Eq. 19) so as to have reaction activity. Good selectivity can be obtained if the catalyst is able inhibit side reactions such as RWSR and carbon formation reactions. Therefore, the desired properties of proposed catalysts can be defined based on the proposed surface mechanism and previous stoichiometric and thermodynamic analysis along with the general principles of catalyst development and the common challenges of catalysts in CO_2 reforming of CH_4. The desired properties are described as P 1-5 given below:

P-1: Surface dehydrogenation sites that can enhance the dissociation of methane to CH_x species and remove H adsorption species from the intermediate to form hydrogen;

P-2: Surface carbon dioxide adsorption sites that promote the activation or participation of CO_2 and the the activated CO_2 or the oxidizing species derived from CO_2 adsorption on P-2 is able to react with the C species derived from the decomposition of CH_4;

P-3: Adjacent surface sites of P-1 and P-2 that will facilitate the reaction between C species and activated CO_2 molecules so that the overall reaction rate can be improved;

P-4: Thermal stability that can retain catalyst physical and mechanic properties thus phase transitions and crystal transformation could be avoided at thermodynamically favourable reaction temperatures as high as 1023 K;

P-5: Uniform and stable dispersion of active components with nano-scale particle sizes which can promote CO_2 reforming of CH_4 while suppress carbon formation or other undesired reactions because carbon formation active sites are believed larger than reforming active sites (*27*).

2.7. Catalyst Components

2.7.1. Selection of Primary Active Component

It is well known that CO_2 reforming reaction with CH_4 can be catalyzed by most transition metals. The activity of common catalytic metals for dehydrogenation or hydrogenation follows the order given below (*35*).

Ru, Rh, Pd, Ir, Pt > Fe, Co, Ni > W, Cr-Cu

Among them, the precious metals, such as ruthenium (Ru) and rhodium (Rh), and the non-precious metal nickel (Ni) have been studied extensively (*32*, *36–38*). It has been found that supported catalysts of precious metals such as Rh, Ru, Pd, Pt, and Ir can provide stable operations for carbon dioxide reforming of

Downloaded by STANFORD UNIV GREEN LIBR on May 31, 2012 | http://pubs.acs.org
Publication Date (Web): January 20, 2012 | doi: 10.1021/bk-2012-1092.ch012

methane and less carbon can be formed during the reaction (*10*) in comparison with non-precious metal catalysts. However, from an industrial standpoint, it is more practical to develop non-precious metal-based catalysts to avoid high cost and restricted availability of precious metals. Ni has drawn remarkable attention in this area due to its high activity and wide availability (*27*). In this research, Ni is chosen as the primary active component to meet the desired catalyst property described in P-1. However, Ni catalysts suffer severe catalyst deactivation due to carbon formation, which has not been solved yet. To overcome the problems of catalyst deactivation, the investigation of secondary active components (or catalyst promoters) and catalyst supports has attracted significant attention (*39–44*). Therefore, it is hoped that the selection of a secondary metal component and other factors such as selection of catalyst support and preparation methods be able to make a Ni-based catalyst with excellent carbón resistance.

2.7.2. Selection of Secondary Active Component

We also know that a secondary active component or promoter can increase the performance and stability of the catalysts for CO_2 reforming of CH_4 in comparison with the corresponding monometallic catalysts (*45*, *46*). Tomisshge et al. (*47*) investigated the additive of Sn, Ge, and Ga to a NiO-MgO solid solution and found that the addition of Sn can effectively decrease the carbon formation which was mainly resulted from the methane decomposition. The addition of Cr (*48*, *49*) and Mn (*40*, *50*) was reported to have significant effect on the inhibition of carbide formation which was believed to be the intermediate for carbon formation (*51*). Catalyst performance can also be improved when partial NiO was replaced with CoO in the NiO-MgO solid solution (*52*). It was also found that a homogeneous alloy of Co and Ni and a small Ni substitution of Co dramatically enhance the catalyst activity and stability by improved resistance to metal oxidation (*53*). Fe and Cu have also been investigated due to their high activity to dehydrogenation or hydrogenation and their close electronic configuration to that of Ni (*35*). In this research, Co, Cu, Fe and Mn are chosen for the secondary active metal component. However, Cr is not considered due to its toxic property which can be a big workplace hazard. We hope that the second metal and nickel form such active metal sites that can improve the metal resistance to oxidation and make the nickel crystal essembles, or particle sizes, smaller, which is one of the keys to suppression of carbon formation, without compromising the high activity of nickel.

2.7.3. Selecion of Catalyst Support

From the thermodynamic point of view, high reaction temperatures are necessary for an endothermic reaction to achieve high reactant conversion. To facilitate the catalyst property stated in P-4, thermostable substance should be selected as catalyst support or framework. MgO is selected at first time not only because of its high melting point of 3346 K, but also its basic surface function centers. Surface basicity was believed to necessary to the activation of acidic CO_2 and suppression of carbon formation (*54*, *55*). However, MgO has low specific surface area. Thus, to compensate this dissatisfaction of MgO, a mixed framework of $AlMgO_x$ is proposed to be the support with the consideration of making use of the high thermal stability of MgO and the high specific surface area of Al_2O_3. The ratio of MgO to Al_2O_3 has to be made right such that the mixture facilitates the properties stated in P-4 and P-2.

At high reaction temperatures, the active metal crystallites of the catalysts would contact each other through thermal motion. Even at the Hutting temperature, which is 0.3 times of the melting point of the substance, the surface atoms would have enough energy to overcome the weak surface crystal forces, then diffuse and form necks to decrease the surface energy (*11*), resulting in sintering deactivation. A thermal stable surface structure of catalyst support cannot guarantee the prevention of active metals from sintering. It is hoped that the active metal sites be anchored on the surface of the support by strong metal-support interaction (MSI) force. Therefore, a proper catalyst preparation method must be used to facilitate strong MSI. Additionally, it also facilitates the uniform dispersion of active components on the catalyst surface (P-5).

Downloaded by STANFORD UNIV GREEN LIBR on May 31, 2012 | http://pubs.acs.org
Publication Date (Web): January 20, 2012 | doi: 10.1021/bk-2012-1092.ch012

3. Catalyst Preparation

3.1. Determination of Catalyst Preparation Method

Most industrial catalysts are manufactured using either precipitation method or impregnation method (*56*, *57*). Precipitated catalysts are generally prepared by rapid mixing of concentrated solutions of metal salts with a precipitating reagent to form solid metal hydroxide mixture. After calcination, thermostable morphological structure of metal oxide is produced. The catalyst id finally made by reducing the active metal components into metal format in a reducing gas such as hydrogen at a certain temperature. On the other hand, impregnated catalysts are made through the impregnation of the solution consisting of active metal components onto a commercially available or customer-made support material, usually metal oxide (*58*). Calcination and reduction are also necessary except that oxide can be used as a catalyst. Details of a catalyst preparation process for a given catalyst are not always patented but rather kept as business secrets. Therefore, only broad principles are available in the published literature. A general comparison between precipitation method and impregnation method is listed in Table 6.

It is presumeable that that using precipitation method molecular scale mixing of the metal oxides can be achieved after calcination of the metal hydroxides. The reduction of such a mixture can result in uniform metal dispersion on the catalyst surface. The reduction extent and the resultant metal nanoparticle size can be relatively easily controlled by the catalyst reduction conditions such as temperature and reducing gas, in comparison with the impregnation method. This consideration leads to the selection of precipitation or co-precipitation method that is to be used in this research. As reference catalysts, impregnation method is used, too, to make the catalysts for comparison.

Table 6. The decision chart for the selection of catalyst preparation method

Merit	*Description*	*Precipitation method*	*Impregnation method*
1	Molecular scale mixing of catalyst components	Easy	Difficult
2	Uniform dispersion of active components	Easy	Difficult
3	Surface area up to 200 m^2/g	Easy	Easy
4	Surface area higher than 200 m^2/g	Difficult	Easy
5	High metal dispersion	Easy	Easy
6	High metal loading	Easy	Difficult
7	Relative low cost	Easy	Easy
8	Instrument availability	Easy	Easy

Downloaded by STANFORD UNIV GREEN LIBR on May 31, 2012 | http://pubs.acs.org
Publication Date (Web): January 20, 2012 | doi: 10.1021/bk-2012-1092.ch012

3.2. Chemistry of Precipitation

Precipitation is usually defined as a process obtaining a solid from a liquid solution (*59*). When a metal salt is dissolved in water, the metal ions are solvated by water molecules. The coordinated water molecules can be deprotonated to produce solids in the form of hydroxide or even oxide species. The deprotonation processes can be expressed by the following equilibria which depend on the charge of the metal and the pH of the solution (*60*).

$$\left[M - OH_2\right]^{n+} \xleftrightarrow{H^+} \left[M - OH\right]^{(n-1)+} \xleftrightarrow{H^+} \left[M = O\right]^{(n-2)+} \tag{22}$$

The formation of the solid is favored for highly charged metal ions and/or using high pH of the solution. There are several possibilities to shift the equilibria from the left-hand side to the right-hand side of Eq. 22, i.e., to obtain a solid mixture from hydrated metal salts. For instance, a compound such as potassium hydroxide (KOH) can be used to raise the pH gradually, i.e., to remove the protons from the equilibrium. This corresponds to equilibrium shift from left-hand side to right-hand side in Eq. 22 at a given charge. Alternatively, the solution can be simply aged at elevated temperatures. A higher temperature promotes dissociation of protons from hydrated metal ions. The mechanism of the polycondensation of the hydroxide compounds eventually leads to precipitates (*60*). This process may be affected by the factors such as salt concentration, pH value of the solution during precipitation, nature of the counter ions, and the temperature at which the precipitation takes place.

3.3. Precipitation Process and Unit Operation

A schematic of the typical precipitation process and major unit operations are shown in Figure 10.

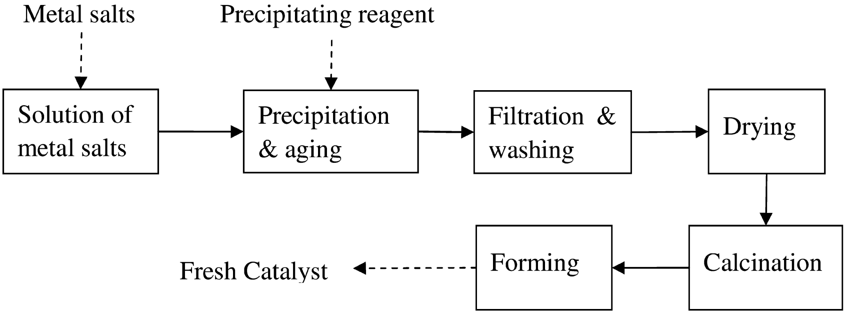

Figure 10. Schematic of typical preparation process of precipitated catalysts.

As presented in the figure, a certain type and amount of metal salts are chosen and dissolved based on catalyst design, and then are precipitated by adding a precipitating reagent. A precipitate is obtained and unwanted ions are removed after filtration and washing. The precipitate is usually in the form of hydroxide, carbonate, oxalate, formate, or citrate, depending on the composition of the solution. Then the solid is aged, filtered and washed to remove undesired water-desolveable ions. Water is removed by drying the precipitate. Designed catalyst is made after calcinating and forming by following certain procedures. The final precipitated catalyst is in the form of oxide or intimate mixed oxides. The size of crystallites present in the precipitated catalysts is typically in the range of 3-15 nm (*61*).

4. Recapitulation of Catalyst Preparation and Test

Based on the catalyst design discussed above, a series of Ni-based bimetallic catalysts with different combinations of Ni-Co, Ni-Mn, Ni-Fe, and Ni-Cu in the frame of $AlMgO_x$, and various Ni, Co loadings were prepared using coprecipitation method (*6*, *8*). In determination of the operation conditions of the coprecipitation method, some of them such as concentrations of the metal nitrates, filtration and washing procedures, and drying temperature and time were chosen based on literature and experience. Others such as calcination and reduction temperature and time were optimized. The performance of the catalysts was tested with a bench-top, micro fixed-bed quartz reactor. And the fresh and spent catalysts were characterized using commonly used techniques such as BET (Brunauer, Emmett and Teller), XRD (X-Ray powder Diffraction), TEM (Transmission Electron Microscopy), XPS (X-ray Photoelectron Spectroscopy), TG/DTA (Thermogravimetric and Differiential Thermal Analysis), and CO (Carbon monoxide) chemisorptions. The work was reported in Zhang, et al. (*6*–*8*).

Downloaded by STANFORD UNIV GREEN LIBR on May 31, 2012 | http://pubs.acs.org
Publication Date (Web): January 20, 2012 | doi: 10.1021/bk-2012-1092.ch012

Downloaded by STANFORD UNIV GREEN LIBR on May 31, 2012 | http://pubs.acs.org
Publication Date (Web): January 20, 2012 | doi: 10.1021/bk-2012-1092.ch012

The major findings are:

1. The initial catalyst activity for CO_2 reforming of CH_4 followed the order of Ni-Co > Ni-Mn > Ni-Fe > Ni-Cu. Ni-Co catalyst maintained longer and better stability.
2. In the 2000 h test at 750 °C, 1 atm and 110,000 mL/g_{cat}-h, the initial CH_4 conversion was 91%. It fluctuated slightly between 88% and 90% from 300th h to 700th h but stabilized at 89-90% after then. No further deactivation was observed until the end of 2000 h test. During the test, the ratio of H_2/CO was maintained between 0.96 and 1. Analysis of the spent catalyst showed the carbon formation rate was as low as 0.000218 g_c/g_{cat}-h.
3. The characterization of the catalyst showed that the designed preparation method resulted in thermostable spinel and solid solution structure and that smaller metal Ni and Co loading led to better metal dispersion and smaller metal nanoparticles.

5. Comparison between Coprecipitation and Impregnation

The catalyst design in this work has led to the successful development of Ni- Co/$MgAlO_X$ bimetallic catalyst. To show whether the designed catalyst preparation procedure is essential to the facilitation of the catalytic performance, reference catalyst was prepared by impregnating the same metal combination on the $MgAlO_X$ support. The support $MgAlO_X$ was made by coprecipitation following the same procedure as Ni-Co/$MgAlO_X$ bimetallic catalyst was prepared. The difference was that only magnesium nitrade and aluminium nitrade solutions were prepared for precipitation. After calcination to obtain the support, Ni and Co were introduced onto it by impregnation of nickel nitrade and cobalt nitrade solution followed by drying and calcination. Now the two groups of catalysts, precipitated catalyst and impregnated catalyst, have the same composition. Table 7 gives the composition and BET specific surface area of the two samples made differently. Both catalysts had similar, if not same, Mg/Al and Ni/Co ratios, Ni and Co loading, and surface area.

Table 7. Composition and BET surface area of the catalysts

Catalyst	*Mg/Al*	*Ni/Co*	*Ni/Metals %*	*Co/Metals %*	*BET area m^2/g*
Precipitated	2.4	0.6	5	9	110
Impregnated	2.3	1	7	7	100

Downloaded by STANFORD UNIV GREEN LIBR on May 31, 2012 | http://pubs.acs.org
Publication Date (Web): January 20, 2012 | doi: 10.1021/bk-2012-1092.ch012

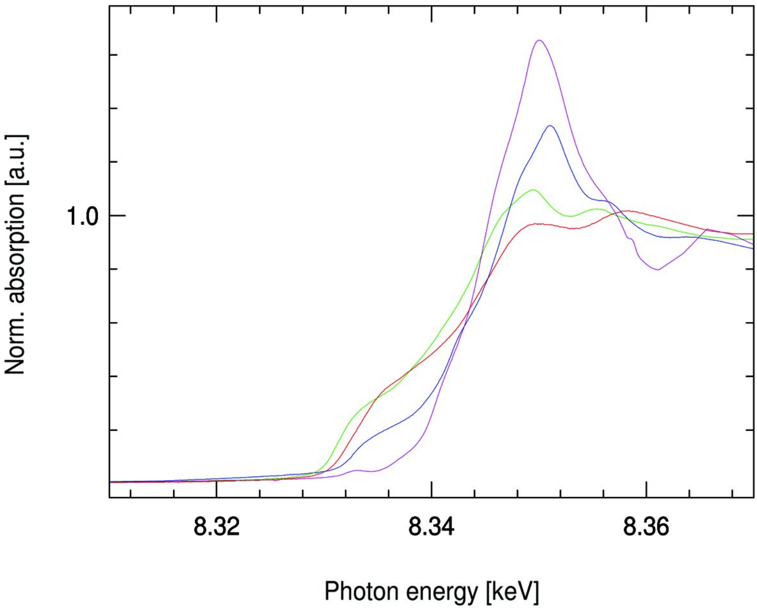

Figure 11. Ni XANES from 8.31 to 8.38 keV of NiCo Catalysts reduced at 750C. Red: Ni foil; green: impregnated catalyst; blue: precipitated catalyst; purple: Ni oxide.

Figures 11 and 12 show the XANES (X-ray absorption near edge spectroscopy) and Fourier-transformed EXAFS (extended X-ray absorption fine structure spectroscopy) of nickel of the reduced catalysts, respectively. The precipitated and impregnated catalysts were reduced at 750 °C in the H2/He mixture gas (H2: 3.5%) for h and cooled to room temperature in He flow. Both Ni and Co K-edge X-ray absorption spectroscopy was scanned at MRCAT (The Material Research Collaborative Access Team) 10-BM (bending magnet) beamline at Advanced Photon Source of Argonne National Laboratory (*62*). Although the figures show that the precipitated catalyst had less metals reduced and grew smaller metal particles than the impregnated catalyst, spectroscopy analysis gives quantitative results which is shown in Table 8. The data indicate that more than half of Ni and 20% of Co in the precipitated catalyst were reduced and that the corresponding numbers for the impregnated catalyst were 83% and 51%. Due to stronger MSI, the metal-metal distance in metal particles resulted from the reduction of the precipitated catalyst is longer than those from the impregnated one; 2.48 vs. 2.48 Å for Ni-Ni and 2.51 vs. 2.49 Å for Co-Co. The EXAFS data also shows that reduction of the precipitated catalyst grew smaller metal nanoparticles. The nickel particle size on the precipitated catalyst is 40 Å or 4 nm. The Co particle size cannot be estimated due to too smalle reduction extent. But the Ni and Co particles are 75 and 80 Å, respectively. Because of the very small portion of Co reduction in the precipitated catalyst, the Co particle size cannot be measured by the EXAFS data. The TEM (transmittance electron microscopy) of the same samples comfirms this observation. The TEM images were obtained by FEI's Titan Field-Emission Environmental Transmission Electron Microscope at 300 keV at the Birck Nanotechnology of Center Purdue University. The TEM photos shown in Figure 13 indicate that the metal particle sizes resulted from the reduction of the precipitated catalyst are not only smaller but also more evenly dispersed. On the other hand, the reduction of the impregnated catalyst led to bigger metal particles and uneven dispersion. The mechanism of the generation of this difference due to the catalyst preparation procedures will be discussed elsewhere.

Downloaded by STANFORD UNIV GREEN LIBR on May 31, 2012 | http://pubs.acs.org
Publication Date (Web): January 20, 2012 | doi: 10.1021/bk-2012-1092.ch012

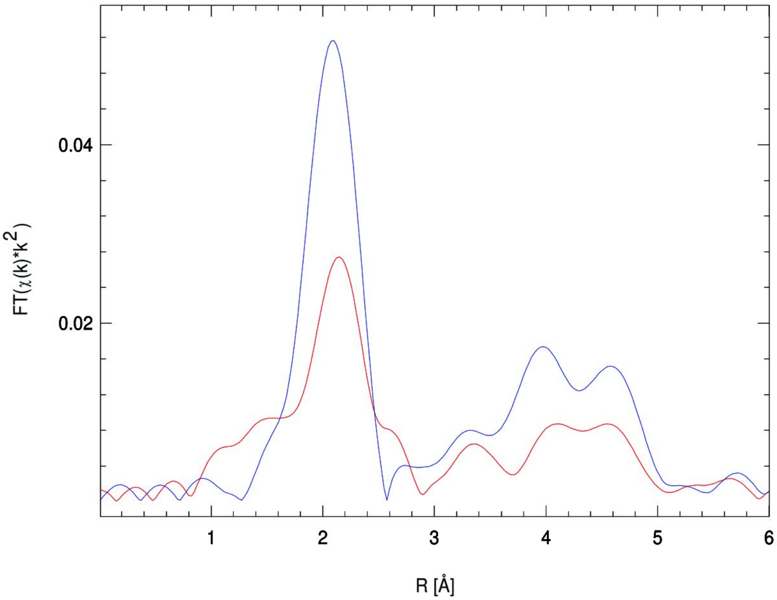

Figure 12. k-Weighted Fourier transform of Ni K-edge EXAFS of NiCo catalyst reduced at 750 °C. k^2: Δk = 2.9 – 11.2 Å-1; red: precipitated catalyst; blue: impregnated catalyst.

Table 8. XANES and EXAFS analysis results

Catalyst	*Metal fraction*		*Metal oxide fraction*		*M-M distance, Å*		*M coordination No.*		*Particle size, Å*	
	Ni	*Co*	*NiO*	*CoO*	*Ni-Ni*	*Co-Co*	*Ni*	*Co*	*Ni*	*Co*
Precipitated	0.52	0.20	0.48	0.80	2.49	2.51	8.8	-	40	-
Impregnated	0.83	0.51	0.17	0.49	2.48	2.49	11.0	11.2	75	80

Downloaded by STANFORD UNIV GREEN LIBR on May 31, 2012 | http://pubs.acs.org
Publication Date (Web): January 20, 2012 | doi: 10.1021/bk-2012-1092.ch012

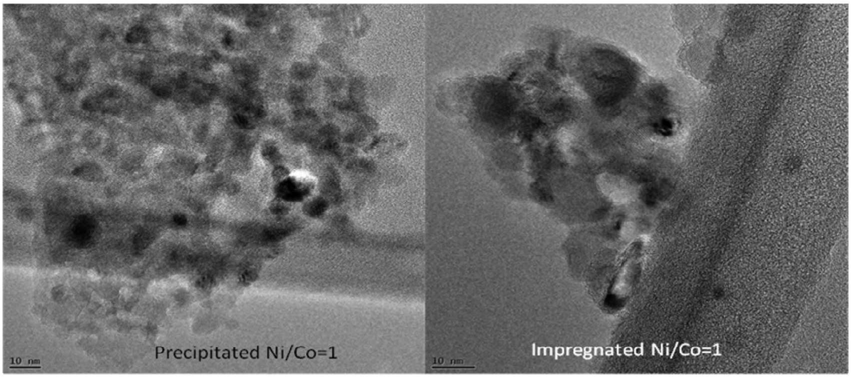

Figure 13. TEM images of the precitated and impregnated catalysts after reduction at 750 °C for 4 h.

6. Conclusions

The catalyst design in this work has led to successful development of a Ni-Co/$MgAlO_X$ bimetallic catalyst that is able to facilitate ultra stable performance of CO_2 reforming of CH_4 with high activity and selectivity due to its exceptional resistance to carbon formation and thermal sintering. Further studies on XANES, EXAFS and TEM of the catalyst and the reference catalyst made by impregnation of the metals have confirmed that not only the catalyst composition but also the precudure to make the catalyst are essential to the formation of the catalyst properties, which are a must to the satisfactory catalytic performance.

Acknowledgments

The authors would like to thank Dr. Jeffery T. Miller of Argonne National Laboratory and Mr. M. Cem Akatay of Purdue University for their respective contributions on X-ray absoption spectroscopy and TEM measurements and helpful discussions on the results.

Downloaded by STANFORD UNIV GREEN LIBR on May 31, 2012 | http://pubs.acs.org
Publication Date (Web): January 20, 2012 | doi: 10.1021/bk-2012-1092.ch012

References

1. Fischer, V. F.; Tropsch, H. Die umwandlung von methan in wasserstoff und kohlenoxyd. *Brennst.-Chem.* **1928**, *25*, 39–46.
2. Reitmeier, R.; Atwood, K.; Bennet, H.; Baugh, H. Production of synthesis gas by reacting light hydrocarbons with steam and carbon dioxide. *Ind. Eng. Chem.* **1948**, *40*, 620–626.
3. Chubb, T. A. Characteristics of CO_2-CH_4 reforming-methanation cycle relevant to the solchem thermochemical power system. *Sol. Energy* **1980**, *24*, 341–345.
4. McCrary, J. H.; McCrary, G. E. An experimental study of the CO_2-CH_4 reforming-methanation cycle as a mechanism for converting and transporting solar energy. *Sol. Energy* **1982**, *29*, 141–151.
5. Slagtern, A.; Olsbye, U.; Blom, R.; Dahl, I. M. The influence of rare earth oxies in Ni/Al_2O_3 catalysts during CO_2 reforming of CH_4. *Stud. Surf. Sci. Catal.* **1997**, *107*, 497–502.
6. Zhang, J.; Wang, H.; Dalai, A. K. The development of Ni-Co bimetallic catalyst for CO_2 reforming of CH_4. *J. Catal.* **2007**, *249*, 300–310.
7. Zhang, J.; Wang, H.; Dalai, A. K. Effects of metal content on activity and stability of Ni-Co bimetallic catalysts for CO2 reforming of CH4. *Appl. Catal., A.* **2008**, *339*, 121–129.
8. Wang, H.; Zhang, J.; Dalai, A. K. Catalyst for Production of Synthesis Gas. U.S. Patent 7,985,701, July 26, 2011.
9. Dowden, D. A.; Schnell, C. R.; Walker, G. T. *The Design of Complex Catalysts*; Fourth International Congress on Catalysis; Rice University: Houston, 1968; pp 1120−1131.
10. Bradford, M. C. J.; Vannice, M. A. CO_2 reforming of CH_4. *Catal. Rev. Sci. Eng.* **1999**, *41*, 1.
11. Richardson, J. T. *Principles of Catalyst Development*; Plenum Press: New York, 1989; pp 28−31.
12. Kyle, B. G. *Chemical and Process Thermodynamics*, 3rd ed.; Prentice Hall PTR: Upper Saddle River, New Jersey: 1999; pp 433−511.
13. Bradford, M. C. J.; Vannice, M. A. CO_2 reforming of CH_4 over supported Pt catalysts. *J. Catal.* **1997**, *173*, 151–157.
14. Fogler, H. S. *Elements of Chemical Reaction Engineering*; Prentice Hall: Upper Saddle River, New Jersey, 1986; pp 452−491.
15. Ginsburg, J. M.; Pina, J.; El Solh, T.; De Lasa, H. I. Coke formation over nickel catalyst under methane dry reforming conditions: Thermodynamic and kinetic models. *Ind. Eng. Chem. Res.* **2005**, *44*, 4846–4854.
16. Hickman, D. A.; Schmidt, L. D. Production of syngas by direct catalytic oxidation of methane. *Science* **1993**, *259*, 343–345.
17. Osaki, T.; Mori, T. Role of potassium in carbon-free CO_2 reforming of methane on K-promoted Ni/Al_2O_3 catalysts. *J. Catal.* **2001**, *204*, 89–97.
18. Yan, Q. G.; Weng, W. Z.; Wan, H. L.; Toghiani, H.; Toghiani, R. K.; Pittman, C. U. Activation of methane to syngas over a Ni/TiO_2 catalyst. *Appl. Catal., A* **2003**, *239*, 43–58.

Downloaded by STANFORD UNIV GREEN LIBR on May 31, 2012 | http://pubs.acs.org
Publication Date (Web): January 20, 2012 | doi: 10.1021/bk-2012-1092.ch012

19. Bradford, M. C. J.; Vannice, M. A. Catalytic reforming of methane with carbon dioxide over nickel catalysts II. Reaction kinetics. *Appl. Catal., A* **1996**, *142*, 97–122.
20. Aparicio, L. M. Transient isotopic studies and microkinetic modeling of methane reforming over nickel catalysts. *J. Catal.* **1997**, *165*, 262–274.
21. Schuurman, Y.; Marquez-Alvarez, C.; Kroll, V. C. H.; Mirodatos, C. Unraveling mechanistic features for the methane reforming by carbon dioxide over different metals and supports by TAP experiments. *Catal. Today* **1998**, *46*, 185–192.
22. Tsipouriari, V. A.; Verykios, X. E. Carbon and oxygen reaction pathways of CO_2 reforming of methane over Ni/La_2O_3 and Ni/Al_2O_3 catalysts studied by isotopic tracing techniques. *J. Catal.* **1999**, *187*, 85–94.
23. Tsipouriari, V. A.; Verykios, X. E. Kinetic study of the catalytic reforming of methane with carbon dioxide to synthesis gas over Ni/La_2O_3 catalyst. *Catal. Today* **2001**, *64*, 83–90.
24. Bitter, J.; Seshan, K.; Lercher, A. Mono and bifunctional pathways of CO_2/CH_4 reforming over Pt and Rh based catalysts. *J. Catal.* **1998**, *176*, 93–101.
25. Bitter, J.; Seshan, K.; Lercher, A. The state of zirconia supported platinum catalysts for CO_2/CH_4 reforming. *J. Catal.* **1997**, *171*, 279–286.
26. Solymosi, F. The bonding, structure and reactions of CO_2 adsorbed on clean and promoted metal surfaces. *J. Mol. Catal.* **1991**, *65*, 337–358.
27. Rostrup-Nielsen, J. R. Industrial relevance of coking. *Catal. Today* **1997**, *37*, 225.
28. Kim, G. J.; Cho, D. S.; Kim, K. H.; Kim, J. H. The reaction of CO_2 with CH_4 to synthesize H_2 and CO over nickel-loaded Y-zeolites. *Catal. Lett.* **1994**, *28*, 41–52.
29. Hei, M.; Chen, H.; Yi, J.; Lin, Y.; Wei, G.; Liao, D. CO_2-reforming of methane on transition metal surfaces. *Surf. Sci.* **1998**, *417*, 82–96.
30. Kroll, V. C. H.; Swaan, H. M.; Mirodatos, C. Methane reforming reaction with carbon dioxide over Ni/SiO_2 catalyst: II. A mechanistic study. *J. Catal.* **1996**, *164*, 387–398.
31. Kroll, V. C. H.; Swaan, H. M.; Mirodatos, C. Methane reforming reaction with carbon dioxide over Ni/SiO_2 catalyst: I. Deactivation studies. *J. Catal.* **1996**, *161*, 409–422.
32. Erdohelyi, A.; Cserenyi, J.; Solymosi, F. Activation of CH_4 and its reaction with CO_2 over supported Rh catalysts. *J. Catal.* **1993**, *141*, 287–299.
33. Mark, M. F.; Maier, W. F. Active surface carbon: A reactive intermediate in the production of synthesis gas from methane and carbon dioxide. *Angew. Chem., Int. Ed. Engl.* **1994**, *33*, 1657–1660.
34. Hu, Y. H.; Ruckenstein, E. Catalytic converstion of methane to syn-gas by partial oxidation and CO2 reforming. *Adv. Catal.* **2004**, *48*, 297–345.
35. Trimm, D. *Design of Industrial Catalysts*; Elsevier: New York, 1980.
36. Ostrupnielsen, J. R.; Hansen, J. H. B. CO_2-reforming of methane over transition metals. *J. Catal.* **1993**, *144*, 38–49.
37. Portugal, U. L.; Santos, A.; Damyanova, S.; Marques, C.; Bueno, J. CO_2 reforming of CH_4 over Rh-containing catalysts. *J. Mol. Catal.* **2002**, *184*, 311.

Downloaded by STANFORD UNIV GREEN LIBR on May 31, 2012 | http://pubs.acs.org
Publication Date (Web): January 20, 2012 | doi: 10.1021/bk-2012-1092.ch012

38. Richardson, J. T.; Garrait, M.; Hung, J. –K. Carbon dioxide reforming with Rh and Pt–Re catalysts dispersed on ceramic foam supports. *Appl. Catal., A* **2003**, *255*, 69–82.
39. Osaki, T.; Mori, T. Role of potassium in carbon-free CO_2 reforming of methane on K-promoted Ni/Al_2O_3 catalysts. *J. Catal.* **2001**, *204*, 89–97.
40. Seok, S. H.; Choi, S. H.; Park, E. D.; Han, S. H.; Lee, J. S. Mn-promoted Ni/Al_2O_3 catalysts for stable carbon dioxide reforming of methane. *J. Catal.* **2002**, *209*, 6–15.
41. Dias, J. A. C.; Assaf, J. M. Influence of calcium content in $Ni/CaO/\gamma\text{-}Al_2O_3$ catalysts for CO_2 reforming of methane. *Catal. Today* **2003**, *85*, 59–68.
42. Quincoces, C. E.; Dicundo, S.; Alvarez, A. M.; Gonzalez, M. G. Effect of addition of CaO on Ni/Al_2O_3 catalysts over CO_2-reforming of methane. *Mater. Lett.* **2001**, *50*, 21–27.
43. Quincoces, C. E.; Vargas, S. P. D.; Grange, P.; Gonzales, M. G. Role of Mo in CO_2 reforming of CH_4 over Mo promoted Ni/Al_2O_3 catalysts. *Mater. Lett.* **2002**, *56*, 698–704.
44. Frusteri, F.; Arena, F.; Calogero, G.; Torre, T.; Parmaliana, A. *Catal. Commun.* **2001**, *2*, 49.
45. Sinfelt, J. H. *Bimetallic Catalysts: Discovery, Concepts and Applications*; Wily: New York, 1983.
46. Ponec,V.; Bond, G. C. *Catalysis by Metals and Alloys*; Elsevier: Amsterdam, 1995.
47. Tomishige, K.; Himeno, Y.; Matsuo, Y.; Yoshinaga, Y.; Fujimoto, K. Catalytic performance and carbon deposition behavior of a NiO-MgO solid solution in methane reforming with carbon dioxide under pressurized conditions. *Ind. Eng. Chem. Res.* **2000**, *39*, 1891–1897.
48. Zhang, H. B.; Chen, P.; Lin, G.-D.; Tsai, K.-R. Development of coking-resistant Ni-based catalyst for partial oxidation and CO_2-reforming of methane to syngas. *Appl. Catal., A* **1998**, *166*, 343–350.
49. Wang, J. B.; Kuo, L.-E.; Huang, T.-J. Study of carbon dioxide reforming of methane over bimetallic Ni-Cr/yttria-doped ceria catalysts. *Appl. Catal., A* **2003**, *249*, 93–105.
50. Choi, J.-S.; Moon, K.-I.; Kim, Y. G.; Lee, J. S.; Kim, C.-H.; Trimm, D. L. Stable carbon dioxide reforming of methane over modified Ni/Al_2O_3 catalysts. *Catal. Lett.* **1998**, *52*, 43–47.
51. Trimm, D. L. Coke formation and minimisation during steam reforming reactions. *Catal. Today* **1997**, *37*, 233–238.
52. Choudhary, V. R.; Mamman, A. S. Simultaneous oxidative conversion and CO_2 or steam reforming of methane to syngas over CoO-NiO-MgO catalyst. *J. Chem. Technol. Biotechnol.* **1998**, *73*, 345–350.
53. Takanabe, K.; Nagaoka, K.; Nariai, K.; Aika, K. I Titania-supported cobalt and nickel bimetallic catalysts for carbon dioxide reforming of methane. *J. Catal.* **2005**, *232*, 268–275.
54. Yamazaki, O.; Nozaki, T.; Omata, K.; Fujimoto, K. Reduction of carbon dioxide by methane with Ni-on-MgO-CaO containing catalysts. *Chem. Lett.* **1992**, *21*, 1953–1954.

55. Horiuchi, T.; Sakuma, K.; Fukui, T.; Kubo, Y.; Osaki, T.; Mori, T. Suppression of carbon deposition in the CO_2-reforming of CH_4 by adding basic metal oxides to a Ni/Al_2O_3 catalyst. *Appl. Catal., A* **1996**, *144*, 111–120.
56. Delmon, B.; Grange, P.; Jacobs, A.; Poucelet, G. Preparation of Catalysts II. In *Studies in Surface and Catalysis*, Volume II; Elsevier: Amsterdam, 1979.
57. Delmon, B.; Jacobs, A.; Poucelet, G. Preparation of Catalysts I. In *Studies in Surface and Catalysis*, Volume I; Elsevier: Amsterdam, 1976.
58. Cornils, B.; Herrmann, W. A.; Schlogl, R.; Wong, C. H. *Catalysis from A to Z*; second, completely revised and enlarged ed.; Wiley-VCH Verlag GmbH & Co. KGaA: Weinheim, 2003.
59. Wijngaarden R. J.; Kronberg, A.; Westerterp, K. R. *Industrial Catalysis – Optimizing Catalysts and Processes*; Wiley-VCH Verlag GmbH: Weinheim, 1998; pp 25−59.
60. Jolivet, J.-P.; Henry, M.; Livage, J. *Metal Oxide Chemistry and Synthesis*; John Wiley & Sons, Ltd.: Toronto, 1994; pp 3−52.
61. Twigg, M. V. *Catalyst Handbook*, second ed.; Wolfe Publishing, Ltd.: London, 1989; pp34−48.
62. Miller, J. T.; Neylon, M. K.; Marshall, C. L.; Kropf, A. J. X-ray Absorption Studies of Catalyst Nanoparticles. In *Dekker Encyclopedia of Nanoscience and Nanotechnology*; Marcel Dekker, Inc.: New York, 2004; pp 3953−3972.

Downloaded by STANFORD UNIV GREEN LIBR on May 31, 2012 | http://pubs.acs.org
Publication Date (Web): January 20, 2012 | doi: 10.1021/bk-2012-1092.ch012

Downloaded by 89.163.35.42 on May 30, 2012 | http://pubs.acs.org
Publication Date (Web): January 20, 2012 | doi: 10.1021/bk-2012-1092.ix002

Subject Index

A

Acetic acid
  effect of concentration, 135, 135*f*
  effect of feed flow rate, 135, 136*f*
  effect of temperature, 131, 131*f*, 132*f*, 133*f*
  reaction involved in steam reforming, 116
  screening of catalysts, 130
  time on stream (run time) on conversion and yield, 133, 134*f*
AHM. *See* Ammonium heptamolybdate (AHM)
Alcoholysis, 94
Alkanethiol, 3
Al_2O_3 cocatalyst, 30
Aluminium-sec-tributoxide, 88
Ammonium heptamolybdate (AHM), 62
Ammonium metatungstate (AMT), 143
AMT. *See* Ammonium metatungstate (AMT)
Anderson-Schulz-Flory (ASF) kinetics, 169
Aquaconversion®, 77
AR. *See* Atmospheric residue (AR)
ASF. *See* Anderson-Schulz-Flory (ASF) kinetics
Atmospheric residue (AR), 52

B

Barrett-Joynes-Halenda (BJH) plots, 119
BET. *See* Brunauer-Emmett-Teller (BET)
Biodiesel production
  catalyst characterization, 96, 97
  catalyst deactivation and reusability study, 103
  catalyst preparation, 95
  catalytic activity, 100
  effect of presence of water, 105
  experimental design, statistical analysis, and optimization, 101
  overvew, 94
  reagents, 95
  textural property of various catalysts, 97
  transesterification of triolein, 96
Bitumen
  distillation curves, 80*f*
  feedstock solution, 78
Boudouard reaction, 2
Bruker Smart6000 CCD detector, 96
Brunauer-Emmett-Teller (BET), 63, 96

C

CA. *See* Citric acid (CA)
CASAXPS software, 6
Catalyst, nomenclature and composition summary, 114*t*
CCD. *See* Central Composite Design (CCD)
Central Composite Design (CCD), 96
Citric acid (CA), 61
Cobalt nitrate hexahydrate, 88
Cobalt–molybdenum catalysts, 77
Constant temperature bath (CTB), 142
Co-supported catalysts, 175
CTB. *See* Constant temperature bath (CTB)
CuO cocatalyst, 29
CuO doping concentration, 30, 31*t*
CuZnNi catalyst
  SEM-EDX image and peaks, 124*f*
  TEM image, 128*f*
  TEM image of freshly prepared Ca12Al7, 127*f*
  TGA-DTA graphs, 126*f*

D

DADS. *See* Dialkyl disulfide (DADS)
DBT. *See* Dibenzothiophene (DBT)
DDO. *See* Direct deoxygenation (DDO)
Deionized water, 113
Density functional theory (DFT), 2
DFT. *See* Density functional theory (DFT)
Dialkyl disulfide (DADS), 1
Dibenzothiophene (DBT), 38
Dimethylbiphenyl (DMBP), 88
1,3-Dimethylcyclopentane, 69
4,6-Dimethyldibenzothiophene (4,6-DMDBT), 38, 88
Direct deoxygenation (DDO), 70
DMBP. *See* Dimethylbiphenyl (DMBP)
4,6-DMDBT. *See* 4,6-Dimethyldibenzothiophene (4,6-DMDBT)

Downloaded by 89.163.35.42 on May 30, 2012 | http://pubs.acs.org
Publication Date (Web): January 20, 2012 | doi: 10.1021/bk-2012-1092.ix002

E

Ester
  response surface plot, 102*f*
  using fresh and spent catalyst, 103*t*
EXAFS. *See* Extended X-ray absorption fine structure spectroscopy (EXAFS)
Extended X-ray absorption fine structure spectroscopy (EXAFS), 196

F

FAME. *See* Fatty acid alkyl esters (FAME)
Fatty acid alkyl esters (FAME), 94
Fe-W catalysts, 139
  acidity determination by FTIR-pyridine adsorption studies, 156
  catalytic activity, 145
  catalytic performance tests, 158
  characterization, 143
  DRIFT spectroscopy for CO adsorption, 155, 155*f*
  effect of precoking on sulfur and nitrogen conversion, 159
  elemental analysis, 146
  elemental composition, CO uptake, and HDS/HDN steady-state activities of SBA-15 supported, 147*t*
  N_2 adsorption-desorption isotherms measurement, 150, 151*f*
  physical properties of SBA-15, 149*t*
  pore size effect on sulfur and nitrogen conversions, 160
  preparation of SBA-15 and γ-Al_2O_3 supported, 143
  results and discussion, 146
  small-angle X-ray scattering analysis, 147
  TEM, HRTEM, and SEM analyses, 152
  temperature effect on sulfur and nitrogen conversions, 161
  transmission electron micrographs, 153*f*
  wide-angle X-ray diffraction, 148, 149*f*
FFA. *See* Free Fatty Acids (FFA); Free fatty acids (FFA)
FID. *See* Flame ionization detector (FID)
Flame ionization detector (FID), 40
Fourier Transform Infrared Spectroscopy (FTIR), 170
Free Fatty Acids (FFA), 94, 105
  effects, 106*f*
  triolein on acid value, 107*f*
FTIR. *See* Fourier Transform Infrared Spectroscopy (FTIR)

G

Gas chromatograph (GC), 171
Gaussian-Lorentzian product, 6
GC. *See* Gas chromatograph (GC)

H

H_2. *See* Hydrogen (H_2)
HDA. *See* Hydrodearomatization (HDA)
HDN. *See* Hydrodenitrogenation (HDN)
HDS. *See* Hydrodesulfurization (HDS)
Heavy gas oil, Athabasca bitumen, 145*t*
Heavy oil
  catalytic cracking
    reaction mechanism, 81
    using oil, 78
  conventional upgrading processes, 77
  experimental procedure, 78
  fractions of bitumen, 79
  overview, 76
  phase change of the metal oxide catalyst during conversion, 82*f*
  production of light oil, 78
  properties, 76*t*
  upgrading process, 77
    using water, 77
Heavy oil treating (HOT), 77
Heteropoly acids (HPA), 94
High-performance liquid chromatography (HPLC), 96
HOT. *See* Heavy oil treating (HOT)
HPA. *See* Heteropoly acids (HPA)
HPLC. *See* High-performance liquid chromatography (HPLC)
HYD. *See* Hydrogenation (HYD) reactions
Hydrocarbons, 84
Hydrocracking, 77
Hydrodearomatization (HDA), 38
Hydrodenitrogenation (HDN), 38, 62, 140
Hydrodeoxygenation (HDO), 62
Hydrodesulfurization
  overview, 88
  results and discussion, 89
Hydrodesulfurization (HDS), 37, 38, 62, 140
Hydrogenation (HYD) reactions, 140
Hydrogen formation, 30
Hydrogen (H_2)
  BET surface areas and pore volume of catalysts, 118*t*
  BJH isotherms, 118*f*
  catalyst characterization, 113
  catalyst preparation, 112

Downloaded by 89.163.35.42 on May 30, 2012 | http://pubs.acs.org
Publication Date (Web): January 20, 2012 | doi: 10.1021/bk-2012-1092.ix002

  experiment, 113
  metal dispersion and particle size distribution, 129*t*
  overview, 112
  results and discussion, 118
  screening of catalysts, 129*t*
  steam reforming, 112
  surface area and pore size analysis, 114

I

ICP-MS. *See* Inductivity coupled plasma-mass spectrometer (ICP-MS)
Inductivity coupled plasma-mass spectrometer (ICP-MS), 96

J

Japanese Industrial Standards (JIS), 54
JIS. *See* Japanese Industrial Standards (JIS)

K

Karl-Fisher titration method, 97
Kratos HS system, 4

L

LGO. *See* Light gas oil (LGO)
LHSV. *See* Liquid hourly space velocity (LHSV)
Light gas oil (LGO), 37
  catalyst in situ synthesis and upgrading reaction, 39
  changes of sulfur concentration, 47*f*
  characterization, 40
  effect of reaction temperature, 47
  effect of water content, 44
  excess water and sulfur removal percentages, 45*f*
  feedstock and product, 39*f*
  fraction distributions at different reaction temperatures, 48*f*
  fraction distributions before and after treatment over MoSx catalysts, 44*f*
  materials, 39
  overview, 38
  product boiling point distributions, 46*f*
  sulfur removals and pitch conversions, 47*t*
  syn-gas composition on HDS, 46
Light oil
  production, 78
  properties, 83
Liquid hourly space velocity (LHSV), 139, 146

M

MCHT. *See* Methylcyclohexyltoluene (MCHT)
Methane conversion, 8*f*
Methylcyclohexyltoluene (MCHT), 88
Micrometrics adsorption equipment, 96
MMT. *See* Montmorillonite (MMT)
Montmorillonite (MMT), 168
  acidity and reduction behavior, 179
  carbon number distribution, 185*f*
  characterization techniques, 170
  Co-supported catalysts, 175
  deviation of ASF distribution, 188
  evolution of pore structure, 178
  FT performance, 182
  FT reaction, 171
  FT synthesis over different catalysts, 184*t*
  long range order, 172
  materials and methods, 170
  mesopore size distribution, 180*f*
  N_2 adsorption-desorption isotherms, 180*f*
  overview, 168
  product analysis, 171
  product distribution, 184
  reaction procedure, 171
  reduction of cobalt oxides, 182
  results and discussion, 172
  short range order, 173
  structural properties, 172
  structure and catalytic performance, 187
  surface area, 177
  textural and crystal properties, 177*t*
  textural properties, 176
  time-on-stream CO conversion, 183*f*
MoP-CA catalysts, 61
  activity, 64
  characterization, 63
  conversion and product selectivity of 4-methylphenol, 68*t*
  HDO consumption rates, 71
  initial HDO rate of 4-methylphenol vs. CO uptake, 72*f*

  - overview, 61
  - physical and chemical properties, 65*t*
  - preparation, 62
  - product selectivity versus 4-methylphenol conversion, 70*f*
  - proposed reaction scheme for hydrodeoxygenation of 4-methylphenol, 70*f*
  - results and discussion, 64
  - site density based on BET, XRD, and TEM size vs. CO uptake, 71*t*
  - 1st-order rate constant versus carbon content, 69*f*
  - TEM images, 67*f*
  - TEM micrographs, 66
  - XRD diffractograms, 66*f*

N

- Na-MMT. *See* Na-type montmorillonite (Na-MMT)
- Na-type montmorillonite (Na-MMT), 167
  - FTIR spectra, 174*f*
  - H_2-TPR profiles, 181*f*
  - NH_3-TPD profiles, 181*f*
  - SEM images, 176*f*
  - XRD patterns, 173*f*
- n-Dodecane, 54
  - distributions of carbon numbers on catalytic cracking, 58*f*
  - product distribution and parameters in gasoline fraction, 59*t*
- NEBULA catalysts, 88
- Ni-based catalysts, 2
  - after use in steam reforming tests (TOS), 9*t*
  - catalytic activity, 19*f*, 20*f*
  - characterization, 6
  - CO/CO_2 ratio obtained, 18*f*
  - experimental set-up and protocol, 4, 6*f*
  - materials and methods, 4
  - overview, 2
  - reproducibility, 16*t*
  - results and discussion, 7
  - time on stream (TOS), with theoretical equilibrium values of steam reforming reactor, 17*f*
- Nickel–molybdenum catalysts, 77
- Ni-Co bimetallic nanocatalyst
  - carbon formation, 205
  - catalyst components, 209
  - catalyst design, 197, 197*f*
  - catalyst preparation method, 211
    - decision chart, 212*t*
    - test, 213
  - catalyst properties, 209
  - catalyst support, 210
  - composition and BET surface area of catalysts, 214*t*
  - coprecipitation and impregnation, 214
  - effects of inert N_2, 204, 205*f*, 207*f*
  - equilibrium composition as a function of initial CO_2/CH_4 molar ratio, 204, 204*f*
  - equilibrium composition as a function of temperature, 201, 202*f*
  - equilibrium composition as a function of total pressure, 202, 203*f*
  - network of reaction, 200
  - overview, 195
  - primary active component, 209
  - primary reactant reaction, 198, 198*t*
  - product-product reaction, 200, 200*t*
  - proposed reaction mechanism, 207
  - reactant cross-interaction reaction, 199, 199*t*
  - reactant self-interaction reaction, 198, 199*t*
  - reactant-product reaction, 199, 200*t*
  - secondary active component, 210
  - stoichiometric analysis, 198
  - target reaction, 197
  - thermodynamic analysis, 201
  - XANES and EXAFS analysis, 217*t*
- NiW catalysts, 141

P

- PD. *See* Pore diameter (PD)
- Perkin-Elmer 2400 Series II CHNS/O analyzer, 63
- PFPD. *See* Pulsed flame photometric detector (PFPD)
- PHILIPS CM12 microscope, 116
- Photocatalyst, 26
- Photocatalytic hydrogen production, 25
  - 10 vol% methanol solution, 28*t*, 29*t*, 30*t*
  - Al_2O_3 doping concentration, 32*t*, 33*t*
  - aqueous methanol solution, 26
  - CuO doping concentration, 31*t*, 32*t*
  - experiment, 26
  - reaction mechanism, 33
  - results and discussion, 27
- Pore diameter (PD), 89
- Pore volume (PV), 89
- Precipitation
  - chemistry, 212
  - process and unit operation, 213, 213*f*

Downloaded by 89.163.35.42 on May 30, 2012 | http://pubs.acs.org
Publication Date (Web): January 20, 2012 | doi: 10.1021/bk-2012-1092.ix002

Downloaded by 89.163.35.42 on May 30, 2012 | http://pubs.acs.org
Publication Date (Web): January 20, 2012 | doi: 10.1021/bk-2012-1092.ix002

Pulsed flame photometric detector (PFPD), 40
PV. *See* Pore volume (PV)
Pyrex column vessel reactor, 27
Pyridine
  adsorption spectra of pure SBA-15 and FeW/SBA-15, 157*f*, 158*f*
  FTIR spectra, 99*f*, 104*f*

Q

Quadrupole mass spectrometer, 4
Quantachrome Autoasorb, 4

R

Refinery gas analyzer (RGA), 40
Reformer evaluation bench, 5*f*
Response surface methodology (RSM), 93
RGA. *See* Refinery gas analyzer (RGA)
RSM. *See* Response surface methodology (RSM)

S

SA. *See* Surface area (SA)
SAGD. *See* Steam-assisted gravity drainage (SAGD)
SAM. *See* Self-assembled monolayers (SAM)
SBA-15 catalysts, 93
  FTIR spectra, 99*f*
  TEM image, 100*f*
  XRD patterns, 98*f*
SBA-15 supports, 142
Scanning electron microscope (SEM), 4, 13*f*, 14*f*, 115
  morphology, 10
  Ni-255 as-synthesized catalyst, 12*f*
SDA. *See* Structure-directing agent (SDA)
Self-assembled monolayers (SAM), 3
SEM. *See* Scanning electron microscope (SEM)
Silica-alumina
  aerogels, 52
  compositions of solution for preparation, 54*t*
  flowchart, 53*f*
  surface area and pore volume, 56*t*
  XRD patterns of various catalysts, 55*f*
Small-angle X-ray scattering analysis, Fe-W catalysts, 147, 148*f*
SnO cocatalyst, 28
SOR. *See* Start-of-run (SOR)
SRM. *See* Steam reforming of methane (SRM)
Start-of-run (SOR), 159
Steam-assisted gravity drainage (SAGD), 78
Steam reforming of methane (SRM), 1, 2
Structure-directing agent (SDA), 142
Sulfur compounds
  GC analysis, 42
  typical removal, 44*t*
Surface area (SA), 89

T

TCD. *See* Thermal conductivity detector (TCD)
Teflon bottle, 95
TEM. *See* Transmission electron microscope (TEM)
Temperature programmed desorption (TPD), 113, 115
  metal dispersion of freshly prepared catalyst, 122*t*
  NH_3 curves, 121*f*
Temperature programmed oxidation (TPO), 113, 114
  used CuZnNi at different temperatures, 123*f*
Temperature programmed reduction (TPR), 62, 113, 114
TEOS. *See* Tetraethyl orthosilicate (TEOS)
Tetraethyl orthosilicate (TEOS), 51, 142
Thermal conductivity detector (TCD), 27, 40, 63, 114
Therminoic specific detector (TSD), 40
Time of flight-secondary ion mass spectroscopy (TOF-SIMS), 8
Time on stream (TOS), 1, 159
TOF. *See* Turn over frequency (TOF)
TOF-SIMS. *See* Time of flight-secondary ion mass spectroscopy (TOF-SIMS)
TOS. *See* Time on stream (TOS)
TPA. *See* 12-Tungstophosphoric acid (TPA)
TPD. *See* Temperature programmed desorption (TPD)
TPO. *See* Temperature programmed oxidation (TPO)
TPR. *See* Temperature programmed reduction (TPR)

In Nanocatalysis for Fuels and Chemicals; Dalai, A.;
ACS Symposium Series; American Chemical Society: Washington, DC, 2012.

Downloaded by 89.163.35.42 on May 30, 2012 | http://pubs.acs.org
Publication Date (Web): January 20, 2012 | doi: 10.1021/bk-2012-1092.ix002

Transesterification reaction, 94
  reaction mechanism of acid catalyzed simultaneous esterification, 107*f*
Transmission electron microscope (TEM), 63, 116
Transmittance electron microscopy (TEM), 196
Triolein
  catalyst loading screening, 101*f*
  effect of presence of water, 105*f*
  metal content, 104*t*
  optimization of stirring speed, 100*f*
  transesterification, 96
TSD. *See* Therminoic specific detector (TSD)
12-Tungstophosphoric acid (TPA), 93
  content fresh and spent catalysts, 104*t*
Turn over frequency (TOF), 61

V

Vacuum gas oil (VGO), 52
VGO. *See* Vacuum gas oil (VGO)

W

Water gas shift reaction (WGSR), 37
  gas content changes, 46*f*
WEO. *See* World Energy Outlook (WEO)
WGSR. *See* Water gas shift reaction (WGSR)
World Energy Outlook (WEO), 140

X

XANES. *See* X-ray absorption near edge spectroscopy (XANES)
XPS. *See* X-ray photoelectron spectroscopy (XPS)
X-ray absorption near edge spectroscopy (XANES), 196
X-ray diffraction (XRD) patterns
  commercial catalyst, 91*f*
  complex metal oxide catalyst of iron, 81*f*
X-ray photoelectron spectroscopy (XPS), 3, 10*f*, 11*f*
  analysis, 12
  spectral deconvolution studies, 13
X-ray powder diffraction (XRD), 115
  freshly prepared CuZnNi, CuZn and Ca12Al7 catalysts, 122*f*
XRD. *See* X-ray powder diffraction (XRD)

Z

Zeolite, BJH pore-size distributions, 57*f*
ZnO cocatalyst, 28